AFOSR-TR. 89-0156

HIGH-TEMPERATURE METAL MATRIX COMPOSITES

AD-A204 966

ANNUAL REPORT

VOLUME 2

AIR FORCE OFFICE OF SCIENTIFIC RESEARCH

Contract No. F49620-87-C-0017

October 1, 1987 - September 30, 1988

CARNEGIE MELLON UNIVERSITY

Pittsburgh, PA 15213

Principal Investigator, A.W. Thompson

and

University of California, Berkeley
Clemson University

DTIC
ELECTE
1 5 FEB 1989
E

October 30, 1988

89   2   15   128

REPORT DOCUMENTATION PAGE

REPORT SECURITY CLASSIFICATION	1b RESTRICTIVE MARKINGS
Unclassified	

SECURITY CLASSIFICATION AUTHORITY	3 DISTRIBUTION/AVAILABILITY OF REPORT
DECLASSIFICATION/DOWNGRADING SCHEDULE	See Distribution List

PERFORMING ORGANIZATION REPORT NUMBER(S)	5 MONITORING ORGANIZATION REPORT NUMBER(S)
	AFOSR·TR· 89-0156

NAME OF PERFORMING ORGANIZATION	6b OFFICE SYMBOL (If applicable)	7a NAME OF MONITORING ORGANIZATION
Dept. of Metallurgical Eng. and Materials Science		AFOSR/NE

ADDRESS (City, State, and ZIP Code)	7b ADDRESS (City, State, and ZIP Code)
Carnegie Mellon University Pittsburgh, PA 15213	BLDG, 410 BOLLING AFB, DC 20332

NAME OF FUNDING/SPONSORING ORGANIZATION	8b. OFFICE SYMBOL (If applicable)	9 PROCUREMENT INSTRUMENT IDENTIFICATION NUMBER
Air Force Office of Sci. Res.	NE	F49620 87-C-0017

ADDRESS (City, State, and ZIP Code)	10 SOURCE OF FUNDING NUMBERS			
BLDG, 410 BOLLING AFB, DC 20332	PROGRAM ELEMENT NO.	PROJECT NO.	TASK NO	WORK UNIT ACCESSION NO.
	61102F	2306	A1	

TITLE (Include Security Classification)

High-temperature Metal Matrix Composites (Vol 2)

PERSONAL AUTHOR(S)
A.W. Thompson and those listed in table of contents

a. TYPE OF REPORT	13b. TIME COVERED	14. DATE OF REPORT (Year, Month, Day)	15 PAGE COUNT
Annual Report	FROM 10/1/87 TO 9/30/88	1988 October 30	430

SUPPLEMENTARY NOTATION

COSATI CODES			18. SUBJECT TERMS (Continue on reverse if necessary and identify by block number)
FIELD	GROUP	SUB-GROUP	High-temperature metal-matrix composites, interfaces, composite processing, aluminides, Ti-aluminides, fatigue, creep, toughness, atomic resolution. (TYS)

ABSTRACT (Continue on reverse if necessary and identify by block number)

The Annual Report for Year 2 of the University Research Initiative grant at Carnegie Mellon University on High-temperature Metal Matrix Structural Composites contains sections on processing, characterization, and mechanical properties. These are further divided into reports from individual tasks on powder blending and consolidation, composite performance, structure and composition of composite interfaces, fatigue crack growth, creep, and fracture behavior.

DISTRIBUTION/AVAILABILITY OF ABSTRACT	21 ABSTRACT SECURITY CLASSIFICATION
☒ UNCLASSIFIED/UNLIMITED ☐ SAME AS RPT ☐ DTIC USERS	Unclassified

NAME OF RESPONSIBLE INDIVIDUAL	22b TELEPHONE (Include Area Code)	22c OFFICE SYMBOL
A.W. Thompson A. ROSENSTEIN	(202) 268-2700 767-4933	NE

FORM 1473, 84 MAR   83 APR edition may be used until exhausted   SECURITY CLASSIFICATION OF THIS PAGE
All other editions are obsolete

TABLE OF CONTENTS

VOLUME 1

Determination of Residual Stress in an Al/SiC Metal Matrix Composite using Convergent Beam Electron Diffraction

Introduction

Residual stresses in metal matrix composites (MMC) are caused by rapid temperature changes and a large difference in the coefficients of thermal expansion between the Al matrix and SiC fiber. The purpose of this work is to determine the strain gradient in the Al matrix near the SiC/matrix interface caused by residual stresses. Accurate determination of these stresses is important for understanding their influence on the mechanical properties and ageing characteristics of the composite.

Experimental Technique

Quenching an Al -10%SiC MMC, after a 505 °C solutionizing heat treatment, will produce residual stresses in the matrix. Dislocations are generated to relieve part of the stress in the matrix. However, residual stresses which are slightly below the yield stress, will remain in the matrix. In an effort to quantify this strain, the technique of convergent beam electron diffraction (CBED) was used. This technique enables determination of lattice parameter and angle changes with an accuracy on the order of 10^{-4} or 0.01%.

Using CBED, an ~20 nm probe is positioned in the matrix at several distances from a specific fiber/matrix interface and a CBED pattern is obtained at each position. The positions of the deficit higher-order Laue zone (HOLZ) lines, observed in the bright field disk, are sensitive to lattice parameter and angle changes and shift in the presence of elastic strain. Once the HOLZ line patterns have been obtained, the normal and shear strains can be determined at each position by matching experimental HOLZ line patterns with computer simulations, as shown in the following figures.

Schematic showing a SiC fiber /Al grain with the Al matrix in a [111] orientation. Bright field TEM micrograph shows the exact probe position where the CBED information is collected.
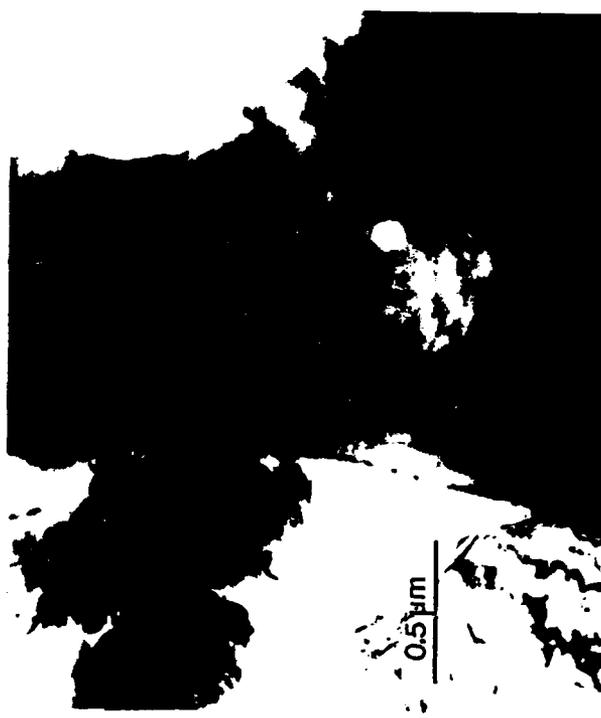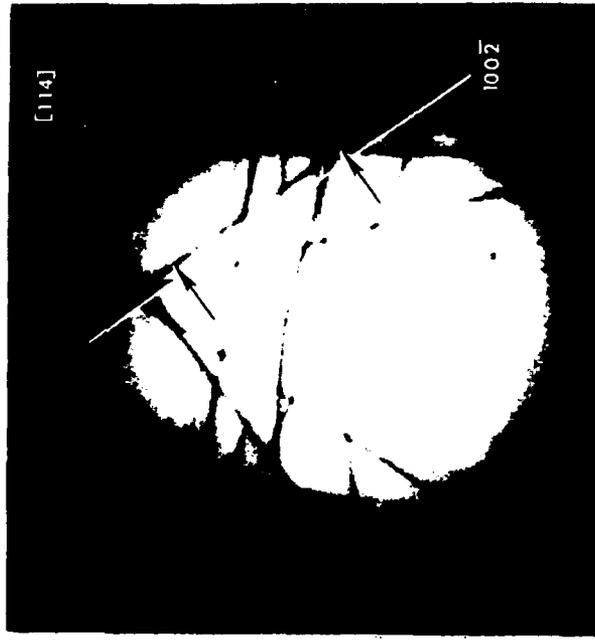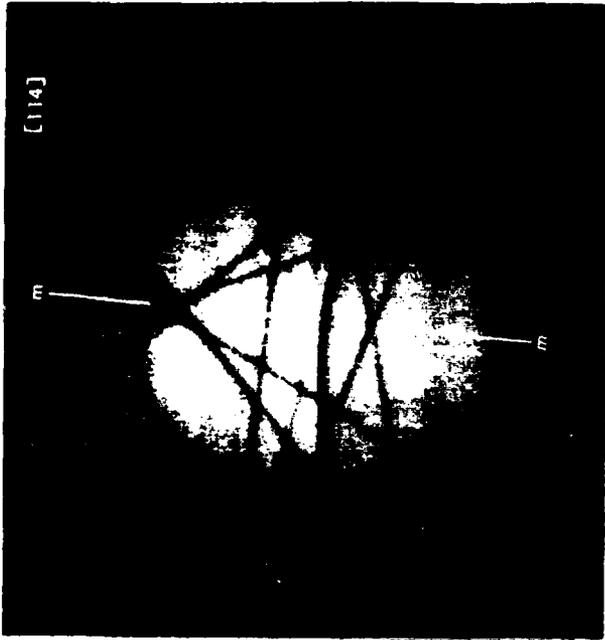
When the probe is positioned near the SiC/matrix interface, a shift of the $(10\,0\bar{2})$ HOLZ line causes a loss of mirror symmetry. This shift occurs because large residual stresses have produced lattice parameter changes.
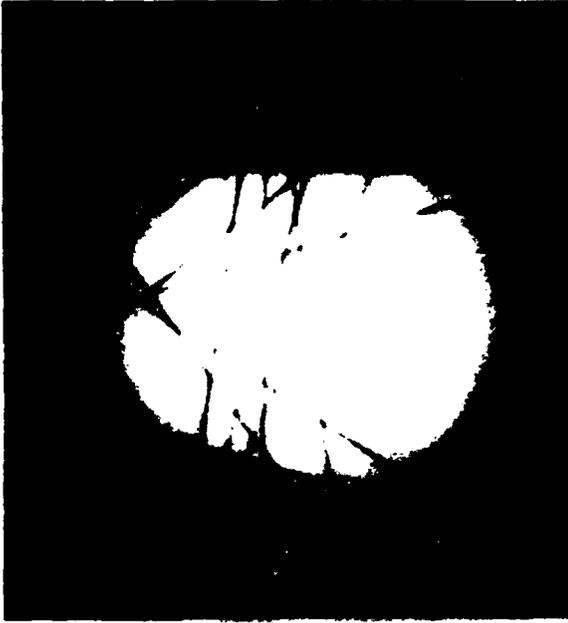
Aluminum   119.4KeV

B = [141]

a = .4043nm   b = c = .4035nm

a = b = c = .4035nm
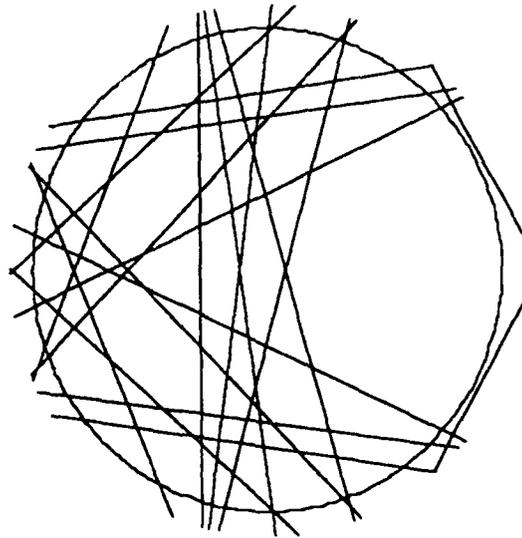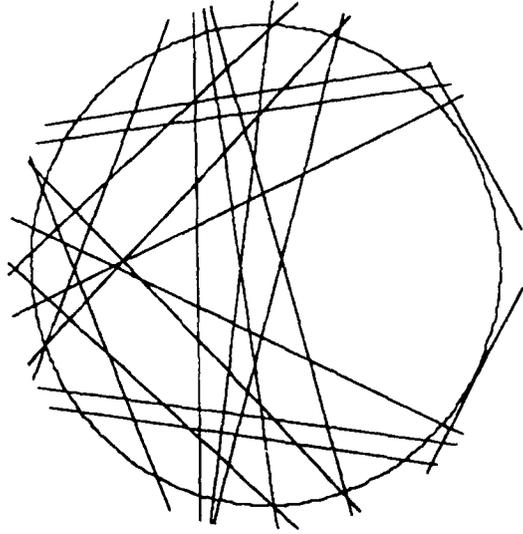
Experimental HOLZ line patterns are shown with the matching computer simulations. The 'a' lattice parameter was increased by 0.2% in the right simulation to fit the experimental image.

Results

Partial analysis of the variation in residual stress as a function of distances has been determined and is shown on the graph.

The plot shows that strains on the order of 0.2% (the macroscopic yield stress) are present near the interface and diminish to zero approximately 1μm away.
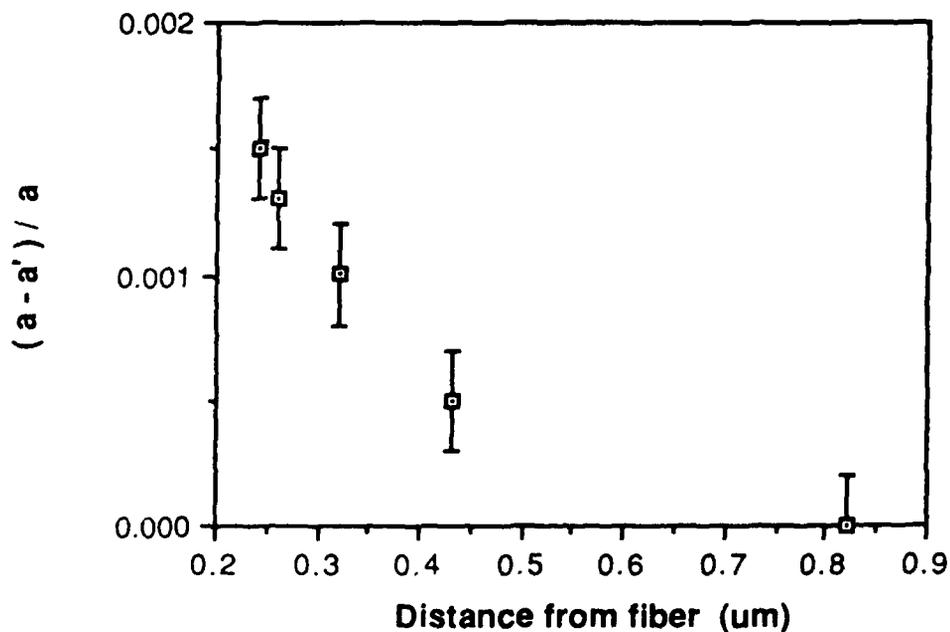
TEM Investigation of Interfaces in a Two-Phase TiAl Alloy

G. J. Mahon and J. M. Howe

Department of Metallurgical Engineering
and Materials Science
Carnegie Mellon University
Pittsburgh, PA 15213

Abstract

The atomic structures of the γ/α_2 and γ/γ_T interfaces in a TiAl alloy were investigated using conventional and high-resolution TEM in order to understand the growth mechanisms and deformation behavior of the two-phase alloy. The results show that the α_2 plates grow from the γ phase by the migration of $a/6\langle 112\rangle$ partial dislocation ledges across the faces and that the γ/α_2 interface usually contains closely spaced arrays of interfacial dislocations. Deformation twins cut through both γ twin boundaries and α_2 plates during deformation although slip of twinning dislocations through α_2 appears to be a difficult process. Both the γ/α_2 and γ/γ_T interfaces can be imaged and modeled at the atomic level although slight crystal and/or beam tilt can complicate image interpretation.

1. Introduction

Nearly eqiatomic TiAl alloys are currently under investigation for use as high-temperature materials in aerospace applications because they exhibit a desirable combination of high modulus retention, creep and oxidation resistance at elevated temperatures and low density [1,2]. These titanium alloys, which contain about 40-50 at.% Al, usually consist of a lamellar mixture of the γ (TiAl) and α_2 (Ti$_3$Al) phases [3-5]. Although several studies have examined the microstructure and deformation mechanisms of the individual γ and α_2 phases [1,6,7], there have been few detailed studies of these phenomena in the two-phase material [3,6]. The purpose of this study is to perform detailed transmission electron microscopy (TEM) analyses of a two-phase TiAl alloy in order to understand: i) the growth mechanism of the α_2 plates from the g phase, ii) the atomic structure of the γ/α_2 and γ/γ_T interfaces, and iii) the role of these interfaces and phase relationships on deformation of the two-phase alloy. Initial results from these areas are discussed in this paper; some aspects are still under investigation and will be discussed in more detail in a future publication.

The γ phase has an L1$_0$ structure (AuCuI prototype) with nominally equal concentrations of Ti and Al, although a range of homogeneity from 49-66 at.% Al depending on temperature has been reported [8,9]. The lattice parameters vary with alloy composition and range from a = 0.397-0.401 nm and c = 0.404-0.408 nm [10]. The γ phase remains ordered up to its melting point of about 1465°C and twin-related γ variants (the c-axis may align along one of three ⟨001⟩ directions) are usually observed after conventional

and rapid solidification of nearly equiatomic TiAl alloys [4,5,7,11]. Several different solidification paths have been proposed for the these alloys depending on the composition, undercooling and kinetics [9,12]. The γ phase has also been reported to grow from an α_2 matrix at dislocations and grain boundaries by the dissociation of a $1/3\langle11\bar{2}0\rangle$ dislocation into two $1/3\langle10\bar{1}0\rangle$ partial dislocations in a Ti-40 at.% Al alloy [13].

Aging of single-phase γ alloys below about 1000°C results in the formation of plates of the α_2 (Ti$_3$Al) phase [4,7], which has a DO$_{19}$ structure (Ni$_3$Sn prototype) and forms with the orientation relationship $(111)_\gamma\|(0001)_{\alpha_2}$ and $\langle110\rangle_\gamma\|\langle11\bar{2}0\rangle_{\alpha_2}$ [4,6,7]. The α_2 phase has a range of homogeneity from about 20-38 at.% Al depending on temperature [8,14] and the lattice parameters vary with composition from a = 0.572-576 nm and c = 0.460-0.464 nm [15,16]. This phase undergoes an order/disorder transformation and thermal antiphase boundaries may be present in α_2 depending on the heat treatment [14].

The γ and α_2 phases are both ordered and exhibit planar slip [1-3,17,18]. The deformation mode of TiAl has been investigated at several temperatures in the range of 25-1000°C [1,7,19] and possible theoretical dislocation structures in AuCuI-type alloys have been proposed [20]. It appears that two types of dislocations are involved in plastic deformation of TiAl, an a/2[110] dislocation and an a[011] superdislocation, with the density of the a[110] dislocations being about twice that of the a/2[110] dislocations. It also appears that the mobility of the a/6[112] partial dislocation, which is a constituent of the a[011] superdislocation as well as the twinning dislocation, controls the plasticity of TiAl. Below about 630°C the a/6[112]

partial is immobile while above 700°C the activity of the a[110] superdislocations increases rapidly with temperature. The same a/6[112] partial is also the twinning dislocation so that twinning becomes an increasingly important deformation mode for TiAl above 700°C, resulting in a ductile/brittle transition between 700-800°C. These twins, which are of the type (111)[112], also play a role in the deformation at room temperature [1].

Deformation studies of the α_2 phase over the composition range from 25-40 at.% Al have shown that slip occurs mainly by closely spaced a/3⟨11$\bar{2}$0⟩ superdislocation pairs on the prism, pyramidal and basal planes although some a/3⟨11$\bar{2}$3⟩ (c+a) dislocations are also involved [6]. These a-type dislocations often occur as long straight segments along ⟨11$\bar{2}$0⟩ directions in a pure screw orientation and it has been suggested that there is a large decrease in the number of a/3⟨11$\bar{2}$3⟩ dislocations formed as the Al content increases above 25 at.% These data are in partial agreement with proposed dislocations for the DO_{19} structure [20], which consists of pairs of superlattice dislocations, each further dissociated into pairs of partials similar to dislocation structures in $L1_2$ alloys. It also becomes increasingly difficult to produce plastic deformation without brittle failure as the Al concentration increases above 25 at.% and this has been largely attributed to an increased tendency to concentrate planar slip within a few bands [6]. It has also been suggested that the number of (c+a) dislocations is nearly constant with temperature for a given α_2 alloy and that the increase in ductility with increasing temperature in α_2 alloys cannot be explained by an increase in the number of (c+a) dislocations to accommodate non-basal slip [21]. Intersection of planar slip bands with twin boundaries has also been shown to induces twins in lamellae of the γ phase [6].

The purpose of this study is to understand the atomic structures of the γ/α_2 and γ/γ_T transformation interfaces in order to better understand the growth mechanisms and deformation behavior of the two-phase alloy. A TiAl alloy was chosen for the study since there is some uncertainity about the nature of the phase diagram at lower Al concentrations [8,9]. Furthermore, in a TiAl alloy it is possible to grow α_2 plates directly from the γ phase by isothermal aging. This produces a relatively simple microstructure which should facilitate observation of the atomic structures of the γ and α_2 phases and the interfaces between these phases.

2. Experimental Procedures

The TiAl alloy in this study was prepared by powder metallurgy techniques [17]. An ingot containing 50 at.% Al (36 wt.% Al) was consumably arc melted, homogenized for one week at 1000°C and converted to powder using the rotary electrode process. The powders were sieved to -35 mesh and consolidated by hot extrusion at 1400°C with an extrusion ratio of 16:1. The extruded rod was then solutionized for 2 hrs. at 1200°C, isothermally aged for 24 hrs. at 900°C and quenched into water. Thin foils were prepared for conventional and high-resolution TEM by cutting 125 μm slices from the rods on a diamond saw, punching 3.0 mm discs from the slices and electropolishing in a twin-jet Fischione apparatus using a 5%H_2SO_4/methanol electrolyte at -35°C and 20 V. After perforation, samples were examined on one of three microscopes: i) a Philips EM420 operating at 120 keV was used for convergent-beam electron diffraction (CBED) and conventional TEM analyses, ii) the Berkeley JEOL ARM1000 operating at 800 keV was used to obtain high-resolution TEM (HRTEM) images of γ twin boundaries, and iii)

the JEOL 4000EX at Case Western Reserve University was used for HRTEM imaging of the γ/α_2 interface. For HRTEM, through-focus series of images were taken in a $\langle 110 \rangle \gamma \| \langle 11\bar{2}0 \rangle \alpha_2$ zone axis using a 6.5 nm^{-1} radius objective aperture and focus increments of 3.0 nm. Simulated HRTEM images were calculated using the SHRLI multislice programs [22] with all reflections to 40.0 nm^{-1} included in the calculations. The microscope parameters used for the JEOL ARM1000 in the simulations were C_s - 2.4 mm, α - 1.0 mrad, Δ - 5.0 nm and $\Delta f_{Scherzer}$ - -60.0 nm and for the JEOL 4000EX: C_s - 1.0 mm, α - 0.8 mrad, Δ - 5.0 nm and $\Delta f_{Scherzer}$ - -50.0 nm

3. Results and Discussion

3.1. Microstructure Produced by Solutionizing and Isothermal Aging

Conventional TEM observations indicate that the TiAl alloy consists of relatively coarse lamellae (about one micrometer thick) of twin-related γ variants at the solutionizing temperature of 1200°C (see Fig. 12(a) for example). In addition, deformation twins are produced prior to aging at 900°C. This can be seen from Fig. 1, which shows an α_2 plate which has grown through a narrow deformation twin during aging at 900°C. The diffusional growth of the α_2 phase has completely eliminated the twin boundary along the line of intersection, indicating that the twin boundary existed before the α_2 phase. Also note that dislocations were produced in the γ phase from the intersection event. Examination of other γ/α_2 intersections showed that additional γ twins are nucleated below 900°C, presumably during the water quench. This is illustrated in Figs. 2 through 4, which show

much thinner twins (sometimes only nanometers thick) intersecting and propagating through preexisting α_2 plates (Figs. 2 and 3), twin-related γ variants (Fig. 2) as well as other deformation twins (Fig. 4). Note that the intersection of the two deformation twins in Fig. 4 has generated dislocations into the γ phase along a well defined slip band. It is important to distinguish these deformation twins from the twin-related γ variants formed previously at the solutionizing temperature. The deformation twins are probably created during quenching in response to quenching strains and in an attempt to accommodate the lattice contraction that occurs in the γ and α_2 phases as the temperature decreases.

Although studies of the deformation behavior of this two-phase alloy have just begun, a number of interesting observations regarding deformation can be inferred from the images in Figs. 2 through 4. Firstly, it is apparent that twinning is a significant mechanism for deformation of the two-phase alloy, similar to observations of deformation in a single-phase γ alloy [1], although the exact temperature at which the twins occurred during quenching is not known. In addition, the deformation twins cut through both preexisting α_2 and twin-related γ variants, indicating that both phases are deformed. This is demonstrated in Fig. 2(a), where a thin deformation twin has cut through both the γ phase and an α_2 plate, displacing dislocations in the γ phase and the α_2 plate edges across the deformation twin plane (arrows in Fig. 2(a)). It was often observed that a particular twin became successively thinner as it crossed through successive α_2 plates, indicating that the deformation twin does not easily propagate across the α_2 plates. This effect is illustrated in Fig. 2(b), where a relatively thick deformation twin has largely arrested at an α_2 plate and a microtwin has formed on the

opposite side of the plate (arrows in Fig. 2(b)). Therefore, it would appear that only a few twinning dislocations are able to propagate through these plates under the initial stress concentration to form a continuing twin on the opposite side. This is supported by the weak-beam dark-field TEM image in Fig. 3(a), which shows dislocation tangles in an α_2 plate at the plane of intersection with a γ deformation twin. Also note from the enlargement of region A in Fig. 3(b), that some of the slip dislocations present in the α_2 phase at the twin intersection consist of pairs of superlattice dislocations (arrows), presumably of the type $a/3\langle 11\bar{2}0\rangle$, although complete Burgers vector analysis of these dislocations remain to be performed.

Clearly, it appears that in order to fully understand the deformation mechanisms and properties of the two-phase alloy, it will be necessary to understand deformation in both phases as well as across the interfaces bewteen the phases. To that end, a complete characterization of the various interfaces in these alloys is necessary, and these are examined in the following sections.

3.2. High-Resolution TEM Investigation of Interfaces

3.2.1. The γ/α_2 Interface

A low-magnification phase-contrast image of an γ/α_2 interface viewed along $\langle 110\rangle\gamma\|\langle 11\bar{2}0\rangle\alpha_2$ is shown in Fig. 5(a). The interface contains regularly spaced ledges about 5 nm apart. The γ phase displays characteristic light/dark contrast among alternate Ti and Al (200) planes (labelled in Fig. 5(b)) and the position of the atomic interface between the

$(1\,1\,1)\gamma$ and $(0001)\alpha_2$ planes is indicated by horizontal lines in Fig. 5(b). From these features, it is evident that the γ/α_2 interface is atomically flat and perfectly coherent except for the presence of the ledges, which are two $(1\,1\,1)\gamma$ planes high in this area. Burgers circuits were constructed around the ledges, similar to the method used to identify edge (90°) and screw (30°) $a/6\langle 112\rangle$ Shockley partial dislocation ledges at the edges of γ' plates in an Al-Ag alloy [23]. Application of these circuits in Fig. 5(b) shows that one 30° Shockley partial dislocation is associated with each two-plane ledge. This indicates that growth of the α_2 phase occurs by the migration of Shockley partial dislocation ledges on alternate $(1\,1\,1)\gamma$ planes parallel to the interface, just as for the f.c.c. $\rightarrow$ h.c.p. transformation between the disordered α matrix and γ' plates in Al-Ag [23-25]. This is the reverse counterpart to the growth of γ plates from the α_2 phase by $a/3\langle 10\bar{1}0\rangle$ partial dislocations [6]. Discrete dislocation cores are not readily visible in Fig. 5 because the dislocations are largely in a screw orientation with respect to the electron beam. This is consistent with conventional TEM contrast analyses which indicate that many of the dislocations in the interface are Shockley partials with a line direction along $\langle 110\rangle\gamma$ (or $\langle 11\bar{2}0\rangle\alpha_2$).

An enlargement of the γ/α_2 interface from region A in Fig. 5 is shown in Fig. 6 with a superimposed simulated HRTEM image of the interface for a crystal thickness of 3 nm, an objective lens defocus of -80.0 nm and 1.0 mrad beam tilt about the $[0001]\alpha_2$ direction. There is excellent agreement between the experimental and simulated image, which was based on the atomic model for the γ/α_2 interface shown in Fig. 7. Analysis of the model interface in Fig. 7 shows that pure Ti columns in the γ and α_2 phases are aligned across the interface. Such alignment could be produced if the

structural component of the $\gamma \to \alpha_2$ transformation occurred by the passage of a Shockley partial dislocation along the C plane in the γ phase, which is consistent with the previous analyses. In addition, the columns of Al atoms in both the B and C planes involved in the transformation must increase by 50 at.% Ti in order for the α_2 phase to achieve the composition Ti$_3$Al as the interface advances.

From the model interface shown in Fig. 7, the HRTEM image should show relatively strong evidence of alignment of the Ti columns in the γ and α_2 phases across the interface from the contrast of the atomic columns. Such contrast is barely revealed in Figs. 5 and 6, and it is clear that these images also exhibit additional contrast from alternate basal planes not predicted for stochiometric Ti$_3$Al. There are two possible reasons for these discrepancies: i) there is additional order among alternate basal planes which is not included in the model in Fig. 7, or the alternate contrast among the basal planes is the result of slight crystal or beam tilt (double diffraction) during HRTEM imaging. By simulating an image based on the model interface but with a 1.0 mrad beam tilt, matching was obtained as shown in Fig. 6, but this result alone does not preclude the first possiblity. Therefore, CBED was performed on the α_2 phase in order to determine whether the 000l, l=odd reflections are forbidden. The results from this study are shown in Fig. 8.

In the <11$\bar{2}$0> zone-axis pattern in Fig. 8(a), characteristic Gjonnes-Moodie lines [26] are apparent in the 0001 disks but not in the higher-order 0003 disks. Hence, this result suggests that the 000l reflections are kinematically forbidden, but it is not conclusive. More convincing evidence is shown in Fig. 8(b), where the electron beam has been tilted about four Bragg

angles about the 000ℓ axis (within the mirror plane containing the 000ℓ reflections) and lines of zero intensity are present in both low and high-order 000ℓ, ℓ=odd disks. This result provides more convincing evidence that the 000ℓ, ℓ=odd reflections are forbidden, indicating that there is no difference in composition or order among alternate basal planes and that beam tilt is probably responsible for the image contrast in Fig. 6 discussed above. Further confirmation of this might be determined by microanalysis of the α_2 phase using ALCHEMI [27].

It is also worth commenting on the contrast at the γ/α_2 interface obtained from conventional TEM. The interface usually contained closely spaced (<50 nm) interfacial dislocations which existed either as a parallel array or as rectangular and hexagonal networks. Such networks are visible on the inclined γ/α_2 interface in Fig. 3. Initial contrast analyses indicate that many of the dislocations in the γ/α_2 interface are mixed Shockley partial dislocations with a line direction along <110>γ. Evidence for such arrays of dislocations can be seen in the TEM images of previous investigators [4] although they were not analyzed in detail. It seems likely that these arrays of interfacial dislocations will play a significant role in determining the response of the γ and α_2 phases to deformation and, in particular, to the passage of dislocations through the interface.

3.2.2. The γ/γ_T Deformation Twin Interface

Figure 9 shows a low-magnification phase-contrast image of four deformation twins with a similar width of several tens of nanometers. The positions of the coherent twin boundaries are indicated by arrows along the

edges in Fig. 9 since they do not display strong contrast in the image. Similar twins are indicated as γ_1 and γ_2 in Fig. 9 and it is apparent that the two sets of twins display different contrast in the HRTEM image. This is more apparent in the enlargement of region A, which is shown in Fig. 10. The twin boundary in Fig. 10 should contain a mirror plane at the position indicated by the horizontal line, as illustrated by atomic model for a (111)[112] twin shown in Fig. 11. However, the (200) planes in Fig. 10 have different contrast across the boundary and there is no mirror plane. This was the case for essentially every twin boundary that was examined by HRTEM in this study. A simulated image of the deformation twin boundary which matched the asymmetric contrast of the experimental image is shown superimposed in Fig. 10. In order to reproduce the experimental image, it was necessary to introduce a tilt of about one Bragg angle between opposite crystals across the twin boundary in the simulation. This indicated that either the twins were slightly misoriented in the bulk alloy or that stress relaxation occurred as the thin foils were produced, i.e., it is due to surface relaxation.

In order to verify that the twins are actually misoriented and that some other effect is not responsible for the observed contrast in the HRTEM images, CBED was performed across successive twin-related γ variants in a <110>γ orientation at approximately constant thickness parallel to the foil edge, as illustrated in Fig. 12(a). The resulting <110>γ CBED patterns are shown in Figs. 12(b) through 12(f). The starting CBED pattern for a preexisting γ variant in Fig. 12(b) was oriented exactly at the zone axis. Comparison with the remaining CBED patterns in Figs. 12(c) through 12(f) shows that the twin variants deviate from an exact zone axis setting by

about one Bragg angle, usually along the 00ℓ systematic row. This deviation occurred precisely at the interface and is not caused by continuous bending of the thin foil. These data indicate that the twin-related γ variants are slightly misoriented with respect to one another.

Also note that some of the planar boundaries (for example between b and c) which appear to be twin boundaries in Fig. 12(a) are not twin related according to their corresponding CBED patterns. Some of these boundaries (such as between b and c) appear to be low-angle grain boundaries within particular twins. This explains why the contrast between twins b and c is the same in Fig. 12(a), as is that of d and e, and why these particular boundaries are not always planar. Since they are low-angle grain boundaries which would not be expected to relax and tilt during polishing it is concluded that the slight misorientation between the twin-related γ variants is probably real and not a surface or thin foil effect. The reason for this slight misorientation may be related to the fact that the twin-related variant plane in TiAl is (111) and not (110). The tetragonality between different twin-related γ variants will not be accommodated perfectly across (111) planes and this could lead to slight misorientation between the variants and/or misfit dislocations at the interface. This subject deserves further investigation and is discussed below. The same effect may not occur for a (111)[112] deformation twin and hence asymmetry in HRTEM images of a (111)[112] deformation twin may be due to a thin foil effect.

It is interesting that the twin plane for both the high temperature twin-related variants and the lower temperature deformation twins is (111) in TiAl. This is in contrast to the (110) twin plane observed for twin-related

variants in the prototype AuCu, combined with a (111) plane for deformation twins in the same alloy [28,29]. The difference in initial twin-related variants may arise from one or a combination of several factors: i) the tetragonality in TiAl is only about 2% compared to AuCu where it is closer to 8% [30] and it thus behaves more like an f.c.c. annealing twin on (111), ii) TiAl is ordered up to the melting point while AuCu goes through a cubic → tetragonal transformation during ordering at a temperature well below the melting point [31], and iii) the TiAl phase may originate from a b.c.c. precursor, which favors a twinning plane of (111) during transformation to f.c.c. as opposed to a (110) twinning plane for a cubic → tetragonal transformation [32]. Symmetry considerations indicate that the twinning plane should be (110) for TiAl so ii) and iii) above are probably not the most important factors for TiAl. Thus, i) is probably the most likely explanation. It should also be noted that the average width of the twin-related γ variants and deformation twins relates to the tetragonality between a and c [32]. Although quantitative comparison with predicted and observed twin widths have not been performed due to the large variation observed at both the microscopic and atomic levels, the deformation twins are generally several orders of magnitude thinner than the twin-related γ variants.

Conclusions

The results from this TEM investigation have shown the following:

i) In addition to α_2 plates, both twin-related γ variants and deformation twins are present in the γ phase after solutionizing, aging at 900°C and quenching to room temperature,

ii) Deformation twins cut through γ twin boundaries and α_2 plates during deformation although slip of superlattice dislocations through α_2 during intersection appears to be a difficult process,

iii) The α_2 plates often possess complicated interfacial dislocation structures and grow from the γ phase by the migration of a/6<112> partial dislocation ledges across the faces, similar to γ'' plates in Al-Ag,

iv) The γ/α_2 interface can be imaged and modeled at the atomic level although crystal and beam tilt readily introduce image artifacts and therefore impose stringent conditions for direct imaging of the atomic structure, and

v) The γ/γ_T deformation twin interface can be imaged and modeled at the atomic level although slight misorientation between twins often leads to asymmetric contrast which destroys the mirror plane in HRTEM images.

Acknowledgements

References

1. H. A. Lipsitt, D. Shechtman and R. E. Schafrik: Metall. Trans., 1975, vol. 6A, 1991-1996.

2. H. Lipsitt: High-Temperature Ordered Intermetallic Alloys, C. C. Koch, C. T. Liu and N. S. Stoloff, eds., Materials Research Society, 1985, pp. 351-364.

3. S. M. L. Sastry and H. A. Lipsitt: Metall. Trans., 1977, vol. 8A, 299-308.

4. J. C. Williams: Precipitation Processes in Solids, K. C. Russell and H. I. Aaronson, eds., The Metall. Soc. AIME, 1978, pp. 191-221.

5. J. J. Valencia, C. McCullough, C. G. Levi and R. Mehrabian: Scripta Metall., 1987, vol. 21, 1341-1346.

6. J. C. Williams and M. J. Blackburn: Ordered Alloys, B. H. Kear, et al., eds., Claitor's Press, 1970, pp. 425-445.

7. D. Shechtman, M. J. Blackburn and H. A. Lipsitt: Metall. Trans., 1974, vol. 5, pp. 1373-1381.

8. J. L. Murray: Metall. Trans., 1988, vol. 19A, pp. 243-255.

9. C. McCullough, J. J. Valencia, H. Mateos, C. G. Levi and R. Mehrabian: Scripta Metall, 1988, vol. 22, pp. 1131-1136.

10. P. Duwez and J. L. Taylor: J. Metals, 1952, Jan., 70-71.

11. C. R. Feng, D. J. Michael and C. R. Crowe: Scripta Metall., 1988, vol. 22, pp. 1481-1586.

12. J. A. Graves, J. H. Perepezko, C. H. Ward and F. H. Froes: Scripta Metall., 1987, vol. 21, pp. 567-572.

13. M. J. Blackburn: The Science, Technology and Applications of Titanium, R. Jaffee and N. E. Promisel, eds., Pergamon Press, 1970, pp. 633-642.

14. M. J. Blackburn: Trans. Metall. Soc. AIME, 1967, vol. 239, pp. 1200-1208.

15. A. J. Goldak and J. Gordon Parr: Trans. Metall. Soc. AIME, 1961, vol. 221, pp. 639-640.

16. F. A. Crossley: Trans. Metall. Soc. AIME, 1966, vol. 236, pp. 1174-1184.

17. P. L. Martin, H. A. Lipsitt, N. T. Nuhfer and J. C. Williams: Proceedings of the 4th International Conference on Titanium, Japan, 1980, pp. 1245-1254.

18. S. M. L. Sastry and H. A. Lipsitt: Proceedings of the 4th International Conference on Titanium, Japan, 1980, pp. 1231-1240.

19. G. Hug, A. Loiseau and P. Veyssiere: Philos. Mag. A, 1988, vol. 57(3), pp. 499-523.

20. M. J. Marcinkowski: Electron Microscopy and Strength of Crystals, G. Thomas and J. Washburn, eds., Interscience Publishers, 1963, pp. 331-439.

21. B. J. Marquardt, G. K. Scarr, J. C. Chesnutt, C. G. Rhodes and H. L. Fraser: Proceedings of the 6th World Congress on Titanium, France, 1988, to be published.

22. M. A. O'Keefe and P. R. Buseck: Trans. Amer. Cryst. Assoc., 1979, vol. 15, pp. 27-46.

23. J. M. Howe, U. Dahmen and R. Gronsky, Philos. Mag. A, 1987, vol. 56(1), pp. 31-61.

24. J. A. Hren and G. Thomas: Trans. Metall. Soc. AIME, 1963, vol. 227, pp. 308-318.

25. C. Laird and H. I. Aaronson: Acta Metall., 1969, vol. 17, pp. 505-525.

26. J. Gjonnes and A. F. Moodie: Acta Cryst., 1965, vol. A31, pp. 65-67.

27. J. C. H. Spence and J. Taftø: J. Microscopy, 1983, vol. 130(2), pp. 147-154.

28. D. W. Pashley, J. L. Robertson and M. J. Stowell: Philos. Mag. A, 1965, vol. 8(11), pp. 83-98.

29. P. N. Syutkin, V. I. Syutkina, O. D. Shashkov, E. S. Yakoyleva and N. N. Buinov: Ordered Alloys, B. H. Kear, et al., eds., Claitor's Press, 1970, pp. 227-239.

30. R. Smith and J. S. Bowles: Acta Metall., 1960, vol. 8, pp. 405-418.

31. D. W. Pashley and A. E. B. Presland: Proc. European Congress on Electron Microscopy, Delft, 1961, pp. 429-439.

32. A. G. Khachaturyan: Theory of Structural Transformations in Solids, John Wiley and Sons, 1983, pp. 171-172.

Figure Captions

Figure 1. Bright-field TEM image of an α_2 plate (approximately edge-on) which has grown through a preexisting γ deformation twin. There is no evidence of deformation in the α_2 plate, in contrast to the intersections shown in Figs. 2 and 3.

Figure 2. (a) and (b) Bright-field TEM images of a deformation twin (horizontal) cutting through α_2 plates and preexisting twin boundaries from twin-related γ variants. The interface of the α_2 plate is displaced across the deformation twin in (a) and a microtwin (arrows) has formed on the left side of the α_2 plate in (b).

Figure 3. (a) Weak-beam dark-field TEM image of a deformation twin intersecting a preexisting α_2 plate. Twinning dislocations appear to penetrate into the α_2 plate. Note the complicated dislocation arrays in the γ/α_2 interfaces. (b) Enlargement from region A in (a) showing pairs of superdislocations about 5 nm apart (arrows).

Figure 4. Bright-field TEM image of a deformation twin (highlighted by arrows) which has intersected a previous deformation twin on another slip plane. Note the dislocations generated from the intersection event and the displacement of the intersected twin.

Figure 5. (a) High-resolution TEM image of the γ/α_2 interface viewed along $<110>\gamma\|<11\bar{2}0>\alpha_2$. A series of ledges (arrows) are present at the interface. (b) Enlargement of the region between A and C showing Burgers

circuits around two interfacial ledges. The S indicates the start of the Burgers circuit and F indicates the finish. The low-index (111) and (200) planes are indicated in the γ phase in (b).

Figure 6. Enlargement of the γ/α_2 interface with a simulated image based on the model structure in Fig. 7 superimposed. Note that it is barely possible to distinguish the Ti and Al-rich columns from the image contrast in the basal planes of α_2 just to the right of the simulated image

Figure 7. Atomic model of the γ/α_2 interface showing the structural change necessary for growth of the interface.

Figure 8. (a) A ‹11$\bar{2}$0› zone axis CBED pattern from the α_2 phase. The 0000 beam is indicated by an asterisk. (b) Gjonnes-Moodie lines present in the 000ℓ, ℓ-odd disks after tilting about four Bragg angles about the 000ℓ axis to increase the intensity of the higher-order 000ℓ reflections.

Figure 9. Low-magnification phase-contrast image of four deformation twins of similar width viewed along a ‹110›γ orientation. The positions of the coherent twin boundaries are indicated by arrows and similar twins are labelled γ_1 and γ_2.

Figure 10. Enlargement of the twin interface from region A in Fig. 9 with a simulated HRTEM image of the twin interface for a crystal thickness of 7.0 nm at -70.0 nm defocus superimposed. The γ_1 and γ_2 twins are slightly misoriented across the twin boundary.

Figure 11. Atomic model of a coherent (111)[112] deformation twin boundary in the γ phase viewed along a [110]γ direction.

Figure 12. (a) Several parallel twin-related γ variants intersecting the foil edge with the approximate positions of the probe corresponding to Figs. (b) through (f) indicated. (b) through (f) <110>γ CBED patterns from twin-related γ variants with the pattern center indicated by an asterisk.

Fig. 1

Figure 2

α_2

γ

0.2 μm

A

50 nm
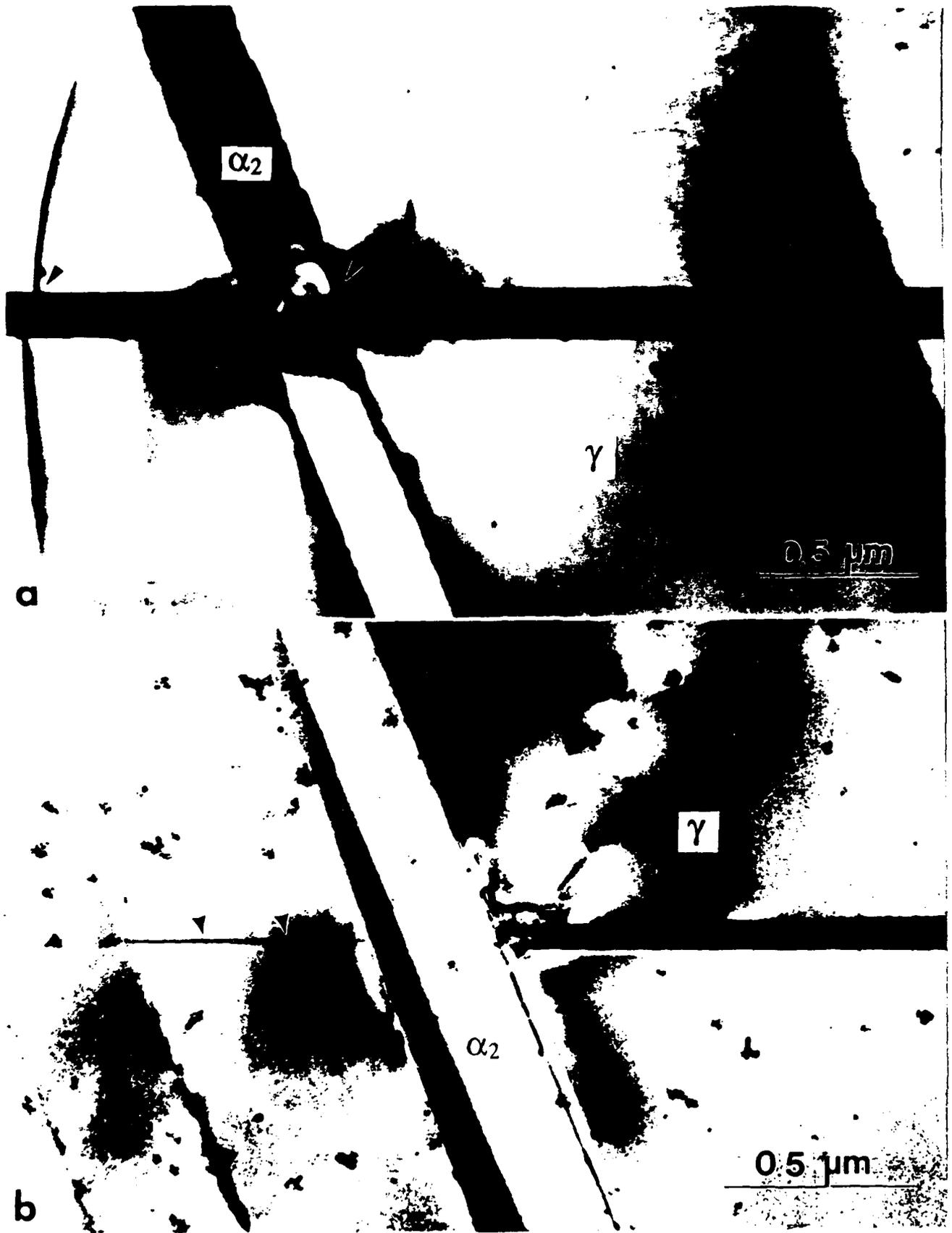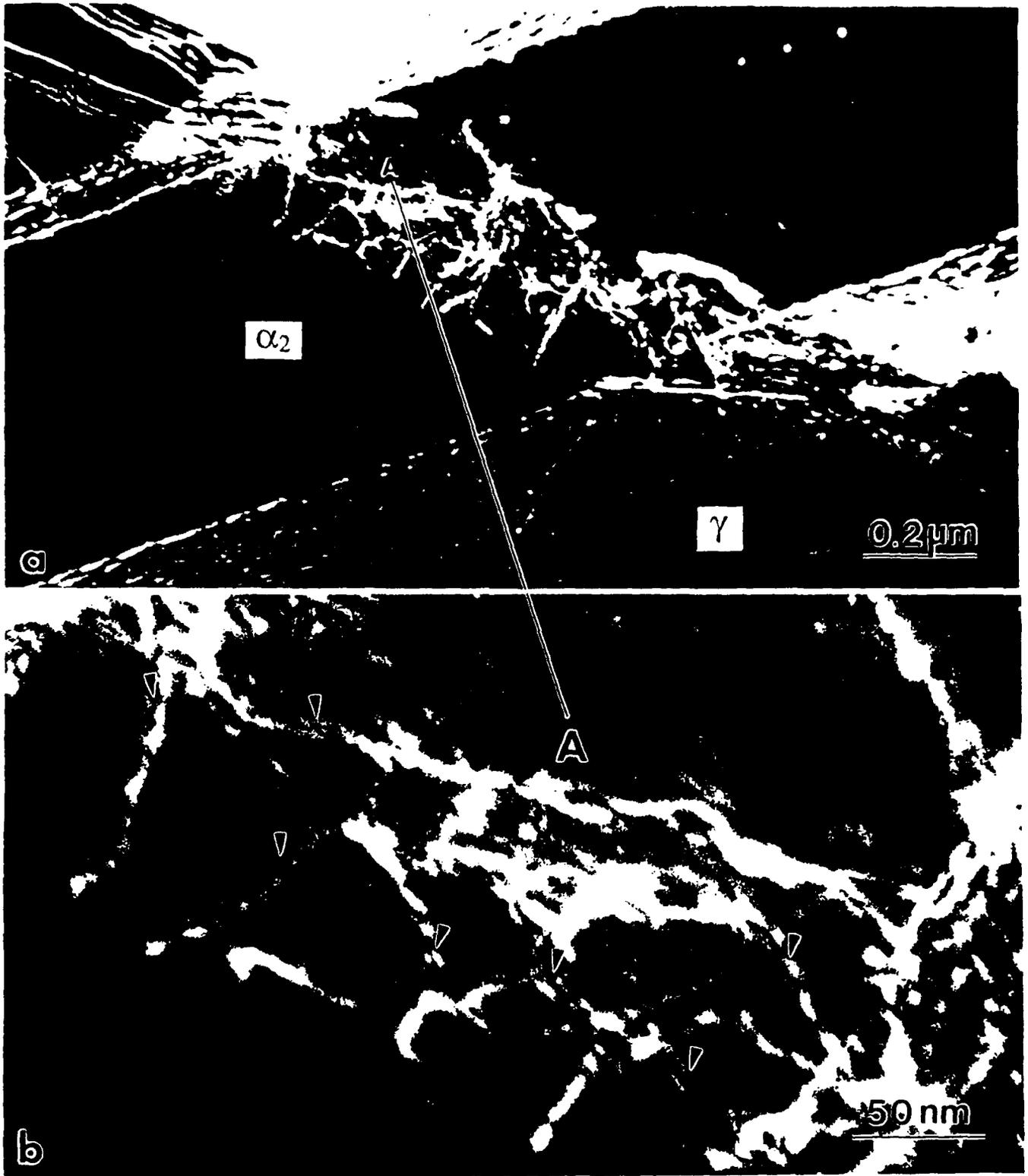
Fig. 3.

Fig. 4.

Fig. 5.

Figure 6

γ-TiAl

α₂-Ti₃Al
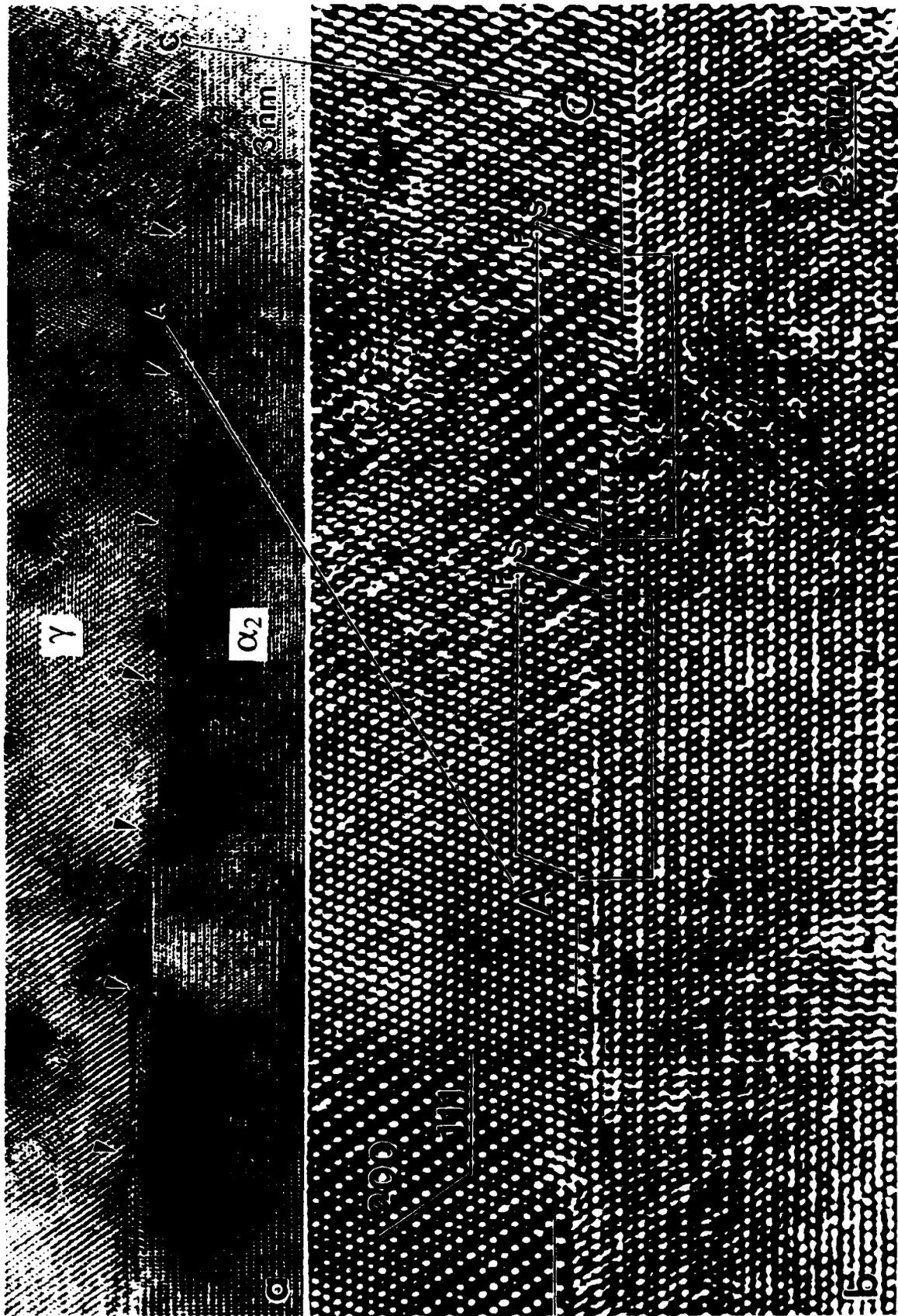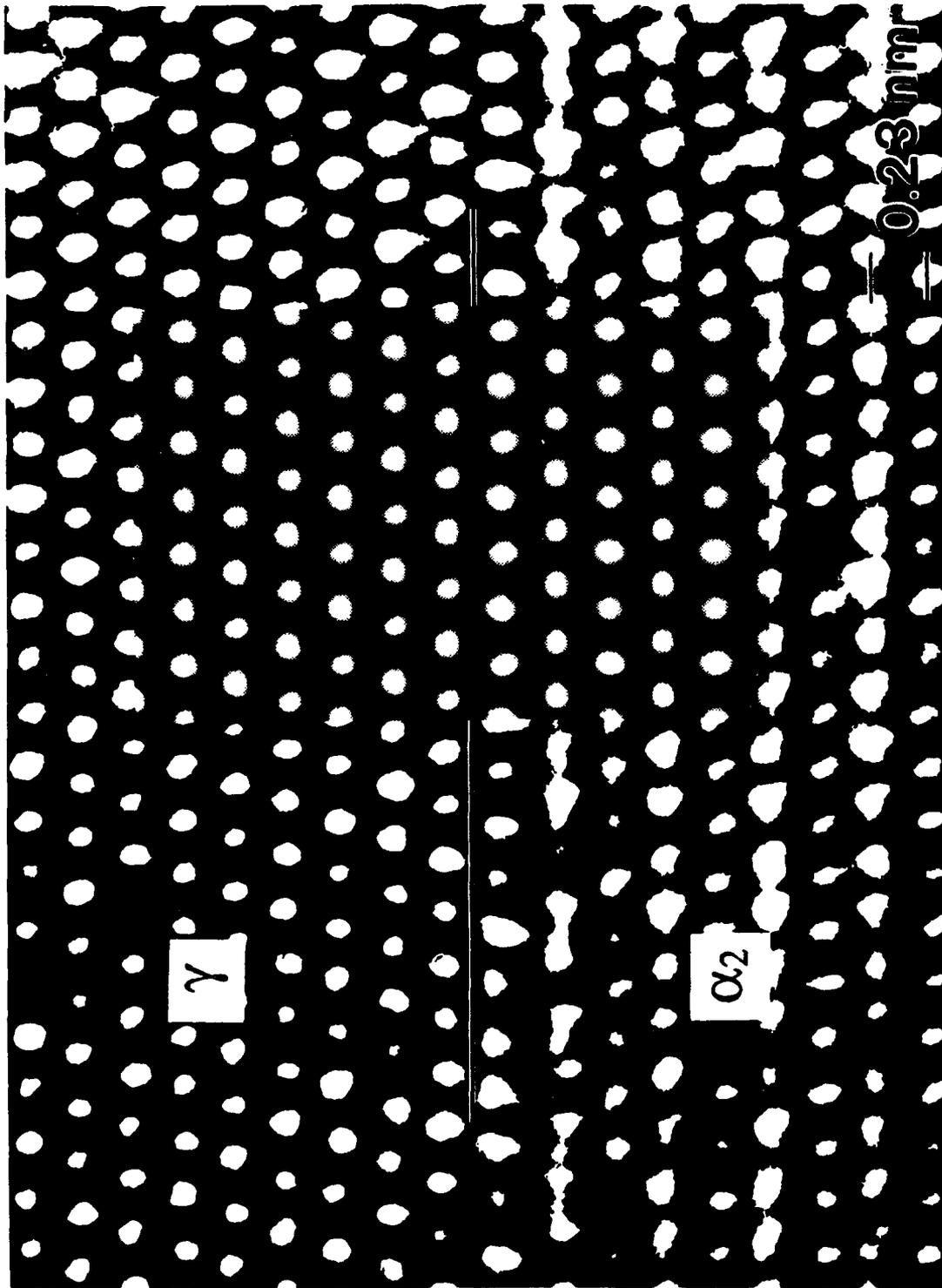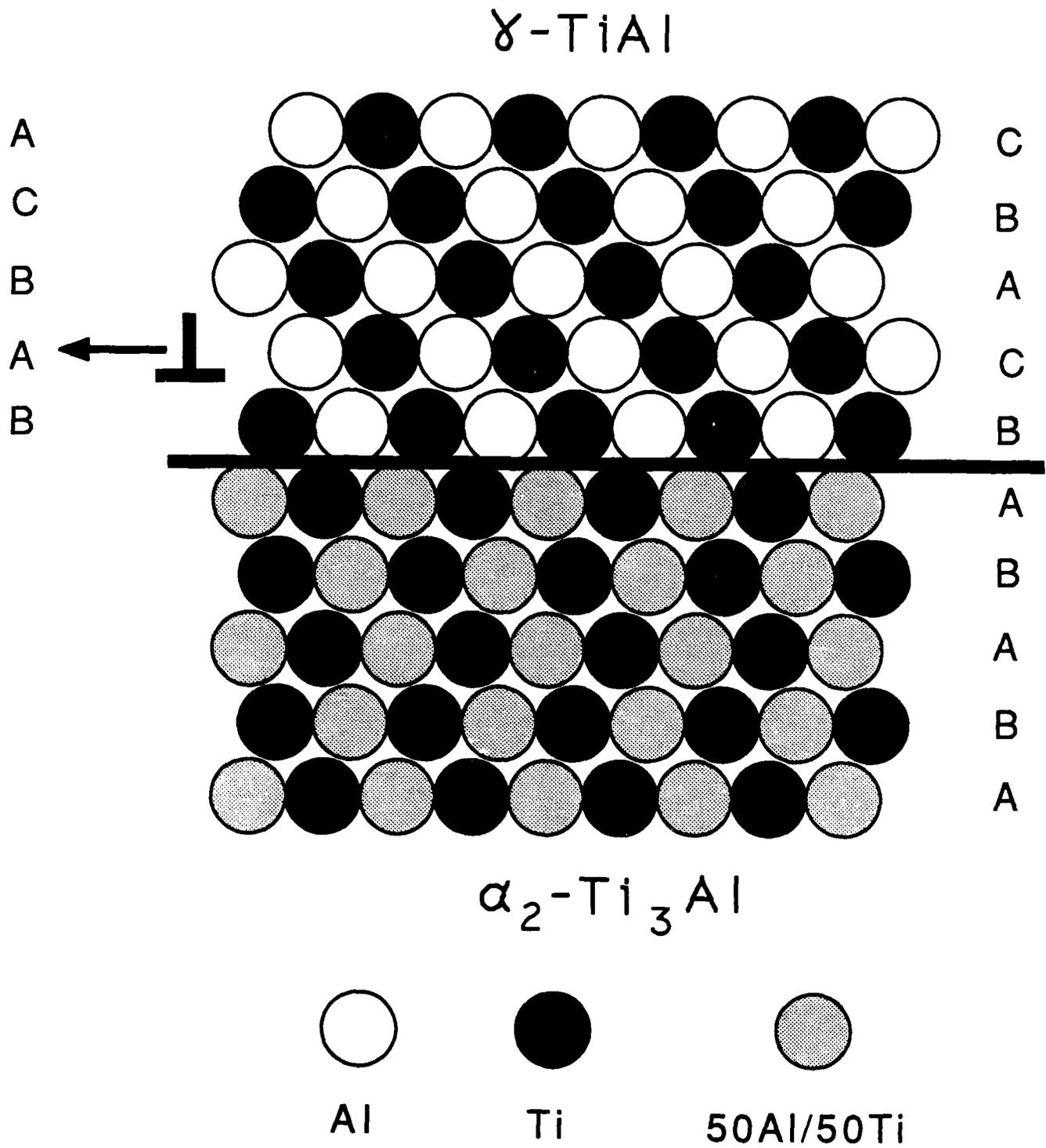
Fig. 7.

Fig. 8.

Fig. 9.

Fig. 10.

$\langle 110 \rangle \gamma$

Fig. 11.

247

Fig. 12.

ATTACHMENT V
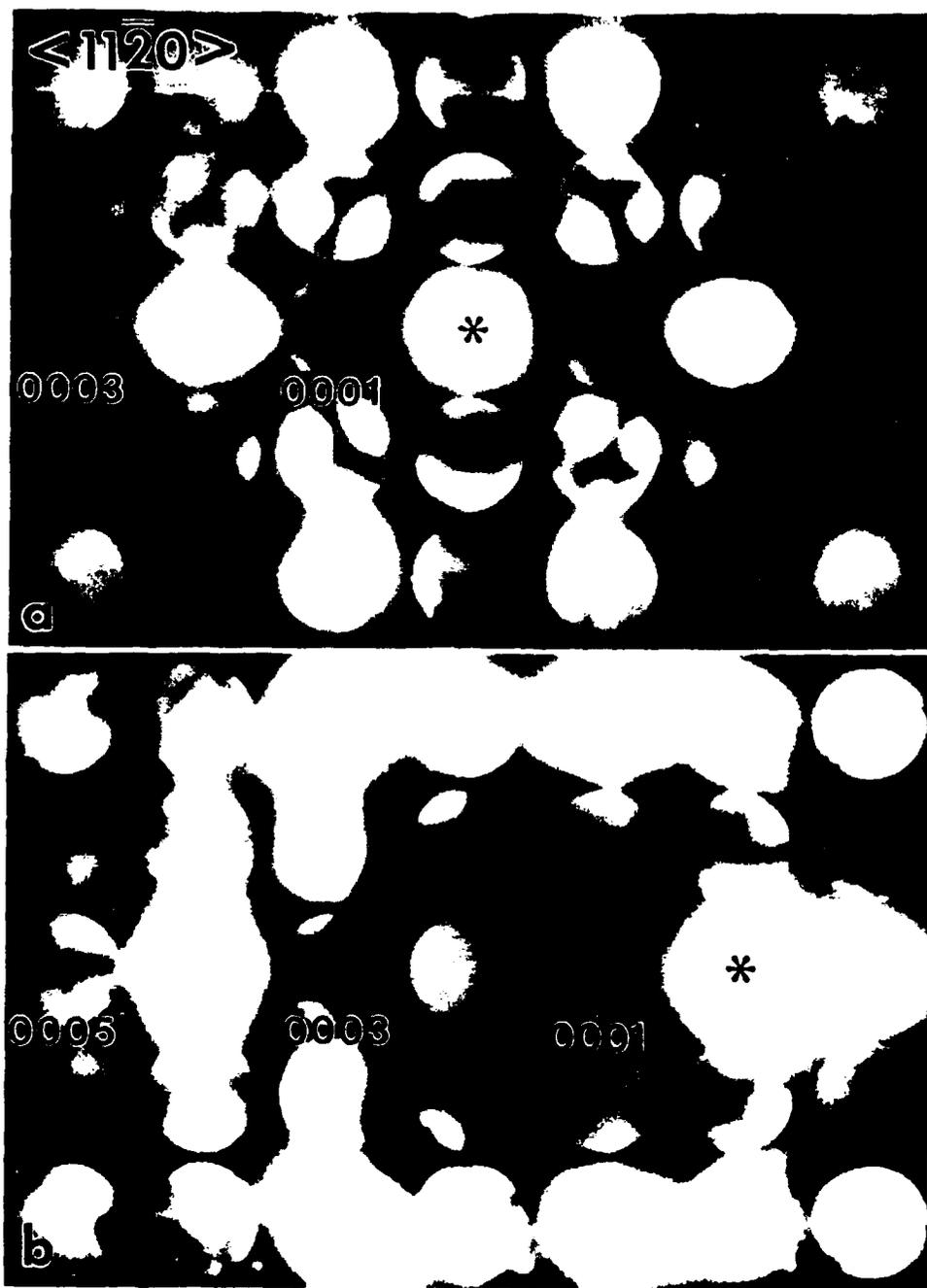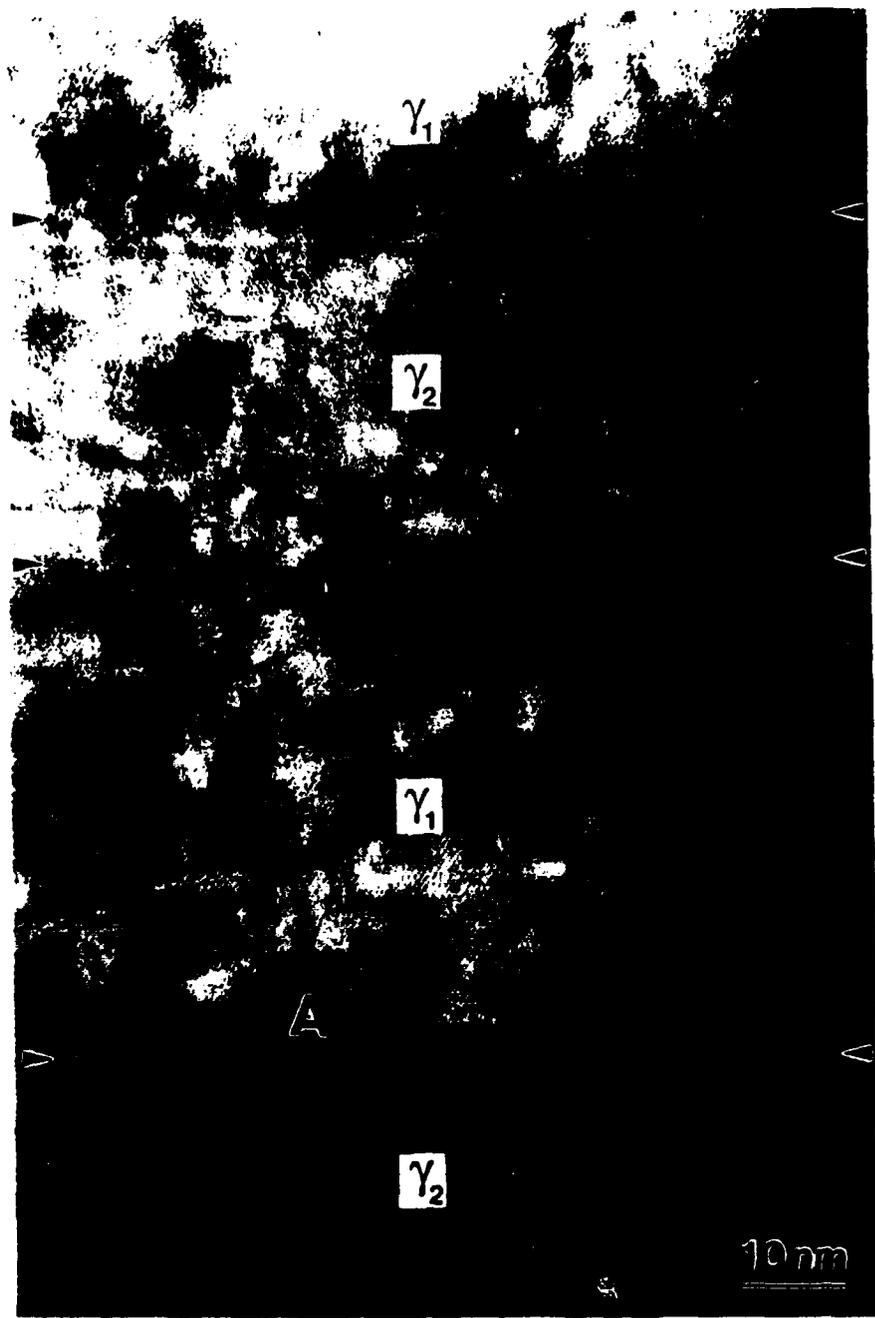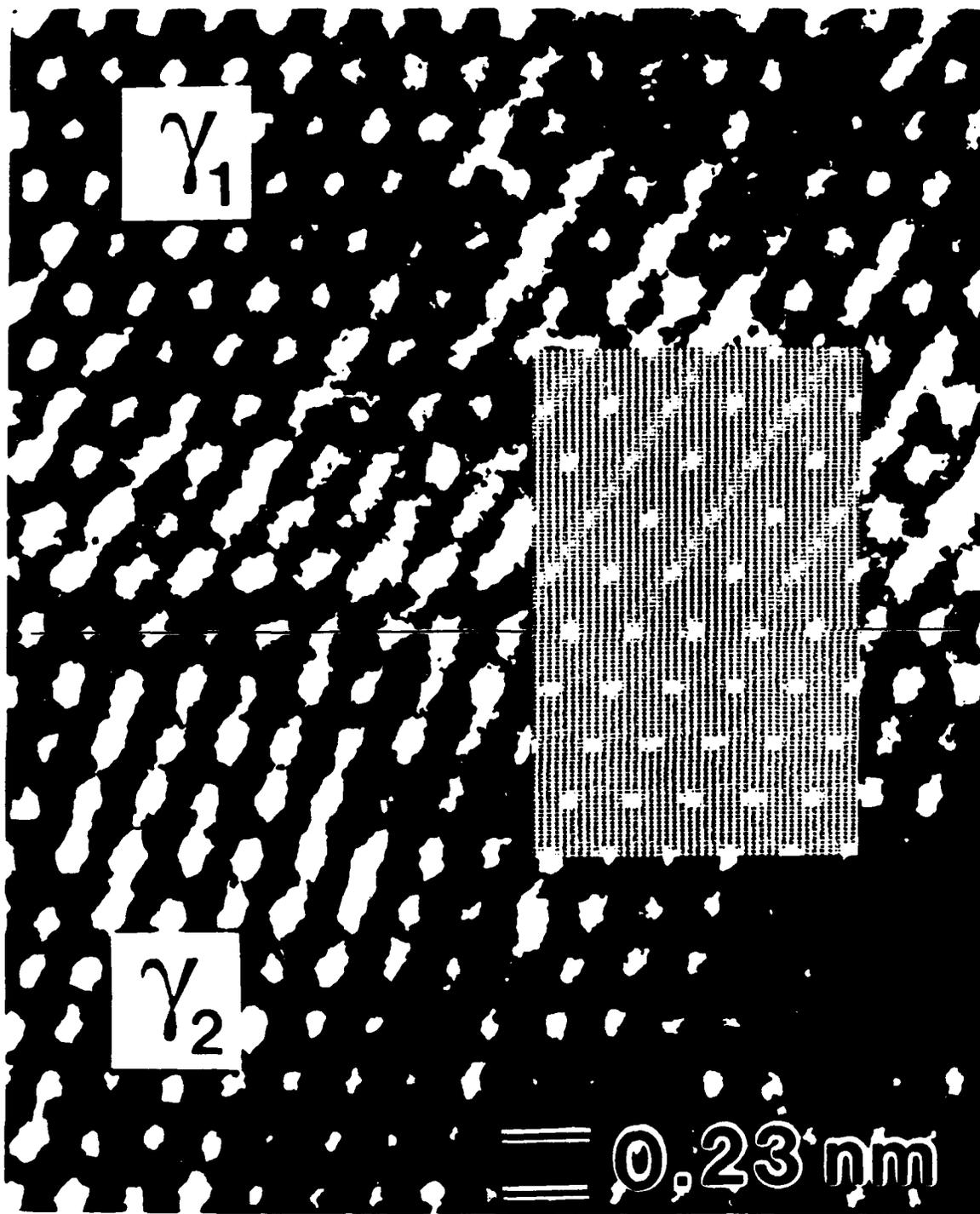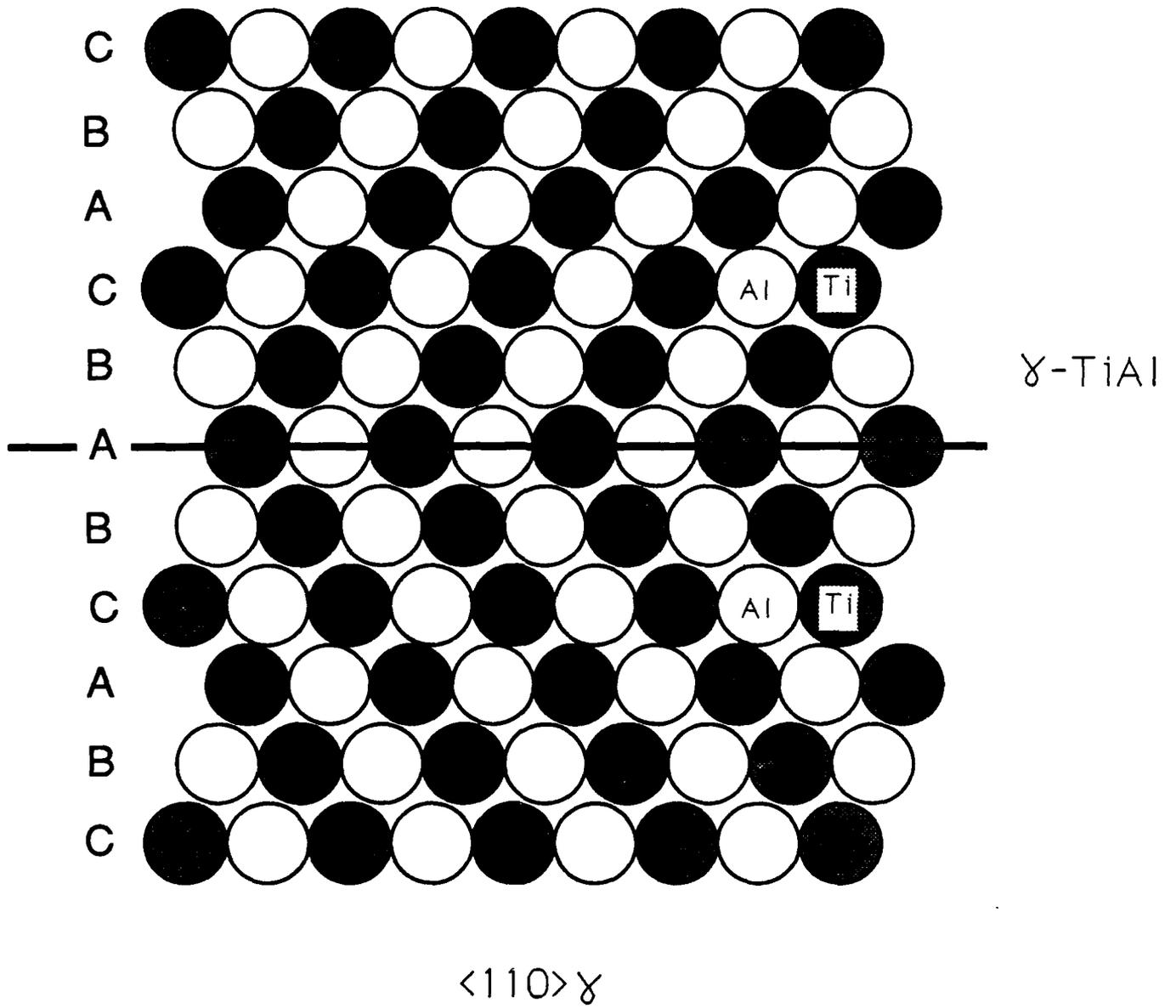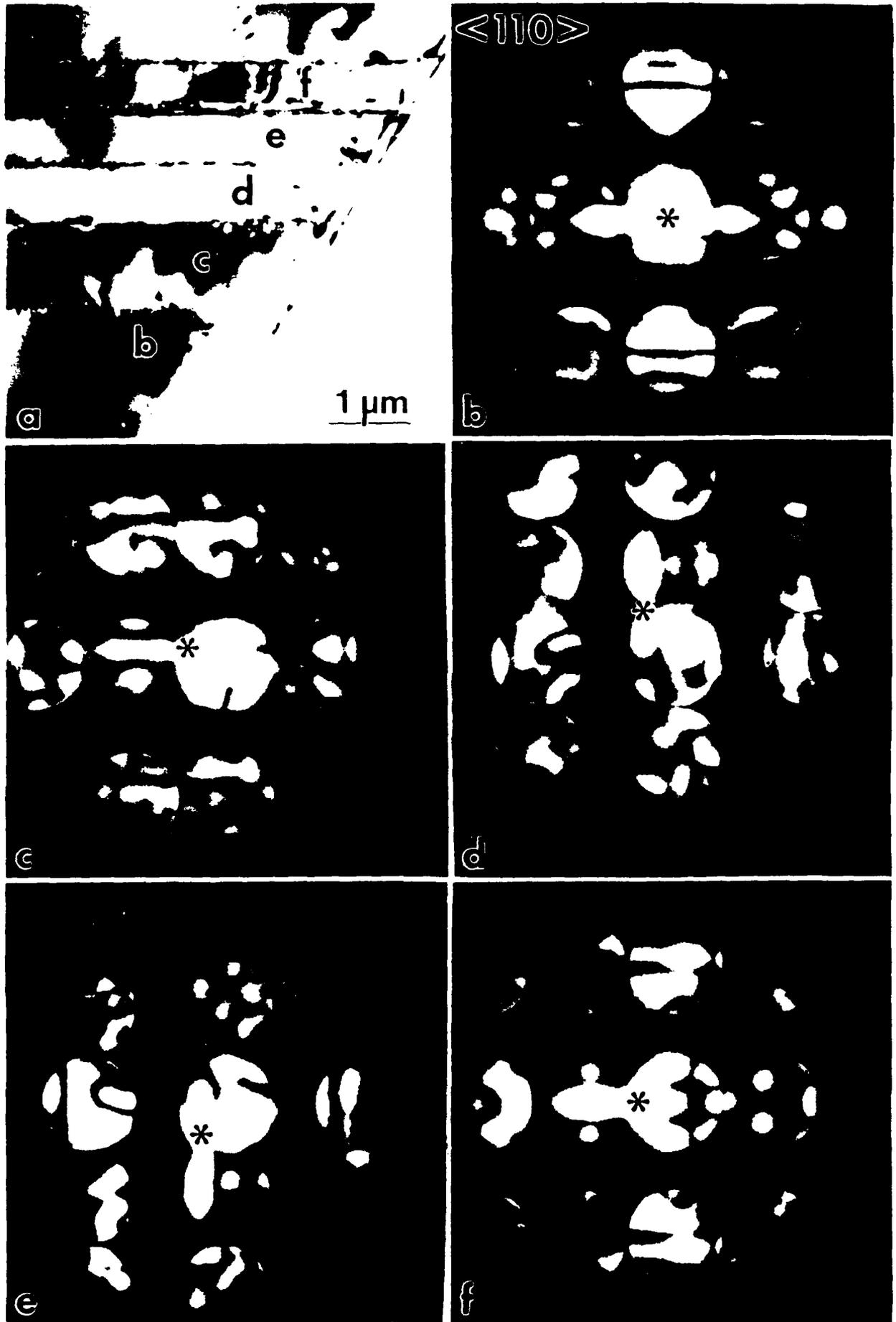
Table II. Ti-7 Pct Mo-16 Pct Al Alloy. Observed Phases for Various Heat Treatments

Heat Treatment	Observed Phases	Size of Precipitates	Vol Pct of Precipitates	Remarks
2 h 1400°C/20°C	$\beta + \beta_2$	≈160Å	*	Size of β_2 particles invariant with annealing temperature
2 h 1200°C/20°C	$\beta + \beta_2$	≈160Å	*	
2 h 1000°C/20°C	$\beta + \beta_2$	≈160Å	*	
24 h 950°C/20°C slow-cooled	$\beta + Ti_3Al$	*	*	Start of precipitation reaction
2 h 1000°C → 910°C 96 h 910°C/20°C	$\beta + Ti_3Al$	≈14μ	≈24	Nearly defect-free Ti_3Al particles
24 h 900°C/20°C	$\beta + Ti_3Al$	≈1.5μ	≈20	Equiaxed Ti_3Al particles
24 h 850°C/20°C	$\beta + Ti_3Al$	≈0.7μ	≈50	
2 h 1000°C/20°C 24 h 800°C/20°C	$\beta + Ti_3Al + \alpha$	≈1.5μ (α)†	≈42 (α + Ti₃Al)	Needle-shaped α particles containing Ti_3Al particles
2 h 1000°C/20°C 24 h 700°C/20°C	$\beta + Ti_3Al + \alpha$	≈2500Å (α)† ≈150Å (Ti₃Al)	≈50 (α + Ti₃Al)	
2 h 1000°C/20°C 180 h 450°C/20°C	$\beta + \alpha + \beta_2$	*	*	α and β_2 particles intimately intermixed
2 h 1000°C/20°C 48 h 375°C/20°C	$\beta + \alpha + \beta_2$	≈100Å (α) ≈100Å (β₂)	*	

*Not determined.
†Thickness.

From T. Hamajima, G. Luetjering and

S. Weissman, Metall. Trans. A (1972)
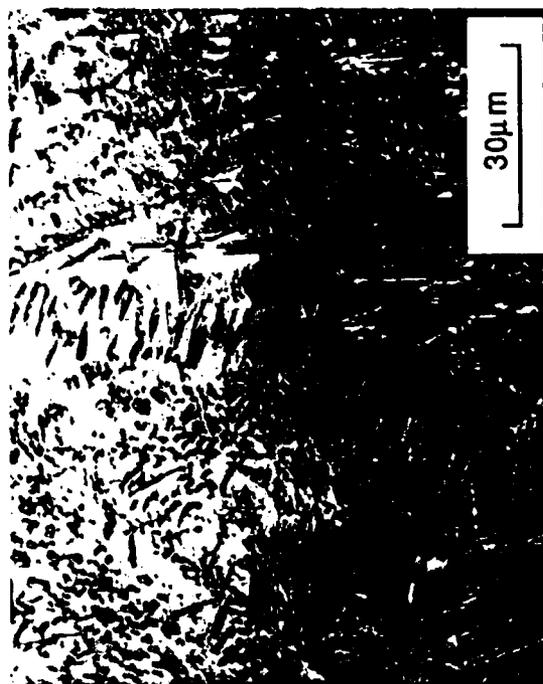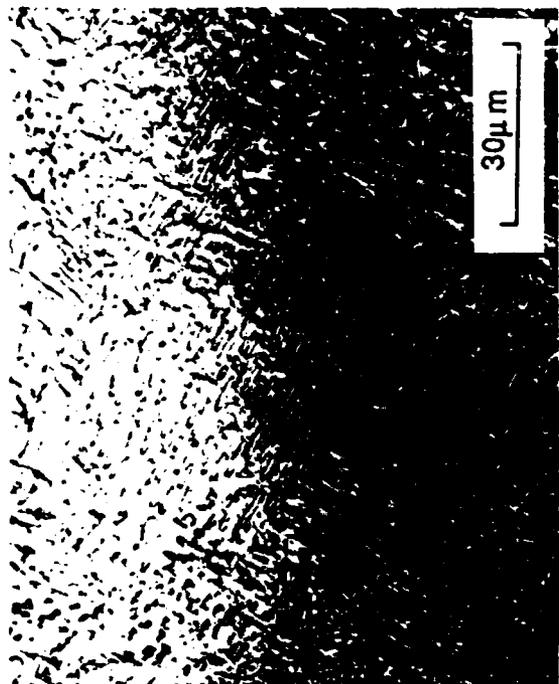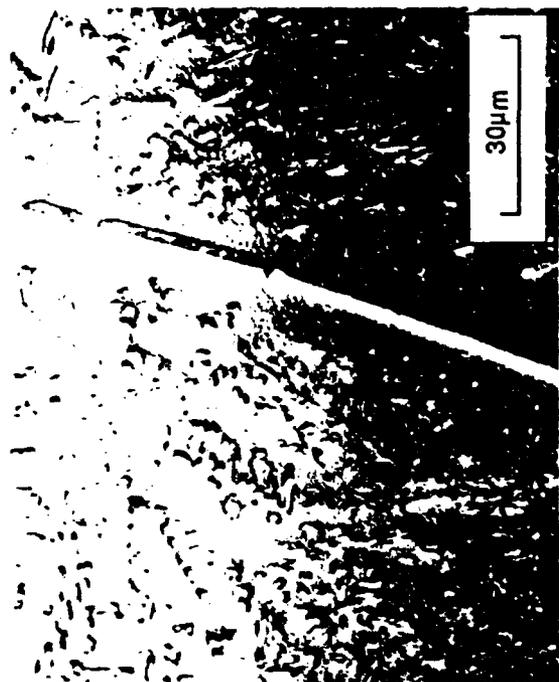
Optical micrographs, of an $\beta + \alpha 2$ alloy aged at 900°C, show that the $\alpha 2$ precipitates as rods in the β matrix and growth of the $\alpha 2$ is noticeably greater along the β grain boundaries.

Burgers   Orientation

$[111]_\beta \parallel [11\overline{2}0]_{\alpha2}$

$(110)_\beta \parallel (0001)_{\alpha2}$

$\alpha2$	a = 5.81	c = 4.43
β	a = 3.25	

Misfit

$d_{(0002)} = 2.21$ $d_{(11\overline{2}0)} = 2.90$

$d_{(110)} = 2.30$ $a'2_{[111]} = 2.81$

□ Al

■ Ti
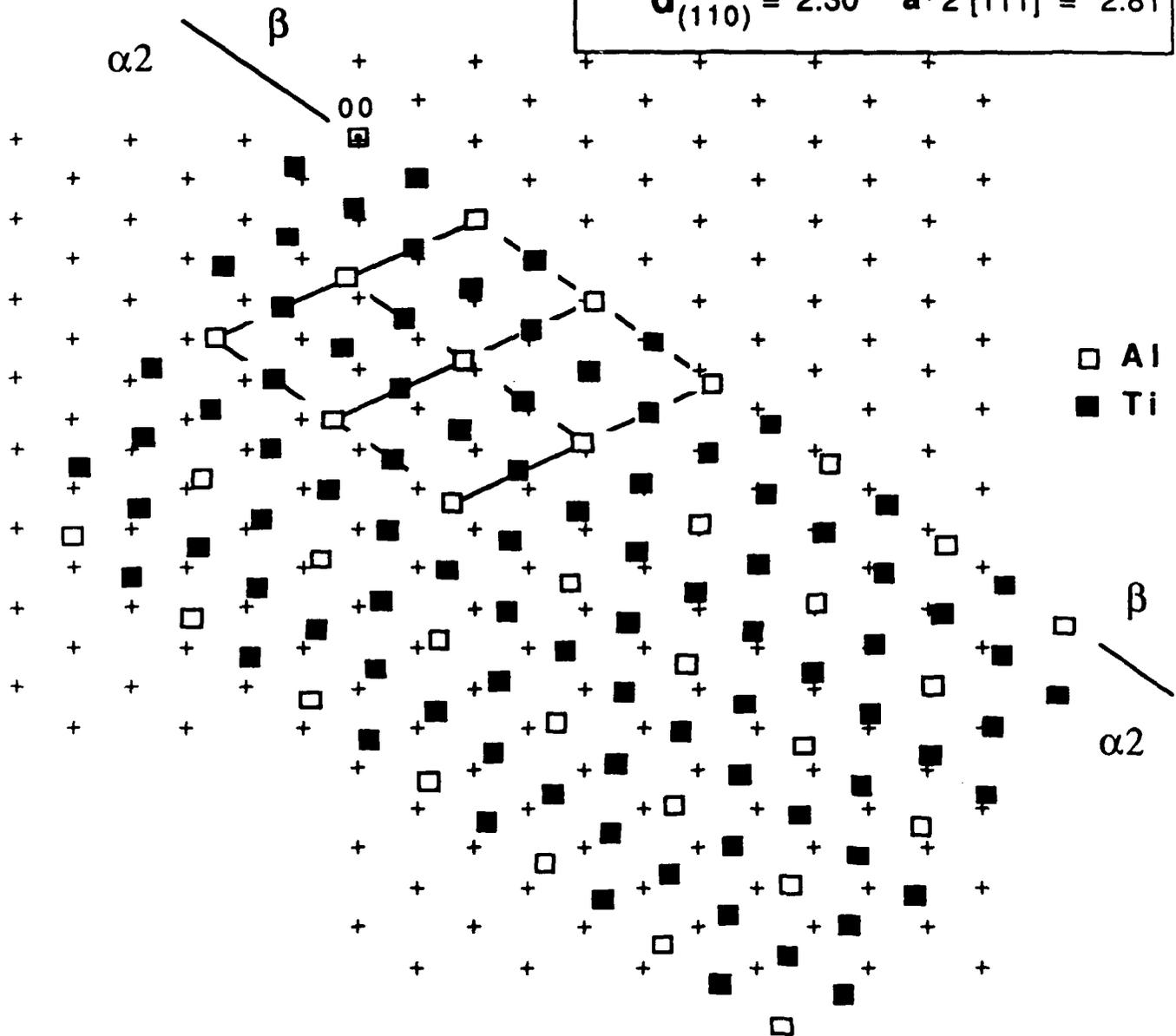
Burgers OR between the $\alpha2/\beta$ as viewed along the [0001] direction. A 3% misfit between the β and $\alpha2$ occurs along the $[\overline{1}2\overline{1}0]\alpha2$, and a 4% misfit occurs along the [0001]$\alpha2$.
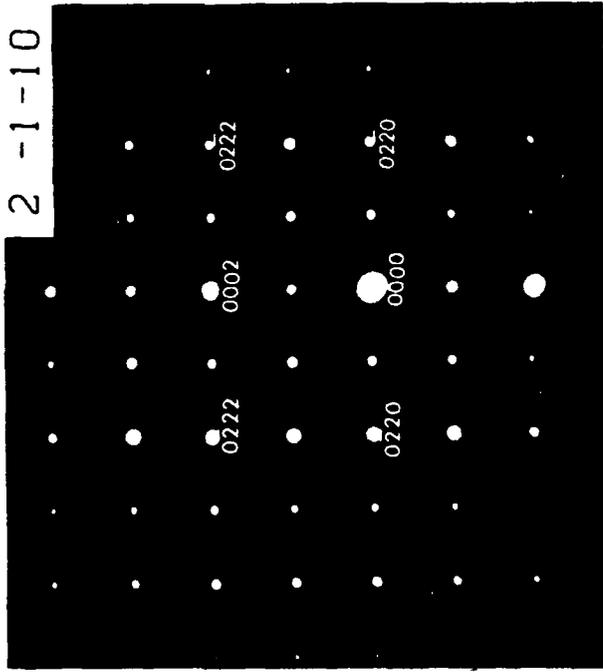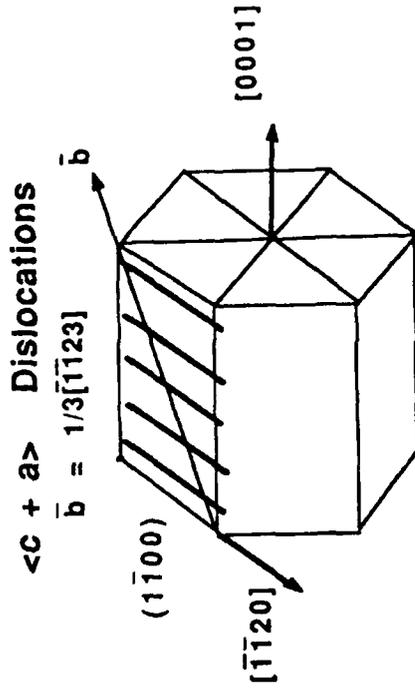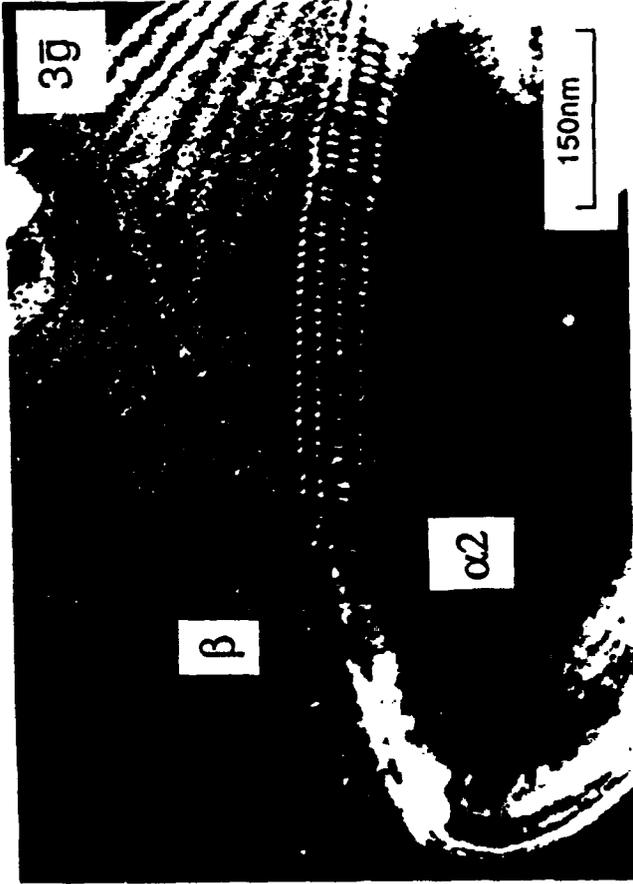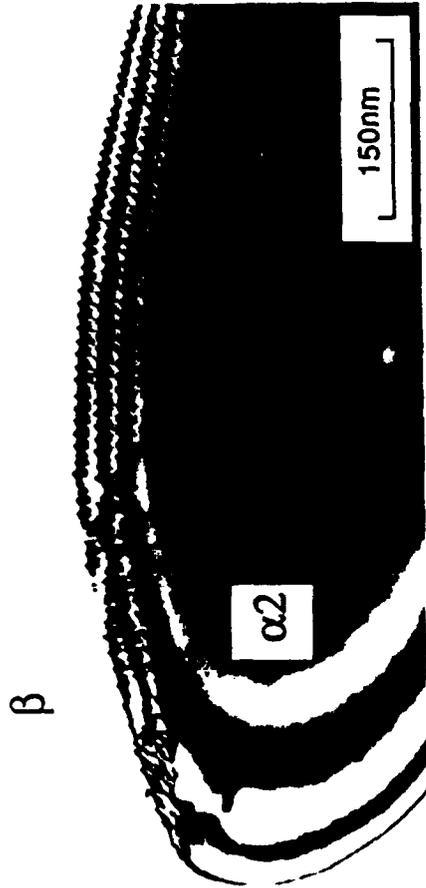
Bright field and weak beam TEM images of a β/α2 interface. Trace analysis results of the interface, presented in the schematic, show <c+a> type dislocations spaced ~10nm apart on the (1$\bar{1}$00) plane and lie along the [1$\bar{1}$20] direction.

Presented at ???? Am. Meeting ?.III. A
Abstd for publication in Stramiorscopy.

High-Resolution Transmission Electron Microscopy of Precipitate Plate Growth by Diffusional and Displacive Transformation Mechanisms

J. M. Howe and G. J. Mahon

Department of Metallurgical Engineering
and Materials Science
Carnegie Mellon University
Pittsburgh, PA 15213

Abstract

High-resolution transmission electron microscopy (HRTEM) is used to investigate the atomic structure of precipitate plates formed by diffusional and displacive transformations in alloys. Comparison among several f.c.c. → h.c.p. diffusional transformations illustrates the capability of HRTEM for understanding the mechanisms of the compositional and structural components of the transformation at the atomic level. Similar analyses are performed for a f.c.c. → b.c.t. displacive transformation and the sensitivity of HRTEM to local changes in composition and strain are discussed.

1. Introduction

Precipitate plates can grow by diffusional, displacive or mixed-mode (for interstitial alloys) mechanisms of interfacial motion [1]. In each case, it is necessary to characterize the atomic details of the structural and/or compositional changes which occur at the matrix/precipitate interface in order to fully understand the transformation mechanisms [2,3]. High-resolution transmission electron microscopy (HRTEM) provides unique capabilities for obtaining such information, although because it is an emerging technique, the full scope of HRTEM has not been explored. The purpose of the present paper is to illustrate the type of structural and compositional information that HRTEM can provide about growth of precipitate plates as well as to elaborate on current limitations and future possibilities of the technique.

2. General Description of Precipitate Plate Growth

The total Gibbs free-energy change ΔG_{tot} accompanying growth of a precipitate plate is given by the expression [4]:

$$\Delta G_{tot} = -\Delta G_v V + \gamma_s A + E_s V + E_{int} , \qquad (1)$$

where ΔG_v is the free-energy change per unit volume of the precipiate phase formed, V is the volume of the precipitate, γ_s is the surface energy per unit area, A is the precipiate area, E_s is the elastic strain energy per unit volume of precipitate and E_{int} is the interaction energy, which can arise due to elastic interactions among transformation dislocations for example. The shape of a precipitate plate at any point during growth is determined by a balance among the terms in Eqn. (1) with due consideration for the mechanisms and kinetics of the transformation.

While HRTEM cannot provide values for each of the terms in Eqn. (1), observation of the atomic structure of precipitate interfaces can indicate the role of surface, elastic strain and interaction energies on the mechanisms of precipitate plate growth and provide information regarding the actual mechanisms involved. Therefore, the strength of HRTEM lies in its ability to provide an understanding of the transformation mechanisms. Precipitate growth by diffusional and displacive (martensitic) mechanisms illustrate two extremes in the types of compositional and structural changes that can occur during a transformation. The capabilities of HRTEM for understanding the mechanisms of these transformations is illustrated below with examples of work performed by the authors, followed by a discussion of the theoretical capability of HRTEM for resolving compositional and structural changes in materials as determined using simulated images.

3. Diffusional Growth of Precipitate Plates

One of the simplest and most complete examples of the application of HRTEM in understanding the role of surface and elastic strain energies, transformation mechanisms and kinetics on the diffusional growth of a precipitate plate is given by recent work on the diffusional growth of γ' precipitate plates in an Al-15wt.%Ag alloy [2,5]. The γ' phase grows as h.c.p. Ag_2Al plates in the f.c.c. Al-rich matrix with the orientation relationship $\{111\}_\alpha //(0001)_{\gamma'}$ and $<110>_\alpha //<11\bar{2}0>_{\gamma'}$. Figure 1 shows a

HRTEM image of a precipitate edge viewed parallel to the habit plane. The precipitate edge is composed of an array of Shockley partial dislocations stacked vertically. Due to the close proximity of the dislocations and the large change in composition across the interface, it is difficult to distinguish individual dislocation cores in the image. However, it is possible to construct two different Burgers circuits around the edge to determine that there are fifteen 30° (screw) and eight 90° (edge) partial dislocations present at the plate edge, which is forty-six (0001) planes thick [2].

The presence of twenty-three transformation dislocations at the edge of the forty-six plane plate confirms previous results [6,7] that growth of γ' precipitates is accomplished by the diffusional glide of Shockley partial dislocations along alternate {111} matrix planes. Furthermore, the 2:1 ratio of 30° to 90° partial dislocations indicates that equal numbers of all three types of a/6<112> partials on a {111} plane are nucleated in order to minimize the elastic strain energy (the $E_s V$ term in Eqn. (1)) at the plate edge. Calculation of the interaction energy of Shockley partial dislocations on alternate {111} planes has shown quantitatively that the elastic interaction energy (the E_{int} term in Eqn. (1)) between the top two partial dislocations ensures nucleation of all three types [8]. It is also evident from the HRTEM image in Fig. 1 that the precipitate edge is coherent in this orientation, with the exception of the one possible misfit dislocation indicated. While a coherent edge is expected for growth by Shockley partial dislocations [9], it is very difficult to reveal such complicated precipitate interfaces using conventional TEM techniques.

The edges of the γ' plates were also examined with the electron beam perpendicular to the habit plane in order to reveal the three-dimensional atomic structure of the matrix/precipitate interface. Figure 2 shows a HRTEM image of several single-atom kinks about 3.5 nm apart along the edge of the plate. It is evident from this image that the precipitate edges are faceted along low-energy $<110>_\alpha // <11\bar{2}0>_{\gamma'}$ close-packed directions at the atomic level, indicating that the surface energy (the $\gamma_s A$ term in Eqn. (1)) strongly influences the precipitate morphology [10]. This effect results in precipitates which usually have a hexagonal shape within the habit plane [5]. In addition, the interface between each kink is atomically flat while the kinks (arrows) appear diffuse, indicating that atomic attachment is occurring at kinks in the Shockley partial dislocations. Thus, the growth of γ' plates occurs by a terrace-ledge-kink mechanism of atomic attachment, as originally proposed for the growth of close-packed interfaces of a solid into a liquid or vapor [11,12].

One final image of the matrix/precipitate interface viewed parallel to the coherent habit plane is shown in Fig. 3. A simulated HRTEM image of this interface [13,14] for a crystal thickness of 3.7 nm and an objective lens defocus of -142.0 nm is shown superimposed on the experimental image. The model interface in Fig. 3 is based on a γ' precipitate which has the composition Ag_2Al, with A planes that are nearly pure Ag and B planes that are two-thirds Al, as shown in Fig. 4. In order for the precipitate to thicken, two processes must occur (i) a Shockley partial dislocation must propagate along the C plane in the matrix and translate these atoms into A positions (indicated in Fig. 4), and (ii) there must be a compositional change which allows the A planes to become nearly pure Ag and the B planes to contain 33at.% Ag. Thus, both the structural and major compositional changes which are necessary for growth of the precipitate plate occur in the atom plane containing the transformation dislocation. Combining this information with the images of kinks in Fig. 2 indicates that the diffusion of Ag to kinks in the Shockley partial dislocations is the rate-limiting step in this transformation. This has recently been confirmed by complementary *in situ* hot-stage TEM experiments [15]. Thus, the technique of HRTEM has enabled the structural and compositional mechanisms of this diffusional transformation to be characterized at the atomic level.

There are several other cases where HRTEM is providing insight into mechanisms involved in the diffusional growth of h.c.p. precipitate plates in f.c.c. matrices [16], although these cases are more complex and have not been studied as thoroughly as the γ' transformation in Al-Ag. One such example is in nearly equiatomic Ti-Al alloys, where ordered (DO_{19}) h.c.p. α_2 plates grow on the {111} planes in the ordered $(L1_0)$ f.c.t. γ matrix with the same orientation relationship described above for γ' in Al-Ag, i.e., $\{111\}_\gamma//(0001)_{\alpha2}$ and $<110>_\gamma//<11\bar{2}0>_{\alpha2}$ [17]. Figure 5 shows a HRTEM image of the matrix/precipitate interface viewed parallel to the habit plane, similar to the image of γ' in Fig. 3. A simulated HRTEM image of the interface for a crystal thickness of 3.0 nm, a defocus of -80.0 nm and 1.0 mrad beam tilt about $[0001]_{\alpha2}$ is shown superimposed on the experimental image. There is good matching between the exprimental and calculated image.

Analysis of the model γ/α_2 interface in Fig. 6, which was the basis for the simulated image in Fig. 5, shows that the pure Ti columns in the α_2 and γ phases are aligned across the interface. Such alignment could be produced if the structural component of the transformation occurred by the passage of a Shockley partial

dislocation along the C plane in the γ matrix as for γ' in Al-Ag. In addition, the columns of Al atoms in both the B and C planes involved in this transformation must increase by 50at.%Ti in order to achieve the composition Ti_3Al as the interface advances. Thus, the compositional change would occur evenly in the new layer rather than being concentrated in only the dislocation plane as in Al-Ag. Although further TEM analysis is needed to confirm this transformation scheme, the similarity with γ' in Al-Ag is apparent and previous conventional TEM analyses have indicated that Shockley partial dislocations are involved in the transformation [18].

An example of a still more complicated f.c.c. $\rightarrow$ h.c.p. diffusional transformation is illustrated by the growth of hexagonal T_1 (Al_2CuLi) precipitate plates on the {111} matrix planes in an Al-2wt.%Li-1wt.%Cu alloy with the orientation relationship {111}$_\alpha$//(0001)$_{T_1}$ and <110>$_\alpha$//<10$\bar{1}$0>$_{T_1}$ [19,20]. This transformation is more complicated in terms of HRTEM image interpretation since it involves a ternary precipitate and the crystal structure of the T_1 phase is still uncertain [21]. Figure 7 shows a HRTEM image of a T_1 plate viewed parallel to the habit plane, as in the previous examples. The plate is twelve {111} planes thick and the spacing of atoms in the (0001) planes of the precipitate is the same as that of atoms in the close-packed {111} matrix planes. The plate also displays strong contrast changes which repeat every four planes, where the second and fourth planes are much darker than the matrix (as for the Ag-rich planes in the γ' precipitate in Fig. 3) and the third plane is much brighter. Based on these image characteristics and the increasing electron scattering factors for Li, Al and Cu, respectively, a model crystal structure for the T_1 phase and the matrix/precipitate interface was constructed. The model structure consists of an A_1BA_2C... stacking of close-packed planes where the A_1 planes are mostly Al, the B and C planes contain a mixture of Cu and Al, and the A_2 planes are mostly Li, as illustrated in Fig. 8.

A simulated image of the matrix/precipitate interface at -60.0 nm (Scherzer) defocus for a crystal thickness of 21.4 nm is shown superimposed on the experimental image in Fig. 7. The simulated image matches the experimental image reasonably well in the area shown, although the contrast of T_1 plates varied considerably throughout experimental images and the positions of the white spots in the precipitate (assumed to represent the atomic columns by comparison with the matrix) sometimes indicated other stacking sequences. However, assuming that the model structure in Fig. 8 is correct, the structural transformation necessary to produce the required A_1BA_2C... stacking sequence could be accomplished by the passage of a pair of Shockley partial

dislocations along every third and fourth matrix plane as indicated in Fig. 8, thereby forming a T_1 unit cell which is four planes high. Such Shockley partial dislocations have been verified to participate in the growth of T_1 by conventional TEM contrast analyses [22]. Again, it is difficult to obtain such detailed information about the crystal structure and transformation mechanisms of such thin plates using a technique other than HRTEM.

4. Displacive Growth of Precipitate Plates

There have been fewer HRTEM studies of precipitate plate growth by displacive (diffusionless) transformations due to several factors (i) the difficulty of preserving the transformation interface, (ii) the smaller atomic spacings in many alloys involved, (iii) the more complicated nature of the transformation interface or habit plane, which is frequently irrational, and (iv) because many displacive transformations are found in ferrous alloys where magnetism is a problem. However, the advent of medium-voltage TEMs and careful selection of alloys has allowed imaging of some martensitic interfaces [23,24], and an illustration is shown below for a Fe-8Cr-1C austenitic steel that was cooled to just below the martensite start temperature [25].

Figure 9 shows a low-magnification phase-contrast image parallel to the $\{252\}_\gamma$ habit plane of an α martensite plate in a $<101>_\gamma//<111>_\alpha$ orientation. The macroscopic habit plane is indicated in the figure and at this magnification, it is apparent that the habit plane deviates considerably from $\{252\}_\gamma$ on a microscopic scale, particularly at the positions indicated by arrows. Furthermore, in contrast to the f.c.c. $\rightarrow$ h.c.p. diffusional transformations discussed above, the habit plane is rough on an atomic scale, as illustrated by the enlargement shown in Fig. 10. In this enlargement, matching of the three low-index planes of atoms in each phase is observed acoss the interface demonstrating that it is coherent and without additional dilatation, as expected from martensite theory [26] and the Kurdjumov-Sachs orientation relationship [27]. In addition, the interface consists of atomic steps which are faceted onto the nearest low-index rational plane, which is $\{111\}_\gamma$. In relation to Eqn. (1), this indicates that the strain energy term E_S dominates over the surface energy term γ_S in determining the macroscopic habit plane, but that γ_S is still influential in causing faceting of the irrational habit plane along low-index matrix planes on an atomic level. Furthermore, from the correspondence between atoms in the close-packed $\{111\}_\gamma$ and $\{110\}_\alpha$ planes it is possible to obtain the magnitude of the shear on each $\{111\}_\gamma$ plane, which is $a/24<112>$ in projection. This indicates that the Burgers vector is probably $a/12<112>$

along the <112> direction out of the plane of projection. Hence, each atomic facet can be viewed as a structural ledge which contains an a/12<112> transformation dislocation in the parallel $\{111\}_\gamma$ and $\{110\}_\alpha$ planes (facet planes), as required for a glissile martensitic interface and predicted by theory [28,29]. However, this is only the lattice variant component of the transformation and it is not possible to observe the lattice invariant component, which lies parallel to the beam direction.

A simulated HRTEM image of the $\{252\}_\gamma$ interface for a crystal thickness of 7.4 nm at -70.0 nm defocus is shown superimposed on the experimental image in Fig. 10. Again, there is generally good matching between the simulated and experimental image with only a small change in image contrast across the austenite/martensite interface since the phases have the same composition. However, the simulated and experimental images are two-dimensional projections of the three-dimensional structure so that even though good matching is obtained, it is not possible to obtain a complete picture of the transformation of atom positions from the one image. In this case, it would be useful to image the interface along other zone axes to obtain a more complete description, as done for γ' in Figs. 1-3. In addition, occasional regions of distortion and anomalous contrast appeared along the interface in the experimental image which are not reproduced in the simulated image. Although the origin of this contrast has not yet been determined, it may be because the interface is slightly tilted with respect to the electron beam. Furthermore, the crystal thickness in the simulated image is known to be less than that of the experimental image. However, it was not possible to simulate thicker crystals due to the excessive amount of diffuse scattering that was induced in the simulated image, as a result of the limited unit-cell size (128x128 array) used and the different crystal structures on either side of the interface [14].

5. Compositional and Structural Sensivity

From the previous images of diffusional and displacive transformations, it is clear that the contrast from an atomic column in HRTEM images depends not only on its position, but also on the composition within the column. There is also a strong dependence on specimen and microscope parameters such as crystal thickness, beam and crystal tilt and objective lens defocus. In order to perform quantitative interpretation of HRTEM images of transformation interfaces, it is necessary no only to appreciate how specimen and microscope parameters affect the results, but also to understand how composition and strain affect image contrast. Although systematic studies of these latter

effects have been limited, work in this area is progressing [30,31]. The results from one study of compositional effects on image contrast are summarized below [32].

The minimum solute concentration required to produce an observable change in contrast in HRTEM images of a 400 keV instrument at -50.0 nm (Scherzer) defocus was determined by multislice image simulation techniques [13,14]. Increasing amounts of a solute were added to a variety of matrices until a change in image contrast was visible, as illustrated in Fig. 11. The corresponding solute concentration was then plotted as a function of the absolute value of the difference in atomic number between the solute and matrix, as shown for matrices of Si, Co and Pt (which represent light, medium and heavy elements with d.c., h.c.p. and f.c.c. crystal structures, respectively) in Fig. 12. The crystals were all one extinction distance thick, since this was found to be the optimum thickness for observing compositional effects.

From data such as Fig. 12, it was found that contrast changes arising from solute additions can be adequately described by a rule-of-mixtures approach based only on the atomic numbers of the matrix and solute. In general, the average atomic number of a column containing solute must increase or decrease by a factor of about two compared to the atomic number of the matrix before the solute becomes visible. Prediction of this minimum detectable solute concentration (C_{min}) for any combination of matrix and solute was obtained with the formula:

$$C_{min} = 2Z_M / |Z_S - Z_M| , \qquad\qquad (2)$$

which indicates that C_{min} increases proportionally with the matrix atomic number (Z_M) and decreases inversely with the difference in atomic number between the solute (Z_S) and matrix. In this study, it was also found that for the microscope and specimen conditions above, addition of a solute with higher atomic number than the matrix caused an increase in intensity of the solute column, while addition of an element with a lower atomic number caused a decrease in intensity, as expected from scattering theory. While this study was only concerned with the contrast change of individual atomic columns, recent analyses of extended defects such as G.P. zones in Al-Ag [33] and δ' precipitates in Al-Li alloys [34] indicate that the same interpretation can be used in these cases as well. However, straightforward application is much less certain in the case of highly ordered precipitates such as the T_1 phase in Fig. 7.

Although the effects of strain on conventional TEM images is well established [35,36], only a few such studies have not been performed for HRTEM [37,38]. However, scattering theory indicates that diffuse scattering from strain and compositional effects is linearly separable, so that the relative contributions of each to HRTEM image contrast can be determined [39]. Further HRTEM image calculations which include both strain and composition effects are being performed [40] to enable more quantitative interpretation of HRTEM images. Further progress in image processing may also improve such analyses in experimental images [41].

Conclusions

High-resolution TEM is capable of revealing the atomic structure and composition of plate-shaped precipitates and their transformation interfaces in diffusional and displacive phase transformations. Observation of the transformation interfaces can explain the role of surface and elastic strain energies on the transformation and is critical for determining the actual transformation mechanism. Electron scattering theory indicates that HRTEM is sensitive to compositional changes within an atomic column. Further systematic analyses of the effects of composition and strain on calculated HRTEM images will allow more quantitative evaluation of the structure and solute concentration of individual columns of atoms at transformation interfaces in experimental images.

Acknowledgements

References

[1] G. B. Olson, Scripta Metall. 21 (1987) 1023.

[2] J. M. Howe, U. Dahmen and R. Gronsky, Philos. Mag. A 56:1 (1987) 31.

[3] J. M. Howe, D. E. Laughlin and A. K. Vasudevan, Philos. Mag. A 57:6 (1988) 955.

[4] G. C. Weatherly, Acta Metall. 19 (1971) 181.

[5] J. M. Howe, H. I. Aaronson and R. Gronsky, Acta Metall. 33 (1985) 639,649.

[6] J. A. Hren and G. Thomas, Trans. Metall. Soc. AIME 227 (1963) 308.

[7] C. Laird and H. I. Aaronson, Acta Metall. 17 (1969) 505.

[8] N. Prabhu and J. M. Howe, Scripta Metall. 22 (1988) 425.

[9] G. B. Olson and M. Cohen, Acta Metall. 27 (1979) 1907.

[10] K. B. Alexander, F. K. LeGoues, D. E. Laughlin and H. I. Aaronson, Acta Metall. 32 (1984) 2241.

[11] W. K. Burton, N. Cabrera and F. C. Frank, Philos. Trans. Roy. Soc London A 243 (1950-51) 299.

[12] A. Rosenberg and W. A. Tiller, Acta Metall. 5 (1957) 565.

[13] J. M. Cowley and A. F. Moodie, Acta Cryst. 10 (1957) 609.

[14] M. A. O'Keefe and P. R. Buseck, Trans. Amer. Cryst. Assoc. 15 (1979) 27.

[15] J. M. Howe, in: Phase Transformations '87 (The Inst. Metals, London) in press.

[16] G. J. Mahon and J. M. Howe, Metall. Trans. A, to be submitted.

[17] J. C. Williams, in: Precipitation Processes in Solids, Eds. K. C. Russel and H. I. Aaronson (The Metall. Soc. AIME, Warrendale, 1977) p. 289.

[18] M. J. Blackburn, in: The Science, Technology and Applications of Titanium, Eds. R. Jaffee and N. E. Promisel (Pergamon Press, London, 1970) p. 633.

[19] J. M. Howe, J. Lee and A. K. Vasudevan, Metall. Trans. A, in press.

[20] M. H. Tosten, A. K. Vasudevan and P. R. Howell, Metall. Trans. A 19 (1988) 51.

[21] J. C. Huang and A. J. Ardell, Mater. Sci. Tech. 3 (1987) 176.

[22] B. Noble and G. E. Thompson, Met. Sci. J. 6 (1972) 167.

[23] F. C. Lovey, G. Van Tendeloo and J. Van Landuyt, Scripta Metall. 21 (1987) 1627.

[24] K. M. Knowles, Proc. Roy. Soc. London A 380 (1982) 287.

[25] G. J. Mahon and J. M. Howe, Scripta Metall., to be submitted.

[26] C. M. Wayman, J. E. Hanafee and T. A. Read, Acta Metall. 9 (1961) 391.

[27] F. C. Frank, Acta Metall. 1 (1953) 15.

[28] U. Dahmen, Scripta Metall. 21 (1987) 1029.

[29] P. F. Gobin and G. Guenin, in: Solid State Phase Transformations in Metals and Alloys (Les Editions De Physique, Orsay, 1978) p. 573.

[30] W. O Saxton and D. J. Smith, Ultramicroscopy 18 (1985) 39.

[31] N. Tanaka and J. M. Cowley, Acta Cryst. A 43 (1987) 337.

[32] J. M. Howe, D. P. Basile, N. Prabhu and M. K. Hatalis, Acta Cryst. A 44 (1988) 449.

[33] F. Ernst and P. Haasen, Phys. Stat. Sol. (a) 104 (1987) 403.

[34] T. Sato, N. Tanaka and T. Takahashi, Trans. Japan Inst. Metals 29:1 (1988) 17.

[35] M. F. Ashby and L. M. Brown, Philos. Mag. 8 (1963) 1649.

[36] Sir P. Hirsch, A. Howie, R. B. Nicholson, D. W. Pashley and M. J. Whelan, Electron Microscopy of Thin Crystals (R. E. Krieger Publ. Co., Malabar, 1977) p. 247.

[37] M. M. J. Treacy, J. M. Gibson and A. Howie, Philos. Mag. A 51:3 (1985) 389.

[38] D. J. H. Cockayne and R. Gronsky, Philos. Mag. A 44:1 (1981) 159.

[39] P. H. Dederichs, J. Phys. F: Metal Phys. 3 (1973) 471.

[40] D. Sundo and J. M. Howe, Mater. Res. Soc. Symp. Proc. (1988), to be submitted.

[41] W. O. Saxton, in: Proc. 45th Annual Meeting EMSA (San Francisco Press, San Francisco, 1987) p. 58.

Figure Captions

Fig. 1. High-resolution TEM image of a γ' precipitate edge in a $<110>_\alpha$ //$<11\bar{2}0>_{\gamma'}$ orientation at -169.0 nm defocus. The symbols S_s and S_θ indicate the start of the 30° and 90° Burgers circuits, respectively, while F indicates the finish of the circuits.

Fig. 2. Tilted-illumination image showing a series of single-atom kinks along the precipitate edge in a $<111>_\alpha$ //$[0001]_{\gamma'}$ orientation. The edge is faceted along close-packed $<11\bar{2}0>_{\gamma'}$ directions at the atomic level.

Fig. 3. Experimental HRTEM image of the γ' habit plane interface with a simulated image of the interface superimposed. An atomic model of the interface is shown in Fig. 4.

Fig. 4. Atomic model of the α/γ' habit-plane interface showing the structural change required to produce an ABAB... stacking from ABC... close-packed planes for growth (thickening) of a γ' plate.

Fig. 5. Experimental HRTEM image of the γ/α_2 habit plane in a $<110>_\gamma$//$<11\bar{2}0>_{\alpha_2}$ orientation with a simulated image of the interface superimposed.

Fig. 6. Atomic model of the γ/α_2 interface showing the structural change necessary for growth of the interface.

Fig. 7. Experimental HRTEM image of the α/T_1 habit plane with a simulated image of the interface superimposed. An atomic model of the interface is shown in Fig. 8.

Fig. 8. Model structure for the T_1 phase and the α/T_1 habit-plane interface based on the HRTEM images, with the structural transformation required to produce an $A_1BA_2C...$ stacking from ABC... close-packed planes indicated.

Fig. 9. High-resolution TEM image of the $\{252\}_\gamma$ habit plane in a $<101>_\gamma$//$<111>_\alpha$ orientation. The exact $\{252\}_\gamma$ habit plane is indicated by a horizontal line and the area enclosed is shown enlarged in Fig. 10.

Fig. 10. Enlargement of the γ/α interface with a simulated image superimposed. The interface is faceted along close-packed γ planes. The families of close-packed planes are indicated for both phases in Fig. 10.

Fig. 11. (a)-(d) Simulated images for Al in a $<110>$ orientation with 0.5, 1.5, 2.5 and 3.5at.%Si in the center atomic column (arrow in c). The percent change in image intensity at the solute column is shown in the top-right corner and the solute is visible in (c) and (d).

Fig. 12. Plot of log $|Z_S - Z_M|$ for $<110>$ Si, $<11\bar{2}0>$ Co and $<110>$ Pt with lines of slope = -1 best-fitted through the data.
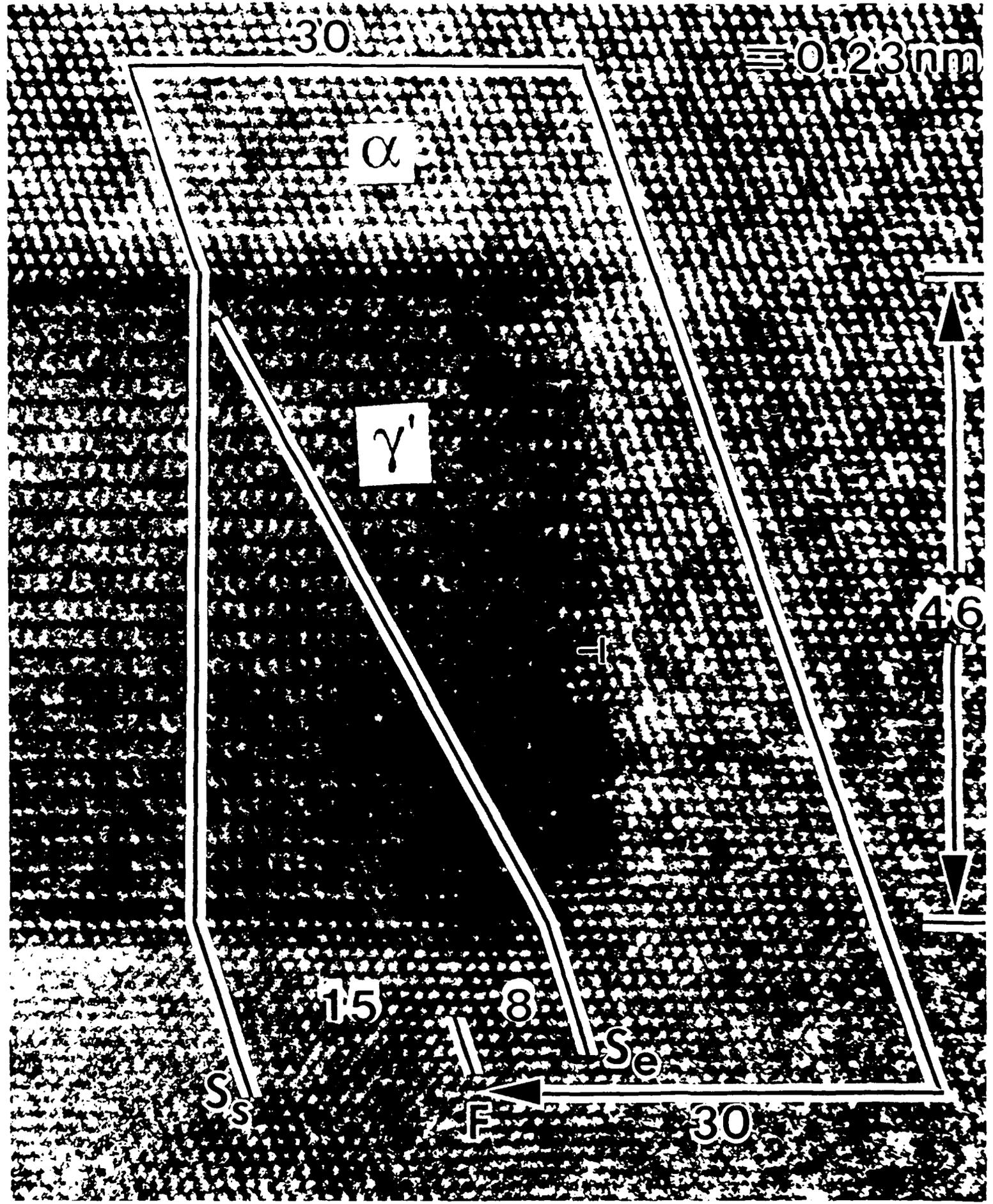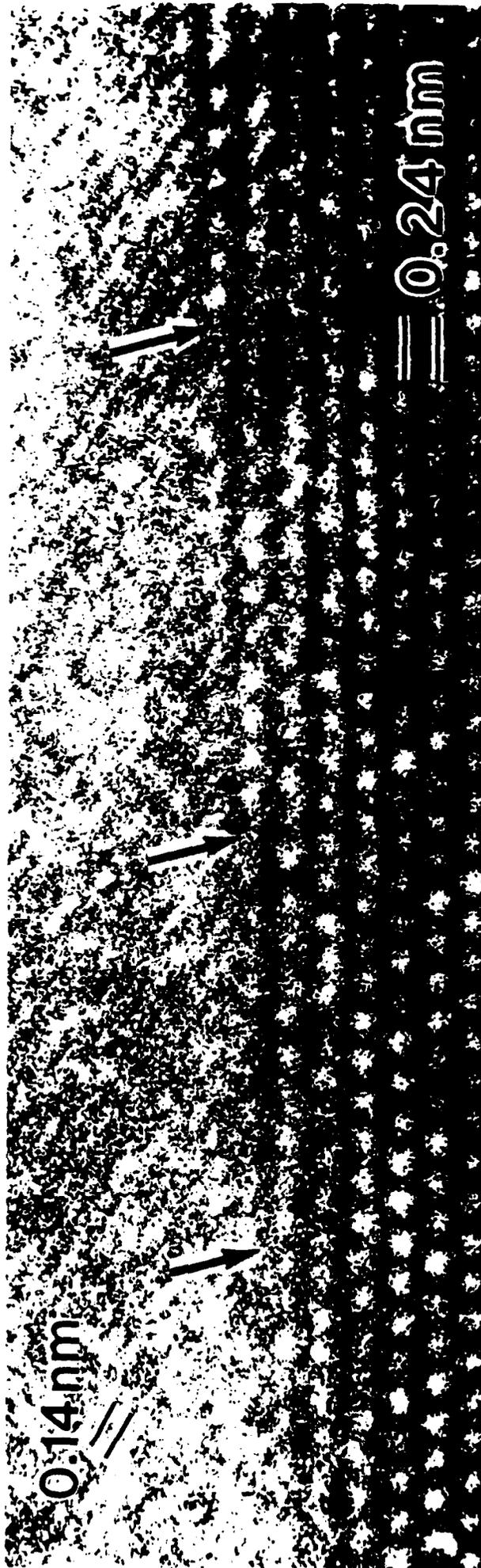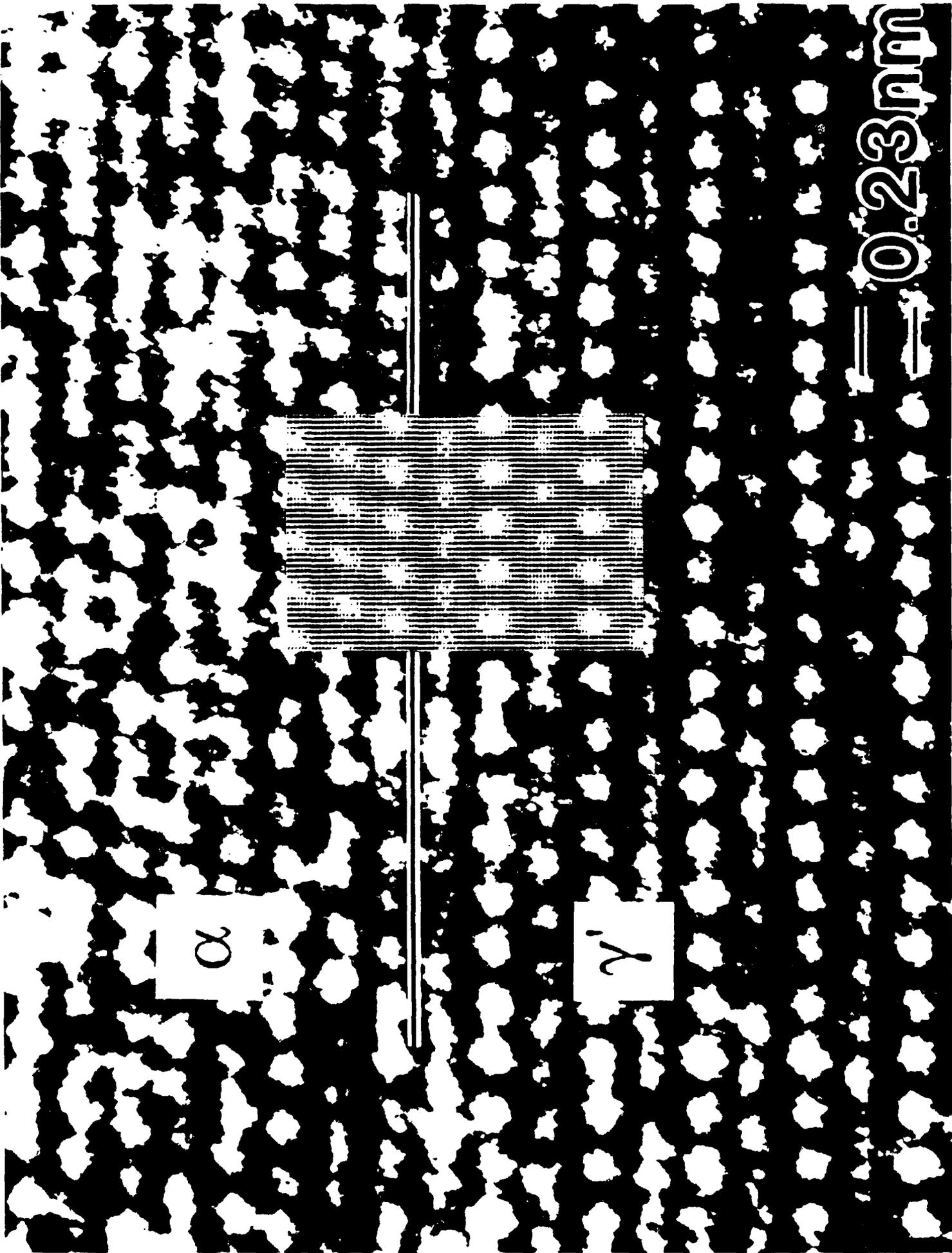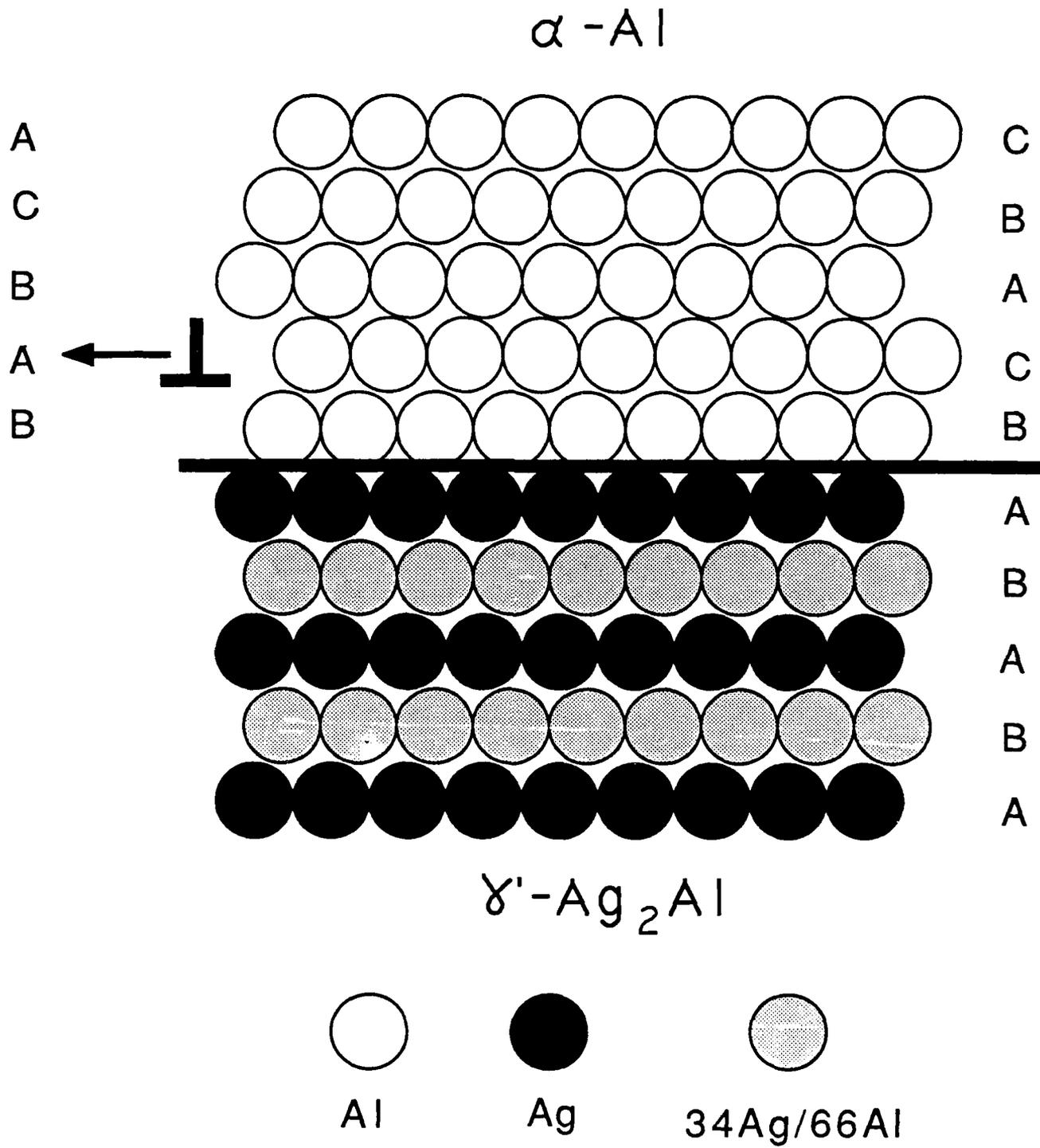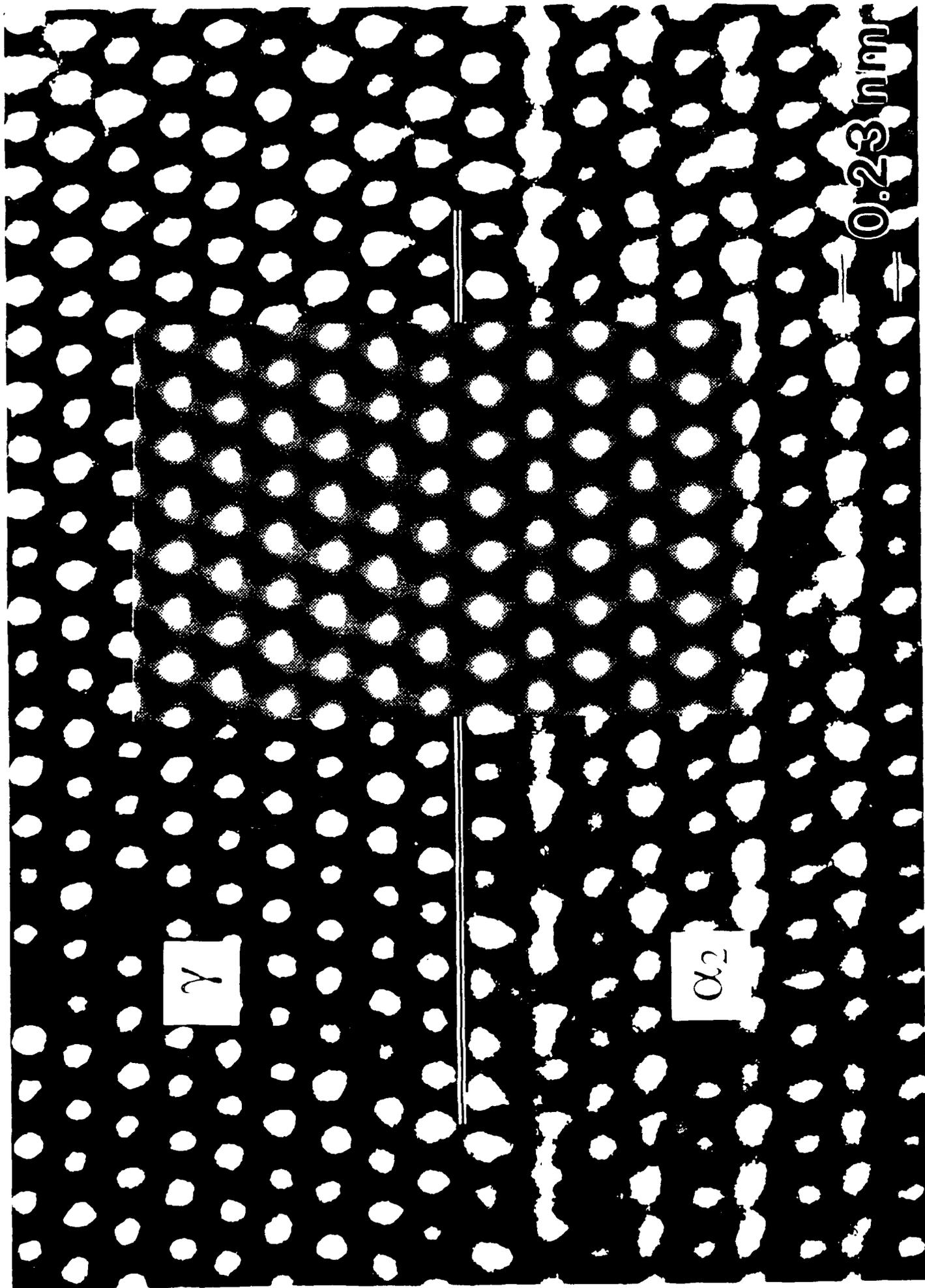
$\equiv$ 0.23nm

α

γ'

30

46

15

8

S_s

Se

F

30

Fig. 1 of Hour & Mahon

Fig 2 of Howard Mehan

α

γ'

= 0.23nm

26

α -Al

A
C
B
A
B

C
B
A
C
B

A
B
A
B
A

γ'-Ag$_2$Al

Al   Ag   34Ag/66Al

Fig. 4 of Howe & Mahon

γ

α₂

0.23 nm

γ-TiAl

α₂-Ti₃Al

Fig. 6 of Howe & Mahon

α

T₁

≡ 0.23 nm

α-Al

T_1

Fig. 8 of Howe & Mahon

α

γ

2.0nm

-0.5%   -1.8%   275

a   b

-3.1%   -4.4%

c   d
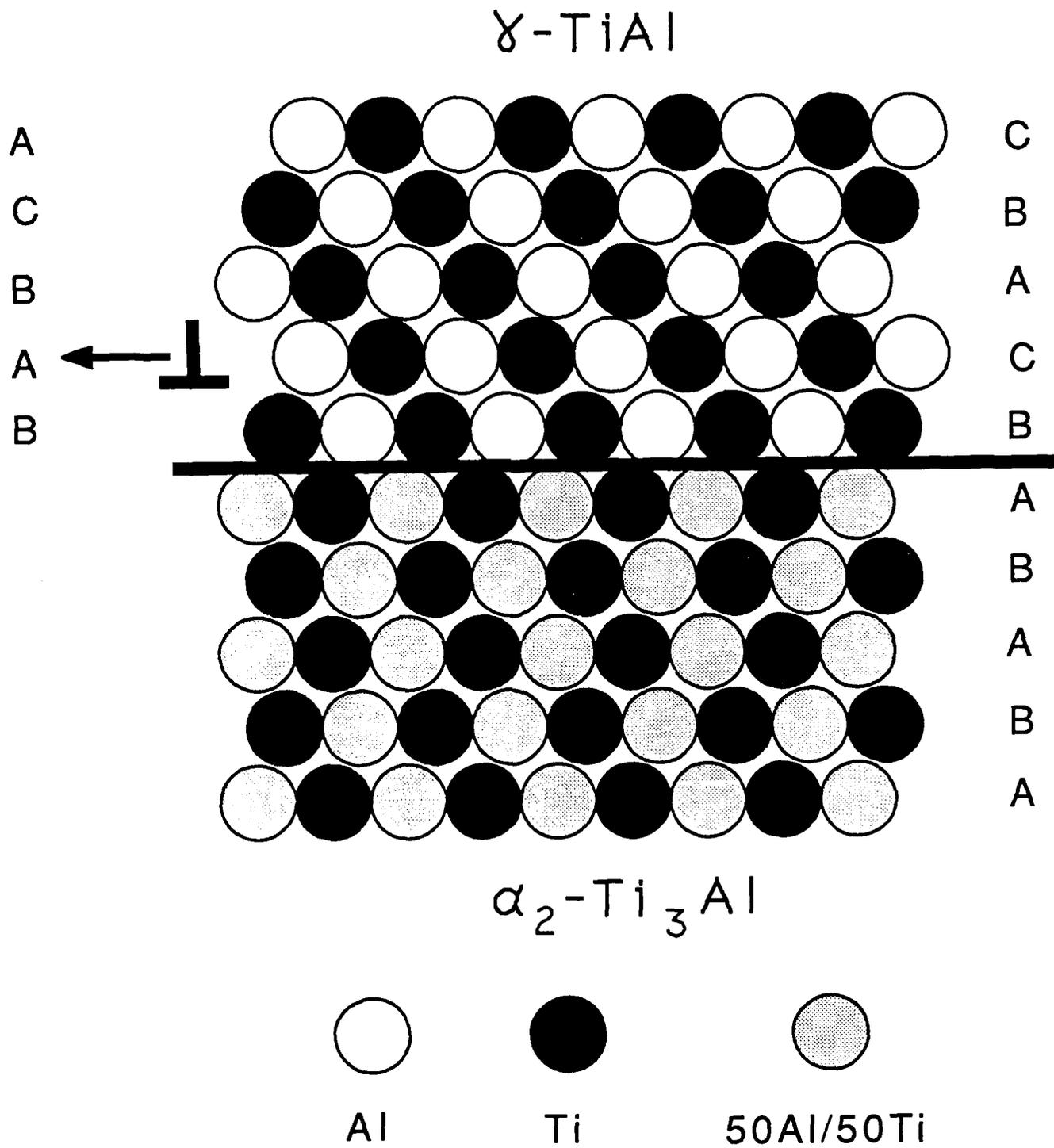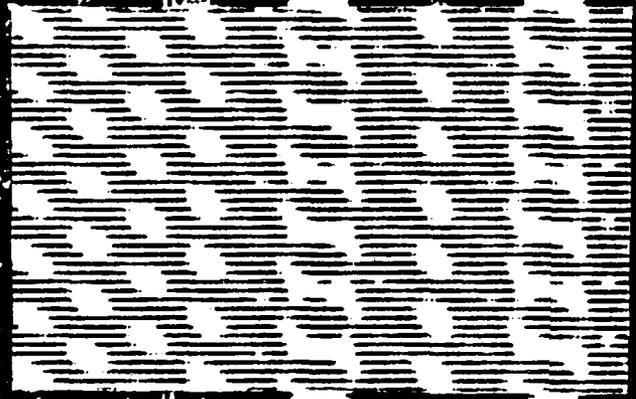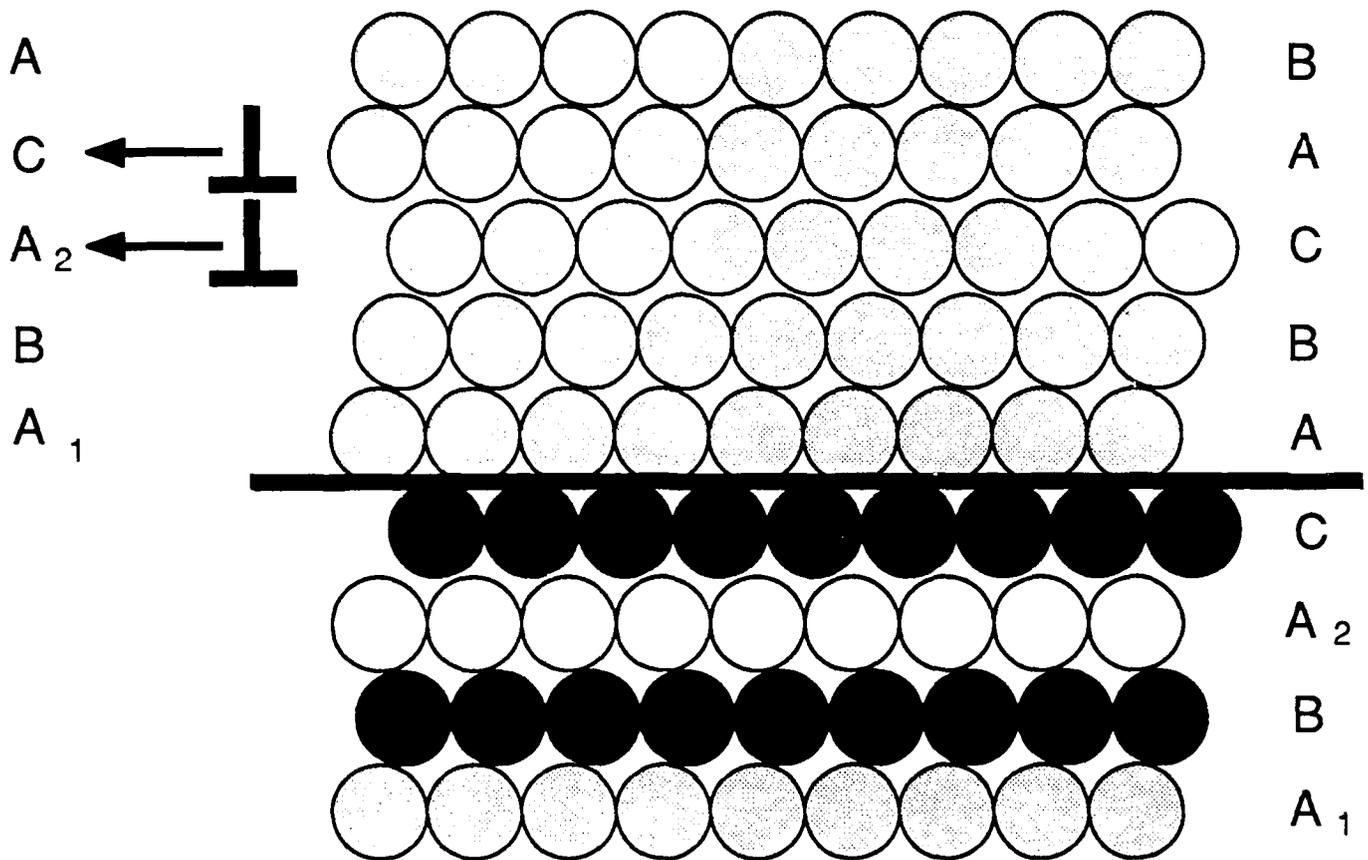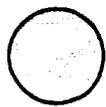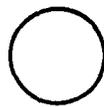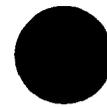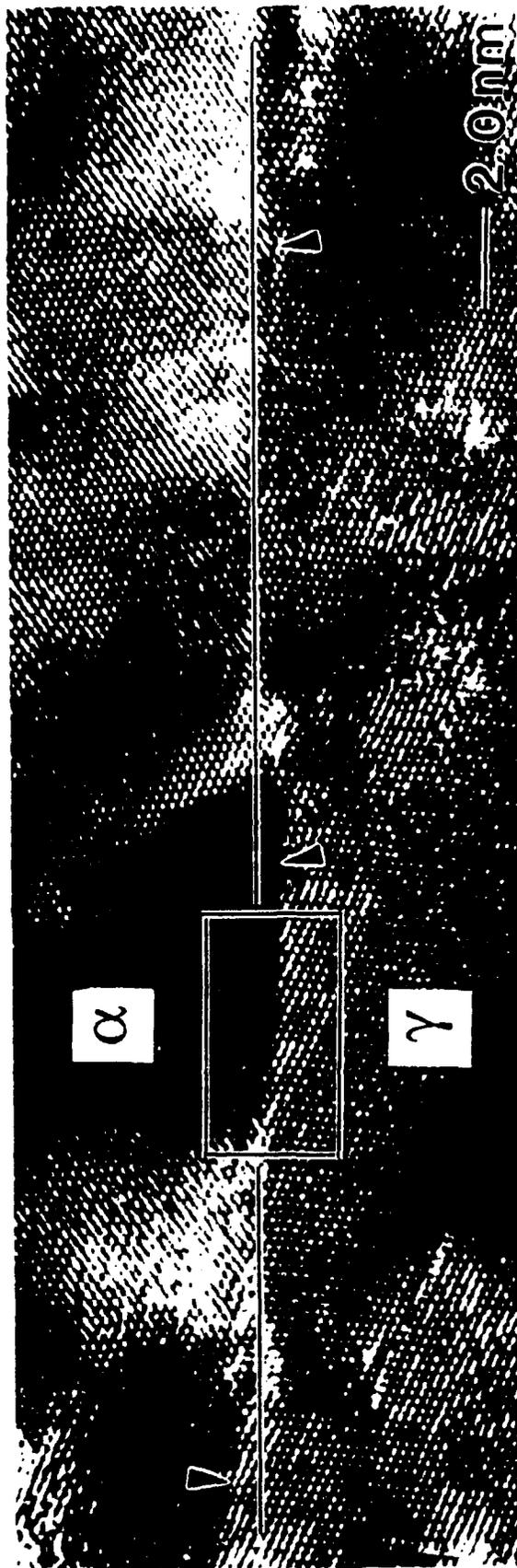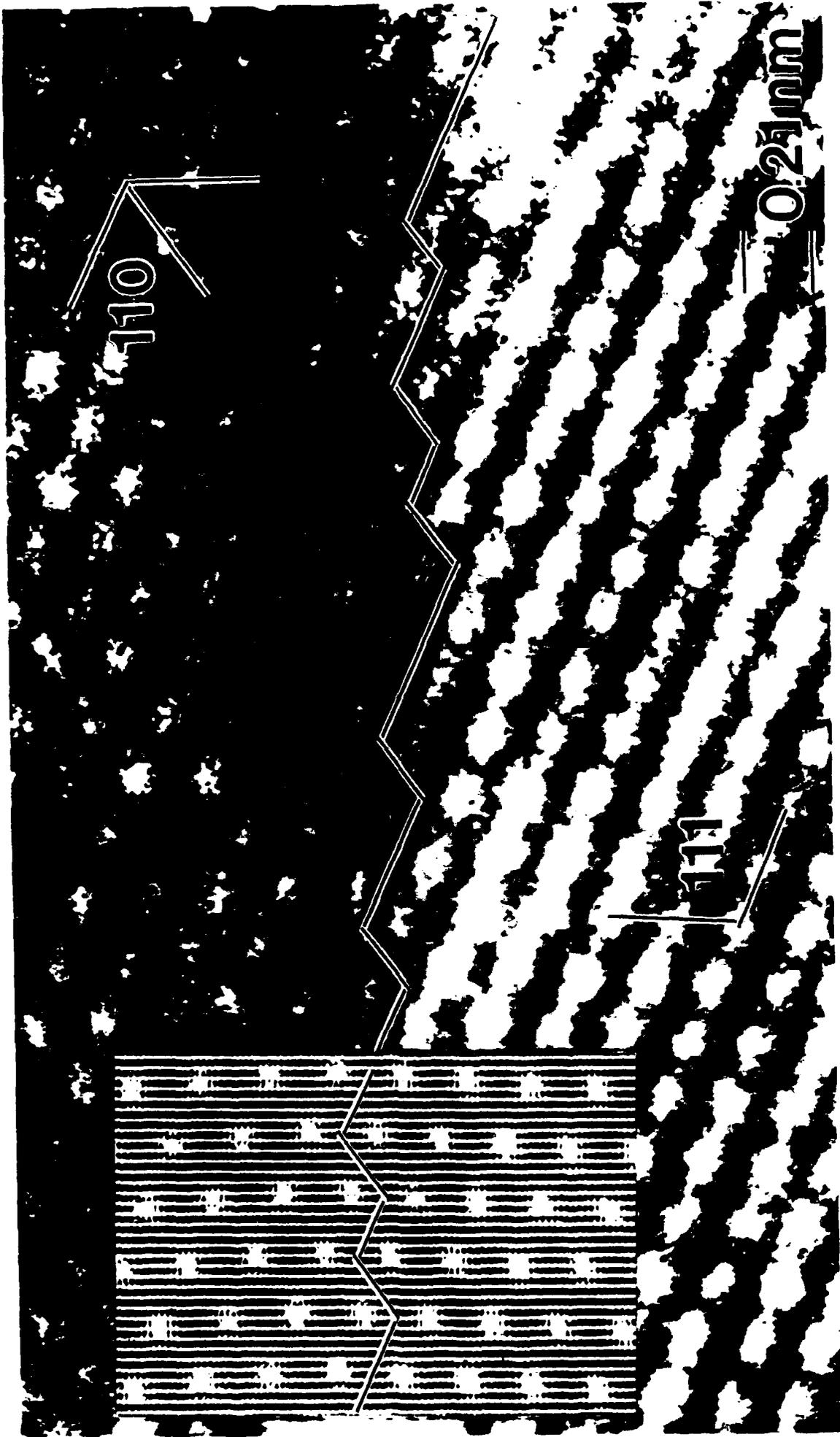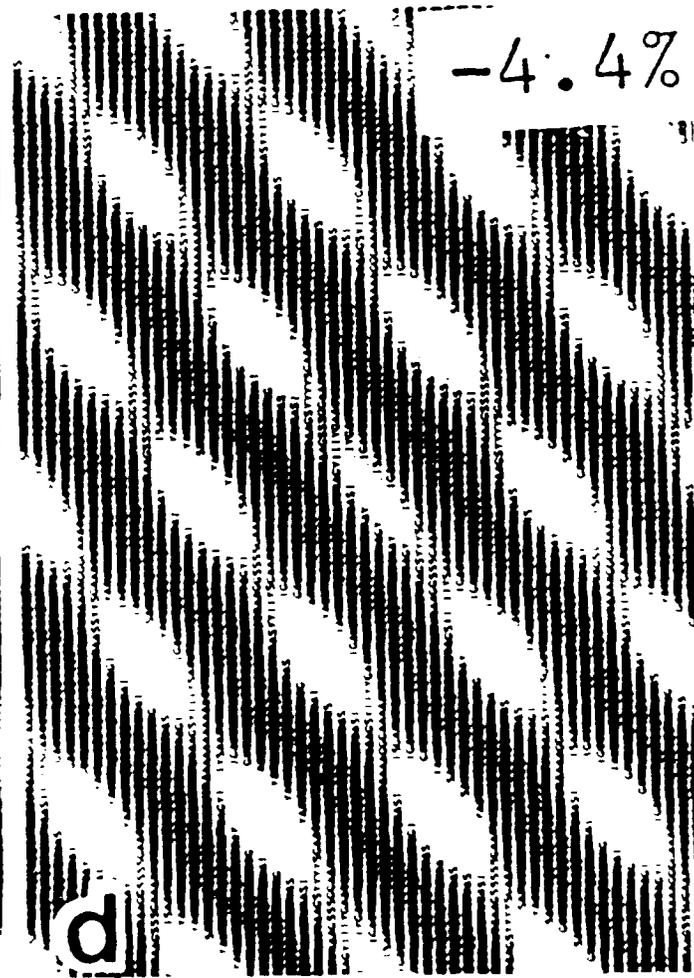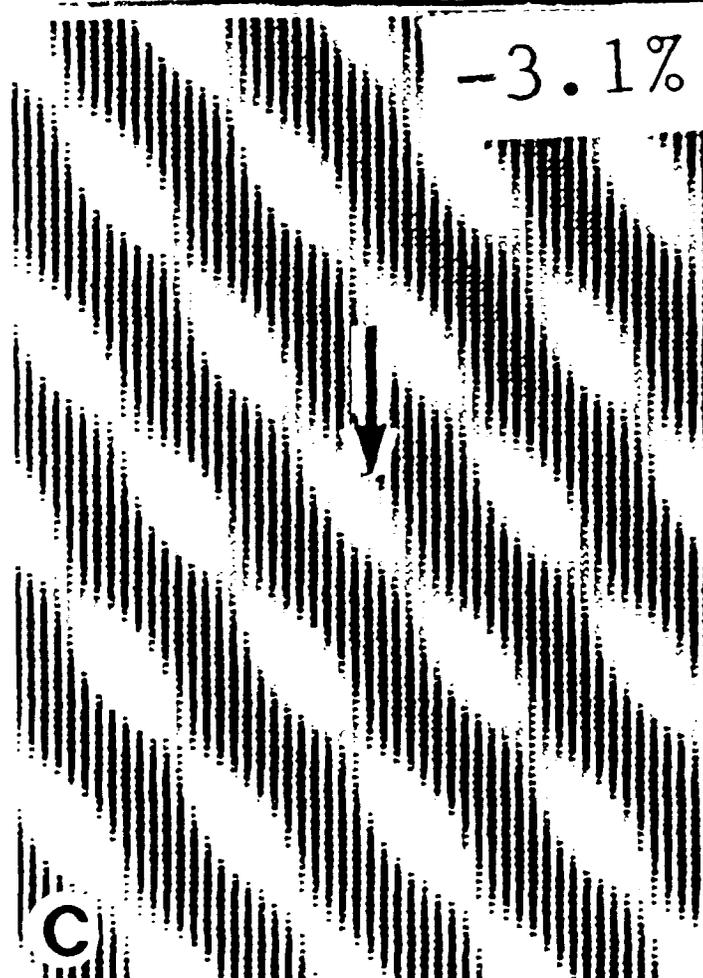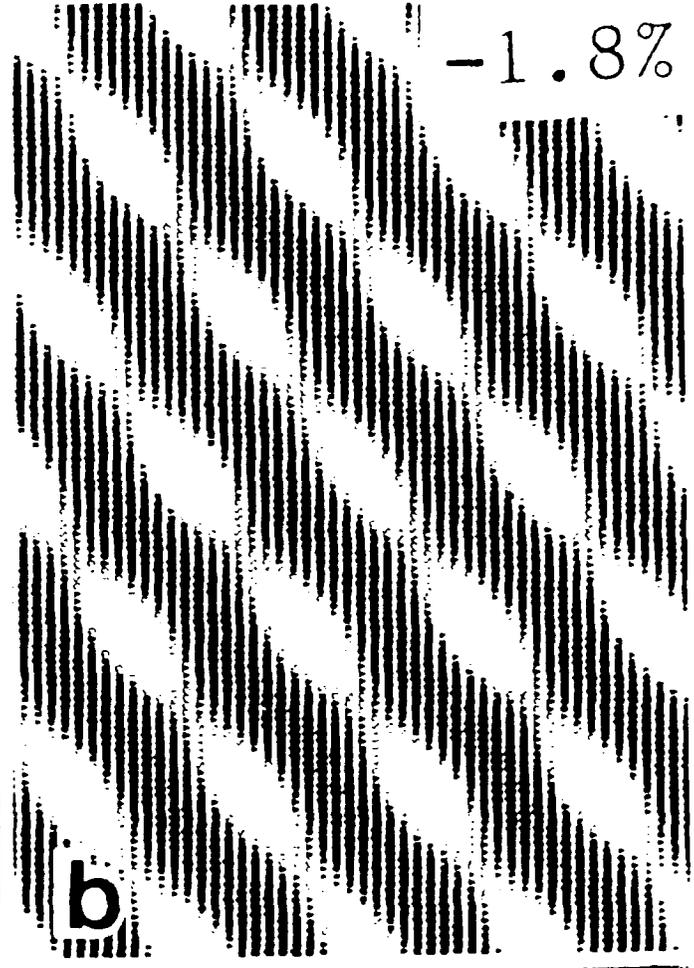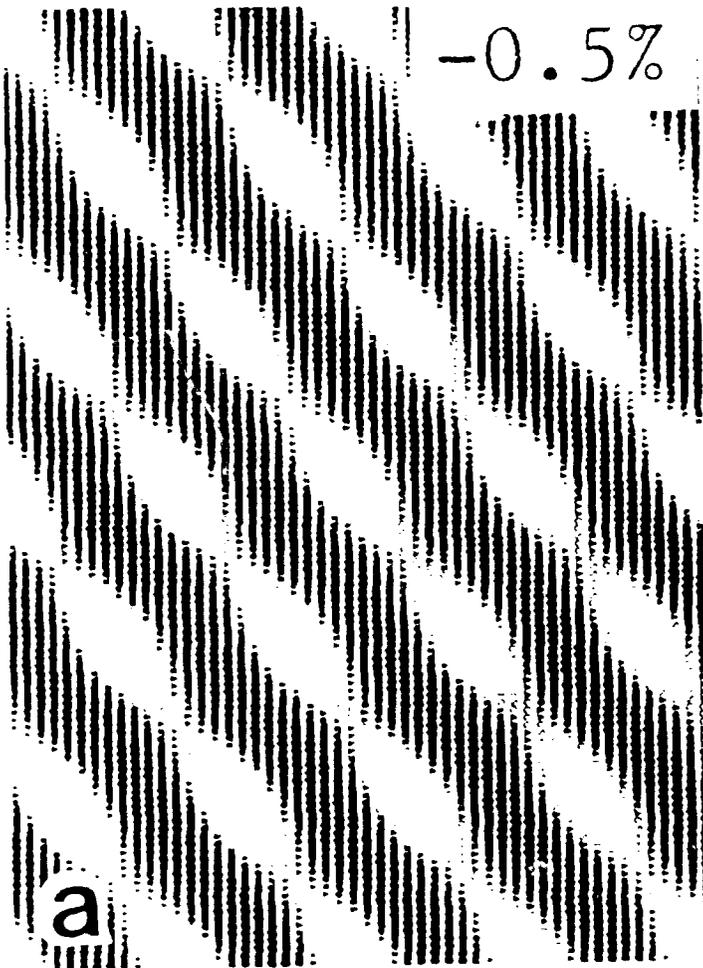
Fig. 11 of Howe and Maher
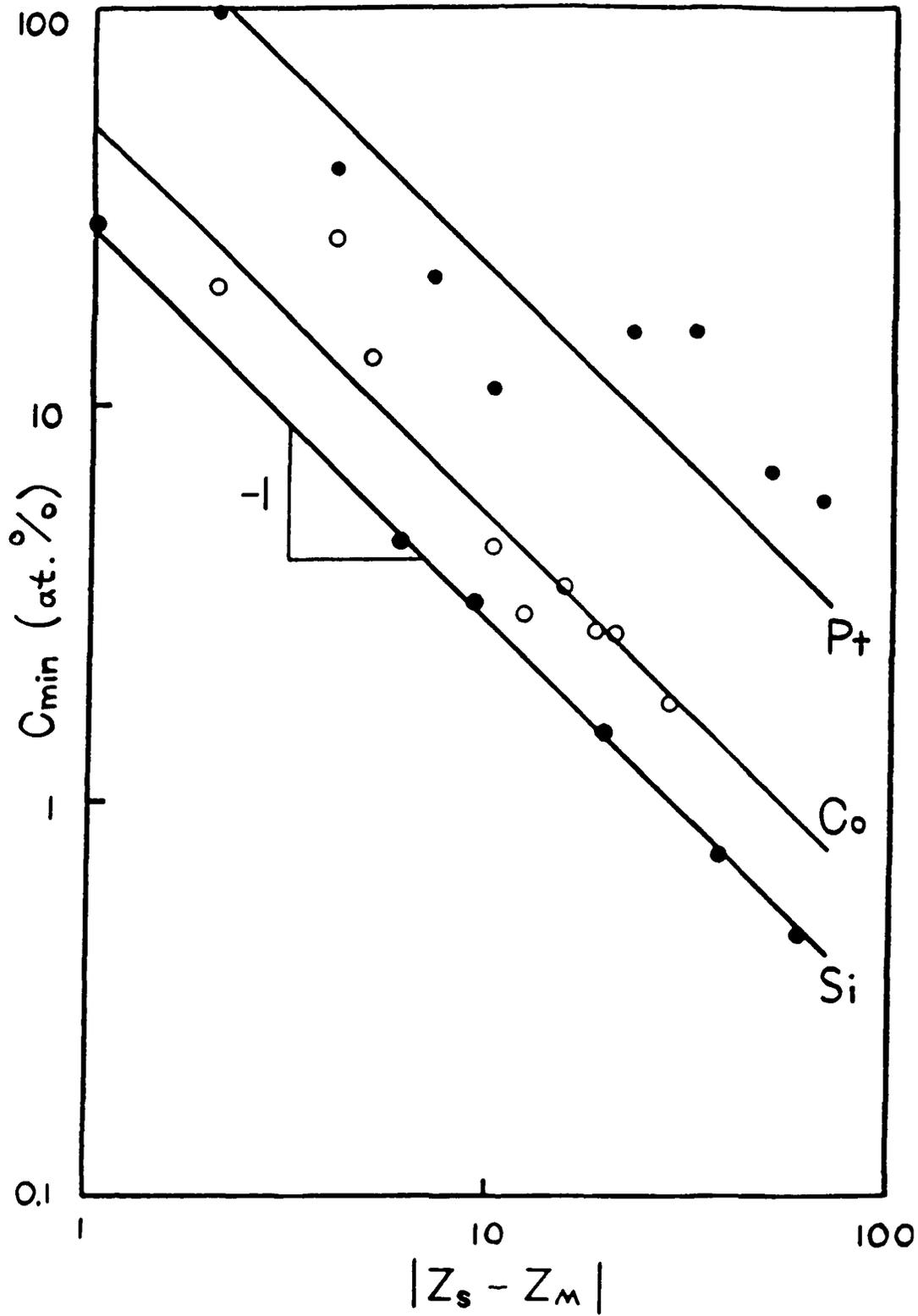
Fig. 12 of Howe & Mahon

PART 3

PROPERTIES and PERFORMANCE

PROPERTIES AND PERFORMANCE

This third section of the Annual Report includes three tasks in the topic area of Properties and Performance. The first of these tasks, entitled "Toughness and Fatigue of Metal Matrix Composites", is being conducted at the University of California at Berkeley under the direction of R.O. Ritchie. The experimental work in this task has focused on aluminum-matrix materials with particulate reinforcement, regarded as model materials for high-temperature particulate composites. The second task in this section is being carried out at Carnegie Mellon University. Entitled "Micromechanisms of High Temperature Composite Behavior", it is directed by A.W. Thompson and (until his departure from Carnegie Mellon in August, 1988) by J.C. Williams. The task has concentrated on high temperature properties of titanium aluminide alloys which are expected to be matrix materials for advanced composites. The third task here, also at Carnegie Mellon, has the topic "Thermal and Mechanical History Effects on Composite Properties", and its investigator is W.M. Garrison. A series of Ti-Al-Nb alloys is being evaluated for thermal and mechanical stability of both microstructure and mechanical properties, with particular emphasis on the mechanical properties resulting from a variety of histories. The individual report sections are as follows.

TOUGHNESS AND FATIGUE OF METAL-MATRIX COMPOSITES

R. O. Ritchie
Department of Materials Science and Mineral Engineering
University of California, Berkeley, CA 94720

The objective of this task is to identify micromechanisms associated with critical and subcritical crack advance in metal-matrix composites, at ambient and elevated temperatures, with particular emphasis on fracture toughness and fatigue-crack propagation.

Work during the past year has focused on characterizing the fatigue resistance (in the presence of long through-thickness cracks) of model particulate-reinforced metallic materials, specifically P/M aluminum alloys reinforced with silicon-carbide particles, with the aim of defining and modelling the role of the reinforcement phase in promoting or impeding cyclic crack extension. Based on a comparison of an unreinforced 9Zn-2½Cu-3Mg aluminum alloy with the same alloy reinforced with 15 or 20 vol.% of either fine (5 µm) or coarse (16 µm) SiC particulate (Al/SiC_p), three separate regimes have been identified where behavior in the monolithic and composite alloys are distinctly different and are controlled by specific crack-tip shielding mechanisms.

At high growth rates typically exceeding 10^{-6} m/cycle, fatigue-crack growth rates in the composites are far in excess of those at comparable stress-intensity levels in the unreinforced alloys; this, however, results from the much lower fracture-toughness K_{Ic} values of the composite materials which causes an accelerated growth rates as K_{max} approaches K_{Ic}.

At intermediate growth rates typically between 10^{-9} and 10^{-7} m/cycle, the composite alloys now show improved fatigue resistance compared to the unreinforced matrix. In this regime, the crack alternatively seeks out "eligible" particles within the plastic zone, leading to limited SiC fracture *ahead* of the crack tip. Although this process tends to accelerate crack advance, the coalescence of these microcracks with the main crack tip additionally leads to the creation of uncracked ligaments *behind* the crack tip, which act to bridge the crack. By modelling the effect of the bridges in terms of a critical crack-opening displacement or critical strain in the ligaments, the degree of crack-tip shielding induced by such crack bridging is computed and shown to be consistent with experiment.

Similarly at near-threshold levels below typically 10^{-9} m/cycle, the composite materials generally show improved fatigue resistance, particularly with the coarser particle distributions, only now due primarily to crack trapping (hindrance of the crack front) and roughness-induced crack closure (crack wedging by fracture-surface asperities) which result from the tendency of the crack path to avoid the SiC particles. By computing the reduction in crack-tip stresses

due to the presence of a SiC particle at the tip, a limiting condition for the fatigue threshold in the composite alloys is derived based on the criterion that the *local* tensile stress in the matrix *beyond the particle* must exceed the yield strength σ_y of the material; this implies that the fatigue threshold should be given by $K_{max,TH} \propto \sigma_y \sqrt{\bar{D}_p}$, where $\bar{D}_p$ is the mean particle size, in agreement with experimental measurement.

Further work is being directed toward examining the comparable fatigue resistance of such metal-matrix composites in the presence of small (1-500 μm) surface cracks which, by virtue of their limited wake, should show accelerated crack-growth rates due to the restricted influence of shielding mechanisms such as crack bridging and crack closure. To complement this, *in situ* studies of deformation and fracture in Al/SiC$_p$ are being performed in the 1.5 MeV Transmission Electron Microscope to examine further the microstructural interaction of the crack path with the reinforcement phase. In addition, limited studies with commence on the long- and small-crack fatigue properties of a recently developed advanced aluminum-lithium alloy reinforced with SiC particulate, and results compared with the traditional alloys.

It is the overall objective of such studies to characterize and model the micromechanisms which govern fatigue-crack advance in metal-matrix composites; it is hoped that through an understanding of such mechanisms at the microstructural scale, new composite alloys can be developed with improved resistance to subcritical crack growth.

Publications

Refereed Journals

1. Jianku Shang, W. Yu and R. O. Ritchie: "Role of Silicon-Carbide Particles in Fatigue Crack Growth in SiC-Particulate-Reinforced Aluminum Alloy Composites," <u>Materials Science and Engineering</u>, vol. 102A, 1988, pp. 181-192.

2. Jianku Shang and R. O. Ritchie: "Crack Bridging by Uncracked Ligaments during Fatigue-Crack Growth in SiC-Reinforced Aluminum-Alloy Composites," <u>Metallurgical Transactions A</u>, vol. 19A, 1988, in press.

3. Jianku Shang and R. O. Ritchie: "On the Particle-Size Dependence of Fatigue-Crack Propagation Thresholds in SiC-Particulate-Reinforced Aluminum-Alloy Composites: Role of Crack Closure and Crack Trapping," <u>Acta Metallurgica</u>, 1988, in review.

Refereed Conference Proceedings

4. Jianku Shang and R. O. Ritchie: "Crack-Tip Shielding in Metal-Matrix Composites: Modelling of Crack Bridging by Uncracked Ligaments," in <u>High Temperature/High Performance Composites</u>, MRS Symposium Proceedings, vol. 120, Materials Research Society, Pittsburgh, PA, 1988.

Invited Presentations

5. R. O. Ritchie: "Ductile Matrix Composites: Fracture and Fatigue," invited presentation at the 1988 Annual Winter Workshop on Composite Materials, University of California, Santa Barbara, CA, Jan. 1988.

6. R. O. Ritchie: "Toughening Mechanisms in Composite Materials," invited keynote lecture, Topical Symp. on Micromechanisms of Fracture in Metal Matrix Composites, 117th TMS Annual Meeting, Phoenix, AZ, Jan. 1988.

7. R. O. Ritchie: "Fracture and Fatigue-Crack Propagation in Advanced Materials," Seminar to the Department of Materials Science and Metallurgy, Cambridge University, Cambridge, U.K., May 1988.

8. R. O. Ritchie: "Fracture and Fatigue Crack Propagation in Ceramics and Metal-Matrix Composites," invited seminar to the Research Institute of Industrial Science and Technology, Pohang, Korea, May 1988.

9. R. O. Ritchie: "Fatigue and Fracture Studies on Advanced Materials," invited seminar to the Metallurgical Engineering and Mechanical Engineering Departments, Tokyo Institute of Technology, Midoriku, Tokyo, Japan, June 1988.

10. R. O. Ritchie: "Kinetics of Crack Growth in Advanced High-Temperature Materials," invited presentation to the Gordon Conference on _High Temperature Chemistry_, Plymouth, NY, July 1988.

11. J.-K. Shang, W. Yu and R. O. Ritchie: "Fatigue Crack Growth in Particulate and Laminate Reinforced Aluminum-Alloy Composites," invited presentation to Topical Symposium on _Mechanical Behavior of Advanced Composites_, TMS Fall Meeting, Chicago, IL, Sept. 1988.

Other Presentations

12. J.-K. Shang and R. O. Ritchie: "Fatigue Crack Propagation Behavior in SiC-Particulate Reinforced Aluminum Alloy Composites," presented at the 117th TMS Annual Meeting, Phoenix, AZ, Jan. 1988.

13. J.-K. Shang and R. O. Ritchie: "On the Role of Crack Tip Shielding during Fatigue Crack Growth in SiC_p/Al Composites," presented at the Symposium on _High-Temperature/High-Performance Composites_, 1988 Spring Meeting of Materials Research Society, Reno, NV, April 1988.

287

CRACK BRIDGING BY UNCRACKED LIGAMENTS DURING FATIGUE-CRACK GROWTH

IN SiC-REINFORCED ALUMINUM-ALLOY COMPOSITES

Jian Ku Shang and R. O. Ritchie

Department of Materials Science and Mineral Engineering
University of California, Berkeley, CA 94720

March 1988

Revised August 1988

submitted to <u>Metallurgical Transactions A</u>

CRACK BRIDGING BY UNCRACKED LIGAMENTS DURING FATIGUE-CRACK GROWTH

IN SiC-REINFORCED ALUMINUM-ALLOY COMPOSITES

Jian Ku Shang and R. O. Ritchie

Department of Materials Science and Mineral Engineering
University of California, Berkeley, CA 94720

ABSTRACT

Micro-mechanisms of crack-tip shielding associated with the growth of fatigue cracks in metal-matrix composites are examined with specific emphasis on the role of crack bridging by uncracked ligaments. Simple analytical models are developed for such bridging induced by both overlapping cracks and by co-planar ligaments in the wake of the crack tip; the models are based on respective notions of a critical tensile strain or critical crack-opening displacement in the ligament. The predicted degree of shielding derived from these mechanisms is not large, but found to be consistent with experimental observations in high-strength P/M aluminum alloys reinforced with 15-20 vol pct of SiC particulate.

I. INTRODUCTION

Recent studies in a wide range of metallic and non-metallic materials have demonstrated the role of crack-tip shielding in enhancing toughness, or more generally in impeding crack advance, by locally reducing the "crack driving force" actually experienced at the crack tip; notable examples are transformation-toughening in ceramics, rubber-toughening in polymers, and fatigue-crack closure in metals, as reviewed in refs. 1 & 2. In certain materials, particularly ceramic composites, a prominent shielding mechanism occurs by bridging between the crack faces (3-17); such bridges can be generated by the presence of brittle fibers (3-8), ductile particles (9-12), or unbroken ligaments in the wake of the crack tip (13-17).

The dominant contribution to toughening from bridging reinforcements can be expressed simply as the product of the volume fraction of the bridging phase with the area under the stress/strain curve, i.e., in terms of the yield strength σ_y, radius R_f and volume fraction V_f of the reinforcement phase (11):

$$G_c = C \, \sigma_y \, R_f \, V_f \tag{1}$$

where C depends on the ductility of the reinforcement phase and the extent of interface debonding. In brittle fiber-reinforced ceramic-matrix composites, such as SiC fibers in alumina where the fibers are sufficiently strong and the fiber/matrix interface sufficiently weak, preferential failure in the matrix can leave intact fibers spanning the crack for some distance behind the crack tip; as the crack opens,

fiber motion is then restrained by, for example, friction in the interface (1,3-8). With ductile-phase reinforcements, such as rubber in polymers or aluminum particles in alumina, particles in the crack path can similarly act as bridges and contribute to the toughness by exhibiting extensive plastic stretching in the crack wake (9-12). In either case, the reinforcement phase, provided it remains unbroken and is intercepted by the crack, can act as a series of springs which restrain crack opening and thereby "shield" the crack tip from the applied far-field loading, resulting in lower, yet crack-size dependent, growth-rate behavior (3-8).

In metallic materials, similar bridging effects are developed in aluminum-alloy laminates reinforced with epoxy-resin sheets impregnated with unidirectional aramid fibers (ARALL® Laminates), where the fiber/epoxy interfaces now are weak enough to permit controlled delamination and thus bridging of unbroken fibers across the crack (18,19). However, in most metal-matrix composites, such as aluminum alloys discontinuously reinforced with SiC fibers (or whiskers or particles), the reinforcement phase invariably fractures due to its strong interface with the matrix, with the result that particle or fiber-bridging is essentially insignificant (17,20).

®ARALL Laminate is a registered trademark of the Aluminum Company of America.

Recently, however, studies on fatigue-crack growth in aluminum alloy/SiC-particulate composites (Al/SiC$_p$) have revealed a different mechanism of bridging, induced by the presence of uncracked ligaments

behind the crack tip (17). Such ligaments, although not necessarily continuous in three dimensions, act in any one two-dimensional section to inhibit crack opening. This mechanism has also been reported for carbide-initiated cleavage cracking in steels (15,16) and from selective fracture of preferential grains in polycrystalline alumina (13). Mechanistically, it appears to result from fracture events triggered ahead of the crack tip or from general non-uniform or discontinuous advance of the crack front; in Al/SiC_p composites it predominates at intermediate fatigue-crack growth rates ($\sim 10^{-9}$ to 10^{-6} m/cycle) where cleavage of SiC particles ahead of the crack tip becomes significant (17).

The objective of the present study is to characterize the nature and significance of such uncracked-ligament bridging in Al/SiC_p composites, and to derive simple models to quantify the magnitude of the induced shielding.

II. EXPERIMENTAL PROCEDURES

The metal-matrix composites used in this investigation were based on a powder-metallurgy (P/M) Al-Zn-Mg-Cu matrix alloy; the alloy, designated Alcoa MB78, is similar to 7091 with composition shown in Table I. Reinforcement was provided by a nominal 15 or 20 vol pct of silicon carbide particulate, of either coarse F-600 grade (nominal size 16 μm) or fine F-1000 grade (nominal size 5 μm). The composite alloys were fabricated by blending prealloyed atomized aluminum-alloy powders with SiC particles, compacting by cold isostatic pressing, vacuum degassing and hot pressing to roughly

Table I. Chemical Composition (in wt pct) of Matrix Al-Zn-Cu Alloy

Zn	Cu	Mg	Si	P	S	Zr	Al
9.44	2.50	3.33	0.14	0.14	0.17	0.08	balance

theoretical density, and finally extruding at an extrusion ratio of 12:1 into 25-mm-thick plates (21); the unreinforced (control) alloy was fabricated in similar fashion, but naturally without the SiC.

In the present study, the alloys (both unreinforced and reinforced) were examined in an overaged condition. The extruded plates were solution treated 4 h at 530°C, quenched in cold water, and (owing to large differences in thermal expansion between the matrix and carbide) immediately compressed 2 to 3 pct by forging to produce a uniform state of deformation to minimize quenching-induced residual stresses. Subsequent aging was performed for 24 h at 121°C followed by 50 h at 171°C (T7X2 temper). Room-temperature uniaxial tensile properties (transverse direction) and fracture-toughness values (S-T orientation) are listed in Table II.

Optical micrographs of the microstructures are shown in Fig. 1. Transmission electron microscopy revealed precipitation of η' ($MgZn_2 \cdot Mg(CuAl)_2$) platelets and equilibrium η ($MgZn_2$) in the matrix, and smaller (~ 0.1 μm) η precipitates on SiC/matrix interfaces. Average SiC particle sizes (aspect ratio $\sim 3:1$) were found to be 11.4 μm in the 15 vol pct alloy and 6.1 μm in the 20 vol pct alloy; grain sizes varied between 2.3 and 4.8 μm. In the 15 vol pct alloy with coarse SiC particles, the distribution of particle sizes was

Table II. Room-Temperature Tensile Properties of Overaged (T7X2)
Alloy

Alloy	Yield Strength σ_y (MPa)	Tensile Strength (MPa)	Elongation on 13 mm (pct)	Reduction in Area (pct)	K_{Ic}* (MPa$\sqrt{m}$)
MB78 unreinforced	380	452	11.9	44.5	46.0[#]
MB78 + 15 pct coarse SiC$_p$	405	460	3.2	10.5	16.6
MB78 + 20 pct fine SiC$_p$	393	439	2.1	9.1	14.3

*S-T orientation.
[#]Invalid result.

more uniform (Weibull modulus of 2.6) than in the 20 vol pct alloy with finer SiC, where distinct clustering of particles was evident (Weibull modulus of 1.6). Further details on the microstructure and particle-size distributions for these materials are given in refs. 17 & 21.

Fatigue-crack propagation tests were performed using 6.4-mm-thick double-cantilever-beam DB(M_z) specimens (S-T orientation), cycled in controlled room air (22°C, 45 pct relative humidity) at a load ratio (R = K_{min}/K_{max}) of 0.1 and a frequency of 50 Hz (sine wave), in general accordance with the guidelines suggested by ASTM Standard E 647-86A. Results were obtained under automated stress-intensity control (with normalized K-gradient of -0.2 per mm) over a wide spectrum of growth rates from 10^{-12} to 10^{-5} m/cycle, using d.c. electrical-potential methods to monitor crack advance. Stress

intensities were computed using the linear-elastic solutions of Srawley and Gross (22). The extent of crack closure was evaluated from crack-mouth opening displacement measurements to determine a closure stress intensity, K_{cl}, defined at first contact of the crack surfaces on unloading (23). Using such measurements, fatigue-crack growth rate data are presented as a function of both the nominal (applied) stress-intensity range, $\Delta K = K_{max} - K_{min}$, and the effective stress-intensity range, $\Delta K_{eff} = K_{max} - K_{cl}$, which allows for the shielding effect of closure.

Fracture morphology was examined in the scanning electron microscope and from crack-path profiles, obtained from metallographic sections (at specimen mid-thickness) on cracks previously impregnated with epoxy. To ensure that uncracked ligaments were indeed uncracked, specimens used for crack profiles were wedge-open loaded to a crack-opening displacement equivalent to $K \approx 10$ MPa$\sqrt{m}$ prior to sectioning. Metallographic sections were also taken at other points along the crack front to reveal the three-dimensional morphology of the crack.

III. EXPERIMENTAL RESULTS

Fatigue-crack propagation rates (da/dN), as a function of both the nominal and effective stress-intensity ranges (ΔK and ΔK_{eff}) for both Al/SiC$_p$ composites, are plotted over a wide spectrum of growth rates from 10^{-12} to 10^{-5} m/cycle in Fig. 2 and are compared with results for the unreinforced matrix alloy; data are presented in terms of ΔK_{eff} to remove confusing effects from shielding by crack

closure. Based on metallographic sectioning, uncracked ligaments in the wake of the crack tip (Fig. 3) were evident primarily in the intermediate growth-rate regime, between typically 10^{-9} and 10^{-6} m/cycle. However, before describing the bridging effect, it is pertinent first to briefly describe behavior in the other regimes.

As discussed elsewhere (17) for peak-aged microstructures, fatigue-crack growth behavior in Al/SiC-particulate composites can be categorized into three regimes. At near-threshold levels below typically 10^{-9} m/cycle, crack closure is the predominant shielding mechanism. This is confirmed in Fig. 2 by the close correspondence below $\sim 10^{-9}$ m/cycle between crack-growth rates for reinforced and unreinforced alloys when closure is subtracted out, i.e., when results are plotted as a function of ΔK_{eff}. In certain microstructures, the crack has a tendency to avoid SiC particles; intrinsic fatigue thresholds, $\Delta K_{TH,eff}$, are generally higher than for the unreinforced constituent matrix, which is in part reflective of the higher stiffness, and hence smaller crack-tip opening displacements (at a given ΔK), in the composite alloys. With increasing ΔK level, the crack starts progressively to seek out SiC particles ahead of the crack tip, consistent with the increase in plastic-zone size and hence statistical sampling volume. This results in an increasing tendency (with increasing ΔK) for the premature fracture of SiC ahead of the crack tip which, because of imperfect coalescence of these cracks with the main crack tip, in turn leads to non-uniform crack fronts, the production of uncracked ligaments, and hence to shielding from crack bridging. Growth rates

in this intermediate regime are thus progressively slower in reinforced alloys, although the effect in certain microstructures, e.g., the 20 vol pct fine SiC_p composite, can be minimal (Fig. 2). At higher ΔK levels above $\sim 10^{-6}$ m/cycle, conversely, growth rates become faster in the composites; this behavior represents the acceleration in growth rates characteristic of stress-intensity levels which approach instability, and reflects the far lower fracture toughness of the reinforced alloys.

IV. EVIDENCE FOR CRACK BRIDGING

In the present Al/SiC_p composites, two distinct types of ligament bridging have been observed during fatigue-crack propagation at intermediate stress intensities. In the alloy with a higher SiC volume fractions and small interparticle spacings (20 vol pct fine SiC_p), the uncracked ligaments are predominantly co-planar with the crack, and directly associated with fracture of carbides ahead of the crack tip (Fig. 3a). In addition, because of their limited size, few SiC particles are present in the ligament. By comparison to behavior in the unreinforced alloy, the resulting effect on crack-growth rates from this form of bridging is small (Fig. 2a,b). Conversely, in alloys with lower volume fractions of more dispersed SiC particles (15 vol pct coarse SiC_p), the uncracked ligaments are principally formed by overlapping cracks on different planes (Fig. 3b), with the result that the beneficial effect on growth rates is now considerably larger (Fig. 2c,d).

As noted above, the creation of uncracked ligaments appears to result from non-uniform growth of the crack front, promoted by the fracture of SiC particles ahead of the crack tip. This is illustrated in Fig. 4 where the "microcracks" created ahead of the tip are clearly associated with cracked particles. Akin to the analogous fracture of iron carbides during cleavage fracture. in steels (24), the particle cracking process may be considered to be stress-controlled and therefore triggered at sites ahead of the crack tip where the tensile stresses are highest (due to crack-tip blunting at the crack tip).[*] This mechanism is promoted at higher stress

---

[*]Based on the asymptotic crack-tip solutions for a power-hardening solid by Hutchinson, Rice and Rosengren (25,26), modified by the blunting solutions of Rice and Johnson (27) and McMeeking (28), the maximum tensile stresses peak at some two crack-tip opening displacements ($\sim K_{max}^2/\sigma_y E$) directly ahead of the crack tip.

---

intensities because at low ΔK levels, where the plastic zone and hence region of high stresses ahead of the tip (i.e., process zone) is small, the probability of finding a weak ("eligible") particle which will crack is limited, due to the small sampling volume; with increasing ΔK levels, the process zone and hence sampling volume increases rapidly such that the probability of finding an eligible particle is much enhanced (17).

Not all "microcracks" in Figs. 3 and 4 appear to be associated with a cracked particle; furthermore, they are generally much larger than the particle size. This follows because the population of particles cracked ahead of the tip is not large (as in low-

temperature cleavage fracture of steels (29,30)), such that in any one two-dimensional micrograph, the particle "microcrack" itself may not be sectioned. However, depending upon the size and orientation of the "microcrack", the stress intensity at the tip nearest to the original crack tip may be as high as 74% of the applied K on the original crack (31-34), such that growth of the "microcrack" will invariably occur. In general, several "microcracks" are formed ahead of the main crack tip (see Figs. 3 and 4); analysis describing the respective stress distributions and stress intensities generated at their tips is outlined in the appendix.

V. MODELLING OF CRACK BRIDGING

There have been several previous models to evaluate the role of crack bridging in metals, ceramics and composites (3-18); in essence, the key problem lies in defining the force in the bridges as a function of the crack-opening displacement or distance from the crack tip. A listing of the force-separation functions utilized in five prominent models (5,9,14-16) is given in Table III. The fiber-bridging model of Marshall et al. (5) and the rubber-particle toughening model of Kunz-Douglass et al. (9) compute the strain in the bridges from the strain compatibility between the fiber and matrix during fiber pull-out or from the shape change of rubber particles, and are thus mechanism-specific. Conversely, Mai and Lawn (14), in their interfacial-bridging model for toughness and resistance-curve behavior in ceramics, simply adopt a trial exponential force-separation function, with parameters set by the

Table III. Force-Separation Functions for Various Models

	Marshall Cox Evans	Mai Lawn	Kunz-Douglass Beaumont Ashby	Gerberich	Rosenfield Majumdar
Separation-Function	$\sigma(x)=2\cdot[u\cdot\tau\cdot E_f\cdot(1+\eta)/R]^{\frac{1}{2}}$ τ - interfacial stress E_f - fiber modulus R - fiber radius $\eta - E_f\,V_f/E_m(1 - V_f)$	$p(u) = p^*(1 - \dfrac{u}{u^*})^m$ u^*,p^* - limiting values m - mechanism-dependent $p = f\cdot\sigma(x)$	$\sigma = G\cdot(\epsilon - \dfrac{1}{\epsilon^2})$ G - modulus ϵ - true strain	$\sigma = \sigma_y$	$\sigma = \sigma_f$
Method	pull-out mechanics (strain compatibility)	trial function	constitutive eqn. for rubber	yield strength	fracture stress
Applications	fiber bridging in ceramic matrix composites	interfacial bridging	rubber-toughened plastics	general	
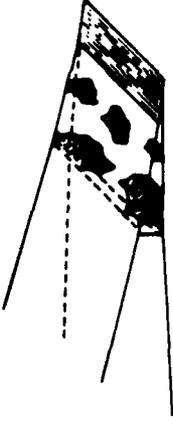
particular mechanism. The equilibrium-crack models of Gerberich (15) and Rosenfield and Majumdar (16), on the other hand, are more general, but assume simply that the stress in the bridges is equal to the yield or fracture stress, respectively.

In the current work, two approaches are taken to model the forms of ligament bridging observed during fatigue-crack growth in Al/SiC_p, i.e., based on a limiting crack-opening displacement or a limiting strain in the uncracked ligaments; analyses are described below.

A. General Considerations

The uncracked ligaments are taken to exist over a distance $x = \ell$ (the bridging zone) behind the crack tip, and are characterized by area fraction, f, occupied on the crack plane (Fig. 5). The ligaments act as bridges which limit crack opening; the stresses introduced into these ligaments consequently depend upon the opening displacements of the crack faces. The resulting restraining effect can thus be represented by forces exerted on the crack faces, which are a function of the stresses in the ligament and the ligament size. As the distribution and size of the ligaments are a complicated function of local microstructure, for simplicity, a uniform distribution is assumed such that the distributed force per unit thickness, dp(x), from uncracked ligaments in an infinitesimal interval, dx, can be represented as:

$$dp(x) = f \, \sigma(x) \, dx \tag{2}$$

where $\sigma(x)$ is the stress in the ligaments. For a semi-infinite

crack, this distributed force induces a stress intensity given by (35):

$$K_s = \frac{\sqrt{2}}{\pi} \int_0^\ell \frac{dp(x)}{\sqrt{x}} \tag{3}$$

If the crack is now subjected to an applied stress field σ_a, superposition of the shielding stress intensity, K_s, due to bridging with the globally applied (far-field) stress intensity, K_a, yields an expression for the effective (near-tip) stress intensity, K_{tip}, experienced locally at the crack tip:

$$K_{tip} = K_a + K_s \tag{4}$$

Solutions to Eqs. 2-4, involving the determination of the stress function, $\sigma(x)$, are given below.

B. Limiting Crack-Opening Displacement Approach

The basis of this approach is that the stress in any ligament behind the crack tip is related to the crack opening at that point; specifically the displacement in the last intact ligament at the end of the bridging zone must approach the limiting crack-opening displacement, δ_c, for fracture of that ligament. By assuming for simplicity that an idealized fatigue crack can be taken as trapezoidal (Fig. 6), the crack-opening displacement, δ_x, at any distance x along the crack length can be determined in terms of the crack-tip opening displacement, δ_{tip}, and specimen ligament, b (36):

$$\delta_x = \delta_{tip} \; (\frac{x + rb}{rb}) \tag{5}$$

assuming that the crack opens about some rotational axis at a distance, rb, ahead of the crack tip; r is the rotational factor and takes values between 0.195 for elastic deformation and 0.470 for plastic deformation (37). The value of the crack-tip opening displacement, δ_{tip}, can be determined from near-tip stress intensity, K_{tip}, in terms of Young's modulus, E, and the yield strength, σ_y, of the ligament (38):

$$\delta_{tip} = d \cdot \frac{K^2_{tip}}{E'\sigma_y} \tag{6}$$

where $E' = E$ in plane stress and $E/(1 - \nu^2)$ in plane strain, ν is Poisson's ratio, and d is a constant varying between 0.3 and 1.0 depending upon the yield strain and work-hardening exponent and whether plane-strain or plane-stress conditions apply (38).

To maintain equilibrium such that the crack may extend without breaking ligaments along the bridging zone, the crack-opening displacement at any point within the zone, δ_x, must satisfy:

$$\delta_x \leq \delta_c \;, \qquad\qquad 0 \leq x \leq \ell \tag{7a}$$

whereas at the end of the bridging zone:

$$\delta_x = \delta_c \;, \qquad\qquad at\; x = \ell \tag{7b}$$

where δ_c, the maximum displacement in the ligament corresponding to its failure, is independent of the size of bridging zone but varies

with the area fraction, f, of ligaments. Thus, assuming that a partially-bridged crack, with $f < 1$, is analogous to a fully-bridged crack with an effective thickness of f times the full specimen thickness, Eq. 4 becomes:

$$\sqrt{\frac{\delta_c \ rb \ E' \ \sigma_y}{d(\ell + rb)}} \ = \ K_a + \frac{\sqrt{2}}{\pi} \int_0^\ell \frac{\sigma(x)dx}{\sqrt{x}} \tag{8}$$

yielding an expression for the stress, $\sigma(x)$, in the ligaments:

$$\sigma(x) \ = \ - \frac{\pi}{2\sqrt{2}} \sqrt{\frac{\delta_c \ rb \ E' \ \sigma_y}{d}} \left[\frac{x^{\frac{1}{2}}}{(x + rb)^{3/2}} \right] \tag{9}$$

With substitution, Eq. 9 provides an expression for the degree of crack-tip shielding due to uncracked-ligament bridging, in terms of the area fraction of ligaments, the applied stress intensity and the ratio ℓ/rb:

$$K_s \ = \ -f \ K_a [(1 + \ell/rb)^{\frac{1}{2}} - 1]/[1 - f + f(1 + \ell/rb)^{\frac{1}{2}}] \tag{10}$$

C. Limiting Strain Approach

An alternative, first-order solution to Eqs. 2-4 can be obtained by representing the bridges as tensile ligaments, where the stress in a ligament is proportional to the strain. The extent of the bridging zone is then determined by the limiting strain in the ligament furthest away from the crack tip being equal to the fracture strain. With reference to Fig. 6, the strain, $\epsilon(x)$, in any ligament within the bridging zone can be estimated by assuming it to be equivalent to the strain in a bent beam, with rotational center at

point C and neutral plane at the crack tip, such that:

$$\epsilon(x) = x/rb \tag{11}$$

Converting to a true strain and substituting into a constitutive law for the uncracked-ligament material, of the form:

$$\sigma(x) = \sigma_y + k\,\epsilon(x) \tag{12}$$

where σ_y is the (initial) yield stress and k is a constant, provides a second expression for the degree of crack-tip shielding due to uncracked-ligament bridging, in terms of the area fraction of ligaments, the ratio ℓ/rb and the (constrained) flow properties of the ligament:

$$K_s = -f \cdot \sigma_y \cdot \frac{2\sqrt{2\ell}}{\pi} \left\{ 1 + \frac{k}{\sigma_y} \left[\ln(1 + \frac{\ell}{rb}) + 2(\sqrt{\frac{rb}{\ell}}\ \tan^{-1}\sqrt{\frac{\ell}{rb}} - 1) \right] \right\} \tag{13}$$

VI. DISCUSSION

To evaluate the proposed expressions for crack bridging in Eqs. 10 & 13, we note that the phenomenon predominates in the Al/SiC$_p$ alloys between $\sim 10^{-9}$ and 10^{-6} m/cycle. Measurements over this range, involving metallographic studies of the crack-path morphology using serial sectioning at an average stress-intensity range ΔK of approximately 8 MPa$\sqrt{m}$ ($K_a = 9$ MPa$\sqrt{m}$), indicated an area fraction of bridges of 27 to 31% along a bridging zone, ℓ, of approximately 400 μm behind the crack tip; rb is typically 1 mm for the DB(M$_z$)

geometry. The constitutive properties of the bridges pertain to deformation under highly constrained conditions. However, in the absence of such information, properties determined uniaxially are assumed; values of σ_y and k are thus respectively taken to be 380 and 1600 MPa for unreinforced bridges, and 405 and 2200 MPa for reinforced bridges.

A. Specific Trends

Some specific trends in the degree of crack-tip shielding predicted by Eqs. 10 & 13 are plotted in Figs. 7 & 8. The influence of the size of the bridging zone is shown for both models in Fig. 7 where the normalized shielding stress intensity, K_s/K_a, is plotted as a function of ℓ/rb. For Eq. 13, K_s is normalized by the shielding stress intensity, K_a', evaluated where the uniform stress in all ligaments is equal to the yield stress (15). Clearly for both models, K_s increases monotonically with ℓ/rb; specifically K_s tends to zero as ℓ approaches zero, and at a finite bridging-zone size, K_s increases with ℓ in a nearly parabolic fashion, consistent with the previous models (14,15) which utilize different stress/separation functions. The dependence of K_s on rb in both equations is hyperbolic (Fig. 8a,b), and may be taken as a consequence of the assumed crack geometry. However, since rb is related to the crack-opening angle (COA) by:

$$COA = \tan^{-1} (\delta_{tip}/2rb) \tag{14}$$

this dependence is expected for crack extension at constant COA (39),

as δ_{tip} must decrease with decreasing rb; as rb approaches zero, δ_{tip} must be zero for a finite COA, leading to $K_{tip} = 0$ or $K_s = K_a$, which is the limiting case for Eq. 10 as rb → 0.

The effect of varying the area fraction of uncracked ligaments, as predicted from Eqs. 10 & 13, is plotted in Fig. 8c,d. Whereas both models yield the obvious limiting case of $K_s → 0$ as f → 0, for the other limit of f → 1, which corresponds to a fully bridged crack, Eq. 10 yields a simple upper bound; the crack-opening displacement at the end of the bridging zone along a crack of length (a) is determined by the stress intensity ahead of a crack of length (a - ℓ). Using Eq. 5, this implies:

$$K_{tip} = K_{a-\ell} \left(\frac{rb}{\ell + rb} \right)^{\frac{1}{2}}$$
(15)

such that:

$$K_s = K_{tip} - K_a = - K_a \left[1 - \frac{K_{a-\ell}}{K_a} \cdot \left(1 + \frac{\ell}{rb} \right)^{-\frac{1}{2}} \right]$$
(16)

which is consistent with the same limit in Eq. 10 provided ℓ/a « 1:

$$K_s = -K_a \left[1 - (1 + \ell/rb)^{-\frac{1}{2}} \right]$$
(17)

Finally, for fixed values of f and ℓ/rb, the shielding stress intensity K_s is predicted to show a linear dependence on both applied stress intensity and yield strength, as illustrated in Fig. 8e,f.

B. Application to Al/SiC$_p$ Composites

To apply these models to the cyclic crack-growth behavior in Al/SiC$_p$ composites (Fig. 2), we note that the stretching of co-planar uncracked ligaments is controlled by the crack opening; the degree of

crack-tip shielding is thus more appropriately described by the limiting crack-opening displacement model (Eq. 10). Using the measured values of f, ℓ and rb defined above, the stress intensity K_s due to bridging is predicted to be approximately 0.5 MPa$\sqrt{m}$ at an applied K_a of 9 MPa$\sqrt{m}$. This form of bridging thus induces minimal shielding ($\sim$6% in this case), consistent with the minimal difference in growth rates between the reinforced and unreinforced 20 vol% SiC alloys at ΔK = 8 MPa$\sqrt{m}$ (Fig. 2a,b). Conversely, the deformation of uncracked ligaments resulting from overlapping cracks is less a function of the crack opening but rather is limited by the strength of the ligament; the limiting-strain model (Eq. 13) is therefore more appropriate. Here using measured values of f, ℓ, rb, σ_y and k at K_a = 9 MPa$\sqrt{m}$, the stress intensity K_s due to bridging is predicted to be $\sim$ 2.4 MPa$\sqrt{m}$ for reinforced ligaments and $\sim$3.2 MPa$\sqrt{m}$ for unreinforced ligaments. This clearly represents a more substantial degree of shielding ($\sim$25 to 30%) and is consistent with the larger shift in growth-rate curves between the reinforced and unreinforced 15 vol% SiC alloys at ΔK = 8 MPa$\sqrt{m}$ (Fig. 2c,d).

It should be noted that such direct application of the bridging models to account for differences in the growth-rate behavior of the unreinforced and reinforced alloys is complicated by the simultaneous action of several mechanisms (Fig. 9). For example, growth rates will be additionally influenced by such processes as limited carbide fracture ahead of the tip, crack deflection and resulting crack closure from fracture-surface asperity contact (17). However, crack closure from asperity-wedging predominates at near-threshold levels

where the crack-opening displacements are comparable to the asperity size (40); in contrast, the influence of uncracked-ligament bridging is essentially insignificant in this regime. This follows, not simply from the mathematics which predict $K_s \to 0$ as $K_a \to 0$ (Fig. 8e), but from the fact that the uncracked ligaments result primarily from fracture events triggered ahead of the crack tip, e.g., SiC-particle fracture, which is only favored at higher stress-intensity levels (17). This can be best explained in statistical terms. The maximum probability of a particle fracture is always located some distance ahead of the tip, because although the stresses are highest very close to the tip, the probability of finding a larger, more crackable particle increases with the sampling volume, i.e., with distance ahead of the crack tip within the plastic zone (17,29,30). Although expressions for the sampling volume (30) are beyond the scope of this paper, upper-bound estimates can be made from the cube of the plastic-zone size; computations of the plastic-zone size are listed for the two Al/SiC$_p$ composite alloys in Table IV. It is apparent that at near-threshold levels, the radius of sampling volume is comparable to the average particle size and much less than the particle spacing; extensive SiC particle fracture ahead of the crack tip, and hence the consequent production of uncracked ligaments, are thus extremely unlikely. However, as the stress intensity is raised, the generation of crack bridges becomes significant as the sampling volume increases rapidly, in actuality with the sixth power of the stress intensity.

Table IV. Plastic-Zone and Particle Dimensions in Al/SiC$_p$ Composites

Alloy	Average Particle Size (μm)	Average Particle Spacing (μm)	Plastic-Zone Size* ΔK_{TH} (μm)	$\Delta K = 8$ MPa$\sqrt{m}$
MB78 + 15 pct coarse SiC$_p$	11.4	56	15	77
MB78 + 20 pct fine SiC$_p$	6.1	23	12	81

*Estimated from $(1/2\pi)(K_{max}/\sigma_y)^2$.

Finally, it might be noted that the "toughening" induced by co-planar uncracked ligaments can be viewed in two different ways: as crack bridging by ligaments in the crack wake, if the "crack" is considered to encompass all of the disconnected coplanar "microcracks" with the "tip" at the leading microcrack (as above); or as shielding derived from the growth of microcracks in a damage zone ahead of the "crack tip", which is then associated with the point of crack continuity, i.e., of failure of the last bridging element. The distinction, whether the ligaments constitute a bridging zone <u>behind</u> the crack tip (which appears beneficial to hindering crack advance) or a damage zone <u>ahead</u> of it (which would appear detrimental), depends solely on the definition of the crack tip. This apparent paradox, however, has recently been treated in some detail by Thouless, who finds that the two approaches are actually equivalent and that identical crack-extension rates are predicted (41).

VII. CONCLUSIONS

Based on a study of crack bridging via uncracked ligaments in P/M Al-Zn-Mg-Cu alloys reinforced with 15-20 vol pct of silicon carbide particulate (Al/SiC$_p$), simple models are developed to predict the magnitude of crack-tip shielding during fatigue-crack growth. It is found that the production of uncracked ligaments is associated with fracture events triggered ahead of the crack tip, specifically the cracking of SiC particles; as such particle fractures are significant only at higher stress-intensity levels, crack bridging is seen to predominate at higher growth rates, typically between 10^{-9} and 10^{-6} m/cycle. Proposed crack-bridging models based upon a limiting crack-opening displacement in the bridge are found to predict only minimal shielding, but are most appropriate to co-planar ligaments. Conversely, models based on a limiting strain are appropriate to ligaments formed by overlapping cracks, and predict larger levels of shielding, consistent with experimental results.

NOMENCLATURE

a	(macro) crack length
b	uncracked specimen ligament
c	half length of "microcrack"
C	constant in Eq. 1
COA	crack opening angle
d	constant in Eq. 6
da/dN	fatigue-crack growth rate per cycle
dp(x)	distributed force per unit thickness (Eq. 2)

D	distance of "microcrack" from macrocrack tip
E	Young's modulus
E'	$= E/(1 - \nu^2)$ in plane strain, and E in plane stress
E_f, E_m	fiber and matrix modulus, respectively
f	area fraction of uncracked ligaments on crack plane
g	variable in elliptic integrals
G	shear modulus
G_c	critical strain energy release rate (toughness)
k	constant in constitutive law (Eq. 12)
K	stress-intensity factor
K_a, $K_I(\infty)$	applied stress intensity
$K_{a-\ell}$	stress intensity ahead of crack of length $(a - \ell)$
K_{cl}	closure stress intensity
K_{Ic}	plane-strain fracture toughness
K_{max}, K_{min}	maximum and minimum stress intensity, respectively
K_s	shielding stress intensity
K_{tip}	near-tip stress intensity
ΔK	(nominal) stress-intensity range $(= K_{max} - K_{min})$
ΔK_{eff}	effective stress-intensity range $(= K_{max} - K_{cl})$
ΔK_{TH}	(measured) fatigue-crack growth threshold
$\Delta K_{TH,eff}$	intrinsic (effective) fatigue-crack growth threshold
ℓ	length of bridging zone
m	exponent
p(x)	bridging force in ligaments
r	rotational factor
R	load ratio $(= K_{min}/K_{max})$

R_f	radius of reinforcement-phase particle
u	displacement
V_f	volume fraction of reinforcement phase
x, y	coordinates, with origin at the crack tip
Γ, Σ	first and second complete elliptic integrals, respectively
δ_c	critical crack opening displacement (at K_{Ic})
δ_{tip}	crack-tip opening displacement
δ_x	crack opening displacement at distance x from the tip
ε	(true) strain
$\varepsilon(x)$	strain in ligament
ν	Poisson's ratio
φ, β	angles associated with microcrack and macrocrack orientations
σ	stress
σ_a	applied stress
σ_f	fracture stress
$\sigma(x)$	stress in ligament
σ_y	yield strength
τ	interfacial stress
θ	dummy variable

ACKNOWLEDGMENTS

supplying the alloys, to Larry Edelson for help in characterizing the microstructures, and to Madeleine Penton for her assistance in preparing the manuscript.

REFERENCES

1. A. G. Evans, in Fracture Mechanics, 20th Symp., ASTM STP, R.P. Wei and R.P. Gangloff, eds., American Society for Testing and Materials, Philadelphia, PA, 1988.

2. R. O. Ritchie, Mater. Sci. Eng. A, 1988, vol. 103, in press.

3. J. Aveston, G. Cooper and A. Kelly, in Properties of Fiber Composites, NPL Conf. Proc., IPC Sci. & Tech. Press, Surrey, U.K., 1971, pp. 15-26.

4. B. Budiansky, J. W. Hutchinson and A. G. Evans, J. Mech. Phys. Solids, 1986, vol. 34, pp. 167-89.

5. D. B. Marshall, B. N. Cox and A. G. Evans, Acta Metall., 1985, vol. 33, pp. 2013-21.

6. L. N. McCartney, Proc. Roy. Soc., 1987, vol. A409, pp. 329-50.

7. L. R. F. Rose, J. Mech. Phys. Solids, 1987, vol. 35, pp. 383-405.

8. B. Budiansky, in Proc. 10th U.S. Cong. Appl. Mech., Austin, TX, 1986.

9. S. Kunz-Douglass, P. W. R. Beaumont and M. F. Ashby, J. Mater. Sci., 1980, vol. 15, pp. 1109-23.

10. A. G. Evans, Z. B. Ahmad, D. G. Gilbert, and P. W. R. Beaumont, Acta Metall., 1986, vol. 34, pp. 79-87.

11. A. G. Evans and R. M. McMeeking, Acta Metall., 1986, vol. 34, pp. 2435-41.

12. L. R. F. Rose, <u>Mech. Mater.</u>, 1987, vol. 6, pp. 11-15.

13. P. L. Swanson, C. J. Fairbanks, B. R. Lawn, Y. Mai, and B. J. Hockey, <u>J. Am. Ceram. Soc.</u>, 1987, vol. 70, pp. 279-89.

14. Y. Mai and B. R. Lawn, <u>J. Am. Ceram. Soc.</u>, 1987, vol. 70, pp. 289-94.

15. W. W. Gerberich, in <u>Fracture: Interactions of Microstructure, Mechanisms and Mechanics</u>, J. M. Wells and J. D. Landes, TMS-AIME, Warrendale, PA, 1984, pp. 49-74.

16. A. R. Rosenfield and B. S. Majumdar, <u>Metall. Trans. A</u>, 1987, vol. 18A, pp. 1053-59.

17. J.-K. Shang, W. Yu and R. O. Ritchie, <u>Mater. Sci. Eng. A</u>, 1988, vol. 102, in press.

18. R. Marissen, in <u>Fatigue 87</u>, Proc. Third Intl. Conf. on Fatigue, R. O. Ritchie and E. A. Starke, eds., EMAS Ltd., Warley, U.K., 1988, vol. 3, pp. 1271-79.

19. R. O. Ritchie, W. Yu and R. J. Bucci, <u>Eng. Fract. Mech.</u>, 1988, in press.

20. T. Christman and S. Suresh, <u>Mater. Sci. Eng. A</u>, 1988, in press.

21. J. J. Lewandowski, C. Liu, and W. H. Hunt, in <u>Powder Metallurgy Composites</u>, M. Kumar, K. Vedula and A. M. Ritter, eds., TMS-AIME, Warrendale, PA, 1987.

22. J. E. Srawley and B. Gross, <u>Mat. Res. Stand.</u>, 1967, vol. 7, pp. 155-62.

23. R. O. Ritchie and W. Yu, in <u>Small Fatigue Cracks</u>, R. O. Ritchie and J. Lankford, eds., TMS-AIME, Warrendale, PA, 1986, pp. 167-89.

24. R. O. Ritchie, J. F. Knott, and J. R. Rice, <u>J. Mech. Phys. Solids</u>, 1973, vol. 21, pp. 395-410.

25. J. W. Hutchinson, <u>J. Mech. Phys. Solids</u>, 1968, vol. 16, pp. 13-31.

26. J. R. Rice and G. R. Rosengren, <u>J. Mech. Phys. Solids</u>, 1968, vol. 16, pp. 1-12.

27. J. R. Rice and M. A. Johnson, in <u>Inelastic Behavior of Solids</u>, M. F. Kanninen, W. G. Adler, A. R. Rosenfield, and R. I. Jaffee, eds., McGraw-Hill, New York, NY, 1970, pp. 641-72.

28. R. M. McMeeking, <u>J. Mech. Phys. Solids</u>, 1977, vol. 24, pp. 357-19.

29. T. Lin, A. G. Evans, and R. O. Ritchie, <u>J. Mech. Phys. Solids</u>, 1986, vol 34, pp. 477-97.

30. T. Lin, A. G. Evans, and R. O. Ritchie, <u>Metall. Trans. A</u>, 1987, vol 18A, pp. 641-51.

31. A. A. Rubinstein, <u>Int. J. Fract.</u>, 1985, vol. 27, pp. 113-19.

32. H. Horii and S. Nemat-Nasser, <u>Int. J. Solids Struct.</u>, 1985, vol. 21, pp. 731-45.

33. M. Hori and S. Nemat-Nasser, <u>J. Mech. Phys. Solids</u>, 1987, vol. 35, pp. 601-29.

34. A. Chudnovsky, A. Dolgopolsky, and M. Kachanov, in <u>Advances in Fracture Research</u>, Proc. 6th Intl. Conf. on Fracture, India, S. R. Valluri et al., eds., Pergamon Press, Oxford, 1984, vol. 2, pp. 825-32.

35 G. C. Sih, <u>Handbook of Stress Intensity Factors</u>, Lehigh University Press, Bethlehem, PA, 1972.

36. J.-L. Tzou, C. H. Hsueh, A. G. Evans, and R. O. Ritchie, Acta Metall., 1985, vol. 33, pp. 117-27.

37. C. C. Veerman and T. Muller, Eng. Fract. Mech., 1972, vol. 4, pp. 25-32.

38. C. F. Shih, J. Mech. Phys. Solids, 1981, vol. 29, pp. 305-30.

39. J. R. Rice, in Mechanics and Mechanisms of Crack Growth, M. J. May, ed., British Steel Corp., London, U.K., 1974, pp. 14-39.

40. S. Suresh and R. O. Ritchie, Metall. Trans. A, 1982, vol. 13A, pp. 1627-31.

41. M. D. Thouless, J. Am. Ceram. Soc., 1988, vol. 71, pp. 408-13.

APPENDIX

Macrocrack/Microcrack Interaction: Local Stress-Intensity Solutions

For a collinear microcrack, length 2c, located at distance D directly ahead of a semi-infinite macrocrack (Fig. A1a), the local stress-intensity factors at the macrocrack tip, O, and macrocrack tips, A and B, are given in terms of the macrocrack stress-intensity factor (in the absence of the microcrack) $K_I(\infty)$ by Rubinstein (31) as:

$$\frac{K_I(0)}{K_I(\infty)} = \sqrt{\frac{D + 2c}{D}} \ \frac{\Sigma\left[1 - \left(\frac{D}{D + 2c}\right)\right]}{\Gamma\left[1 - \left(\frac{D}{D + 2c}\right)\right]} \tag{A1}$$

$$\frac{K_I(A)}{K_I(\infty)} = \left\{ \frac{D + 2c}{D} \cdot \frac{\Sigma\left[1 - \left(\frac{D}{D + 2c}\right)\right]}{\Gamma\left[1 - \left(\frac{D}{D + 2c}\right)\right]} - 1 \right\} \Bigg/ \sqrt{\frac{2c}{D}}$$

and

$$\frac{K_I(B)}{K_I(\infty)} = \left\{ 1 - \frac{\Sigma\left[1 - \left(\frac{D}{D + 2c}\right)\right]}{\Gamma\left[1 - \left(\frac{D}{D + 2c}\right)\right]} \right\} \Bigg/ \sqrt{1 - \left(\frac{D}{D + 2c}\right)} \qquad (A2)$$

where the first and second complete elliptic integrals Γ and Σ are given by:

$$\Gamma(g) = \int_0^{\pi/2} \frac{d\theta}{\sqrt{1 - g^2 \sin^2\theta}}$$

and

$$\Sigma(g) = \int_0^{\pi/2} \sqrt{1 - g^2 \sin^2\theta} \; d\theta \quad .$$

Note Eq. A2 has been modified to correct an error in the original paper (31).

In the present case of fatigue-crack growth in Al/SiC_p composites where the region of "microcracks" is bounded by the plastic-zone size and is therefore only ~5 to 15 times larger than the particle size, Eqs. A1 and A2 are evaluated at D/2c values of order unity. The presence of the microcrack leads to an increase in the stress intensity at the macrocrack tip, $K_I(0)$, of up to 23%;

conversely, the stress intensity at the microcrack tip A, $K_I(A)$, is increased by up to 74% of the far-field $K_I(\infty)$ acting on the macrocrack.

For arbitrarily inclined microcracks located ahead of a macrocrack (Fig. A1b), the local stress-intensity factors are a complex function of the relative size and position of the microcrack (32-34). For the same case of D/2c of order unity, the corresponding elevation of the stress intensity at the macrocrack tip, $K_I(0)$, is now reduced to only ~2%; the stress intensity at the microcrack tip, $K_I(A)$, however, is enhanced by ~40% representing a 100% increase over the stress intensity in the absence of the macrocrack (for $\varphi = \beta = \pi/5$, a = 25c).

These solutions must be considered approximate as they pertain to two-dimensional cracks; the "microcracks" generated in the Al/SiC$_p$ composites conversely are not continuous through the specimen thickness.
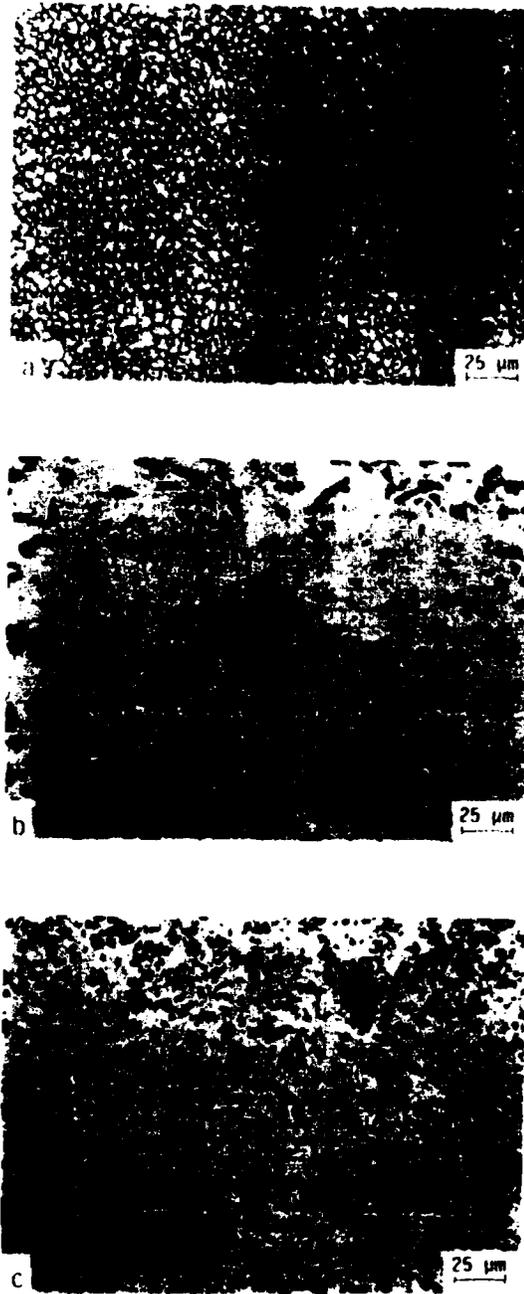
Fig. 1: Optical micrographs of the overaged microstructures of a) unreinforced matrix alloy, b) 15 vol pct coarse Al/SiC$_p$ composite, and c) 20 vol pct fine Al/SiC$_p$ composite.
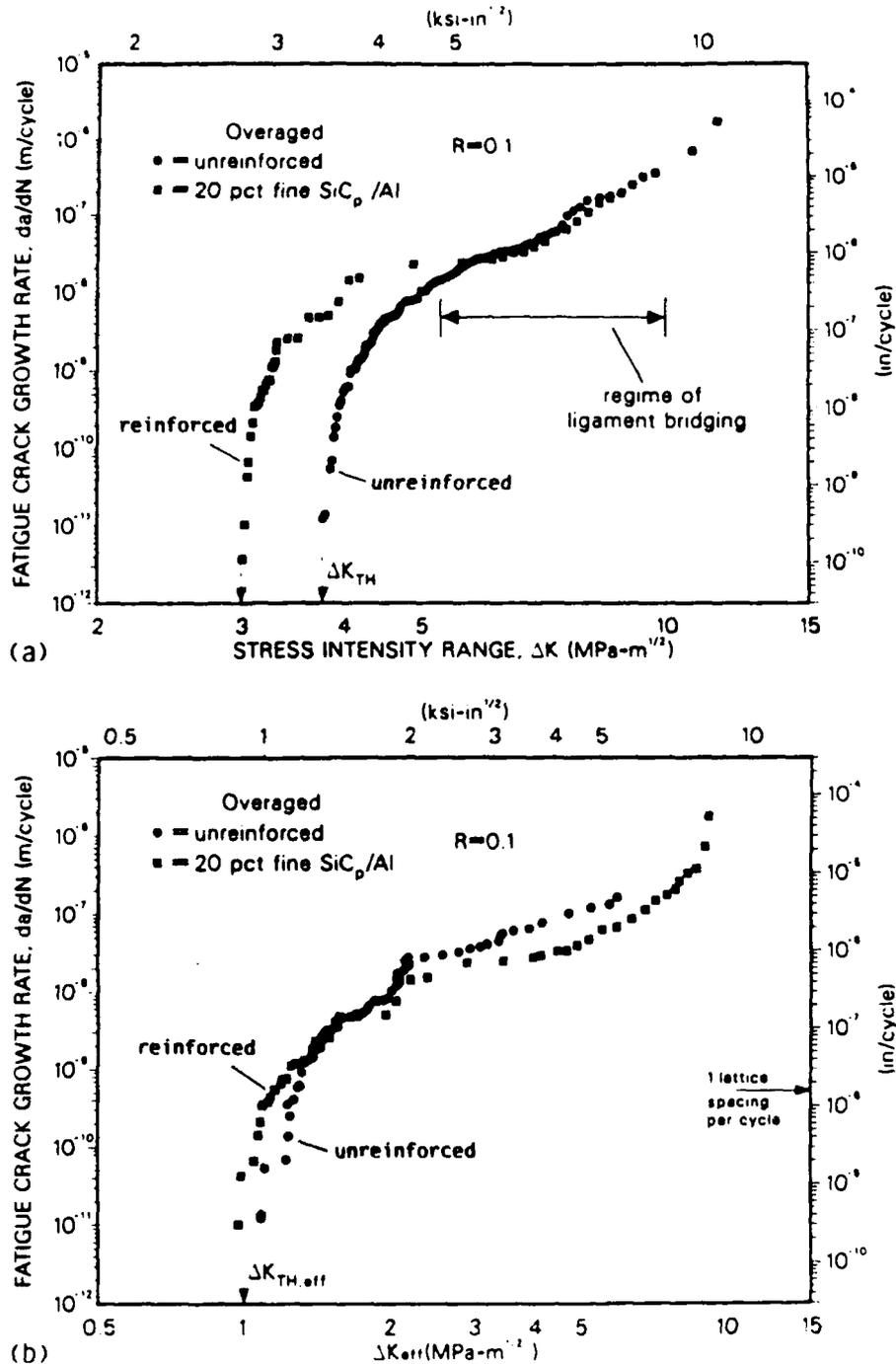
Fig. 2: Variation in fatigue-crack growth rates, da/dN, with nominal and effective stress-intensity ranges, ΔK and ΔK_{eff}, for a,b) 20 vol pct fine Al/SiC$_p$ composite, and c,d) 15 vol pct coarse Al/SiC$_p$ composite, compared to corresponding behavior in unreinforced constituent-matrix alloy. Crack bridging in Al/SiC$_p$ predominates over the range ($\sim 10^{-9}$ - 10^{-6} m/cycle). Growth-rate differences at low ΔK levels are seen to be associated primarily with crack closure; no bridging is observed in this regime.
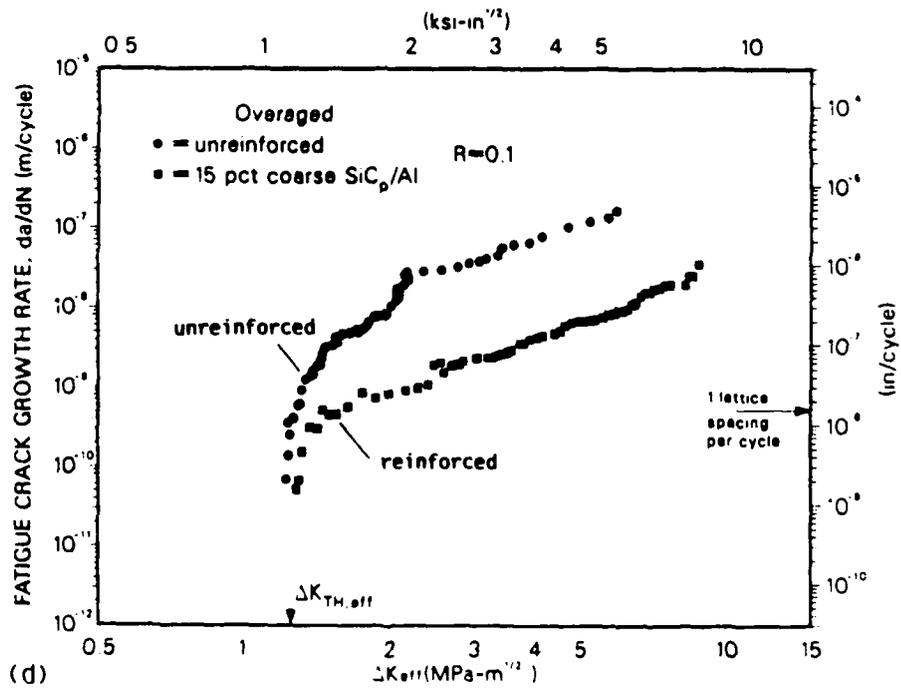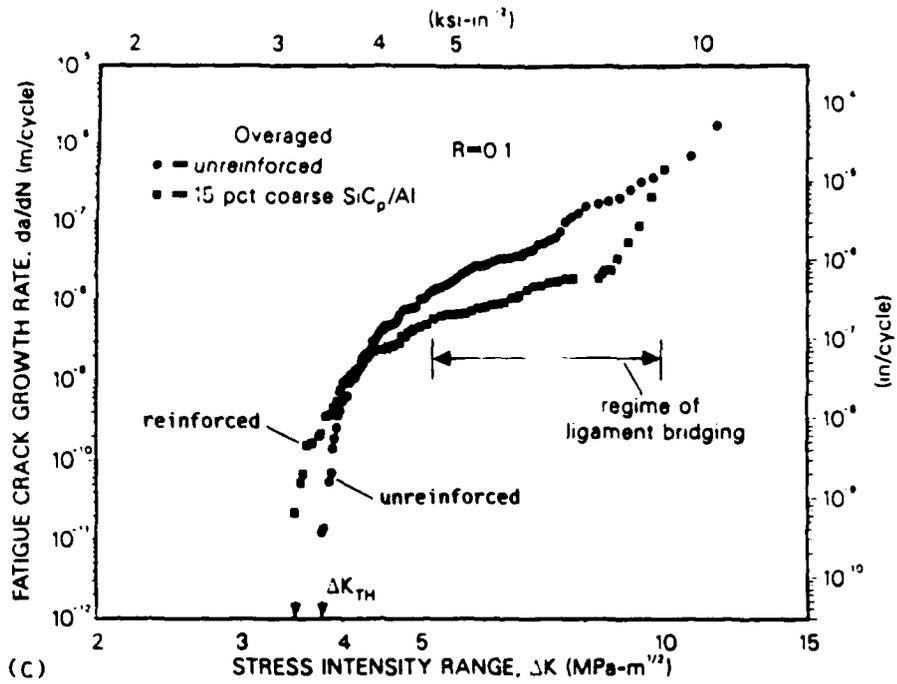
Fig. 2 (Cont.)
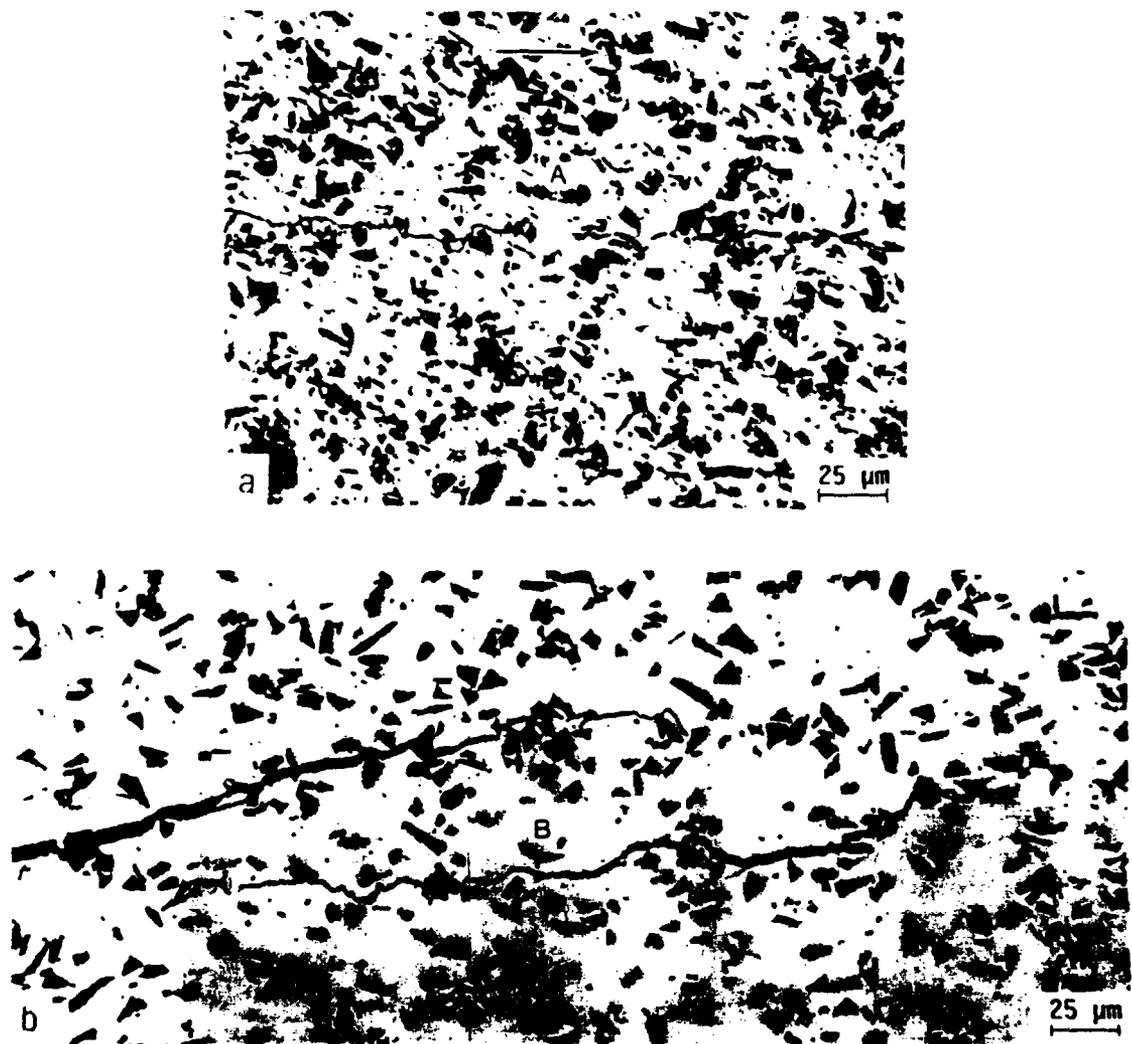
Fig. 3: Uncracked-ligament bridging in Al/SiC$_p$ composites, showing a) co-planar ligaments in 20 vol pct fine Al/SiC$_p$ composite (region A), and b) "overlapping" ligaments in 15 vol pct coarse Al/SiC$_p$ composite (region B). Horizontal arrow indicates general direction of crack growth.
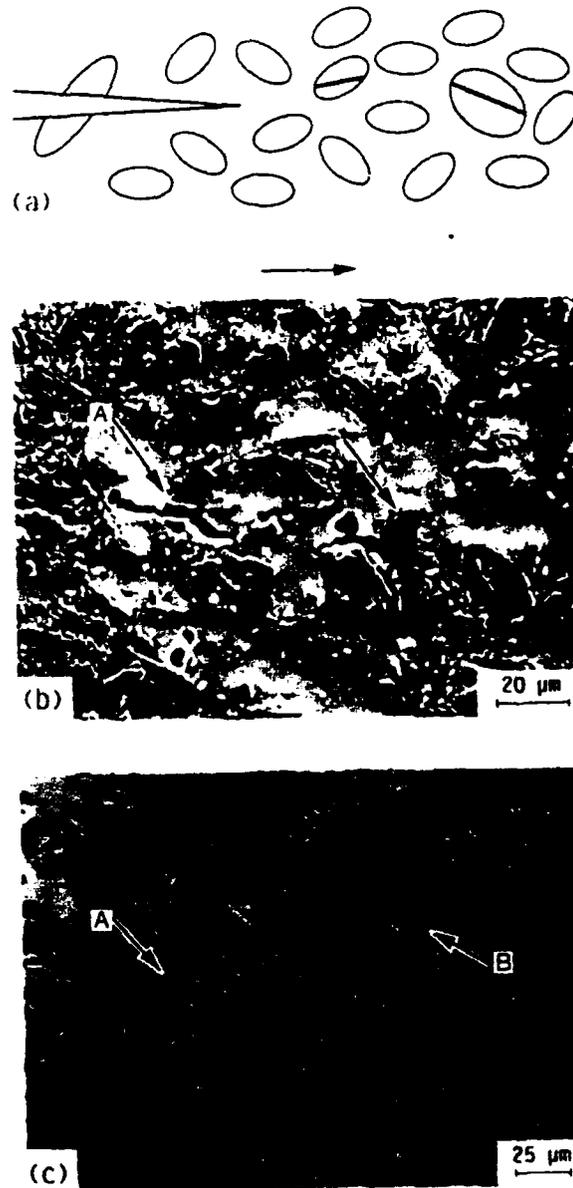
Fig. 4: Evidence for the creation of uncracked ligaments in Al/SiC_p composites resulting from SiC fracture, both ahead (location B) and in the wake (location A) of the crack tip (indicated by inclined arrows). Shown are a) schematic illustration of the cracking process, and bridging from b) co-planar uncracked ligaments in 20 vol. pct fine Al/SiC_p composite, and c) "overlapping" ligaments in 15 vol. pct coarse Al/SiC_p composite. Horizontal arrow indicates general direction of crack growth.
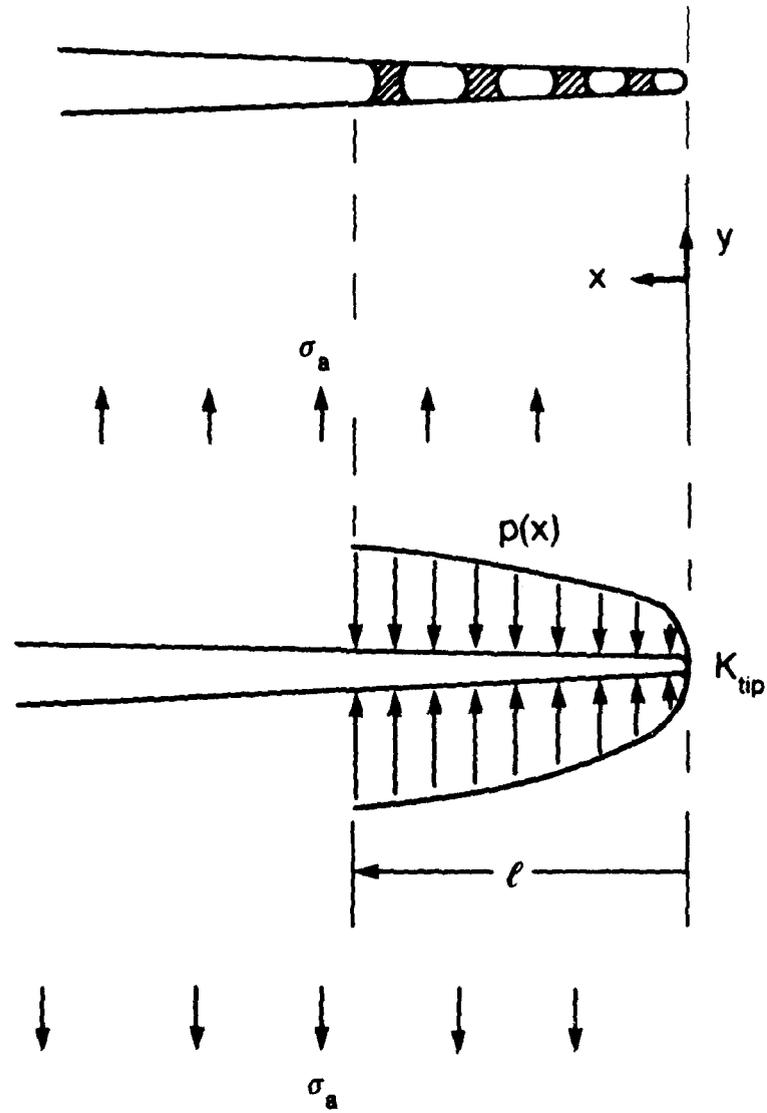
XBL 883-9587

Fig. 5: Idealization of the bridging zone over distance ℓ behind the tip of a crack subjected to an externally applied stress σ_a.

325
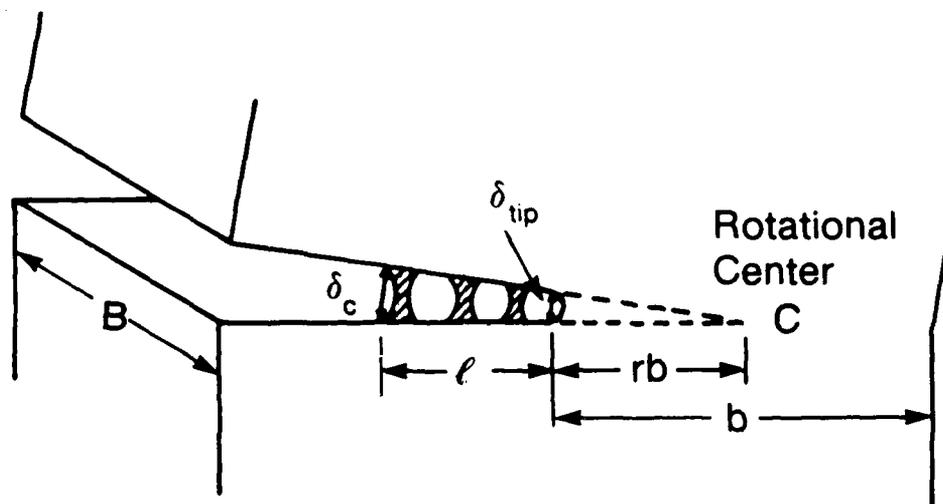
XBL 883-9586

Fig. 6: Schematic illustration of idealized fatigue crack with bridging zone, showing definitions of the rotational center and crack-opening displacements.
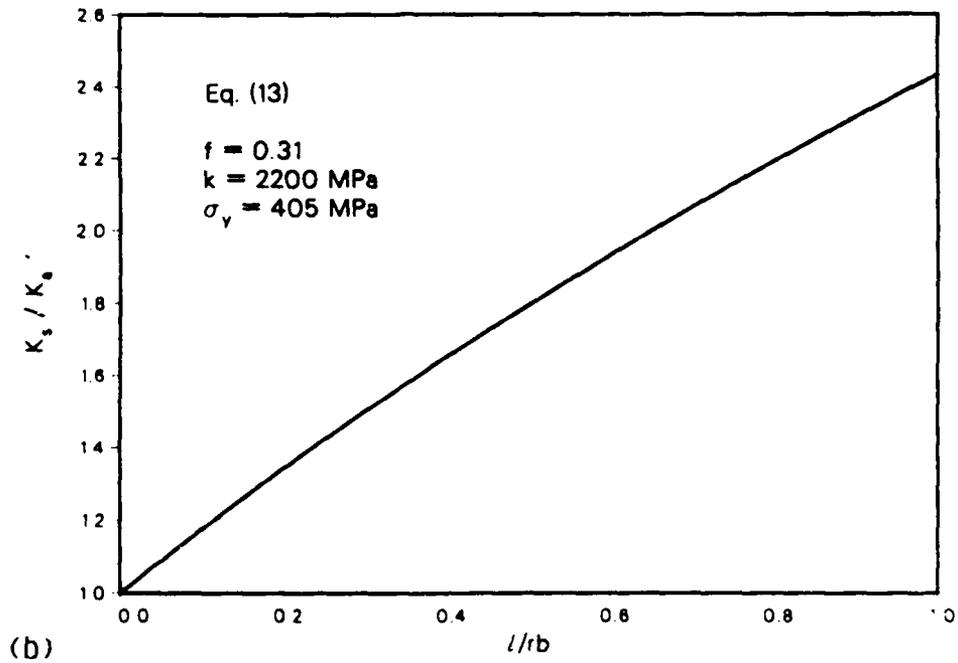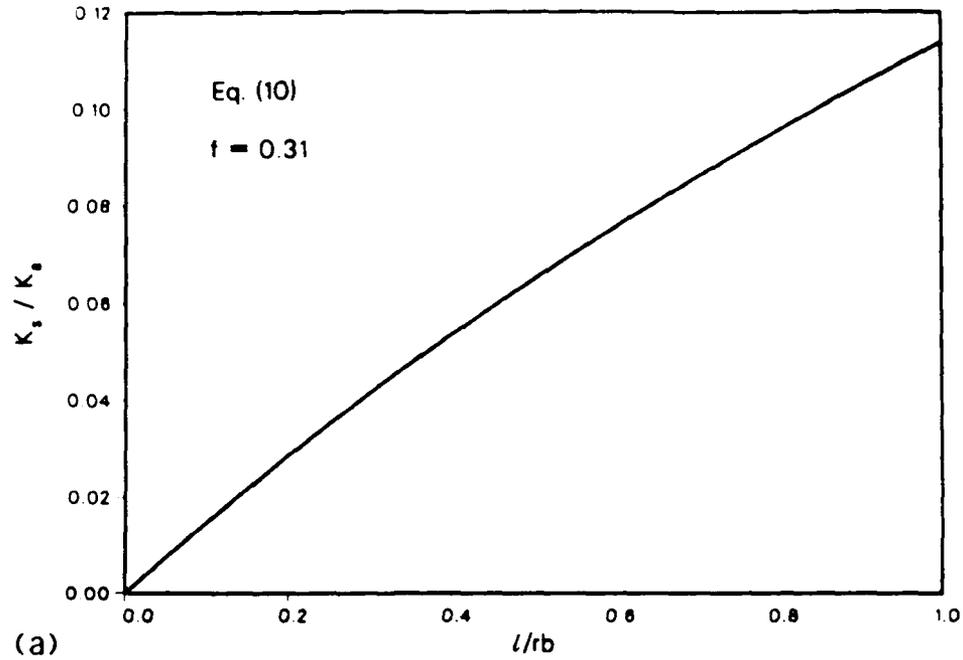
Fig. 7: Predictions of normalized shielding stress intensity, K_s/K_a, as a function of normalized bridging-zone length, ℓ/r_b, from a) limiting crack-opening displacement (Eq. 10) and b) limiting-strain (Eq. 13) crack-bridging models.
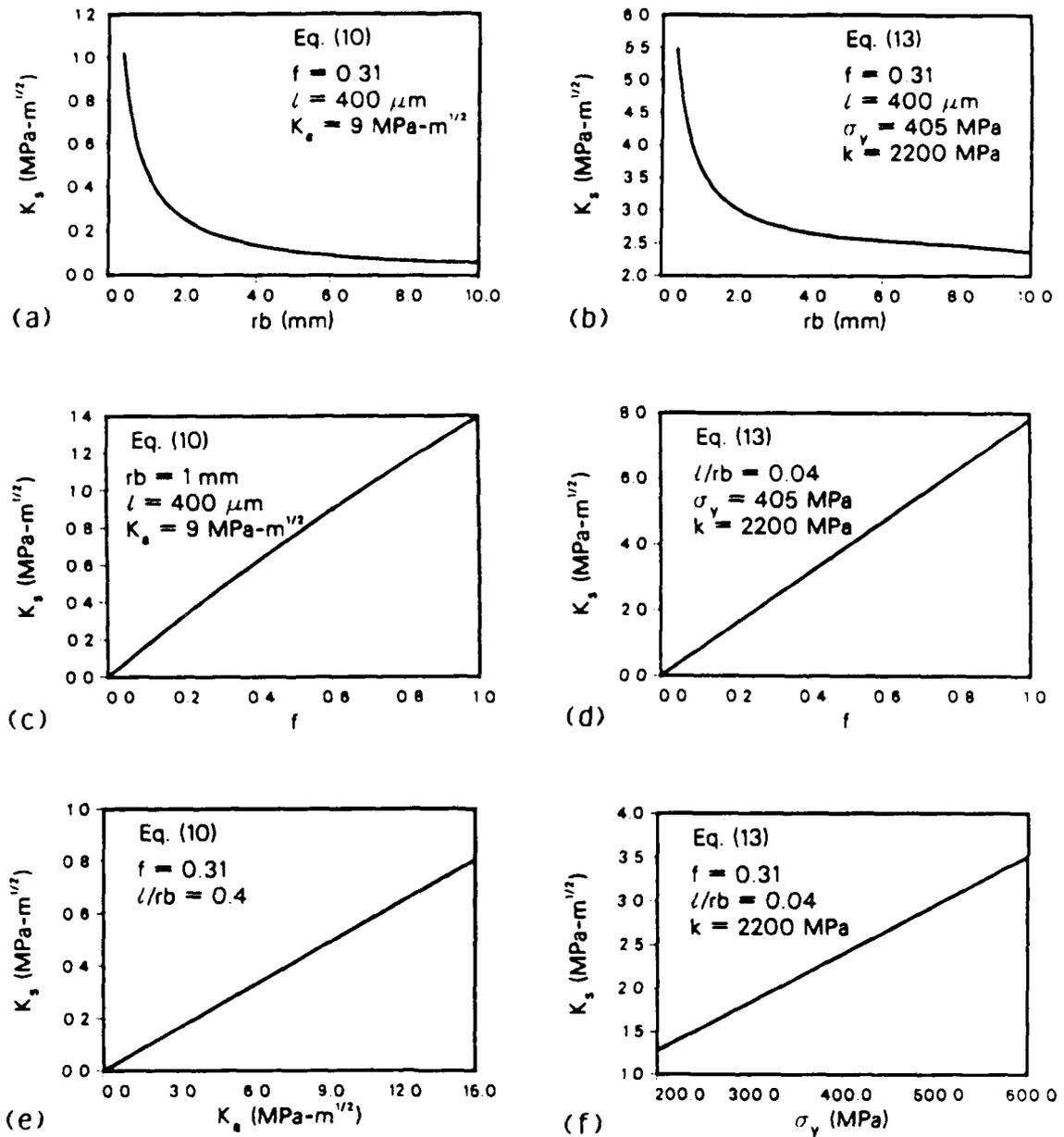
XBL 883-999

Fig. 8: Predictions of the shielding stress intensity, K_S, as a function of a,b) rb, c,d) area fraction of uncracked ligaments, f, e) applied stress intensity, K_a, and f) yield strength, σ_y, of ligament material; a,c,e) are based on limiting crack-opening displacement model (Eq. 10), b,d,f) are based on limiting-strain (Eq. 13) model.
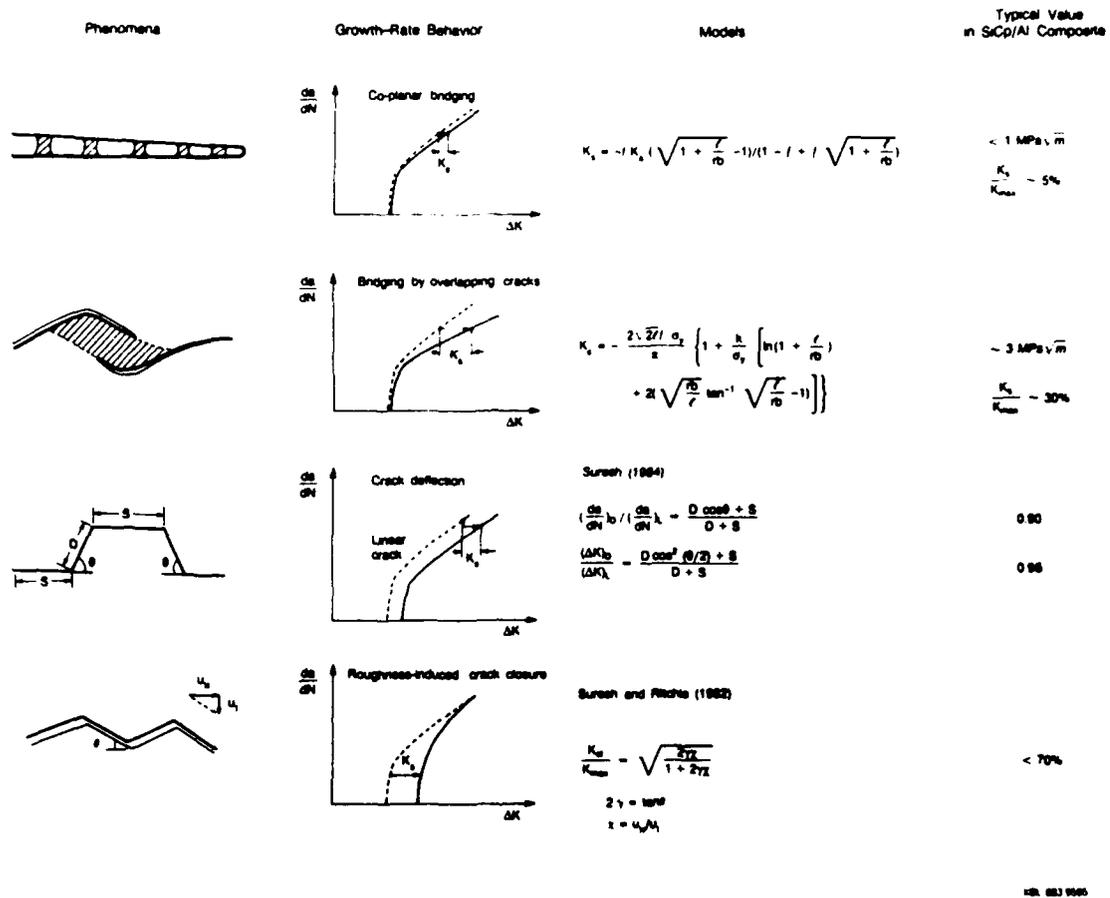
Fig. 9: Schematic illustration of primary mechanisms, models and implications of crack-tip shielding in metal-matrix composites.

(a)

(b)
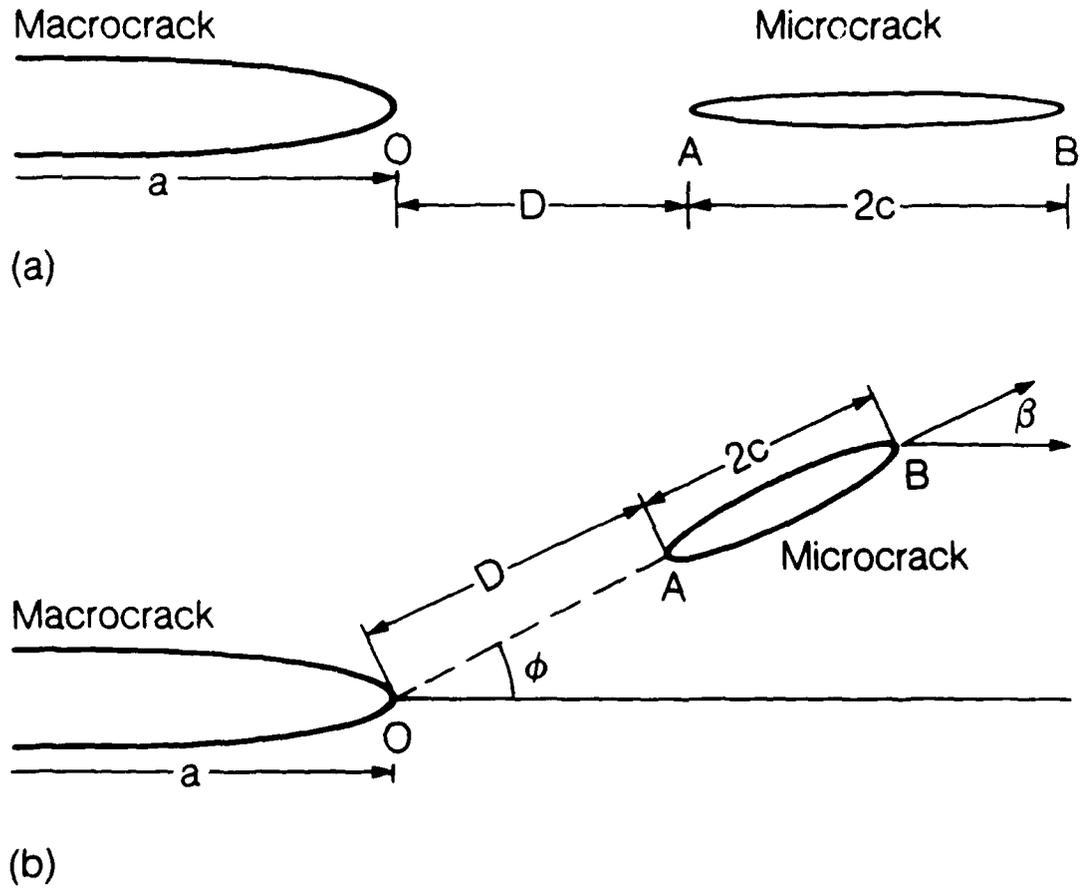
XBL 888-8498

Fig. Al: Geometry of macrocrack/microcrack interaction for a) coplanar and b) off-angle microcracks.

ON THE PARTICLE-SIZE DEPENDENCE OF FATIGUE-CRACK PROPAGATION

THRESHOLDS IN SiC-PARTICULATE-REINFORCED ALUMINUM-ALLOY COMPOSITES:

ROLE OF CRACK CLOSURE AND CRACK TRAPPING

Jian Ku Shang and R. O. Ritchie

Department of Materials Science and Mineral Engineering
University of California, Berkeley, CA 94720

June 1988

ON THE PARTICLE-SIZE DEPENDENCE OF FATIGUE-CRACK PROPAGATION

THRESHOLDS IN SiC-PARTICULATE-REINFORCED ALUMINUM-ALLOY COMPOSITES:

ROLE OF CRACK CLOSURE AND CRACK TRAPPING

Jian Ku Shang and R. O. Ritchie

Department of Materials Science and Mineral Engineering
University of California, Berkeley, CA 94720

ABSTRACT

A study has been made of ambient-temperature fatigue-crack propagation behavior in P/M Al-Zn-Mg-Cu metal-matrix composites reinforced with either 15 or 20 vol.% silicon-carbide particulate, with specific emphasis on the role of SiC-particle size on the fatigue-crack growth threshold condition. It is found that measured threshold stress-intensity levels, ΔK_{TH}, are a function of both SiC-particle size and volume fraction; however, whereas coarse-particle distribution results in higher ΔK_{TH} values at low load ratios, fine particles give higher thresholds at high load ratios. Such behavior is analyzed in terms of the interaction of SiC particles with the crack path, both in terms of the promotion of (roughness-induced) crack closure at low load ratios and by crack trapping by particles. Consideration of the latter mechanism yields a limiting requirement for the *intrinsic* threshold condition in these materials that the maximum plastic-zone size must exceed the effective mean particle size; this implies that for near-threshold crack advance, the tensile stress in the matrix must exceed the yield strength of the material beyond the particle.

I. INTRODUCTION

Particle size has long been known to play a major role in influencing the mechanical properties of materials containing distributions of second-phase particles. For example, the presence of large inclusions or brittle particles in metallic alloys typically can reduce ductility by an order of magnitude and fracture toughness by a factor of two [1-6]. Moreover, in many precipitation-hardened systems, the growth of coherent precipitates, from a few Å in size, to incoherent precipitates, several hundred Å in size, results in a profound change in deformation mechanism from one of planar slip (due to shearing of particles) to wavy slip (from dislocation bypassing) [7].   In addition, the degree of slip planarity markedly affects fracture and fatigue properties, with respect to such factors as the ease of strain localization and the morphology of the crack path [8-10].

Despite processing attempts over the years to rid materials of such unwanted particles in metallic materials, with the current development of metal-matrix composites reinforced for improved strength and stiffness, high volume fractions of coarse particles are often deliberately added.   One such case is in SiC-particulate-reinforced aluminum alloys, where the size of the added silicon carbide particles can range from typically 1-20 μm in powder-metallurgy (P/M) fabricated alloys to well over 100 μm in cast alloys.   These materials in general show *superior elastic modulus*, strength, wear and high-temperature properties compared to unreinforced alloys, yet predictably are plagued

by poor tensile ductility, fracture toughness and fatigue-crack growth resistance [2-4,11-14].

Recently, studies on fatigue-crack propagation in SiC-particulate and whisker-reinforced aluminum alloys have suggested properties strongly dependent upon the size and morphology of the reinforcement phase [4,11,14-16]. For example, in whisker-reinforced alloys, crack-growth rates have been reported to show a minimal influence of crack closure* and are correspondingly insensitive to the load ratio ($R = K_{min}/K_{max}$) [15]. In contrast, with particulate-reinforced alloys, growth rates are characterized by high levels of closure at near-threshold levels, at least with coarse SiC-particle additions [11,14], and are accompanied by a substantial degree of SiC fracture [14]. Moreover, coarse-particle distributions were found to show higher fatigue-threshold ΔK_{TH} values, and to induce superior crack-growth properties at higher growth rates, typically between 10^{-9} and 10^{-6} m/cycle, by promoting crack bridging* via uncracked ligaments in the wake of the crack tip [14,16].

---

*Crack closure and crack bridging are mechanisms of crack-tip shielding, whereby crack advance is impeded by processes which act to lower the *local* "crack driving force" actually experienced in the vicinity of the crack tip [17,18].

In the present work, mechanisms underlying the influence of reinforcement-particle size, specifically on fatigue-crack propagation ΔK_{TH} thresholds, are examined in several SiC-particulate-reinforced Al-Zn-Mg-Cu metal-matrix composites of varying SiC volume fractions. It is found that, although measured low load-ratio ΔK_{TH} values vary in seemingly arbitrary fashion with volume fraction and particle size, by

considering the role of crack closure, the intrinsic threshold condition can be shown to be a primary function of the SiC-particle size only.

II. EXPERIMENTAL PROCEDURES

Materials and Microstructures

The metal-matrix composites studied in this work were based on a P/M Al-Zn-Mg-Cu alloy matrix similar to 7091 (designated ALCOA MB78), particulate reinforced with either 15 or 20% by volume of coarse F-600 grade SiC_p (nominal size 16 μm) or fine F-1000 grade (nominal size 5 μm) SiC_p. The alloys, of matrix composition shown in Table I, were fabricated by blending prealloyed atomized aluminum-alloy powders with SiC particles, cold isostatic pressing, vacuum degassing and hot pressing, before finally extruding at an extrusion ratio of 12:1 into 25-mm-thick plates [13,14].

Table I. Chemical Composition in wt% of Matrix Al-Zn-Mg-Cu Alloy

Zn	Cu	Mg	Si	P	S	Zr	Al
9.44	2.50	3.33	0.14	0.14	0.17	0.08	balance

The extruded plates were solution treated 4 hr at 530°C, quenched in cold water, and (due to the large difference in the thermal expansion coefficients of the matrix and carbide) immediately compressed 2 to 3% by forging to minimize quenching-induced residual stresses. Subsequent peak aging (T6 condition) was performed for 24 hr

at 121°C; the resulting room-temperature mechanical properties (transverse . orientation) are listed in Table II.

Microstructures and SiC-particle-size distributions are illustrated in Fig. 1. Quantitative metallography indicated that the coarse SiC_p composite had a more uniform distribution of particle sizes (Weibull modulus of 2.6), with an average size of over 10 μm; the fine SiC_p composite, conversely, showed a smaller matrix grain size (2.3 vs. 4.8 μm) and distinct evidence of particle clustering (average particle size 6 μm, Weibull modulus of 1.6). The aspect ratio of the particles was of the order of 3:1. Results are summarized in Table III. The matrix microstructure was characterized by homogeneous precipitation of η′ ($MgZn_2.Mg(CuAl)_2$) platelets, with signs of small ($\geq$ 100 nm) equilibrium η ($MgZn_2$) precipitates on SiC_p/matrix interfaces [13,14].

Fatigue-Crack Propagation Testing

Fatigue-crack propagation tests were performed along the guidelines suggested by ASTM Standard E 647-86A using 6.4-mm-thick double-cantilever-beam DB(M_z) specimens machined in S-T orientation. Tests were conducted in controlled room air (22°C, 45% relative humidity) with a sinsuoidal frequency of 50 Hz at a load ratio of R = 0.10; additional threshold measurenents were performed at R = 0.5 and 0.75. D.C. electrical-potential methods were used to monitor crack length and crack-mouth opening compliance measurements to measure (global) crack closure [17]. Closure measurements were performed

Table II. Room-Temperature Mechanical Properties of Peak-Aged Alloys

Alloy	Young's Modulus E (GPa)	Yield Strength σ_y (MPa)	Tensile Strength σ_u (MPa)	True Fracture Strain ε_f	Reduction in Area (%)	Fracture Toughness K_{Ic}* (MPa$\sqrt{m}$)
20% coarse SiC$_p$/Al	101.4	500	560	0.018	4.9	16
20% fine SiC$_p$/Al	94.1	400	470	0.019	13.5	14
15% coarse SiC$_p$/Al	99.1	490	535	0.011	4.5	-
15% fine SiC$_p$/Al	90.7	480	530	0.031	4.9	-
unreinforced matrix	68.5	520	590	0.102	35.2	33

*S-T orientation.

Table III. SiC Particle Size and Interparticle Spacing

Alloy	Volume Fraction f_p (%)	Average Size $\bar{D}_p$ (μm)	Standard Deviation (μm)	Maximum Size (μm)	Minimum Size (μm)	Average Spacing* $\bar{d}_p$ (μm)
20% coarse SiC$_p$/Al	22.5	10.5	3.4	21.8	1.7	36
20% fine SiC$_p$/Al	20.9	6.1	2.8	21.1	1.9	23
15% coarse SiC$_p$/Al	16.9	11.4	3.6	28.6	2.2	56
15% fine SiC$_p$/Al	18.2	4.5	2.9	25.1	1.5	20

*Computed from $\bar{d}_p = \bar{D}_p [(1 - f_p)/f_p]$ [19].

in situ using a clip gauge to determine the closure stress intensity, K_{cl}, which was defined at first contact of the crack surfaces on unloading from deviations in the elastic compliance slope [17]. Data were obtained over a wide spectrum of growth rates, from 10^{-12} to 10^{-4} m/cycle, with fatigue thresholds (ΔK_{TH}) approached under automated stress-intensity control at a normalized K-gradient of -0.15 per mm of crack extension.

Based on the K_{cl} measurements, growth-rate behavior is presented in terms of both the nominal and effective stress-intensity ranges, given respectively by $\Delta K = K_{max} - K_{min}$ and $\Delta K_{eff} = K_{max} - K_{cl}$, computed using the K solution of Srawley et al. [20]. Similarly, the fatigue-threshold condition is described both in terms of nominal (measured) threshold values, ΔK_{TH}, and intrinsic threshold values, $\Delta K_{eff,TH}$, the latter being computed in terms of ΔK_{eff} by subtracting out the effect of crack closure.

III. RESULTS

Fatigue-Crack Growth Rate Behavior

The variation in fatigue-crack growth rates, da/dN, for the coarse and fine SiC_p/Al composites is shown as a function of the nominal stress-intensity range, ΔK, in Fig. 2. At low load ratios, three distinct regimes of behavior are evident, namely at i) near-threshold levels below typically 10^{-9} m/cycle, where crack-growth resistance, as reflected by the threshold ΔK_{TH}, varies with both volume fraction and average size of the SiC phase, ii) intermediate growth rates between $\sim 10^{-9}$ and 10^{-7} m/cycle, where growth rates are essentially independent

of the size and volume fraction of SiC, and iii) high growth rates approaching instability, where similarly behavior is independent of the size and volume fraction of SiC.

With respect to near-threshold behavior, it is apparent that at low load ratios the composites with coarse SiC_p distributions show threshold ΔK_{TH} values which are between 40 and 65% *higher* than in the fine SiC_p composites. With coarse SiC_p distributions, ΔK_{TH} values are independent of the SiC_p volume fraction, whereas with fine distributions, thresholds are 15% higher with the 20% SiC alloys. Trends are somewhat reversed at high load ratios. First, threshold ΔK_{TH} values at R = 0.75 are typically 40 to 70% lower than at R = 0.10; second, the composites with coarse SiC_p distributions now show thresholds which are between 5 and 20% *lower* than in the fine SiC_p composites. Threshold data are listed in Table IV.

Crack Closure

Levels of crack closure at R = 0.10, from crack-mouth clip gauge measurements, are plotted for the four composites in Fig. 3 as a function of the nominal ΔK. Characteristic of crack-tip shielding induced by wedging phenomenon [17,18], crack closure predominates in the near-threshold regime; the value of K_{cl} decreases progressively with increase in the stress-intensity range, such that K_{cl}/K_{max} levels are less than 0.2 to 0.4 in the intermediate growth-rate regime above $\sim 10^{-9}$ m/cycle. In general, the SiC_p/Al composites with coarse particles show markedly increased levels of closure at near-threshold levels, consistent with their higher ΔK_{TH} values; closure levels are

also somewhat larger with the higher SiC_p volume fractions, again consistent with their higher ΔK_{TH} values (Table IV).

Table IV. Fatigue-Threshold Conditions for SiC_p/Al Composite Alloys

Alloy	R	ΔK_{TH} (MPa$\sqrt{m}$)	$\Delta K_{eff,TH}$ (MPa$\sqrt{m}$)	K_{cl}/K_{max}	K_{cl} (MPa$\sqrt{m}$)	δ_{cl}^* (nm)
20% coarse SiC_p/Al	0.10	4.2	1.3	0.73	3.37	112
	0.50	2.2	1.4	0.68	3.03	90
	0.75	1.3	1.3	-	-	-
20% fine SiC_p/Al	0.10	3.0	1.9	0.42	1.38	25
	0.50	1.7	1.7	-	-	-
	0.75	1.6	1.6	-	-	-
15% coarse SiC_p/Al	0.10	4.3	1.3	0.73	3.45	123
	0.75	1.5	1.5	-	-	-
15% fine SiC_p/Al	0.10	2.6	1.9	0.34	0.98	11
	0.75	1.6	1.6	-	-	-

*Computed from $\delta_{cl} = \frac{1}{2}K_{cl}^2/E\sigma_y$ [21].

As computed estimates [21] of the near-threshold crack-tip opening displacements (CTODs) at the closure stress intensity, δ_{cl} (Table IV), are some 100 to 200 times smaller than the average particle size, it is clear that the presence of the SiC particles presents a potentially potent source of crack closure at low load ratios. Moreover, as previous studies in SiC_p/Al composites [14] have shown that at lower growth rates the crack in general tends to avoid the SiC particles thereby promoting crack-tip shielding by crack deflection and (due to the rougher fracture surface) crack closure (Fig. 4a), it is to be expected that closure levels will be higher with the coarse SiC-particle distributions.

Crack closure levels at R = 0.75, conversely, could not be detected as K_{cl} values were always less than K_{min}, i.e., the maximum K_{cl}/K_{max} ratios never exceeded 0.75. Crack-closure mechanisms can thus be assumed to have a negligible influence on high load-ratio fatigue-crack propagation behavior in these composite alloys, such that in terms of effective stress-intensity range, at R = 0.75, $\Delta K_{eff} \approx \Delta K$. This similarity, shown in Table IV, of the high load-ratio thresholds and the intrinsic $\Delta K_{eff,TH}$ threshold values (based on closure-adjusted low load-ratio data), strongly suggests that, as reported for monolithic alloys [e.g., refs. 22,23], the principal origin of the influence of the load ratio on near-threshold fatigue behavior is crack closure.

Particle-Size Dependence

The variation in intrinsic fatigue thresholds, $\Delta K_{eff,TH}$, with particle size and volume fraction can be discerned from Fig. 5, where the growth-rate data from the four composites in Fig. 2 have been replotted in terms of ΔK_{eff}, after subtracting out the effect of closure. It is apparent that intrinsic near-threshold behavior is essentially independent on the volume fraction of SiC particles, yet markedly dependent upon the average particle size, i.e., values of $\Delta K_{eff,TH}$ are approximately 50% larger for the finer-particle composites (Table IV).* Note that since the role of closure is minimal at

*Note that higher growth-rate behavior above $\sim 10^{-9}$ m/cycle is not normalized by plotting in terms of ΔK_{eff} rather than ΔK. This follows because the effect of crack closure is diminished at the higher stress-intensity levels (Fig. 3), and further contributions to crack-tip shielding arise from uncracked-ligament bridging [14,16], which are not reflected in the ΔK_{eff} measurements.

R = 0.75, the measured high load-ratio threshold values are essentially identical to the intrinsic $\Delta K_{eff,TH}$ values.

Hence paradoxically, the nominal (measured) *low load-ratio* stress-intensity range associated with a fatigue threshold, ΔK_{TH}, is *increased* with coarse-particle sizes in SiC_p/Al composites due to enhanced roughness-induced crack closure; conversely, in the absence of closure, the *high load-ratio* threshold and intrinsic threshold values, $\Delta K_{eff,TH}$, are *decreased*.

IV. DISCUSSION

Crack-Closure Models

The present study has shown that the fatigue-threshold condition in SiC-particulate-reinforced aluminum alloys is sensitive to the average size of the SiC particles. In common with monolithic aluminum alloys, measured threshold ΔK_{TH} values *at low load ratios* are strongly affected by crack-closure mechanisms, especially induced by crack deflection and rough fracture surfaces [e.g., ref. 10]. As described elsewhere for SiC_p/Al composites [14], at near-threshold levels there is a tendency for the crack to avoid the SiC particles, leading to meandering crack paths and correspondingly enhanced closure from the wedging of enlarged fracture-surface asperities (Fig. 4a); a process clearly promoted in composites with coarser carbide sizes. Estimates of the extent of such roughness-induced closure can be made from simple geometric modelling [24] of the wedging of asperities (height h, width w) inside a crack deflecting through angle θ (where $\theta = \tan^{-1}(2h/w)$); this gives the closure stress intensity K_{cl} in terms of θ, K_{max} and

mismatch X, as:

$$K_{cl} = K_{max} [X \tan\theta/(1 + X \tan\theta)]^{\frac{1}{2}} , \qquad (1)$$

where X is the ratio of Mode II to Mode I unloading displacements (u_{II}/u_I). Using this relationship for R = 0.1, predicted values of K_{cl}/K_{max} for angles of θ between 30 and 75 deg range from 0.36 to 0.70 for a mismatch of 0.25, consistent with the measured maximum closure ratios of 0.34 to 0.73, listed in Table IV.

Intrinsic Threshold Models

What is perhaps surprising in the current work is that intrinsic threshold $\Delta K_{eff,TH}$ values in these materials, which are essentially identical to the measured thresholds at high load ratios, are independent of the SiC volume fraction, and more importantly show an entirely opposite dependence on the particle size. Moreover, published models [25-30] for intrinsic fatigue thresholds in monolithic alloys in general appear to be inconsistent with this observed dependence of $\Delta K_{eff,TH}$ on particle size, as discussed below.

CTOD Models: Models [25,26] have been proposed based on the notion that the threshold is associated with the CTOD being of the order of a critical microstructural dimension, which in this case could be taken as either the mean interparticle spacing, $\bar{d}_p$, or mean particle size, $\bar{D}_p$:

$$\Delta K_{eff,TH} \propto \{\sigma_y E \bar{d}_p\}^{\frac{1}{2}} ,$$

or
$$\propto \{\sigma_y E \bar{D}_p\}^{\frac{1}{2}} . \qquad (2)$$

Aside from the fact that computed CTODs at the threshold are some three orders of magnitude smaller than such microstructural dimensions, these models imply lower intrinsic thresholds with the finer SiC-particle distributions, which is contrary to experimental observations (Table IV).

Dislocation Models: Similarly, models [27] for the intrinsic threshold condition based on the minimum shear stress τ required to nucleate and move a dislocation from the crack tip give:

$$\tau = \frac{G}{4\pi(1-\nu)}\{ln(4r/b)+(b/r)\}+\{\gamma_e/b\sqrt{2}\}+\{\sigma_y/2\} ,$$

such that $\Delta K_{eff,TH} \propto \tau\sqrt{b}$, $\qquad\qquad\qquad$ (3)

where G is the shear modulus, ν is Poisson's ratio, b is the Burgers vector, γ_e is the surface energy, and r is the distance traveled by the dislocation along the slip plane at 45 deg to the crack plane. Eq. 3 implies that the intrinsic threshold is proportional to the shear modulus, yet in SiC_p/Al composites the coarse SiC-particle distributions have the higher moduli but the lower $\Delta K_{eff,TH}$ values.

Critical Stress/Strain Models: Weiss and Lal [28,29] postulated that fatigue-crack growth per cycle could be modelled as crack advance over a microstructurally-significant characteristic distance r_o^* where the crack-tip stress or strain exceeds some critical value, i.e., σ_c or ε_c, respectively; this approach gives an intrinsic threshold condition in the form [28]:

$$\Delta K_{eff,TH} = (3\pi/2)^{\frac{1}{2}} \sigma_c \sqrt{r_0^*} , \tag{4}$$

where at the threshold σ_c is taken as the ideal cohesive strength, $E/10$. Again the model predicts the wrong dependence of $\Delta K_{eff,TH}$ on particle size if the characteristic dimension r_0^* is equated to the SiC particle size or spacing. Moreover, associating the value of r_0^* with the interparticle spacing would imply a dependence of the intrinsic threshold on the volume fraction of SiC, which is not observed. Other choices for r_0^*, such as the grain size, clearly fail to predict any dependence at all of thresholds on particle size.

More recently, Yu and Yan [30] proposed that at the intrinsic threshold, the cyclic plastic strain, ε_p, at a crack tip of finite radius, ρ, should equal the true (uniaxial) fracture strain, ε_f, such that:

$$\Delta K_{eff,TH} = 2\sigma_y \{E\varepsilon_f/2\sigma_y\}^{\frac{1}{2}(1+n)} \{2\pi\rho\}^{\frac{1}{2}} , \tag{5a}$$

where n is the strain-hardening coefficient and the minimum value of ρ is equated to the Burgers vector b; for n = 1 (elastic conditions), Eq. 5a reduces to:

$$\Delta K_{eff,TH} = E\varepsilon_f \{2\pi\rho\}^{\frac{1}{2}} . \tag{5b}$$

Since the ductility of the fine SiC_p/Al composites is generally higher than in the coarse SiC_p/Al composites (Table II), this model does predict the correct trend of the intrinsic thresholds with particle size. However, it should be noted that the suggestion [30] that the crack-tip fracture strain is equal to the uniaxial fracture strain ε_f is incorrect as, aside from the influence of cyclic deformation on

ductility, fracture strains in the highly triaxial field close to the crack tip will be significantly lower due to constraint [31].

Limiting Condition for the Intrinsic Fatigue Threshold

It is apparent that the models summarized above for intrinsic fatigue-threshold behavior in monolithic alloys, do not describe the threshold condition in particulate-reinforced composite materials. Specifically, the clear relationship between particle size and the intrinsic thresholds is simply not reflected in the analyzes. Accordingly, a new limiting condition associated with the intrinsic fatigue threshold is presented, specifically for composite alloys, based on the restraining effect of the reinforcement particles on the advancing crack front.

In brittle solids, the interaction of a crack front with a distribution of second-phase particles can be considered [32-35] to impede crack advance in a way somewhat analogous to hardening from dislocation-particle interactions (i.e, dislocation bowing around obstacles or particle shearing). This phenomenon, which is now referred to as crack trapping [35], can be applied to the current case of fatigue-crack growth in particulate-reinforced metal-matrix composites by simply postulating that for cyclic crack advance, the crack must penetrate or bypass a silicon-carbide particle. The arrest of a crack at a SiC particle is shown in Fig. 4b. Since this process must involve plastic flow at the crack tip, crack extension cannot be contemplated unless the plastic zone engulfs the particle. Accordingly, a limiting condition for fatigue-crack advance, i.e., the intrinsic fatigue-threshold condition, can be represented by the

assertion that *the maximum plastic-zone size must exceed the average particle size at stress intensities above the threshold ($r_y > \bar{D}_p$).*

Table V. Relationship of Particle Size and Maximum Plastic-Zone Size and CTOD Values at the Threshold Condition

Alloy	Maximum Plastic Zone Size* $r_{y,TH}$ (μm)	Effective Mean Particle Size $\bar{D}_p'$ (μm)	$r_{y,TH}/\bar{D}_p'$ Ω	CTOD at $\Delta K_{eff,TH}$ $\Delta\delta_{eff}$ (nm)
20% coarse SiC$_p$/Al	13.0	11.8	1.1	15.4
20% fine SiC$_p$/Al	10.4	10.7	1.0	50.0
15% coarse SiC$_p$/Al	14.3	13.0	1.1	15.1
15% fine SiC$_p$/Al	5.4	6.3	0.9	41.9

*Computed from $r_{y,TH} = 0.15 \, (K_{max}/\sigma_y)^2$ [36].

This limiting criterion for the threshold, that the maximum plastic-zone size is at least comparable with the average particle size, is supported by the present data on SiC$_p$/Al composites. Estimates (based on ref. 36) of the maximum plastic-zone size ($r_{y,TH}$) at the threshold stress intensity ($K_{max,TH}$) indicate that values of $r_{y,TH}$ scale with the effective mean particle size ($\bar{D}_p'$), computed as the average size of particles actually sampled (i.e., cracked or decohered) by the crack path (Table V). Specifically, the ratio Ω of $r_{y,TH}/\bar{D}_p'$ is found to be similar, and of order unity, for the four composites, such that the intrinsic threshold condition can be expressed, in terms of the maximum stress intensity at ΔK_{TH} and the yield strength σ_y, by the simple relationship:

$$K_{max,TH} \approx \beta \sigma_y \sqrt{\bar{D}_p'} , \qquad (6)$$

where the constant of proportionality β is approximately 2.6, based on a least-squares regression analysis of the current data on SiC_p/Al in Fig. 6.

The intrinsic threshold condition, given by Eq. 6, can be evaluated for composites where the particle spacing is a few times larger than their average size by considering the problem of a crack with an isolated particle at its tip (Fig. 7a). In the absence of local plasticity, which is required to induce fatigue "damage" in metals, fatigue-crack growth is inhibited when the crack is impinged by the rigid particle (Fig. 4b). To resume crack advance, the applied loads must be sufficient either to fracture the particle or to induce fatigue damage beyond it.

The interaction of a crack with isolated defects has been analyzed by several authors [37-44], with specific solutions for the crack-inclusion problem by Tamate [37], Atkinson [39] and Rubinstein [40]. In Tamate's analysis [37], Muskhelishvili's stress function is expanded into a Laurent series, i.e., as an inverse power series of the distance of the inclusion from the crack tip; the convergency of which decreases as the inclusion moves closer toward the crack tip. By representing a crack by a distribution of dislocations, Atkinson [39] conversely adopts the interaction function between a dislocation and an inclusion as the influence function for the crack-inclusion interaction; from this analysis, he found that the crack-tip stress intensity factor decreases as the distance between the inclusion and the crack tip

decreases, or when the ratio of the moduli of the inclusion and the matrix increases.

When applied to fatigue-crack advance at *near-threshold levels*, these results exclude the possibility of breaking SiC particles elastically. An alternate way of developing high stresses in the particle, however, is through plastic deformation in the matrix, which additionally promotes matrix fatigue "damage". Accordingly, *for the crack to propagate, the stress in the matrix adjacent to the inclusion must be sufficient to induce plastic flow, i.e., to be greater than the yield strength of the matrix.*

The stress in the matrix for a rigid inclusion at the tip of a semi-infinite crack has been given by Rubinstein [40]; this solution showed that although the stress is markedly reduced in the matrix immediately adjacent to the inclusion, it increases over a distance of a few inclusion sizes away from the crack tip to reach a constant level. However, as the crack/inclusion interaction function depends critically on the moduli ratio of inclusion to matrix [41], which is infinitely high in the Rubinstein analysis [40], it is required here to estimate the stress in an aluminum matrix (with $G = 70$ MPa, $\nu = 0.33$) beyond a SiC particle (with $G = 210$ GPa, $\nu = 0.25$) located at the tip of a finite crack (Fig. 7a). This is carried out by adapting the analyzes of Atkinson [39] and Erdogan and Gupta [42]; details are given in the appendix. The resulting crack-tip stress distribution in the matrix is shown in Fig. 7b (for a ratio of crack size to particle size of 1250), and compared to the crack-tip stresses in a homogeneous

material. This stress, in the matrix immediately adjacent to the particle, can be expressed as:

$$\sigma_{yy} = C\, K/\sqrt{\bar{D}_p'}\,, \tag{7}$$

where the constant C equals 2.4^{-1}, and only depends on material constants for a crack large compared to particle size. Note that the results are similar to those given in ref. 40 in that the stress in the matrix at the crack tip in the presence of the particle is significantly reduced; the stress gradient, however, is different.

By comparing Eq. 7 with Eq. 6, the limiting condition for the threshold reduces to:

$$\sigma_{yy} = \sigma_y, \quad \text{at} \quad r = r_0^* \approx \bar{D}_p'\,. \tag{8}$$

Thus, for particulate-reinforced composites where at low stress intensities crack trapping at particles can retard crack advance, a limiting intrinsic condition for the intrinsic fatigue threshold can be established in terms of the maximum plastic-zone size exceeding the average particle size, such that for crack extension the *local* tensile stress in the matrix *beyond the particle* must exceed the yield strength of the material.

Particle-size dependence: The particle-size dependence of fatigue thresholds in SiC-particulate-reinforced composites is thus a consequence of higher crack-closure levels generated in coarse-particle composites, which result primarily from the crack avoiding the particles, and higher stresses generated in the matrix in fine-particle composites, resulting from the interaction of the crack and fine particles at the crack tip. At low load ratios where crack-closure

processes are dominant, the coarse-particle distributions provide the larger contribution to impeding crack growth; conversely, at high load ratios where the effect of closure is minimal, the fine particles are more effective.

In either case, it can be concluded that at near-threshold levels, the role of reinforcement particles which lie along the crack front is to retard fatigue-crack advance (a notion, incidently, which is consistent with early fractographic observations of fatigue striation formation in the presence of particles in monolithic aluminum alloys [45]), the effectiveness of the retardation depending upon the particle size, crack-closure level and intrinsic cyclic resistance of the matrix.

Limitations: It should be noted that the intrinsic threshold condition given in Eq. 6 is only valid if the particles lie on the crack front and act as crack traps. This process naturally is far less effective where particle/matrix decohesion readily occurs (this is promoted with overaging in these composites due to interface precipitation [13]), where particles fracture prematurely (due to poor quality, clustering or failure during processing), or where the particle volume fraction is low such that particle/crack interactions are rare [46]. Similarly, the condition in Eq. 6 may also be inappropiate for very high particle volume fractions (e.g., greater than 0.5) where interparticle spacings become comparable with particle sizes, as the approach relies on the crack/isolated-inclusion interaction.

V. CONCLUSIONS

Based on a study on fatigue-crack propagation, and specifically the fatigue-threshold condition, in P/M Al-Zn-Mg-Cu metal-matrix composites particulate reinforced with either 15 or 20 vol.% of silicon carbide (SiC_p/Al), the following conclusions can be drawn:

1. Measured (nominal) fatigue-crack propagation thresholds, ΔK_{TH}, at high load ratios (R = 0.75) are found to be typically 40 to 70% lower than at R = 0.10. When compared on the basis of ΔK_{eff}, however, after adjusting for crack closure, $\Delta K_{eff,TH}$ threshold values (i.e., intrinsic thresholds) for both load ratios are virtually identical, indicating that the main source of the load-ratio effect on near-threshold behavior is crack closure.

2. At low load ratios (R = 0.10), measured ΔK_{TH} thresholds are found to vary with both volume fraction and the average size of SiC particles. Whereas low load-ratio thresholds are between 40 and 60% higher in the SiC_p/Al composites with coarse-particle distributions, high load-ratio thresholds are between 5 and 20% lower.

3. The increased low load-ratio ΔK_{TH} thresholds in the coarse SiC-particle composites are attributed to far higher levels of crack closure (by a factor of roughly two); such increased closure levels are associated with rougher fracture surfaces as the crack path seeks to avoid the SiC particles.

4. After allowing for crack closure, intrinsic $\Delta K_{eff,TH}$ thresholds are found to be solely a function of the effective mean SiC-particle size and to be independent of volume fraction. In contrast to

measured low load-ratio ΔK_{TH} thresholds, intrinsic thresholds are found to be somewhat higher in the fine SiC-particle composites.

5. SiC particles which interact with the crack path are considered to impede near-threshold crack extension in two ways: i) by promoting crack deflection (in avoiding the particle) and hence enhanced roughness-induced crack closure at low load ratios, and ii) by crack trapping. Analysis of the latter mechanism in terms of the crack/particle interaction (for a ratio of shear moduli of 3) yields a limiting requirement for the *intrinsic* threshold condition that the maximum plastic-zone size at the crack tip must at least exceed the average particle size; by considering the effect of the particle on the crack-tip stresses, this implies one limiting criterion for near-threshold crack extension that the tensile stress in the matrix *beyond* the particle reaches the yield strength of the material.

REFERENCES

1. J. Gurland and N. M. Parikh, in H. Liebowitz (ed.), *Fracture, An Advanced Treatise*, Academic Press, New York, NY, vol. 7, 1972, pp. 841-78.

2. D. F. Hasson, C. R. Crowe, J. S. Ahearn and D. C. Cooke, in W. Harrigan, J. Strife and A. K. Dhingra (eds.), *Proc. 5th Intl. Conf. on Composite Materials*, The Metallurgical Society of AIME, Warrendale, PA, 1985, p. 147-56.

3. D. L. McDanels, *Metall. Trans. A*, **16A** (1985) 1105.

4. D. L. Davidson, *Metall. Trans. A*, **18A** (1987) 2115.

5. I. L. Mogford, *Metall. Rev.*, **12** (1967) 49.

6. G. T. Hahn and A. R. Rosenfield, *Metall. Trans. A*, **6A** (1975) 653.

7. R. E. Reed-Hill, *Physical Metallurgy Principles*, McGraw-Hill, New York, NY, 1973, pp. 370-74.

8. K. C. Prince and J. W. Martin, *Acta Metall.*, **27** (1979) 1401.

9. L. Edwards and J. W. Martin, *Metal Science*, **17** (1983) 511.

10. K. T. Venkateswara Rao, W. Yu and R. O. Ritchie, *Metall. Trans. A*, **19A** (1988) 549.

11. W. A. Logsdon and P. K. Liaw, *Eng. Fract. Mech.*, **24** (1986) 737.

12. C. P. You, A. W. Thompson and I. M. Bernstein, *Scripta Metall.*, **21** (1987) 181.

13. J. J. Lewandowski, C. Liu and W. H. Hunt, in M. Kumar, K. Vedula and A. M. Ritter (eds.), *Powder Metallurgy Composites*, The Metallurgical Society of AIME, Warrendale, PA, 1987.

14. J.-K. Shang, W. Yu and R. O. Ritchie, *Mater. Sci. Eng.*, **102** (1988) in press.

15. T. Christman and S. Suresh, *Mater. Sci. Eng.*, (1988) in press.

16. J.-K. Shang and R. O. Ritchie, *Metall. Trans. A*, **19A** (1988) in review.

17. R. O. Ritchie and W. Yu, in R. O. Ritchie and J. Lankford (eds.), *Small Fatigue Cracks*, The Metallurgical Society of AIME, Warrendale, PA, 1986, pp. 167-89.

18. R. O. Ritchie, *Mater. Sci. Eng.*, **103** (1988) in press.

19. C. W. Corti, P. Cotterill and G. A. Fitzpatrick, *Int. Metall. Rev.*, **19** (1974) 77.

20. J. E. Srawley and B. Gross, *Mat. Res. Stand.*, **7** (1967) 155.

21. C. F. Shih, *J. Mech. Phys. Solids*, **29** (1981) 305.

22. R. A. Schmidt and P. C. Paris, in *Progress in Flaw Growth and Fracture*, ASTM STP 536, American Society for Testing and Materials, Philadelphia, PA, 1973, pp. 79-93.

23. S. Suresh and R. O. Ritchie, *Eng. Fract. Mech.*, **18** (1983) 785.

24. S. Suresh and R. O. Ritchie, *Metall. Trans. A*, **13A** (1982) 1627.

25. C. J. Beevers and R. L. Carlson, in R. A. Smith (ed.), *Fatigue Crack Growth*, Pergamon Press, Oxford, U.K., 1984, pp. 89-101.

26. R. J. Donahue, H. McI. Clark, P. Atanmo, R. Kumble, and A. J. McEvily, *Int. J. Fract. Mech.*, **8** (1972) 209.

27. K. Sadananda and P. Shahinian, *Int. J. Fract.*, **13** (1977) 585.

28. V. Weiss and D. N. Lal, *Metall. Trans. A*, **5** (1974) 1946.

29. V. Weiss, in H. Liebowitz (ed.), *Fracture, An Advanced Treaties*, Academic Press, New York, NY, vol. 3, 1971, pp. 228-67.

30. C. Yu and M. Yan, *Fat. Eng. Mater. Struct.* **3** (1980) 189.

31. J. R. Rice and D. M. Tracey, *J. Mech. Phys. Solids*, **17** (1969) 201.

32. A. G. Evans, *Phil. Mag.*, **26** (1972) 1327.

33. D. G. Green, P. S. Nicholson and J. D. Embury, *J. Mater. Sci.*, **14** (1979) 1413.

34. L. R. F. Rose, *Mechanics of Materials*, **6** (1987) 11.

35. J. R. Rice, in R. P. Wei and R. P. Gangloff (eds.), *Fracture Mechanics: 20th. symp.*, ASTM STP in press, American Society for Testing and Materials, Philadelphia, PA, 1988.

36. D. M. Tracey, *J. Eng. Mater. Technol.*, **98** (1976) 146.

37. O. Tamate, *Int. J. Fract. Mech.*, **4** (1968) 257.

38. I. Kunin and B. Gommerstadt, in S. R. Valluri (ed.), *Advances in Fracture Research*, Proc. ICF-6, New Delhi, India, Pergamon Press, Oxford, U.K., 1984, vol. 2, pp. 849-855.

39. C. Atkinson, *Int. J. Engng. Sci.*, **10** (1972) 127.

40. A. A. Rubinstein, *J. Appl. Mech.*, **53** (1986) 505.

41. J. Dundurs and T. Mura, *J. Mech. Phys. Solids*, **12** (1964) 177.

42. F. Erdogan and G. D. Gupta, *Quart. Appl. Math.* (1972) 525.

43. F. Erdogan and G. D. Gupta, *Int. J. Fract.*, **11** (1975) 13.

44. A. Chudnovsky and M. Kachanov, *Lett. Appl. Engng. Sci.*, **21** (1983) 1009.

45. D. Broek, *Int. Met. Rev.*, **19** (1974) 135.

46. F. A. Heiser and R. W. Hertzburg, *J. Basic Eng.*, Trans. ASME, Ser. D, **93** (1971) 211.

APPENDIX: CRACK/INCLUSION INTERACTION

Considering the interaction of an edge dislocation (with Burger's vector b), located at coordinates (c, 0) in a matrix (with shear modulus G_1, and Poisson's ratio ν_1), with an inclusion (with shear modulus G_2 and Poisson's ratio, ν_2), located at the origin (Fig. A1), the stress component $(\sigma_{yy})_{1(y=0)}$ in the matrix at a point (x, 0) along the x-axis is given by [41]:

$$(\sigma_{yy})_{1(y=0)} = \frac{G_1\, b_y}{\pi(k_1+1)} \left\{ \frac{2}{x-c} - \frac{A+B}{x-a^2/c} - 2A\frac{\beta^2-1}{\beta^3}\left[\beta^2 + \frac{1-\beta^2}{\beta}\cdot\frac{a}{x-a^2/c}\right]\frac{a}{(x-a^2/c)^2} \right.$$

$$\left. + \frac{A+B}{x} + \frac{A(2\beta^2-1) + M(k_2+1) - 1}{\beta}\cdot\frac{a}{(x-a^2/c)^2} + \frac{2A\,a^2}{x^3} \right\} \tag{A1}$$

where

$$\beta = c/a \geq 1$$

$$\Gamma = G_2/G_1$$

$$A = (1 - \Gamma)/(1 + \Gamma \cdot k_1)$$

$$B = (k_2 - \Gamma k_1)/(k_2 + \Gamma)$$

$$M = \Gamma\,(k_1 + 1)/\{(k_2 + \Gamma)(k_2 - 1 + 2\Gamma)\}$$

and k_1 and k_2 are the respective bulk moduli for the matrix and inclusion.

To simulate a crack as a stress-free surface between $c = \alpha_1$ and α_2, the required dislocation density N(c), which gives an infinitesimal displacement of:

$$db_y = b\, N(c)\, dc, \tag{A2}$$

in the interval dc, is determined by:

$$\sigma_{app} + (\sigma_{yy})_{1(y=0)} = 0, \qquad \alpha_1 < c < \alpha_2 \tag{A3}$$

subject to the condition:

$$\int_{\alpha_1}^{\alpha_2} N(c) \ dc \ = \ 0 \qquad\qquad (A4)$$

where σ_{app} is the applied stress acting on the crack faces. Combining Eqs. A1-A3 yields:

$$\frac{\sigma_{app}(x)}{D} + \int_{\alpha_1}^{\alpha_2} \frac{N(c) \ dc}{x-c} + \int_{\alpha_1}^{\alpha_2} H(c,x) \ N(c) \ dc \ = \ 0 \qquad (A5)$$

where

$$D = \frac{2G_1 b}{\pi(k_1 + 1)}$$

and

$$H(c,x) = -\frac{A + B}{2(x - a^2/c)} - A \cdot \frac{\beta^2 - 1}{\beta^3} \left[\beta^2 + \frac{1 - \beta^2}{\beta} \cdot \frac{a}{x - a^2/c} \right] \cdot \frac{a}{(x - a^2/c)^2} + \frac{A + B}{2x}$$

$$+ \frac{A(2\beta^2 - 1) + M(k_2 + 1) - 1}{2\beta} \cdot \frac{a}{(x - a^2/c)^2} + \frac{A \ a^2}{x^3} \ .$$

On substitution of:

$$c = \tfrac{1}{2}(\alpha_2 - \alpha_1)(c_1 + v)$$

$$a = \tfrac{1}{2}(\alpha_2 - \alpha_1)a_1$$

$$x = \tfrac{1}{2}(\alpha_2 - \alpha_1)(x^* + v)$$

and

$$v = (\alpha_2 + \alpha_1)/(\alpha_2 - \alpha_1)$$

Eq. A5 becomes

$$\sigma_1(x^*) + \int_{-1}^{1} \frac{N_1(c_1) \ dc_1}{x^* - c_1} + \int_{-1}^{1} N_1(c_1) \ H_1(c_1,x^*) \ = \ 0 \qquad (A6)$$

subject to

$$\int_{-1}^{1} N_1(c_1) \ dc_1 \ = \ 0 \qquad\qquad (A7)$$

where
$$\sigma_1(x^*) \quad = \quad \sigma_{app}\,\{x(x^*)\}/D$$

$$N_1(c_1) \quad = \quad N\{c(c_1)\}$$

and
$$H_1(c_1,x^*) \quad = \quad \tfrac{1}{2}(\alpha_2 - \alpha_1)\,H\{c(c_1),x(x^*)\}.$$

Noticing that the fundamental equation for the integral equation (Eq. A6) is:

$$R(c_1) \quad = \quad (1 - c_1^2)^{-\frac{1}{2}} \, ,$$

the solution to Eq. A6 can be expressed in the form [42]:

$$N_1(c_1) \quad = \quad N_0(c_1)/(1 - c_1^2)^{\frac{1}{2}} \, , \tag{A8}$$

where N_0 is bounded. Eq. A6 can then be written as:

$$\sigma_1(x^*) + \int_{-1}^{1} \frac{N_0(c_1)\,dc_1}{(x^* - c_1)(1 - c_1^2)^{\frac{1}{2}}} + \int_{-1}^{1} \frac{N_0(c_1)\,H_1(c_1,x^*)}{(1 - c_1^2)^{\frac{1}{2}}} \; = \; 0 \tag{A9}$$

Since for a function $F(t)$ satisfying the Hölder condition [42]:

$$\frac{1}{\pi} \int_{-1}^{1} \frac{F(t)\,dt}{(t - x)(1 - t^2)^{\frac{1}{2}}} \; \simeq \; \sum_{k=1}^{n} \frac{F(t_k)}{n(t_k - x_r)} \, , \qquad -1 < x < 1 \tag{A10}$$

where
$$t_k = \cos\{(\pi/2n)(2k - 1)\}, \qquad k = 1, 2, \ldots, n$$

and
$$x_r = \cos\{\pi r/n\}, \qquad r = 1, 2, \ldots, n-1$$

applying Eq. A10 and the Gauss-Chebyshev integration formula

$$\frac{1}{\pi} \int_{-1}^{1} \frac{f(t)\,dt}{(1 - t^2)^{\frac{1}{2}}} \; \simeq \; \sum_{k=1}^{n} \frac{f(t_k)}{n}$$

to Eqs. A7 & A9, we obtain:

$$\sum_{k=1}^{n} \frac{\pi\,N_0(t_k)}{n(t_k - x_r)} - \sum_{k=1}^{n} \frac{\pi\,N_0(t_k)\,H_1(t_k,x_r)}{n} \; = \; \sigma_1(x_r) \tag{A11}$$

which reduces to:

$$\sum_{k=1}^{n} N_0(t_k) \left[\frac{1}{(t_k - x_r)} - H_1(t_k, x_r) \right] = \frac{n \, \sigma_1(x_r)}{\pi} \qquad (A12)$$

and

$$\sum_{k=1}^{n} N_0(t_k) = 0 \qquad (A13)$$

Eqs. A12 & A13 are n linear equations with n unknowns $N_0(t_k)$. By solving for N_0 and substituting back into Eq. A8 to give N_1, the tensile stress at any point ahead of the crack, beyond the inclusion along x-axis can be calculated from Eq. A1 as:

$$(\sigma_{yy})_{1(y=0)} = D \left[\int_{\alpha_1}^{\alpha_2} \frac{N(c)}{x - c} \, dc + \int_{\alpha_1}^{\alpha_2} N(c) \, H(c,x) \, dc \right] \qquad (A14)$$

This crack-tip stress distribution is illustrated in Fig. 7 for a SiC particle located at the tip of a center crack of length 2ℓ in an aluminum matrix, i.e., for $\Gamma = G_2/G_1 = 3$, where σ_{app} can be calculated as [39]:

$$(\sigma_{yy})_1 = T_0 \left(1 - \frac{B_1}{2x^2} - \frac{3C_1}{x^4} \right) , \qquad y = 0, \; |x| > a \qquad (A15)$$

where $\quad B_1 = \dfrac{a^2 [(k_1 - 1)\Gamma - (k_2 - 1)]}{(k_2 - 1) + 2\Gamma}$

and $\quad C_1 = -\dfrac{a^4}{2} \cdot \dfrac{1 - \Gamma}{1 + k_1 \cdot \Gamma}$
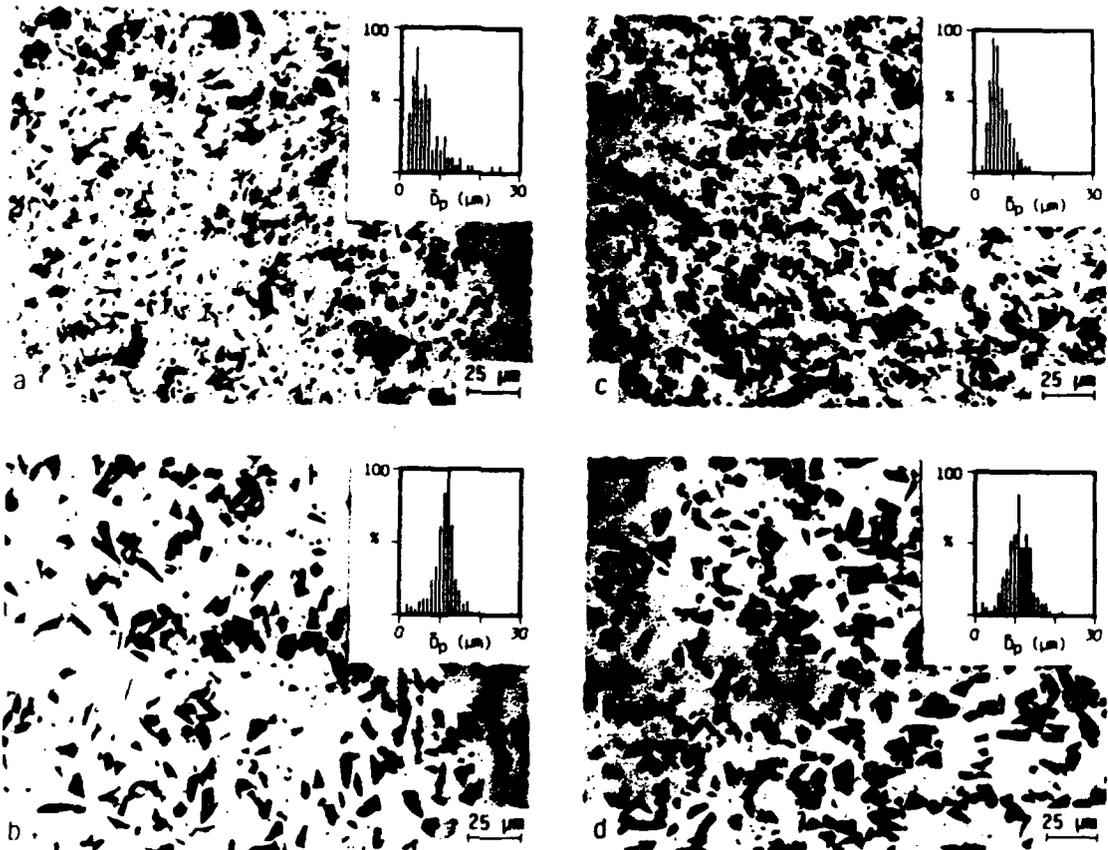
Fig. 1: Optical micrographs of the microstructures, with corresponding
particle-size distributions, for 15 vol.% SiC_p/Al composites
with a) fine and b) coarse SiC particles, and for 20 vol.%
SiC_p/Al composites with c) fine and d) coarse SiC particles.
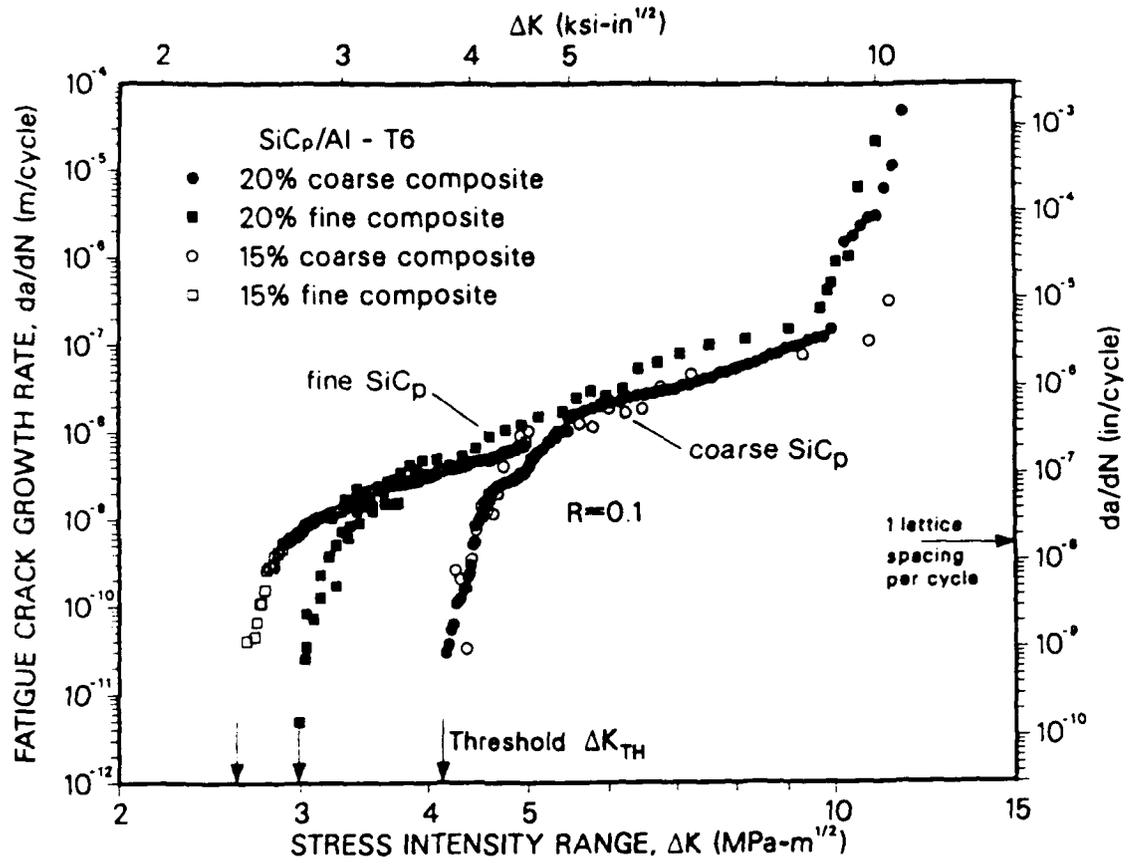
Fig. 2: Variation in fatigue-crack propagation rates, da/dN, with the nominal stress-intensity range, ΔK, for the 15 and 20% fine and coarse SiC$_p$/Al composites (T6 peak-aged microstructures) at room temperature, showing behavior at a load ratio of 0.10.
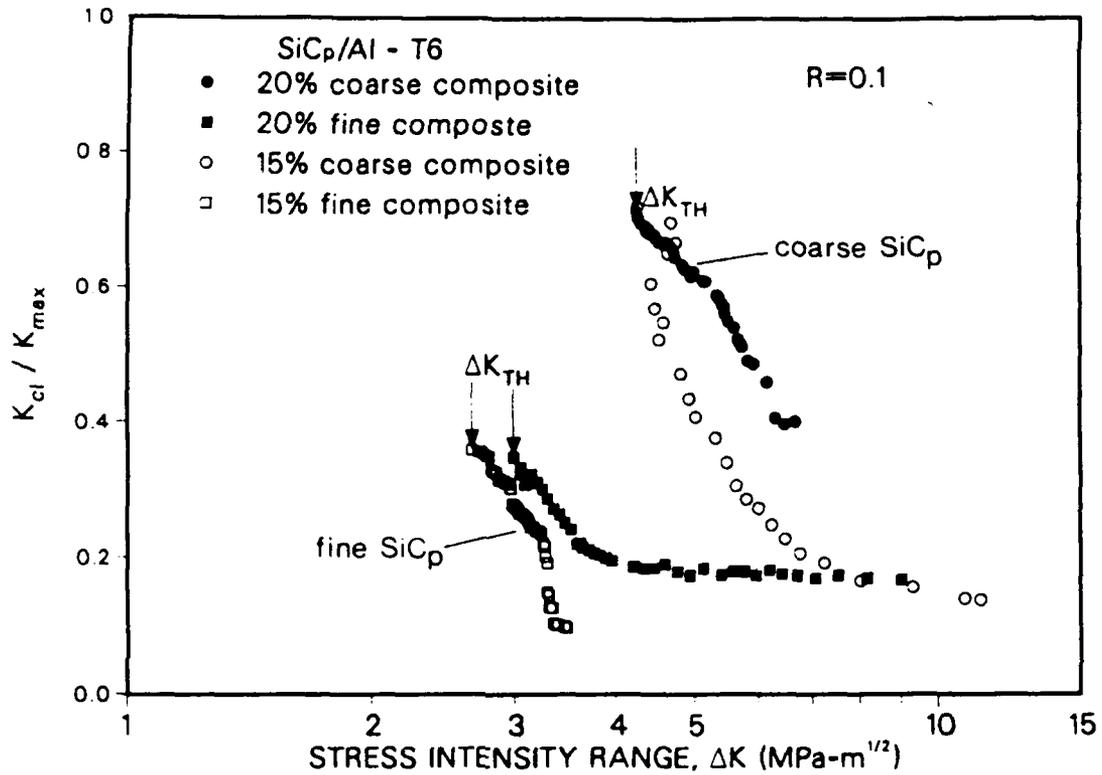
Fig. 3: Variation in crack closure, plotted as a function of the normalized closure stress intensity, K_{cl}/K_{max}, with nominal stress-intensity range, ΔK, for the 15 and 20% fine and coarse SiC_p/Al composites. Closure data correspond to the crack-growth results in Fig. 2.
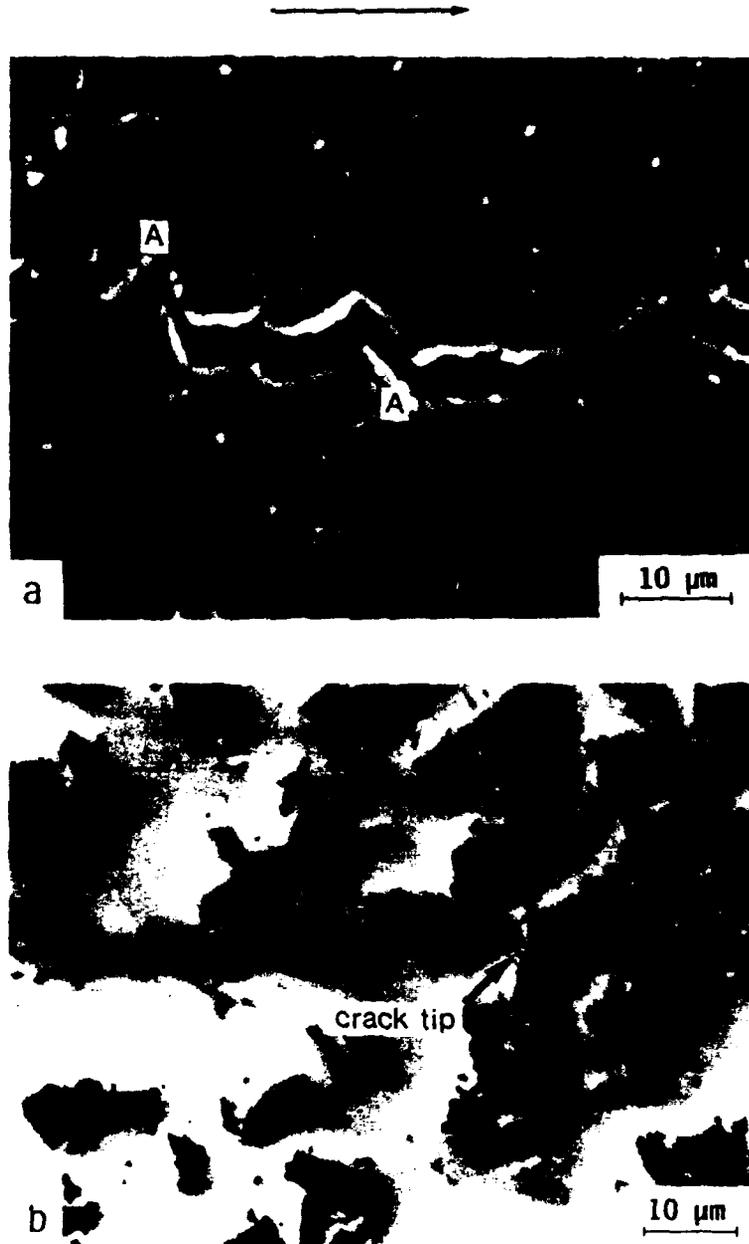
Fig. 4: Mechanisms associated with the interaction of the fatigue crack with SiC particles in SiC_p/Al composites, showing a) crack deflection and consequent enhanced crack closure (due to asperity wedging) at low load ratios where the crack seeks to avoid the particles (locations A), and b) crack trapping at SiC particles (at the crack tip). Horizontal arrow indicates general direction of crack growth.
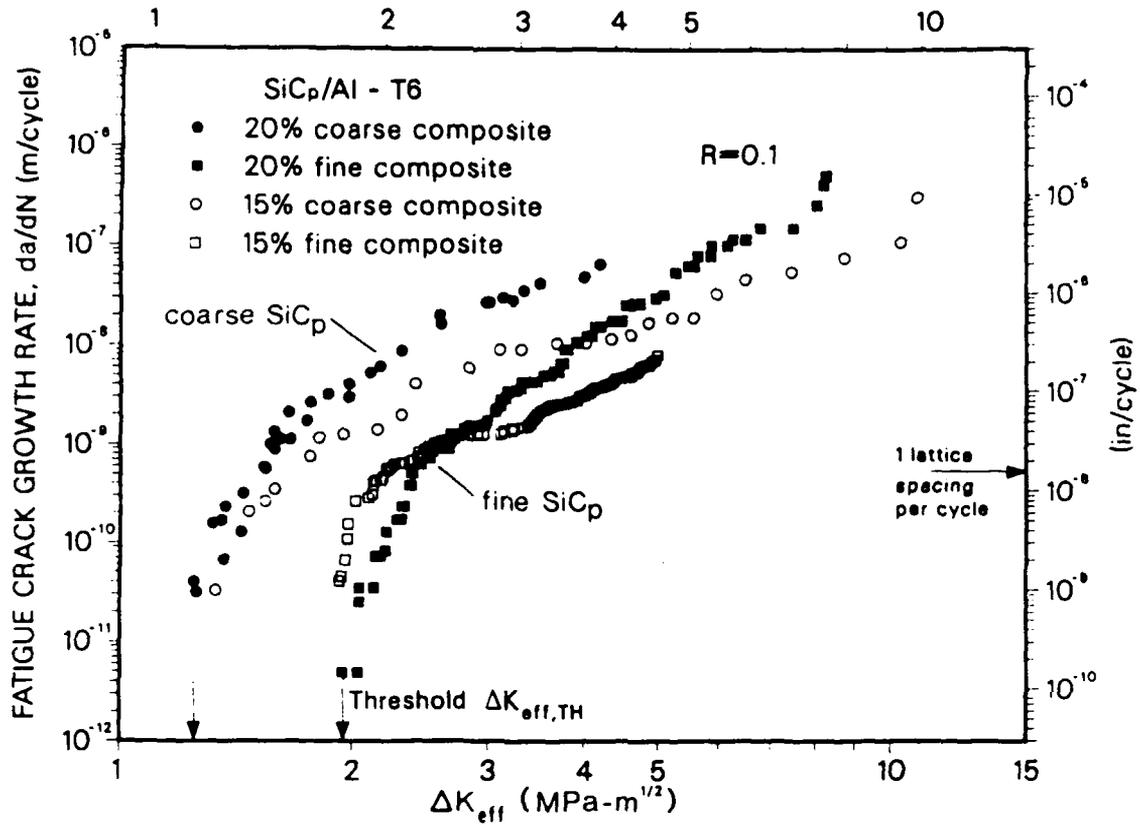
Fig. 5: Variation in fatigue-crack propagation rates, da/dN, as a function of the effective stress-intensity range, ΔK_{eff}, for the 15 and 20% fine and coarse SiC_p/Al composites. Note that after subtracting out the effect of crack closure, near-threshold behavior is a sole function of particle size.
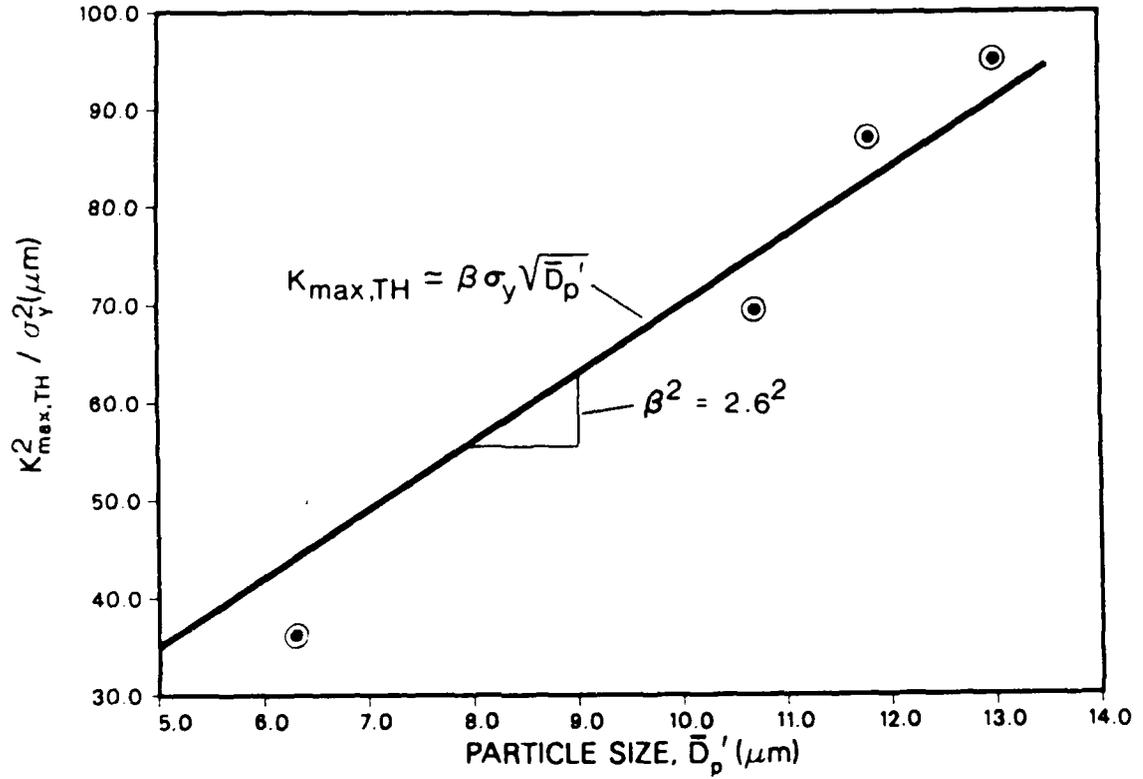
Fig. 6: Relationship between the threshold K_{max}, plotted as $K^2_{max,TH}/\sigma^2_y$, and the effective mean particle size, $\bar{D}'_p$, for the 15 and 20% fine and coarse SiC_p/Al composites at R = 0.10.
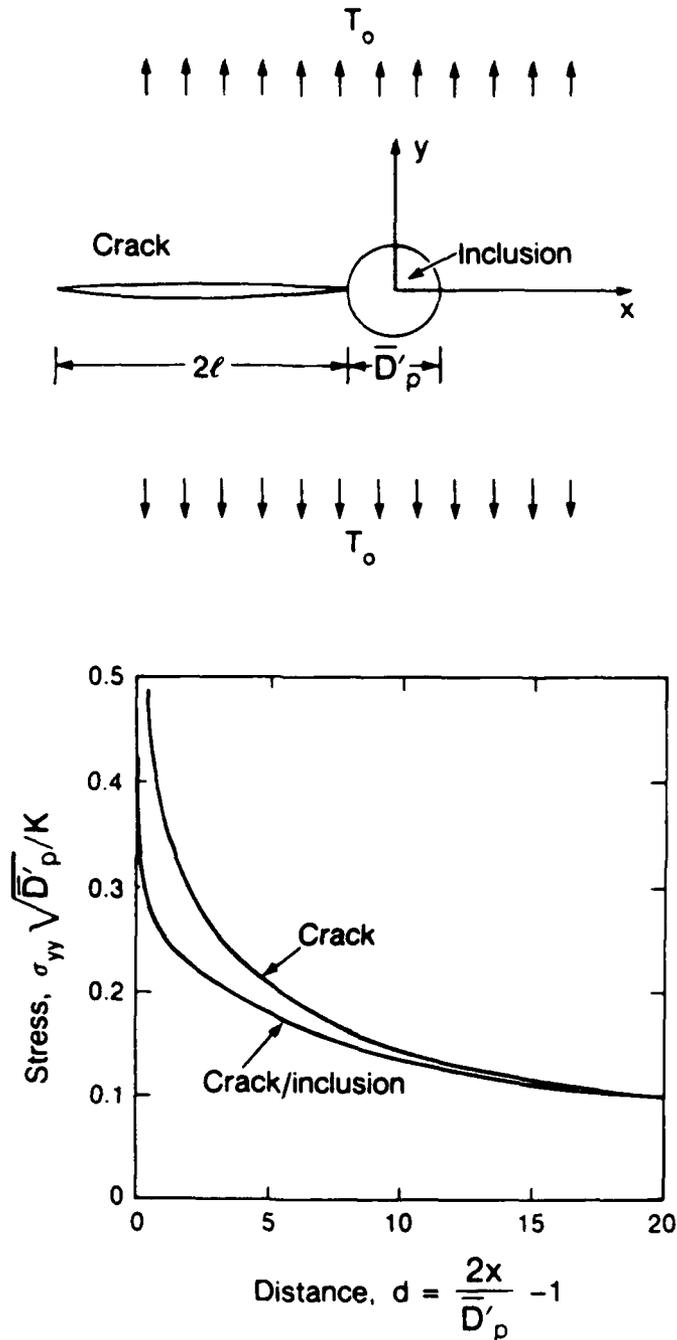
Fig. 7: a) Schematic illustration of the crack/inclusion interaction,
showing b) predicted distribution of normalized tensile stress
in the matrix, σ_{yy}, as a function of normalized distance ahead
of a crack/inclusion (Eq. A14), compared to the crack-tip
stress distribution in a homogeneous material. Results are for
a ratio of crack size to inclusion size of 1250, and a ratio
of shear moduli of inclusion and matrix of 3.
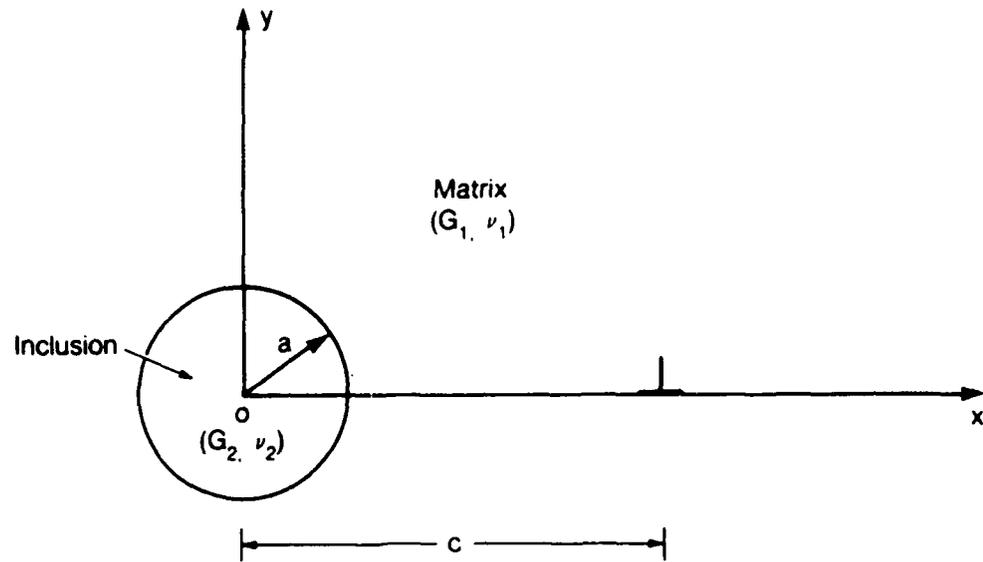
XBL 886-9695

Fig. Al: Configuration for dislocation/inclusion interaction.

TASK 5

Creep of High Temperature Composite Matrices

A.W. Thompson and J.C. Williams, Co-investigators

Task 5 of the URI on High-Temperature Metal Matrix Composites has the task title of "Micromechanisms of High Temperature Composite Behavior". Work is concentrating on matrix materials for such composites, in particular titanium aluminide alloys. The current effort has utilized two such alloys, Ti-24 Al-11 Nb and Ti-25 Al-10 Nb-3 V-1 Mo (atomic percentages), both of which are based on the compound Ti_3Al and are near-commercial alloys. A variety of both ambient and elevated temperature mechanical properties is being explored, with particular interest in creep behavior and high-temperture fracture of the alloys. The most complete and extensive work has been done on 25-10-3-1, and accordingly the Annual Report for this Task contains a report on that effort. It has been carried out by Dr. W. Cho, a Postdoctoral Associate, while the 24-11 work is being conducted by a Ph.D. student, D. Albert. The former co-investigator on this task, Dr. J.C. Williams, left Carnegie Mellon University in August, 1988, to join the Aircraft Engines Business Group of General Electric, but helped supervise work on the task for most of the contract year.

The attached report, co-authored by W. Cho, is being submitted for publication. In addition to that report, the following oral presentations, based on work done in the task, were presented in the course of the year.

A.W. Thompson, "Ductile Fracture in Metal Matrix Composites", in *Mechanical Performance of Metal-Matrix Composites*, TMS Physical and Mechanical Metallurgy Committees Symposium, Fall Meeting, TMS-AIME, Cincinnati, OH, 14 Oct. 1987.

A.W. Thompson, "Studies of Creep and Ductile Fracture in Metal Matrix Composites", presentation at 1988 Annual Winter Workshop on Composite Materials, University of California, Santa Barbara, CA, 11 Jan. 1988.

C.H. Ward, J.C. Williams, A.W. Thompson and F.H. Froes, "Microstructural Development in Alpha-2 + Beta Titanium Aluminides", in *High Temperature Mechanical Properties of Ordered Intermetallics*, TMS Physical and Solidification Committees Symposium, Annual Meeting, AIME, Phoenix, AZ, 25 Jan. 1988.

A.W. Thompson, "Hydrogen and Mechanical Properties of Titanium Aluminides at Room and Elevated Temperature", *2nd NASP Workshop on Hydrogen-Materials Interaction*, Scottsdale, AZ, 2 June 1988.

A.W. Thompson, "Ductile Fracture Processes in Composites", *Interfaces in Polymer, Ceramic and Metal Matrix Composites* (2nd Internat. Conf. on Composite Interfaces, H. Ishida, Chairman), Cleveland, OH, 14 June 1988.

W. Cho, J.C. Williams and A.W. Thompson, "Effect of Microstructure on Deformation Behavior of Ti-25-10-3-1", in *Mechanical Performance of Advanced Composites*, TMS Mechanical Metallurgy Committee Symposium, Fall Meeting, TMS-AIME, Chicago, IL, 28 Sept. 1988.

CREEP BEHAVIOR OF Ti-25-10-3-1

W.CHO*, A.W.THOMPSON*, AND J.C.WILLIAMS**

*; Department of Metallurgical Engineering and Materials Science
Carnegie Mellon University, Pittsburgh, PA 15213-3890

**; Engineering Materials Technology Laboratories, General Electric
Cincinnati, Ohio, 45215-6301

A study has been made of the role of microstructure on room temperature tensile properties as well as elevated temperature creep behavior of an advanced Ti_3Al alloy, Ti-25Al-10Nb-3V-1Mo (a/o). Creep studies have been performed on this alloy as a function of stress and temperature between 650°C and 870°C, below which the use of conventional titanium alloys has generally been limited. A pronounced influence of microstructure on creep resistance was found. Generally, the β solution treated colony type microstructure shows superior creep resistance, even though at 650°C, increasing stress increases steady state creep rate of this microstructure compared to other microstructures. This improved creep resistance in β/SC is accompanied by lower room temperature tensile strength and ductility. Study of stress dependence of steady state creep rate indicates that increasing temerature causes a gradual decrease in "n" and a transition in creep mechanism at 870°C, depending on applied stress level. TEM observations of deformed dislocation structures developed during steady state creep and room temperature tensile, and fracture modes are discussed as a function of temperature. Finally, creep behavior of Ti-25-10-3-1 is compared to those of conventional near-α titanium alloys.

I. INTRODUCTION

In recent years, considerable effort has been made to develop advanced titanium aluminide alloys based on Ti_3Al for aircraft turbine engine components and other high temperature applications. These aluminides retain adequate creep strength to much higher temperatures than do conventional titanium alloys, but they shows low ductility at room temperature.[1] Therefore, the alloy development concept has been focussed on the optimum combination of room temperature ductility and elevated temperature creep strength. With this alloying concept, most recently, Ti-25Al-10Nb-3V-1Mo (atomic percent) was developed with additions of β phase stabilizers. Additionally, it was recognized that substitution of some vanadium for niobium would be desirable to cause a lighter alloy and cost benefit would be expected.[2]

To date, most studies on creep behavior of alloys based on titanium have been performed on near-α titanium alloys, such as Ti-6242S[3] and IMI 685[4]. The past creep studies have shown that the creep resistance of conventional near-α titanium alloys was strongly dependent on microstructure. In general, Widmanstatten microstructures, produced by solution treating above the β–transus, offer creep resistance at high temperatures superior to that provided by equiaxed microstructures produced by processing in the $\alpha+\beta$ phase field. They also revealed that creep resistance is maximized at intermediate cooling rates from the β solution treatment temperatures.

In contrast, very little data on creep behavior of Ti_3Al based alloys were obtained. In particular, there is little systematic investigation of the creep behavior in terms of microstructural influences for the optimization of mechanical behavior in this important class of alloys. The only significant study[5][6] was performed to investigate the steady-state creep behavior of Ti_3Al and Ti_3Al+10 w/o Nb in the temperature range of 550 to 825°C. In that study, it was shown that at temperatures above 700°C, the stress exponent "n" of the power law creep equation indicated a transition in mechanism and in the high stress and temperature regime addition of Nb increased apparent activation energy for creep deformation.

In the present investigation, room temperature tensile and elevated temperature creep studies have been performed on various microstructures of Ti-25%Al-10%Nb-3%V-1%Mo (a/o). A special interest is shown for the creep behavior of this alloy at the temperatures between 650°C and 870°C below which the use of conventional titanium alloys has generally been limited. The influence of microstructure, stress, and temperature on creep behavior is discussed. Fracture modes and TEM observations of dislocation structures responsible for each deformation are also discussed.

II. EXPERIMENTAL PROCEDURE

Microstructures were controlled by solution treating in either the $\alpha_2+\beta$ or the β phase field and controlling the cooling rate from the solution treatment temperature. Transformed β microstructures were produced by a 1hr/β solution treatment at 1150°C followed by one of the following cooling schemes: furnace cooling, SC; controlled cooling, CC; air cooling, AC. The SC,CC and AC treatments produced average cooling rates of 0.1°C/sec, 0.5°C/sec and 10°C/sec, respectively, when measured between the solution treatment temperature and 760°C. α_2/β microstructures were produced by solution treating at 1045°C for 1hr. and same cooling schemes as above. The β transus temperature for the alloy Ti-25-10-3-1 has been reported to be in the range of 1065-1093°C.[2]

Tensile testing was performed at room temperature with various cross head speeds from 0.05mm/min to 500mm/min. Creep tests were conducted in air under constant tensile load. Test procedures followed ASTM E139-79. Specimens were machined with a 6.4mm diameter and a 37mm effective gage length with sufficient metal removal during machining to ensure that contaminated surfaces were removed. Creep strain was measured using a SLVC tranducer which allowed a strain resolution of 5×10^{-6}.

The fracture surfaces were examined in Cam Scan scanning electron microscope and the dislocation structures were studied by transmission electron microscopy in a Philips EM420 operated at 120kV.

III. RESULTS AND DISCUSSION

(1) As-received microstructure and thermal stability

The as-received microstructure taken from the pancake with 4.4cm thickness and 35cm diameter, as shown in Fig.1, a (optical), Fig.1, b (TEM) consisted of very fine Widmanstatten α_2 platelets and retained ordered β phase, since this was forged in the $\alpha_2+\beta$ phase field and solution treated in the β phase region followed by air cooling. The microstructure has relatively large prior β grains with 0.74mm of average intercept length and shows little effect of forging direction.

The thermal stability of Ti-25-10-3-1 was investigated by long term aging of the as-received microstructure at 650°C and 760°C for time up to 1000 hours and by monitoring microstructural changes and determining changes in micro-hardness as a function of aging time. Exposures at both temperatures led to β-phase decomposition resulting in "break-up" in the ordered β phase film, as shown in Fig.1,c. In addition, the decomposition process left behind the dislocation structures which are believed to occur for accommodation. Detailed analysis for the decomposition product remains for future work. Room temperature micro-hardness data (Fig.2) obtained as a function of aging time can be related to microstructural changes. Micro-hardness decreases rapidly just after short term aging at both temperatures. The ordered β phase decomposition, or recovery of rapid cooled substructures of as-received material, is thought to be responsible for the loss in hardness. Therefore, it is worthwhile to mention that at both temperatures, "microstructural changes" in a Widmanstatten type microstructure can be finished in a reasonably short period to reach quasi-equilibrium microstructure. This can be also true for microstructural evolution during creep exposures.

(2) Microstructural development

Optical microscopy was used to characterize the various microstructures after heat treating, as well as the relationship between the structure and the creep properties.

Fig.3 shows the microstructures resulting from three different cooling schemes from the β solution treatment temperature. The significant variables in these microstructures are the size and morphology of α_2 phase and the amount of ordered retained β phase. Air cooling (β/AC), the fastest cooling rate, produced fine α_2 precipitates with a large amount of retained β phase. Additionally, in the β/AC microstructure, relatively small sub-grain boundaries were etched out by much longer etching exposure (5 minutes) than the normal etching condition, using Kroll's reagent which produced β/CC, β/SC microstructures. With normal etching condition (10 sec. exposure), only prior β grain boundaries were visible. Furnace cooling (β/SC), the slowest cooling rate, produced moderate size of colonies of similarly aligned, coarse Widmanstatten α_2 plates. These Widmanstatten α_2 plates are separated by thin films of retained β phase. At intermediate cooling rate, β/CC, the microstrcture consists of thin, basketweave α_2 with a substantial amount of retained β phase. The resulting morphologies are quite similar to those found in conventional high temperature near-α alloys, particularly in basketweave and colony microstuctures. However, the kinetics of β phase transformation seem to be different in different alloy systems.

Here, it is necessary to consider the nature of retained β phase. Even though the details of retained β phase were not yet investigated via TEM in the present study, it is believed that retained β phase has a fully transformed ordered structure (B_2, CsCl type). Recently, in Strychor et. al's study[7], the nature of β phase ordering even in water quenched specimens of Ti-27.8Al-11.7Nb (a/o) was confirmed through the examination of β zones which show superlattice reflections characteristics of a B_2 (CsCl) structure. This type of behavior has been observed in Ti_3Al+Nb alloys whose Nb contents lie between about 15 and 35w/o, even though the extent of this field at the high Nb end is still undetermined in detail.

The microstructures resulting from α_2/β solution treatment followed by three cooling schemes are shown in Fig.4. The α_2/β process produced elongated primary α_2 in a transformed β matrix similar to that of β solution treated microstructures. The microstructure with slow cooling (α_2+β/SC) was selected as a representative of α_2/β processed microstructures in order to compare room temperature tensile properties as well as elevated temperature creep behavior with β processed microstructures.

(3)   Room temperature tensile properties

Room temperature tensile properties were characterized as a function of strain rate with microstructures discussed above. Four cross head speeds were used; 0.05mm/min (0.00097/min), 5mm/min (0.097/min), 50mm/min (0.97/min), 500mm/min(9.7/min). The tensile properties, ultimate tensile strength or fracture strength, 0.2% yield strength and percent elongation, are all shown in Fig. 5. Particularly, the influence of cooling rate after β solution treatment on 0.2% yield stress and ductility is highlighted in Fig. 6, using the slow strain rate (0.00083/min) and 6.4mm diameter x 137mm gage length specimens. On the other hand, the properties in Fig. 5 were obtained from pin-loaded small sheet specimens which have 12.7mm gage length.

The $\alpha_2+\beta$ processed microstructures exhibited higher strength values (yield and ultimate) than β processed micrstructure ($\alpha_2+\beta$/SC vs. β/SC). It is thought that this behavior resulted from microstructural unit difference controlling deformation which is pronounced if one takes into account the dimensions of the colonies for β processed microstructures and of the elongated primary α_2 grains for $\alpha_2+\beta$ processed microstructure, as similarly explained in α/β titanium alloys[8]-[10]. The $\alpha_2+\beta$/SC microstructure was observed to be more ductile as compared to β/SC microstructure. This increase in ductility might be attributed to the reduced dislocation pile-up length[8] with decreasing microstructural unit size.

In β processed microstructures, generally, both the strength and ductility increase as cooling rate is increased, except at very high strain rate. At very high strain rate, only σ_F was determined and $\sigma_{Y.S}$, $\sigma_{U.T.S}$ were not distinguished, because X-Y chart recorder speed lagged the strain rate. Very little information is available on the influence of cooling rate on the mechanical properties of titanium aluminide alloys. Blackburn et. al[11] found the similar behavior in Ti-24Al-11Nb as that of the present investigation, using three cooling rates from β solution treatment. Slow cooling rate resulting in a colony microstructure produced low strength and ductility, while intermediate cooling rate resulting in a fine Widmanstatten (basketweave) microstructure caused good ductility and strength level. A rapid cooling rate (15°C/sec) producing a partially transformed structure, also brought a highest yield strength, but a very low ductility, even lower than that of colony microstructure. In near-α alloys, such as IMI 829[12], any significant change in the

strength and ductility was not found in the β heat treated condition due to a change in the cooling rate which resulted in similar morphologies as in the case of the present α_2 alloy.

When the room temperature tensile properties are considered from the viewpoint of the strain rate variable, it can be seen that the influence of strain rate on the flow stress depends on microstructure. For as-received, β/CC and $\alpha_2+\beta$/SC microstructures, the flow stress is independent of strain rate, whereas for β/AC and β/SC microstructures, the flow stress decreases rapidly at the very high strain rate (9.7/min), but attains a constant value for strain rates slower than 0.97/min. The degree of decrease is much higher in the β/SC microstructure than that in the β/AC microstructure. As can be seen in Fig.5,a, the tensile strength or the fracture strength of β/SC microstructure dropped to approximately half of that of lower strain rates . Even though some data scatter is found, ductility measured by % total elongation of all the microstructures seems to be independent of strain rate.

The observed strain rate independence of room temperature strength would naturally be consistent with temperature dependence of strength. In the case of monolithic α_2 , the static strength and stiffness did not degrade very rapidly with increasing temperature[13]. Similar behaviors were observed both in monolithic γ' (Ni_3Al, $L1_2$ structure)[14] and γ/γ' alloys[15]. It was shown that samples deformed before the peak temperature, where a positive temperature dependence in monolithic γ' and a temperature independence in γ/γ' alloys of the flow stress were characterized, exhibited a very small positive strain rate depenednce of the flow stress. However, samples deformed at higher temperatures after the peak, where the flow stress decreased very rapidly with increasing temperature, demonstrated a very strong positive effect of strain rate on the flow stress.

(4) Creep behavior

Role of microstructure

The effect of microstructure on creep behavior was studied as a function of stress and temperature between 650°C and 870°C. Apparent stress exponent "n" measurements were made by decreasing load from the load pan during testing in order to provide a step change in stress and thus strain rate. At each new stress level, the test continued until a new steady state creep rate could be determined, thus minimizing structural changes for each successive decrease in load. Most tests were terminated during steady state creep and the specimens were cooled down under load to preserve and investigate dislocation structures responsible for creep deformation.

As shown in Fig.7 and Fig.8, the creep curves obtained at 650°C/60ksi and 760°C/30ksi, demonstrate the pronounced influence of microstructures. Generally, most of the creep curves have a classical behavior with a primary or transient period followed by a steady state regime. It is useful, here, to characterize creep behavior with two processing parameters; (1) solution treatment temperature (β/SC vs. α_2+β/SC), (2) cooling rate from β region (β/AC, β/CC, β/SC). At both temperatures, the α_2+β processed microstructure (α_2+β/SC) which has elongated primary α_2 grains shows lower creep resistance, when compared to the β solution treated microstructure (β/SC), although the magnitude of the effect of solution treating process was much greater at 760°C/30ksi.

The β solution treatment alone is not sufficient to characterize creep resistance. The effect of cooling rate from the β phase region on microstructure and its role in creep performance needs to be taken into account. Fig.9 shows the effect of cooling rate on creep strain after a certain amount of time obtained from Fig.7 and Fig.8. Creep resistance increases with decreasing cooling rate of which we have investigated at 760°C/30ksi, and thus creep resistance of the furnace cooled colony microstructure (0.1°C/sec) is significantly improved. However, at 650°C/60ksi, creep resistance increases with increasing cooling rate through a maximum at an intermediate cooling rate of 0.5°C/sec which produced basketweave microstructure.

To further investigate the role of microstructure on creep resistance, steady state creep rates were measured as a function of stress at constant temperatures of 650°C and 760°C, as shown in Fig.10 and Fig.11. The apparent exponents "n" were obtained to show the stress dependence of steady state creep rate, using the power law creep equation; $\dot{\varepsilon}_s = A\sigma^n\exp(-Q_c/RT)$, where $\dot{\varepsilon}_s$ is the steady state creep rate at a tensile stress σ, n and A are constants, Q_c is the apparent activation energy, R the gas constant, and T the absolute temperature. At 760°C (Fig.11), microstructural variation doesn't affect "n" values very much in the range of stress studied, and thus at all stresses the colony microstructure (β/SC) shows lower creep rate than that of fine Widmanstatten microstructure(as-received). In contrast, at 650°C (Fig.10), it can be seen that the influence of microstructure on steady state creep depends on stress level. β/SC has larger n value(5.8) than that of β/CC(4.2), and thus a cross-over point was found on the stress vs. steady state creep rate plot. At high stresses, β/CC exhibits the lowest steady state creep rate, while at low stresses β/SC does, again.

For different microstructures, the difference in creep response under identical testing conditions can be attributed to variations in structural variables. Moreover, the role of microstructure is thought to differ for the different creep regimes. Based on determined "n" values, it can be concluded that in the present regimes studied, creep strain accumulation is controlled by dislocation motion. Most recently, a phenomenological model[3][16] was proposed to correlate creep behavior of near-α titanium alloys with structural factors. In this model, the existence of an optimum cooling rate for maximum creep resistance was explained in terms of the trade-off between an increasing amount of retained β phase (detrimental in creep resistance) and decreasing α plate size (beneficial in creep resistance). The present observations on the interaction between microstructure and creep deformation can be rationalized in a similar manner as in the case of near-α titanium alloys.

First, it is suggested that the effective slip length in elevated temperature creep deformation is controlled by primary α_2 size in $\alpha_2+\beta$ processed microstructures and by Widmanstatten α_2 in β processed microstructures. Even though the Burgers relationship exists between α_2 and ordered β phase, it is not surprising that α_2/B2 boundaries are effective barriers to slip and act to confine active dislocations to individual α_2 platelets, because of the relatively low applied stresses, necessitated by the high creep temperatures.

Therefore, inferior creep resistance of the α_2+ β/SC microstructure is attributed to a larger slip length than that of the β/SC microstructure.

If only α_2 platelet size controlled creep deformation it would be expected that the microstructure with fine Widmanstatten α_2 platelets exhibits superior creep resistance. The maximum in creep resistances that occurs in slow cooled microstructure (β/SC) at 760°C and 650°C and low stresses suggests that other microstructural factors must be considered. The other microstructural factor competing with α_2 plate dimension is the amount of retained ordered β phase (B2). Fast cooling increases the amount of B2 phase, resulting in poor creep resistance, because of its intrinsic high diffusion coefficient. It is, therefore, required to have optimum α_2 plate size and optimum amount of retained B2 phase for the superior creep resistance at elevated temperatures. However, at 650°C and high stresses, a somewhat complicated role of microstructure was observed, because of difference in stress dependence. Minimum creep resistance in β/SC microstructue in this regime suggests that a different structural unit beyond α_2 plate size would be active, similar to that of room temperature tensile, or that the thermally activated deformation process in retained B2 phase would not be significantly important to control creep deformation. Generally, 650°C creep seems to show a transient behavior between room temperature deformation and high temperature creep deformation above 760°C.

Evaluation of creep parameters

One of the most powerful means of establishing the controlling mechanism in creep deformation is based on a knowledge of the activation energy (Qc) and the stress exponent, n. Apparent temperature dependence of steady state creep rate was determined for the as-received microstructure between 650°C and 760°C at a constant stress of 30ksi, using the power law creep equation described previously, as shown in Fig.12. A creep activation energy of 305kJ/mol was obtained from a least-square calculation. Mendiratta and Lipsitt[6] measured the activation energy in Ti_3Al and Ti_3Al + 10w/o Nb in the temperature range of 550°C to 825°C, even though they failed to relate this data to the controlling mechanism because of the non-availability of diffusion data for α_2 alloys. They found that addition of Nb increased the activation energy from 206kJ/mol in monolithic α_2 to 285kJ/mol in α_2 + 10 w/o Nb which is relatively consistent with the present investigation, in the temperature range of 650°C to 825°C. It is , therefore, recognized

that more additions of β phase stabilizers do not affect creep activation energy significantly. In addition, from their work, it was found that the activation energy of the α_2+Nb alloy decreased to a value of 195kJ/mol below 650°C to 550°C, which shows the transition in mechanism. This observation can validate the fact that 650°C creep in the present investigation shows the transient deformation behavior between room temperature and high temperatures above 760°C.

The obtained stress exponents "n" indicate that the creep process is dominated by the generation and movement of dislocations in the test regimes studied. These exponents are generally within the range of values (n=3 - 5) predicted by theoretical models[17] of dislocation controlled creep which depend on the detailed dislocation hardening and recovery process. In Fig.13, stress dependence of steady state creep rate was obtained as a function of temperature with the use of as-received microstructure (fine Widmanstatten). It is pointed out that there is a tendency to decrease "n" as temperature is increased and at very high temperature (870°C), a transition in mechanism might occur, even though a very clear change in "n" value is not shown (n=2.8 - 3.5). It is believed that with increasing temperature, emergence of grain boundary sliding would occur and thus the exponent, n decreases. Eventually, it is apparent that two dominant mechanisms are operative at the test temperature of 870°C. At 870°C and high stresses, grain boundary sliding is occurring accommodated by power law creep, while at low stresses, the lower exponent indicates that grain boundary sliding may be accommodated by a diffusional creep process.

Mandiratta and Lipsitt[6] also obtained the stress exponents for temperatures varying from 650°C to 800°C in Ti_3Al + 10 w/o Nb. As consistent with the present results, a transition in mechanism was found for both intermetallics above around 700°C; for Ti_3Al, 4.5 to 2.5 and for Ti_3Al + 10 w/o Nb, 6.5 to 2.5. However, in contrast to the present investigation, the data for all temperatures could be represented by nearly parallel straight lines at high stresses, indicating temperature independence of the stress exponent.

In Fig.14, creep behavior of Ti-25-10-3-1 is compared at 650°C and 760°C with those of two near-α titanium alloys; Ti-6242S and Ti-1100 which is the most newly developed alloy to improve creep resistance with larger amount of Si(0.45%) and smaller amount of β phase stabilizers. For the comparison, the optimum microstructure (colony) was used for all alloys. Generally, creep resistance of Ti-25-10-3-1 is much improved by

one order of magnitude over Ti-1100 and even much more, two orders of magnitude over Ti-6242S. Unlike near-α alloys, a transition in mechanism in Ti-25-10-3-1 was not found at 760ºC in the similar stress range studied.

(5) Fracture modes and dislocation structures

Fractography

Fig.15 shows the influence of cooling rate on tensile fracture mode (β/AC, β/CC, β/SC). As the cooling rate is increased (the amount of retained β phase is increased), a ductile fracture mode becomes increasingly evident. In basketweave and colony microstructures, fracture modes were found to be consistent with microstructural unit. The ridges of the ductile tearing are seen to be lie along the length of the ordered β phase film, parallel to the α_2/B2 interfaces, while the fracture is totally cleavage in the α_2 plate.

Creep fracture modes were investigated at 650ºC and 760ºC for the as-received microstructure, as shown in Fig.16 and Fig.17. At 650ºC (Fig.16), a similar transgranular mode of failure was found as that of room temperature. However, at the edge of the specimen, fine dimples for overload fracture were found. At 760ºC (Fig.17), it was observed that creep ductility increased very rapidly and an increased tendency for intergranular cracking was recognized. This observation is quite consistent with previous findings in Ti$_3$Al.[13] In addition, at 760ºC, larger dimples than those in 650ºC crept specimens were found around the edge of specimens.

Dislocation structures

Thin foils prepared from the gage sections of the room temperature tensile and elevated temperature crept samples (β/SC) were examined to establish the associated slip character. Fig.18 shows the room temperature tensile deformation mode in which ao/3 <1120>, ā type dislocations are predominant. A slip trace analysis indicates high degree of slip planarity on prism planes and some evidences of basal slip bands . In addition, some extended faults were found. At high temperatures, cross slip of ā dislocations between the basal, prismatic and pyramidal planes, which is difficult at low temperatures, is easier to

accomplish, as shown in Fig.19. At all temperatures, most of the dislocations are homogeneously distributed.

In addition to $\bar{a}$ type dislocations, a moderate number of fairly straight dislocations with non-basal Burgers vector which are in contrast with g_{0002} were found at all temperatures. Increasing temperature did not significantly change the mode and occurrence of these dislocations.

IV. SUMMARY

1.   The influence of microstructure on creep behavior of Ti-25Al-10Nb-3V-1Mo (a/o) has been determined as a function of stress and temperature (650°C - 870°C). In addition, room temperature tensile properties were characterized as a function of strain rate.

2.   Generally, increasing cooling rate from β solution treatment temperature increased room temperature tensile strength and ductility. The strain rate dependence of room temperature tensile strength was dependent on microstructure.

3.   At theses high temperatures, β solution treated microstructure exhibited superior creep resistance compared to $\alpha_2+\beta$ processed microstructure. ($\alpha_2+\beta$/SC vs. β/SC)

4.   Moreover, a pronounced influence of cooling rate from the β solution treatment temperature on creep was observed. At 760°C, β/SC (colony) was proven to be an optimum microstructure for creep resistance at all stresses studied. However, at 650°C, a somewhat complicated effect that depends on stress level was found. At this temperature, β/SC shows superior creep performance only at relatively low stresses. It is believed that 650°C creep shows transient deformation behavior between room temperature and elevated temperature behavior.

5.   Increasing temperature decreased the stress exponent "n" and caused a transition in creep mechanism at 870°C, depending on stress level. The obtained exponents are generally within the range of values predicted by theoritical models of dislocation controlled creep. A creep activation energy of 305 kJ/mol was measured in the temperature range of 650°C to 760°C.

6.   Creep resistance of Ti-25-10-3-1 is much improved by one order of magnitude in steady state creep rate over Ti-1100 which is most newly developed near-α titanium alloy

and even much more, two orders of magnitude over Ti-6242S, in the test regimes studied, when the optimum microstructure (colony) is used for all alloys.

References

1. H.A.Lipsitt; Mat. Res. Soc. Symp. Proc. Vol.39, 1985, p.351
2. M.J.Blackburn and M.P.Smith; Technical Report, AFWAL-TR-82-4036, 1982
3. W.Cho, J.W.Jones, J.E.Allison and W.T.Donlon; Proc. of Sixth International Conference on Ti, Cannes, France, 1988 (In-printing)
4. P.A.Blenkinsop, D.F.Neal and R.E.Goosey; Titanium and Titanium Alloys, Prenum Press, 1976, p.2003
5. M.G.Mendiratta and N.S.Choudhury; Technical Report, AFML-TR-78-112, 1978
6. M.G.Mendiratta and H.A.Lipsitt; Journal of Meterials Science, Vol.15, 1980, p.2985
7. R.Strychor, J.C.Williams and W.A.Soffa; Met. Trans. Vol.19A, 1988, p.225
8. J.C.Williams and G.Lütjering; Proc. of Fourth International Conference on Ti, 1980, p.671
9. A.Gysler and G.Lütjering; Met. Trans., Vol,13A, 1982, p.1435
10. F.S.Lin, E.A.Starke, Jr.,S.B.Chakrabortty and A.Gysler; Met. Trans. Vol.15A, 1984, p.1229
11. M.J.Blackburn, D.L.Ruckle and C.F.Bevan; Technical Report, AFML-TR-78-18, 1978, p.68
12. G.Sridhar, V.V.Kutumbarao, and D.S.Sarma; Met. Trans., Vol.18A, 1987, p.877
13. H.A.Lipsitt, D.Shechtman and R.E.Schafrik; Met. Trans., Vol.11A, 1980, p.1369
14. J.K.Tien, S.Eng and J.M.Sanchez; High Temperature Ordered Intermetallic Alloys II, MRS, Vol.61, 1987, p.183
15. G.R.Leverant, M.Gell and S.W.Hopkins; Mater. Sci. Engn., Vol.125, 1971, p.125
16. W.Cho; "Creep behavior of near-α titanium alloys", Ph.D Thesis, The University of Michigan, 1987
17. W.D.Nix and B.Ilschner; Proc. of 5th Inter. Conf. on Strength of Metals and Alloys, 1979, p.1507
18. W.Cho, J.W.Jones and J.E.Allison; Unpublished Research, 1987.

Fig. 1　As-received microstructure and thermal stability: a) and b) optical and TEM micrographs of as-received microstructure, c) after aging of 100hrs. at 760°C.
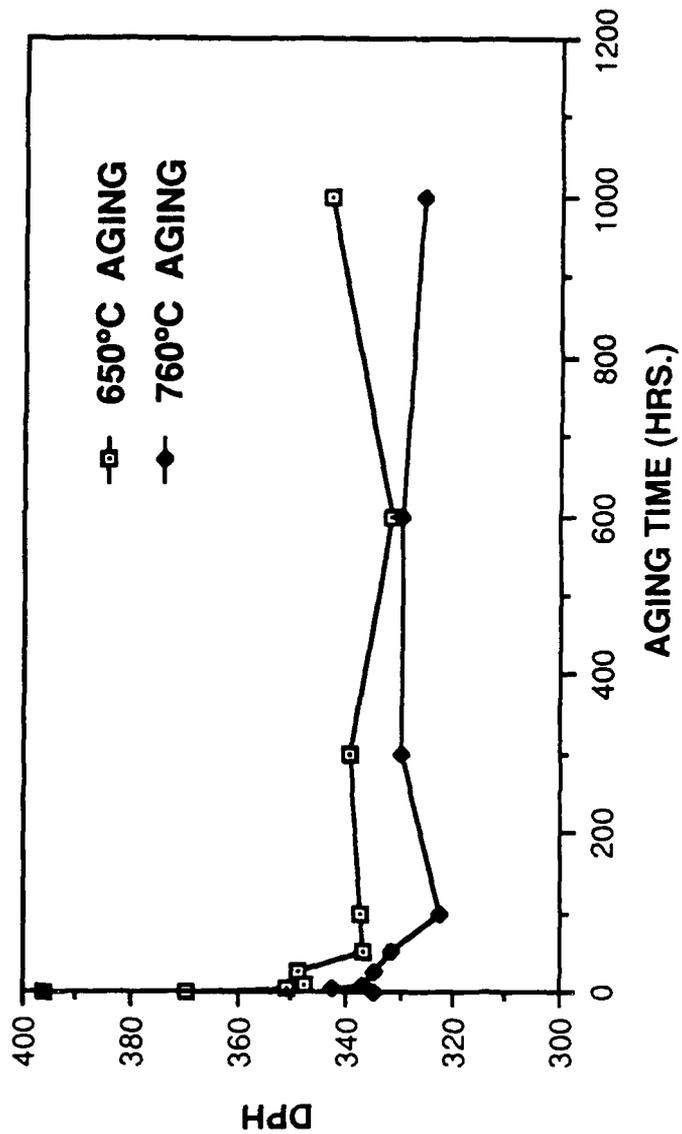
Fig. 2   Influence of thermal exposure on room temperature micro-hardness for the as-received microstructure (very fine Widmanstatten).

AIR COOLING (10C/Sec)   CONTROLLED AIR COOLING   SLOW COOLING (0.1C/Sec)
(0.5C/Sec)

Fig. 3   Effect of cooling rate from β region on microstructure: a) β/AC, b) β/CC, c) β/SC
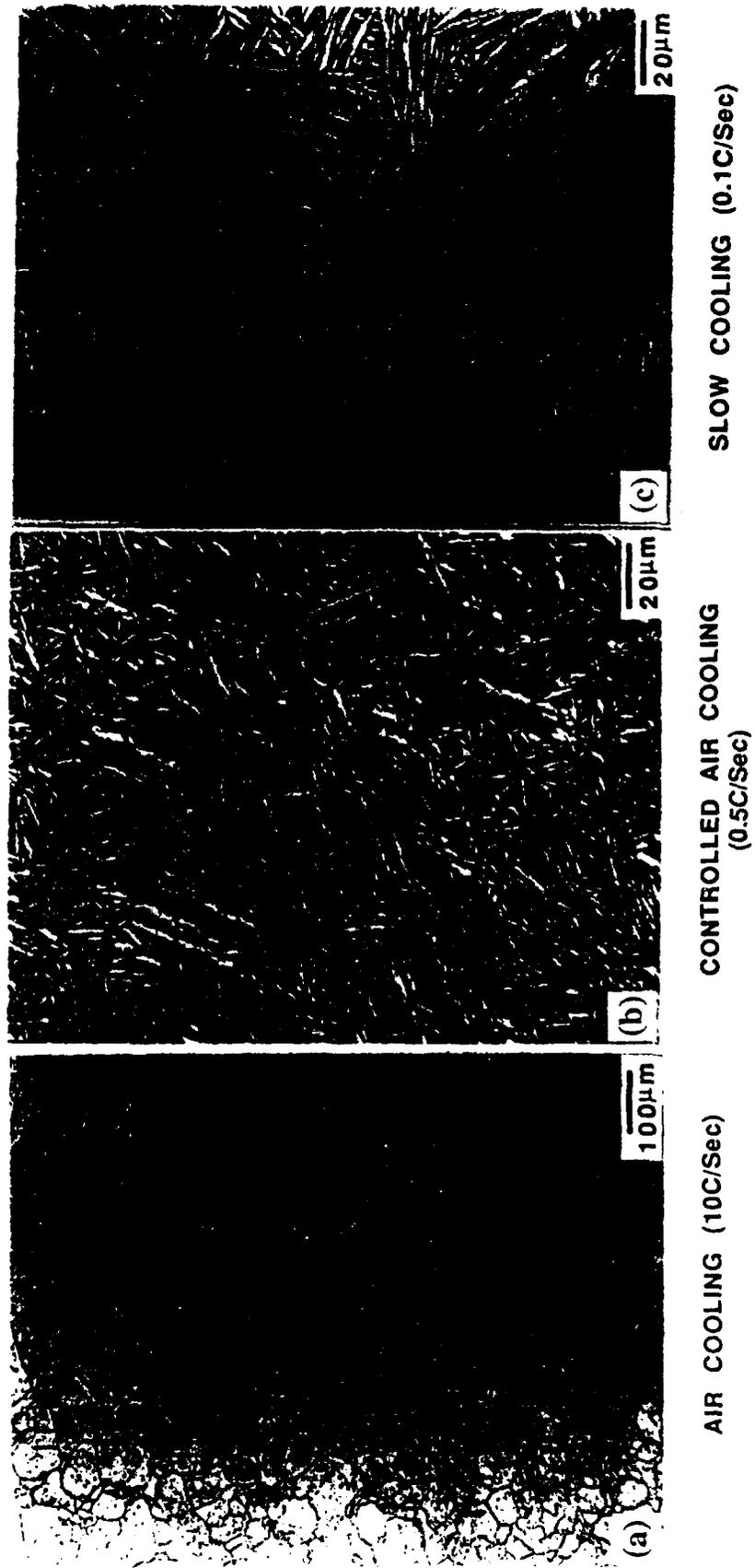
AIR COOLING (10C/Sec)   CONTROLLED AIR COOLING   SLOW COOLING (0.1C/Sec)
(0.5C/Sec)
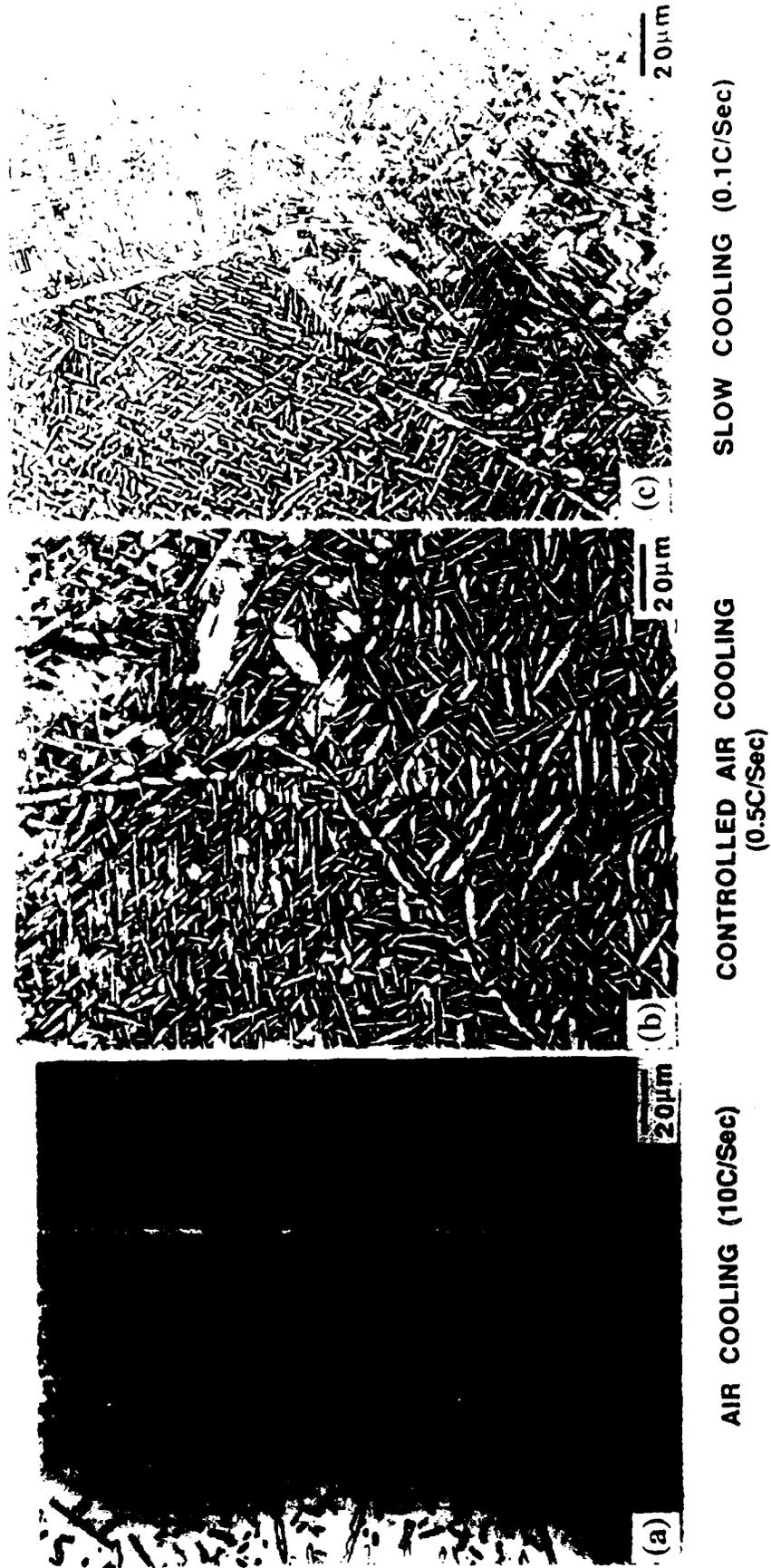
Fig. 4   Effect of cooling rate from $\alpha_2+\beta$ region on microstructure:
a) $\alpha_2+\beta$ /AC, b) $\alpha_2+\beta$ /CC, c) $\alpha_2+\beta$ /SC
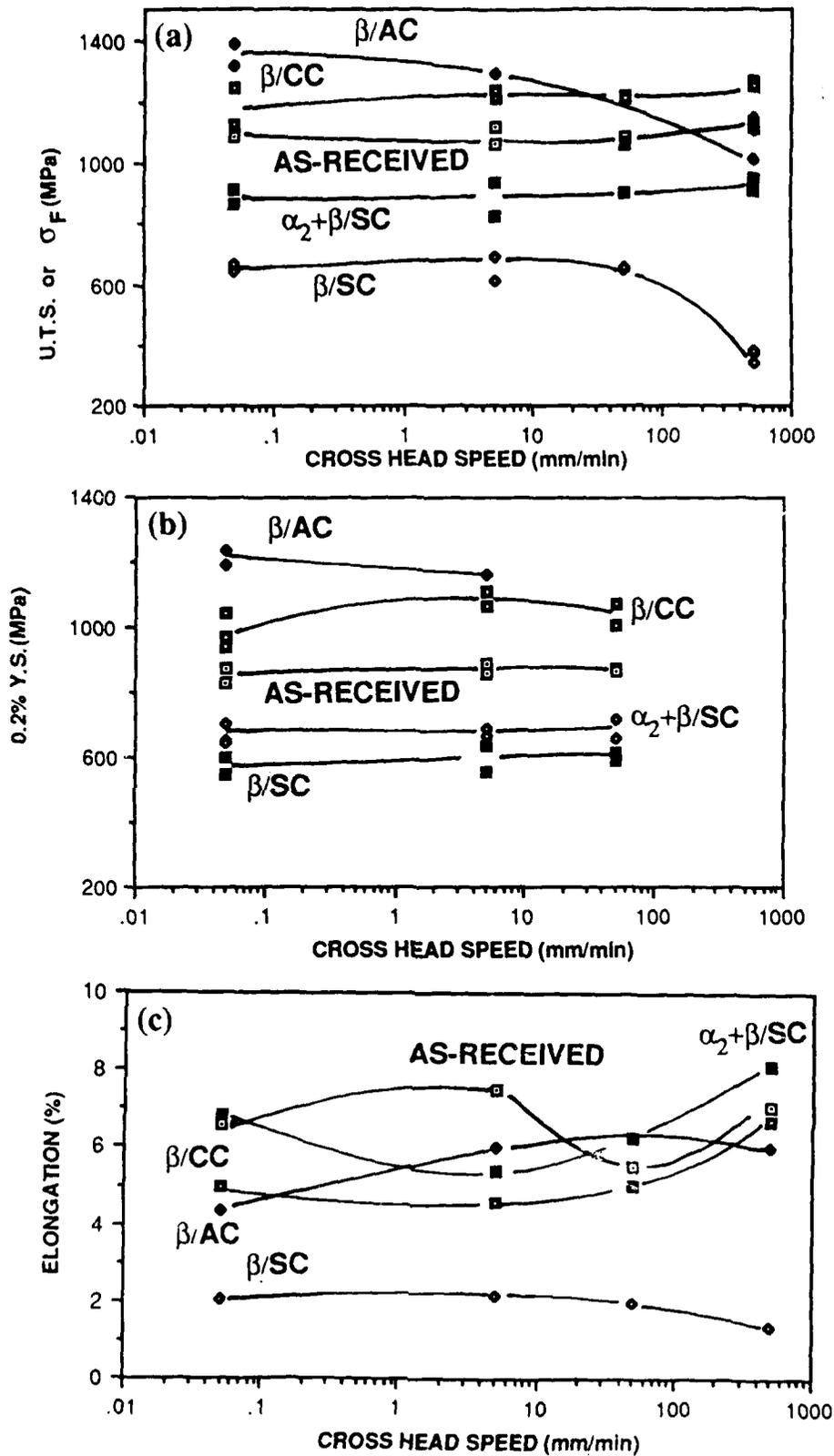
Fig. 5 Effect of microstructure on room temperature tensile properties:
a) U.T.S or σ_F, b) 0.2% Y.S, c) Elongation.
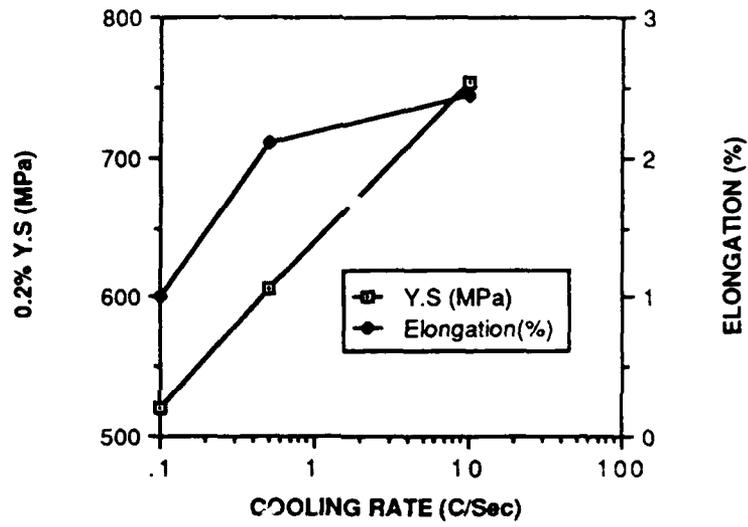
Fig. 6   Effect of cooling rate from β solution treatment on room temperature tensile properties.
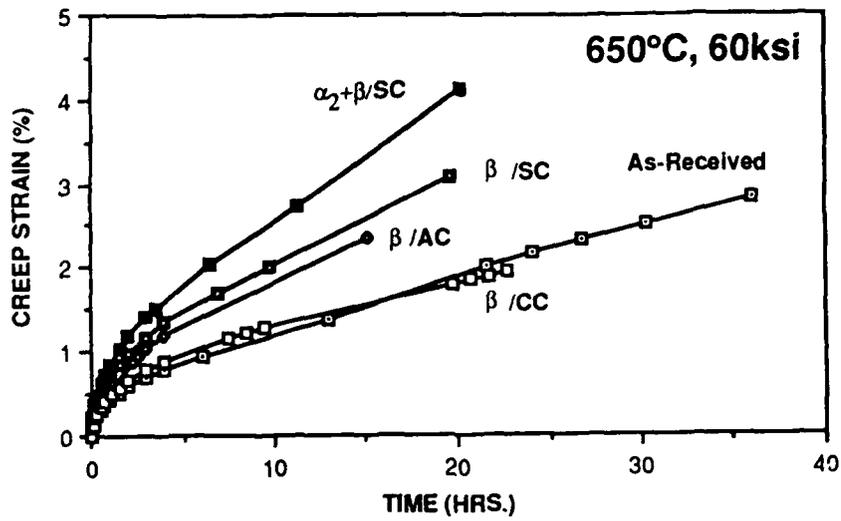
Fig. 7 Effect of microstructure on creep behavior   at 650°C/60ksi. .
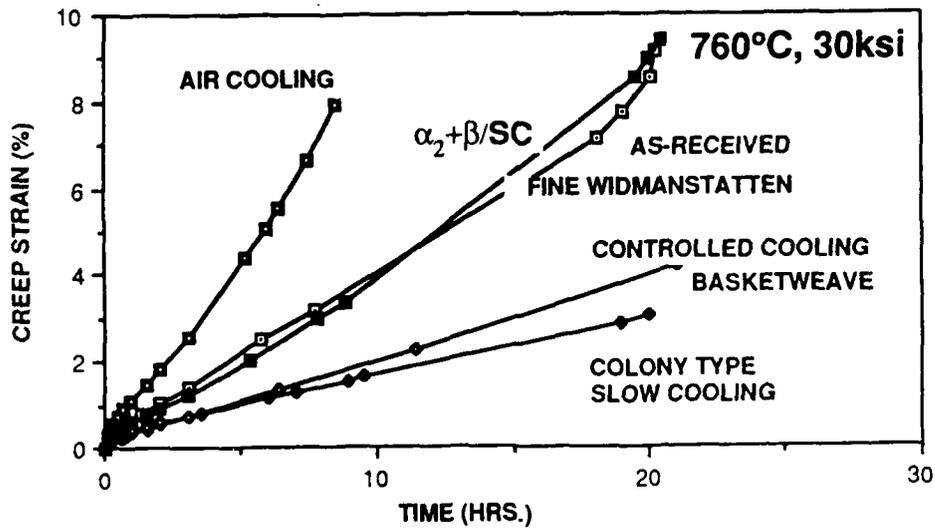
Fig. 8 Effect of microstructure on creep behavior at 760°C/30ksi.
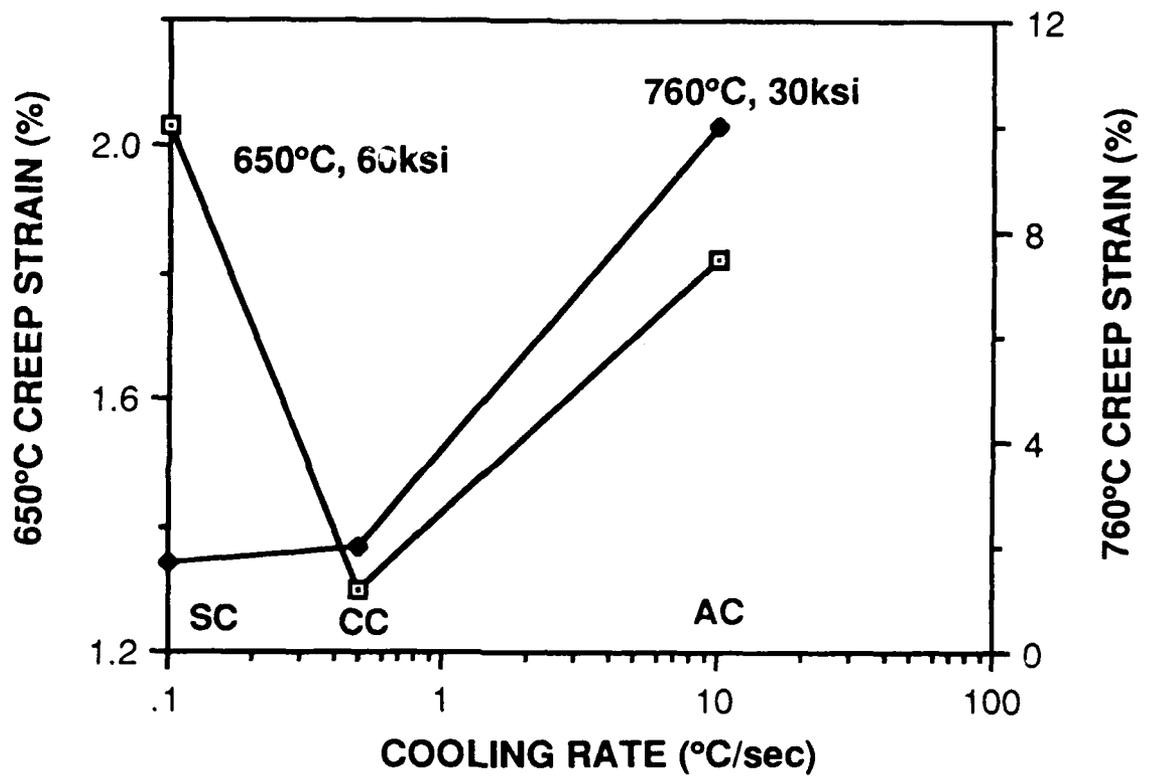
Fig. 9   Effect of cooling rate from β solution treatment on creep strain.
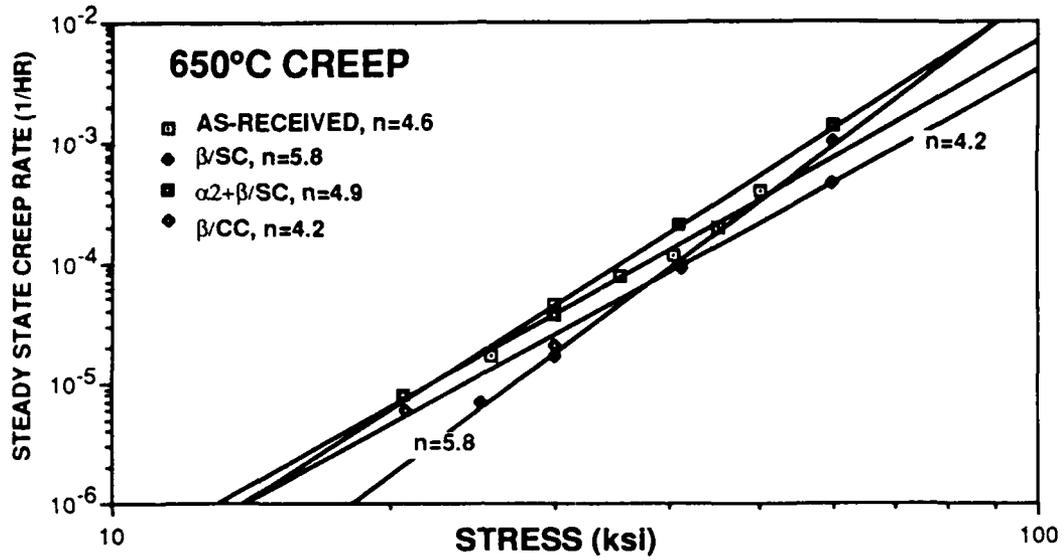
Fig. 10 Stress dependence of steady state creep rate at 650°C.
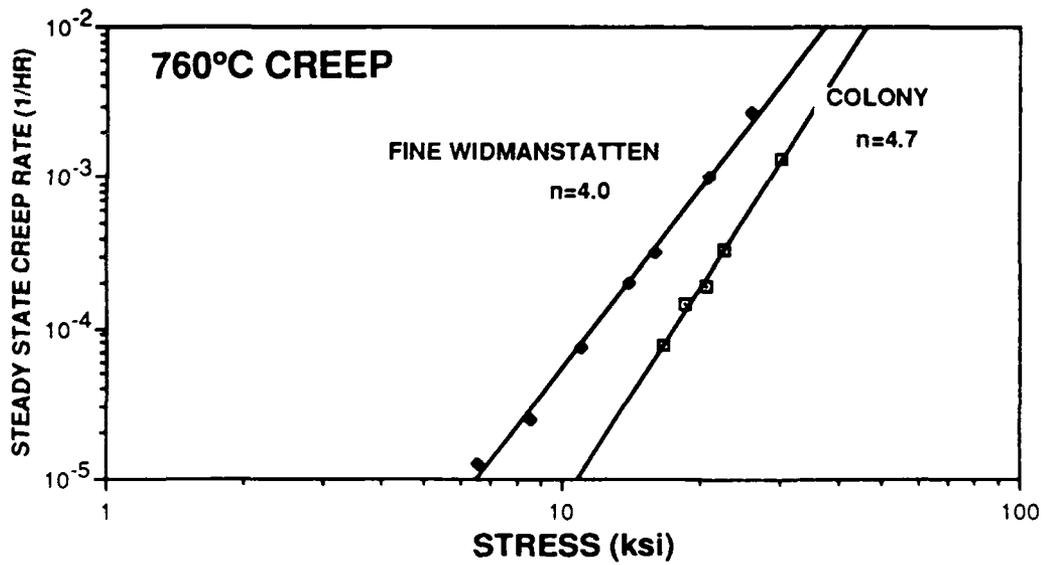
Fig. 11 Stress dependence of steady state creep rate at 760°C.
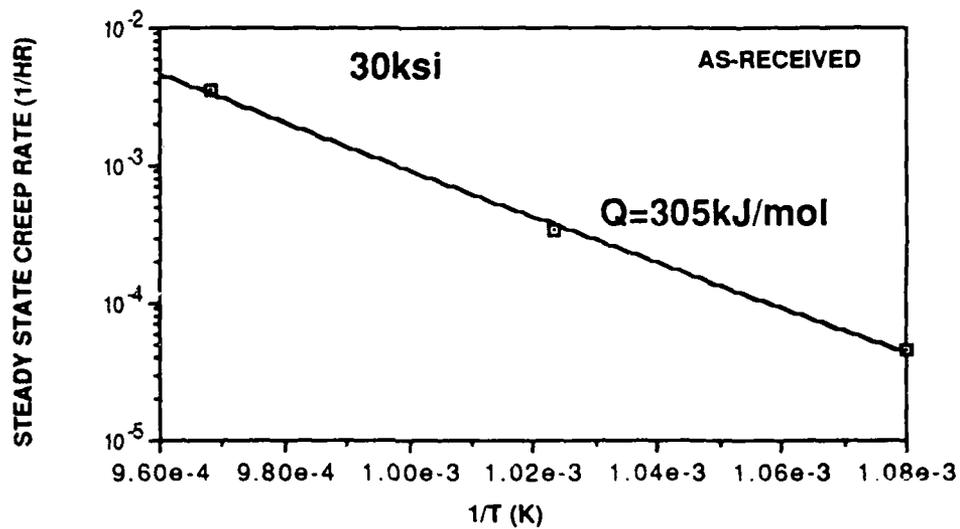
Fig. 12 Temperature dependence of steady state creep rate of as-received microstructure in the range of 650°C to 760°C.
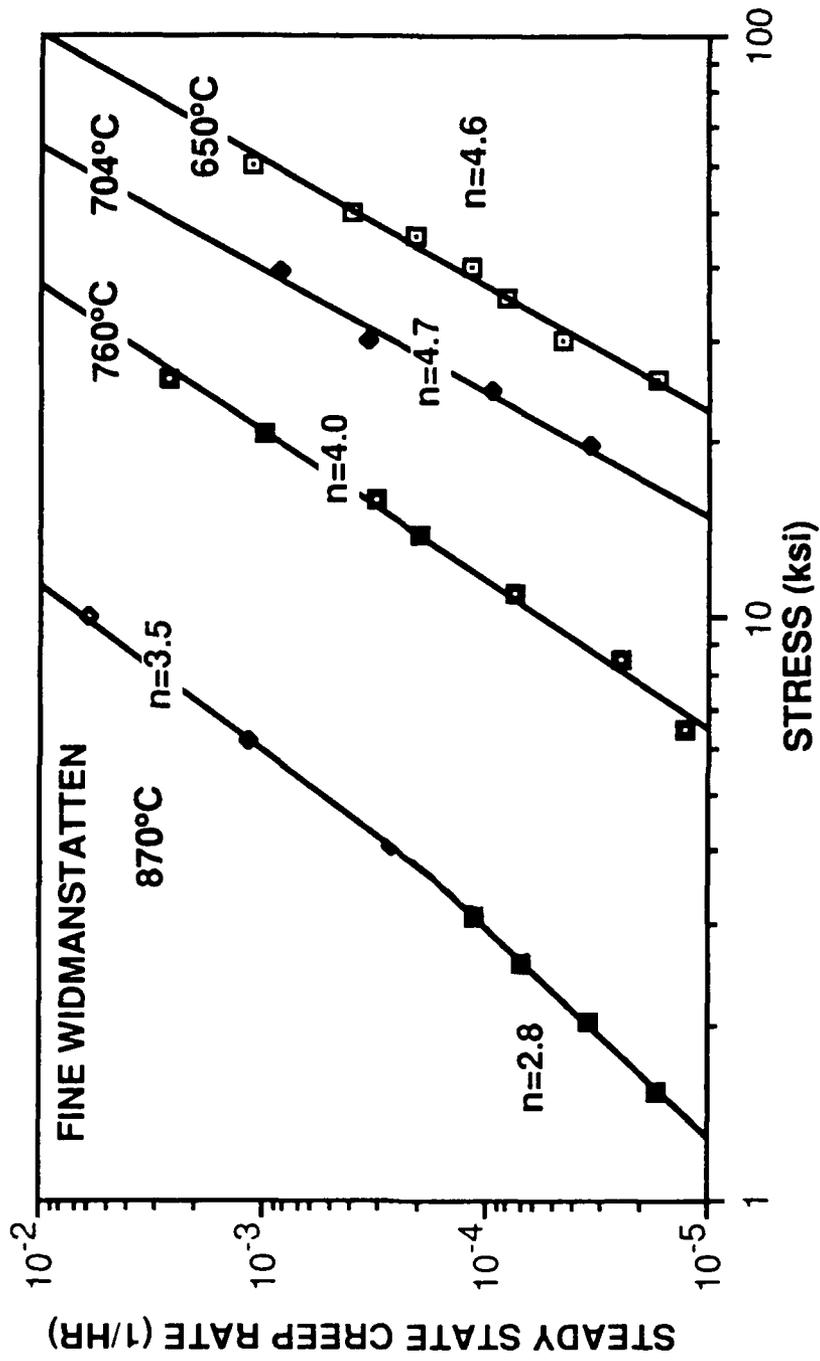
Fig. 13 Stress dependence of steady state creep rate of as-received microstructure as a function of temperature.
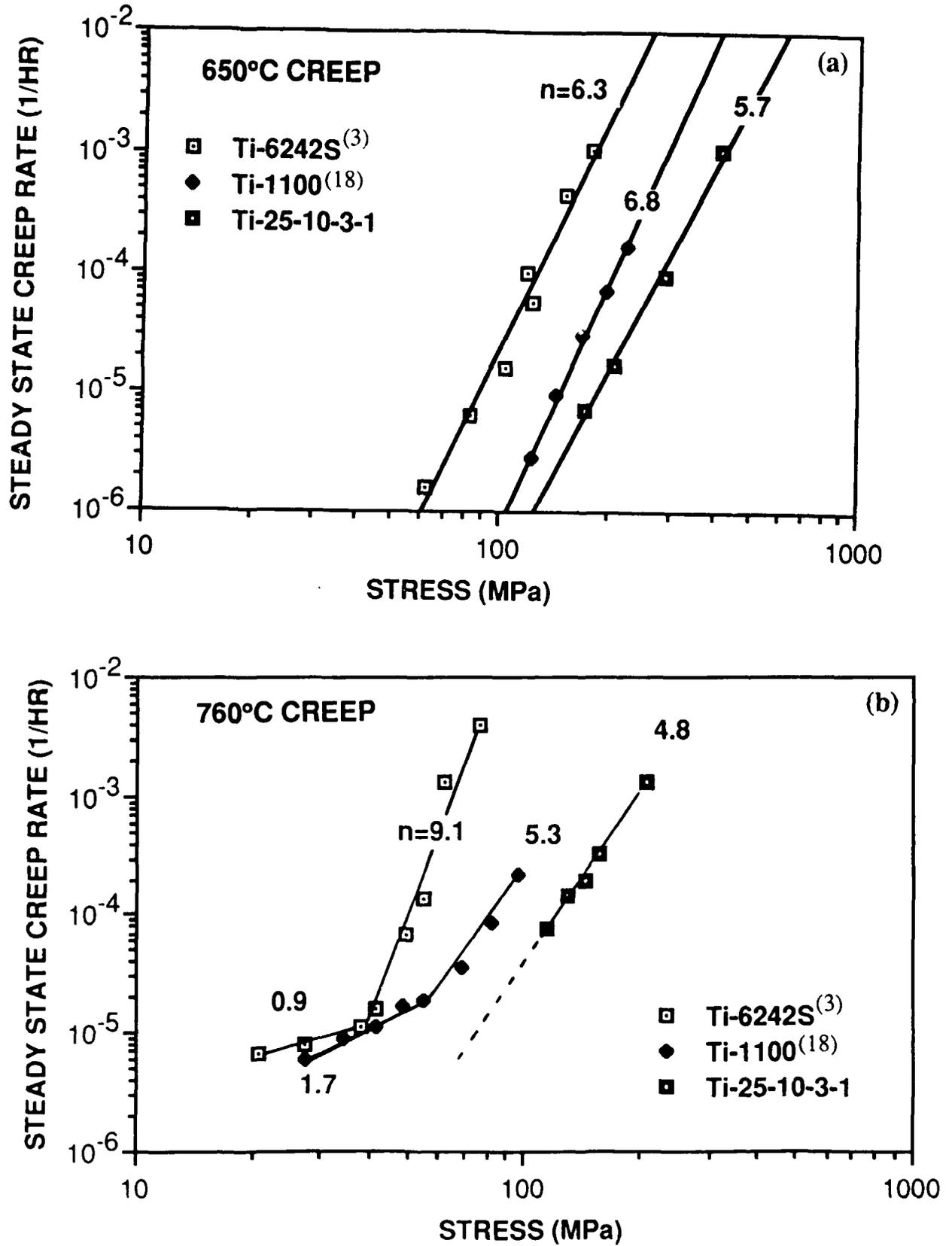
Fig. 14 A comparison of creep behavior of Ti-25-10-3-1 with two conventional near-α titanium alloys (Ti-6242S and Ti-1100), using colony microstructure; a) 650°C creep, b) 760°C creep.

β/S C   β/CC   β AC
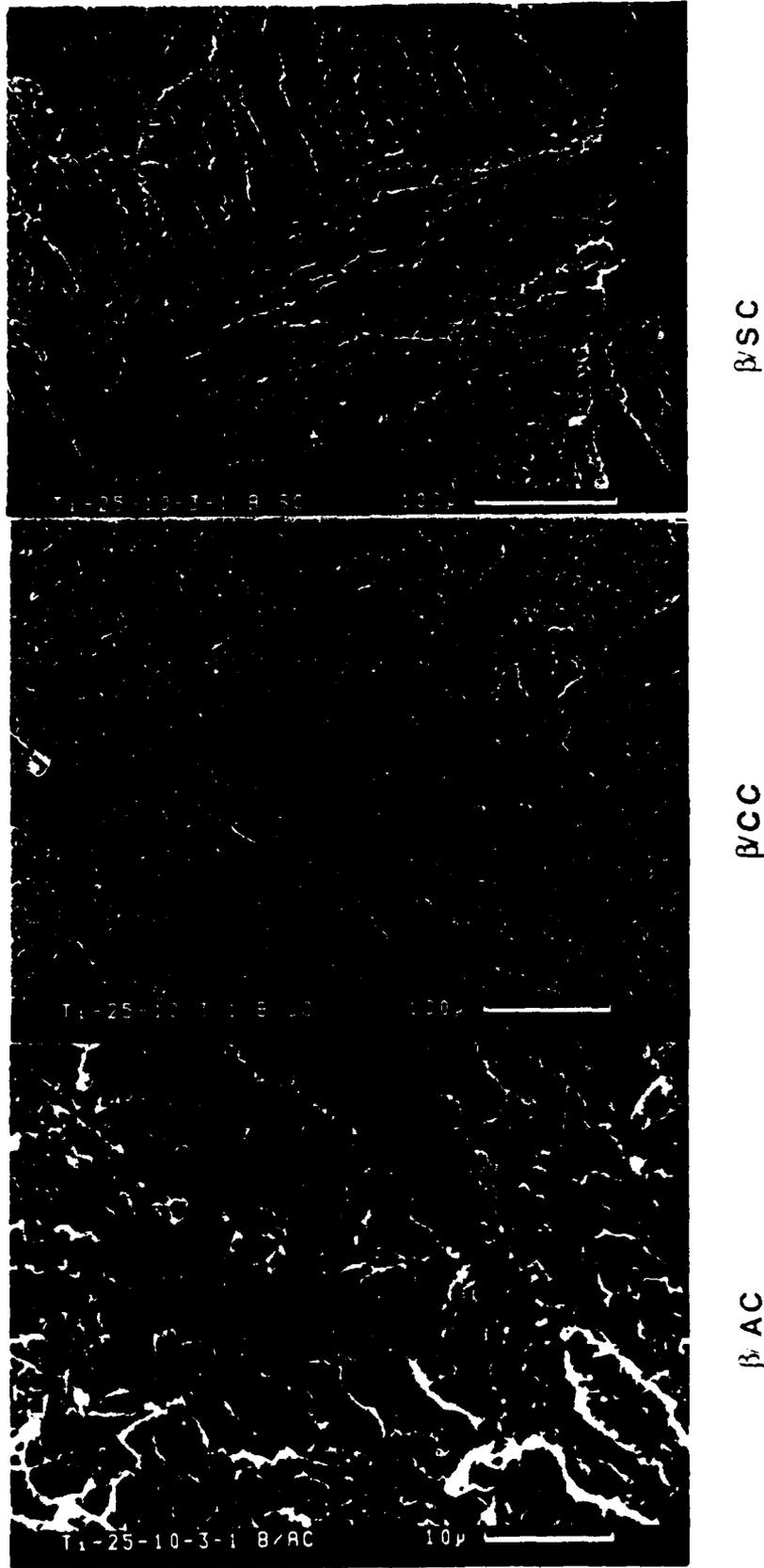
Fig. 15   Effect of cooling rate on room temperature tensile fracture mode.
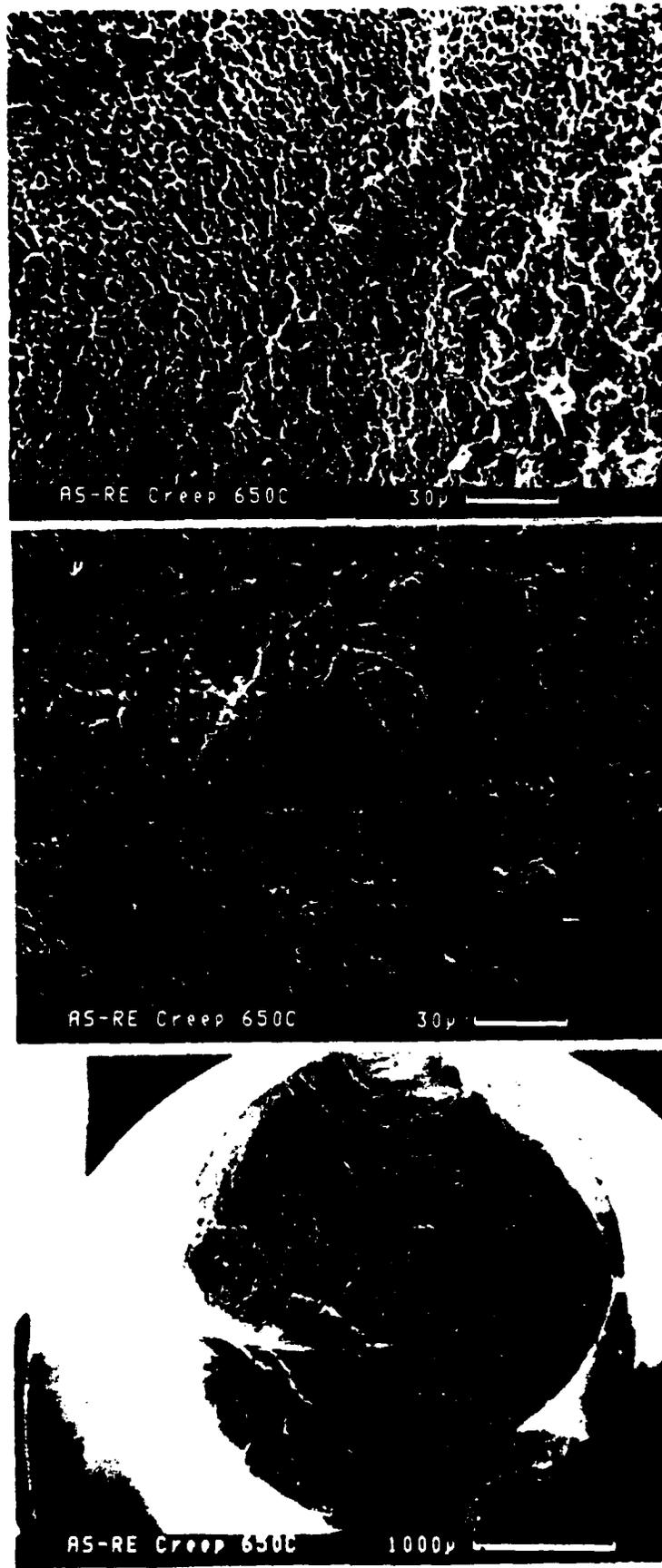
Fig. 16   High temperature creep fracture mode at 650°C (as-received microstructure).

AR 760C 15K CREEP 10μ

AR 760C 15K CREEP 10μ

AR 760C 15K CREEP 1000μ
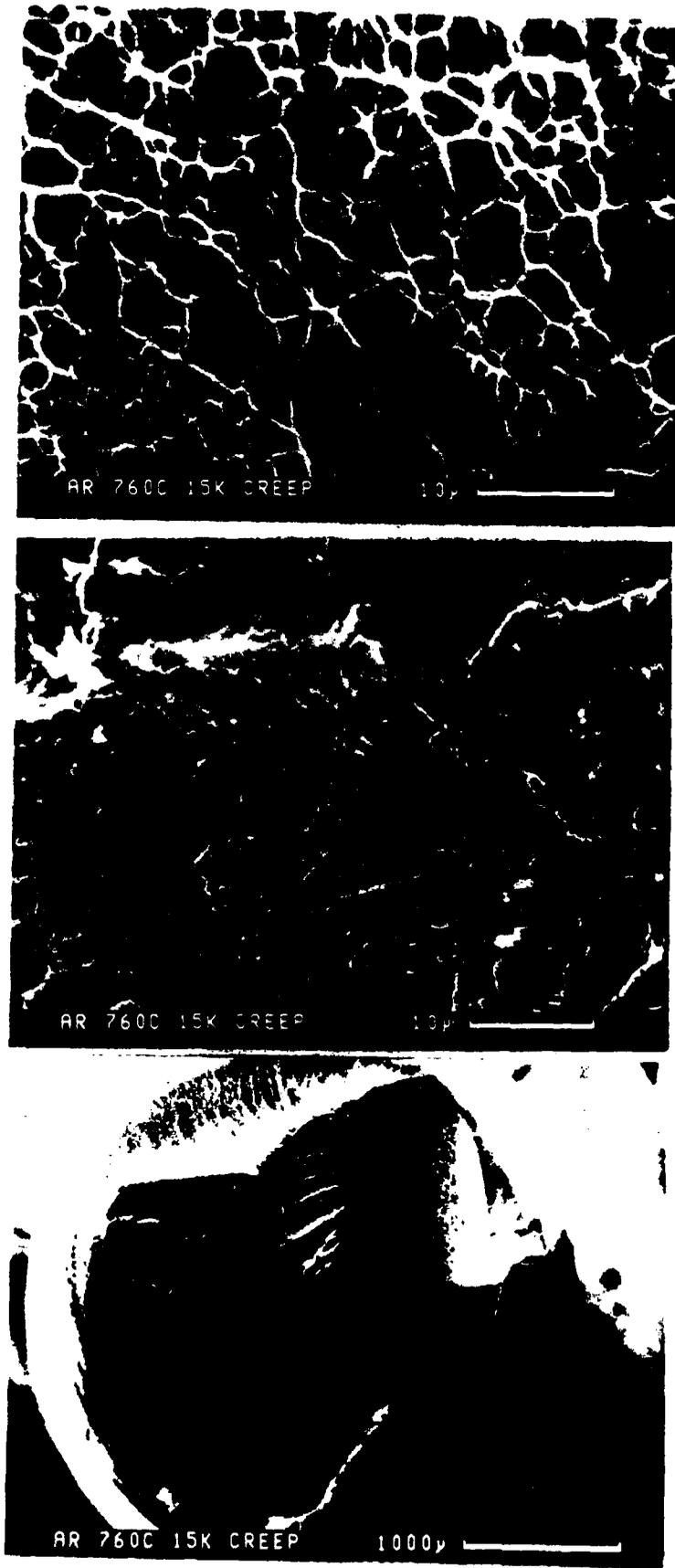
Fig. 17 High temperature creep fracture mode at 760°C (as-received microstructure).
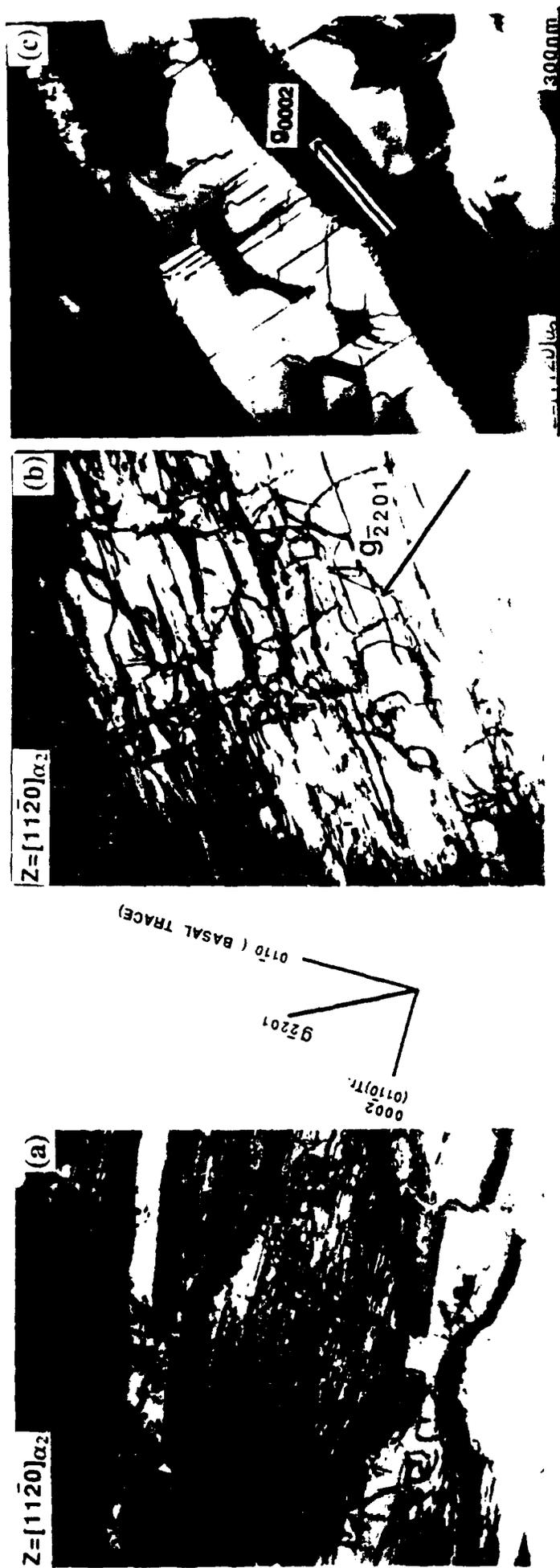
Fig. 18 TEM showing room temperature tensile deformed dislocation structures:
a) overall slip mode, b) higher magnification of a). c) dislocations with non-basal Burgers vector.

Fig. 19 TEM showing elevated temperature creep deformation: a) 650°C , b) 760°C c) dislocations with non-basal Burgers vector in 760°C crept sample.

THERMAL AND MECHANICAL HISTORY EFFECTS

W. M. Garrison and D. Symons

I. Introduction

An important factor in the design of materials for high temperature service is that their microstructures will not be altered during service in a manner which would impair their mechanical properties. It is possible that prolonged exposure at elevated temperatures during service could alter the microstructure in such a way as to degrade mechanical properties. Further, especially in the case of high temperature composite materials, there is the possibility that service stresses could enhance high temperature microstructural changes as well as introducing damage or defects during creep deformation of the material. The broad objectives of this program are to investigate how and to what extent service temperature and stresses degrade the microstructure, strength and fracture behavior of high temperature materials, particularly composites, and to model the observed fracture behavior in terms of the microstructures and the micromechanisms of the fracture process. In this summary the following topics will be considered. First, the materials selected and the rationale for their selection will be discussed. Second, we will discuss the fracture behavior of these materials and how various microstructural parameters may influence the fracture process. Next the importance of rigorous microstructural control in this work will be emphasized and studies designed to permit this microstructural control and perhaps to allow independent variation of the key microstructural variables will be discussed. Finally initial results concerning the effect of microstructure and test temperature on tensile properties and fracture mode will be presented as will be the effects of long time aging on strength and ductility.

II. Materials Selection

The focus of this work will be monolithic titanium aluminides. While composite aluminides would be desired, such materials are simply not available in the quantities desired except at great, and for this program, prohibitive cost. Monolithic alloys, while

expensive, have been prepared for this program. The selection of compositions for study has been guided by a large body of information which suggests that both strength and tensile ductility of the Ti3Al materials can be substantially improved by substituting niobium for the titanium. The data of Blackburn (2) shown in Table I shows that at 425°C the yield strength and tensile ductility of titanium aluminide air cooled from the solutionizing temperature increased from 69 ksi to 97 ksi and 1.4% to 8%, respectively, as the niobium content was increased from 11 to 15 atomic percent. According to our reading of the literature the beneficial effects of niobium on both strength and ductility have not been carefully examined and are not understood. Accordingly we have ordered three heats of aluminide material: Ti-24Al-11Nb, Ti-24Al-15Nb and Ti-24Al-19Nb. While there was difficulty in preparing these materials two of the three heats appear to be usable, having compositions of Ti-24Al-11Nb and Ti-24Al-17Nb.

III. Program Objectives

The specific objectives of this program are the following. They are first to understand how niobium additions influence the strength, tensile ductility and fracture toughness as a function of test temperature. Second they are to investigate the degree to which the initial microstructures and their associated mechanical properties are degraded by prolonged exposure to high temperatures and high temperatues in combination with high stresses.

IV. Microstructure and Mechanical Properties

Niobium additions apparently can influence both the strength and the fracture behavior of Ti3Al material (1-3). Niobium additions can unfortunately introduce a variety of microstructural changes which may influence the mechanical properties. Assuming for the present that the structure with or without the niobium is a Widmanstatten structure of α_2 plates formed by the transformation of the β during either isothermal or continuous transformation, the available phase diagrams (4,5) suggest niobium will lead to an increased amount of β in the structure, with the caveat that the β may become ordered (6).

Further the niobium may also increase the amount of c+a slip in the α_2 (2). Finally the niobium additions could possibly result in a finer α_2 plate size if a constant transformation path is used. (We suggest this possibility based on our results which suggest the α_2 plate size can significantly influence the yield strength at constant niobium level and the known influence of Nb on strength.)

While the effect of niobium on strength may be related to its effect on α_2 plate size it is possible that the improvement in tensile ductilities with increasing niobium content may be due to any (or possibly to some extent all) of the above possible microstructural changes. The titanium aluminides appear to fracture by a cleavage related process. Therefore niobium could possibly improve the ductility by increasing the amount of the second phase (presumed and likely to be ductile). It has also been suggested that increasing the niobium will increase the amount of c+a slip and this will result in greater uniformity of strain and an improvement in ductility. Finally the possible refinement of α_2 plate size by niobium additions could improve resistance to cleavage type fracture by increasing the cleavage fracture stress. Thus to understand how niobium additions alter fracture behavior it would be desirable to vary these microstructural variables, amount of second phase, degree of c+a slip and α_2 plate size independently. If this is to be done it is important to understand how niobium influences the transformation characteristics of the titanium aluminide.

V. Microstructural Evolution

It is possible to vary the microstructures of the Ti_3Al type aluminides extensively by varying the solution treatment temperature and the temperature-time path used to cool from the solutionizing temperature. Our first instinct is to solutionize in the single phase β field and select the solutionizing temperature for each alloy so that the β grain size is a constant. Thus the microstructure will be varied by changing the cooling path from the solutionizing temperature. In selecting heat treatments for the alloys with the goal of varying microstructural parameters independently it is necessary to determine how various cooling

paths will influence the microstucture. Preliminary work of this type has been carried out for Ti-24Al-11Nb using a heat of the composition given in Table 2.

In this work the alloy was solution treated for 45 minutes at 1200°C and then transformed isothermally or by continuous cooling. The isothermal transformation temperatures investigated were 700°C and 400°C, both as a function of time. The continuous cooling was done by an air cool and a control cool which was ten times slower than the air cool. As shown in Fig. 1, for the 700°C isothermal the isothermal transformations were extremely rapid and are almost 50% complete after one minute. As shown in Figure 2, lowering the isothermal transformation from 700°C to 400°C led to marked refinement of the microstructure. For both transformation temperatures the microstructure was a Widmanstatten structure of α_2 plates. Air cooling produced a Widmanstatten microstructure almost identical to the microstructure after isothermally transforming at 700°C. The slower control cool resulted in a colony microstructure as shown in Fig. 2.

VI. Mechanical Properties

The room temperature tensile properties of the microstructures associated with the two continuous cooling paths and the 700°C (20 min.) and 400°C (20 min.) isothermal transformations are listed in Table 3. The 400°C isothermally transformed material has the highest yield strength, 138 ksi, which is 52 ksi greater than the yield strength of the 700°C isothermally transformed material. This higher strength of the 400°C isothermally transformed material is coincident with a dramatic reduction in α_2 plate size. The material transformed during air cooling has almost the same microstructure as the 700°C isothermal and almost the same yield strength. The control cool and the as-received material, both of which have colony type microstructures, have the lowest yield strengths. In addition to the tensile properties cleavage fracture stress has been measured for the above microstructures except for the as-received material. The fracture stress was taken as the maximum tensile stress at fracture of a single edge notch bend specimen containing a notch of the geometry

used in Charpy impact specimens. These stresses are listed in Table 3. The fracture stress is lowest for the 700°C isothermal (141 ksi) and highest for the 400°C isothermal (338 ksi). Although the 700°C isothermal and the air cool microstructures appear very similar and have similar yield strengths, the fracture stress of the air cool microstructure is higher (217 ksi).

A fracture surface of the as-received microstructure is shown in Fig. 3. The fracture is cleavage or quasi-cleavage through the α_2 grains. Plateau etching suggests a second phase between the α_2 grains. The fracture surfaces of the control cool are very similar; as shown in Fig. 4. The cleavage facets are often relatively smooth and through steps join together to form relatively large regions where the fracture appears to follow the same crystallographic planes. The fracture surface of the air cool structure is much rougher as shown in Fig. 5 and as shown in Fig. 6, the fracture surfaces of the air cool and 700°C isothermal are very similar. The fracture surface of the 400°C isothermal is shown in Fig. 7 and exhibits only rarely large facets which can be unambiguously identified with cleavage or quasi-cleavage.

The tensile properties have been measured as a function of room temperature for the microstructure obtained after isothermal transformation at 700°C for twenty minutes. These tests differed from the previous tensile tests in that the specimen diameters were smaller by a factor of two (0.25 inches vs. .125 inches) and were carefully polished in the longitudinal direction to remove all circumferential machining scratches. The results are shown in Table IV. The ductilities, although small, did increase with test temperature. In addition, the tensile fracture stress remained constant with test temperature and was the same as the tensile fracture stress determined from the SENB specimens. However, the results of the room temperature tests were not in agreement with the previously determined room temperature tensile properties for this microstructure. While one might expect the tensile ductilities to be lower for the smaller specimens, the yield strength and fracture were higher for these specimens than for the previous specimens. Based on metallographic

examination at the optical level there was no difference in the microstructures. Therefore the differences in the yield strengths and fracture stresses are tentatively attributed to differences in sample preparation. These specimens were polished (polishing direction along the tensile direction) on the gage section until all machining scratches were removed; the previous specimens were polished, but the polishing direction was along the circumference of the gage section. Two sets of specimens have been prepared, one set polished longitudinally and the other transverse to the gage section to determine if specimen preparation could indeed account for these differences in properties.

III. Microstructural coarsening

Specimens of the material isothermally transformed for 20 minutes at 700°C were aged at 700°C for 316 hours. The microstructure was substantially coarsened by this aging treatment and the yield strength reduced to 62 ksi from 92 ksi prior to aging. These results suggest, given the similarity of the 700°C isothermal and air cooled microstructures, that the microstructures of conventionally prepared materials may coarsen readily with a resulting impairment of mechanical properties.

VIII. Future Work

Future work will focus on the two stated objectives: to understand how niobium additions influence strength, ductility and fracture toughness as a function of test temperature and to investigate the degree to which initial microstructures and their associated mechanical properties are influenced by prolonged exposure to service stresses and/or service temperatures. The materials will be Ti-24Al-11Nb and Ti-24Al-17Nb. The first goal will be to determine how microstructure evolves in the two alloys as a function of cooling path from the solutionizing temperature. This information will be used to select heat treatments for the two alloys which permit the most direct isolation of the three variables which may influence the fracture properties: α_2 plate size, the volume fraction of second phase and the amount of c+a slip. In addition these microstructures will be used to

assess microstructural stability during exposure to service stresses and/or service temperatures.

References

1. M.J. Blackburn and M.P. Smith, "Research to Conduct an Exploratory, Experimental and Analytical Investigation of Alloys", AFML-TR-80-4175, Aug. 1980.

2. S.M.L. Sastry and H.A. Lipsitt, *Met. Trans. A*, 1977, Vol. 8A, 1543.

3. C.F. Yolton, T. Lizzi, V.K. Chandok and J.H. Moll, *Titanium-Rapid Solidification Technology*, ed. by F.H. Froes and D. Eylon, TMS-AIME, Warrendale, PA, 1986, pg. 263.

4. O.N. Andreyev, *Russian Metallurgy*, 1970, Vol. 2, 127.

5. T.T. Nartova and G.G. Sopochkin, *Russian Metallurgy*, 1970, Vol. 2, 138.

6. D. Banerjee, A.K. Gogia, T.K. Nandi and V.A. Joshi, *Acta Met.*,

Table 1

Influence of Nb Additions on the Tensile Properties

for β Solutionized and Air Cooled Material Tested at 425°C[1]

Nb (At%)	Yield Strength (ksi)	Elongation (%)
0	68.8	1.4
11	76	6.5
15	97	8

Table II

Chemistry of Ti-24Al-11Nb Alloy Used In Preliminary Studies (at%)

<u>Ti</u>	<u>Al</u>	<u>Nb</u>	<u>C</u>	<u>O</u>	<u>H</u>
Bal.	25	11.1	0.17	0.18	0.34

Table III

Influence of Microstructure on the Room Temperature Tensile and

Single Edge Notch Bend Properties of Ti-24Al-11Nb

Heat Treatment	Microstructure	Yield Strength (ksi)	Elongation (%)	SENB σ_f (ksi)
400°C Iso.	Fine Widmanstatten	138	1.6	338
700°C Iso.	Coarse Widmanstatten	87	1.4	141
Air Cool	Coarse Widmanstatten	92	3.0	217
Control Cool	Colony	67	0.8	156
As Received	Colony	78	1.4	-

Table IV

Influence of Test Temperature on the Tensile Properties of the

700°C Isothermal Microstructure

Test Temperature	Yield Strength (ksi)	Fracture Stress (ksi)	Elongation (%)	Dimple Diameter (µm)
R.T.	141	141	0.18	0.71
300°C	128	140	0.5	1.16
500°C	115	137	1.9	1.4

0 sec

30 sec

60 sec
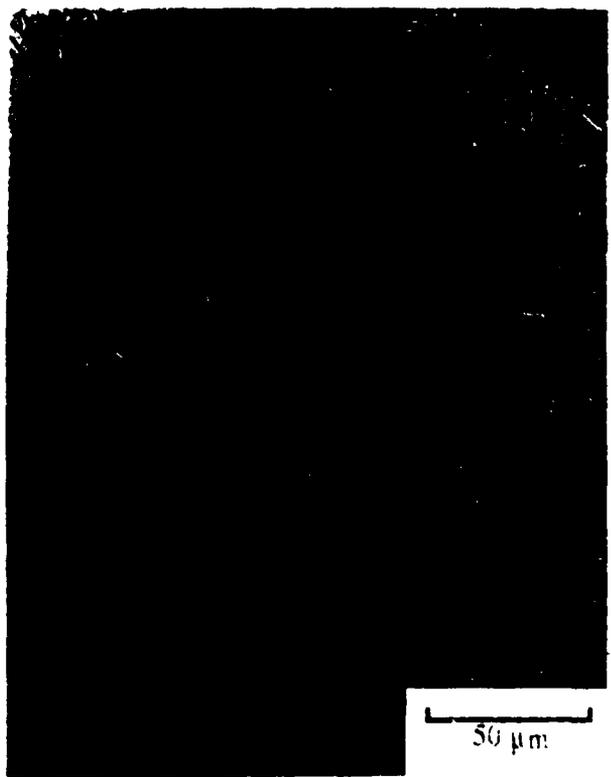
20 min

Fig. 1   Microstructures obtained after (a) quenching directly from the solutionizing
temperature and after isothermally transforming for (b) 30 sec., (c) 60 sec.
and for (d) 20 min.
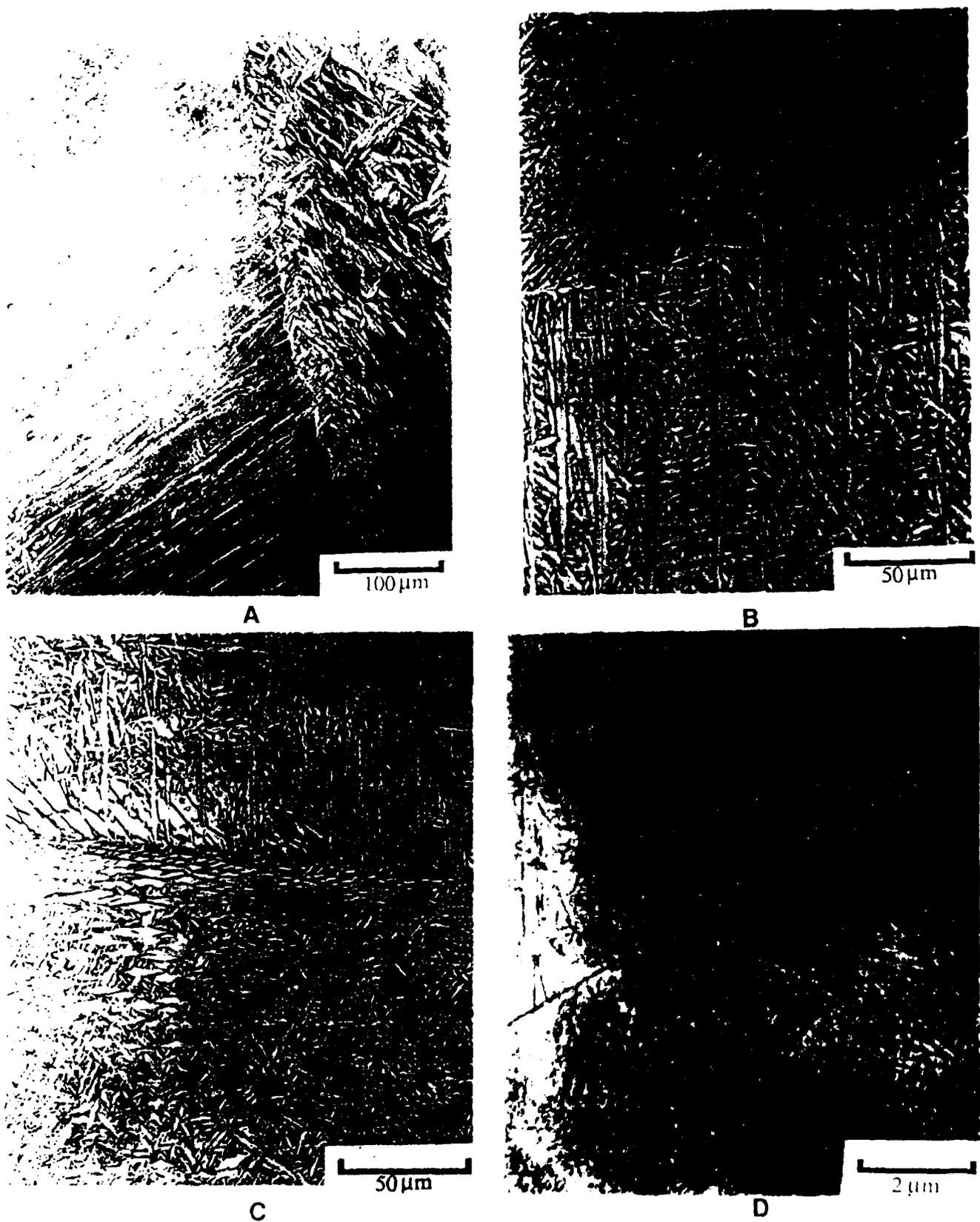
Fig. 2   Microstructures obtained by (a) control cool, (b) air cool, (c) isothermally transforming for 20 min. at 700°C and (d) isothermally transforming for 20 min. at 400°C.

Fig. 3   Fracture surface as as-received material which has been plateau etched.
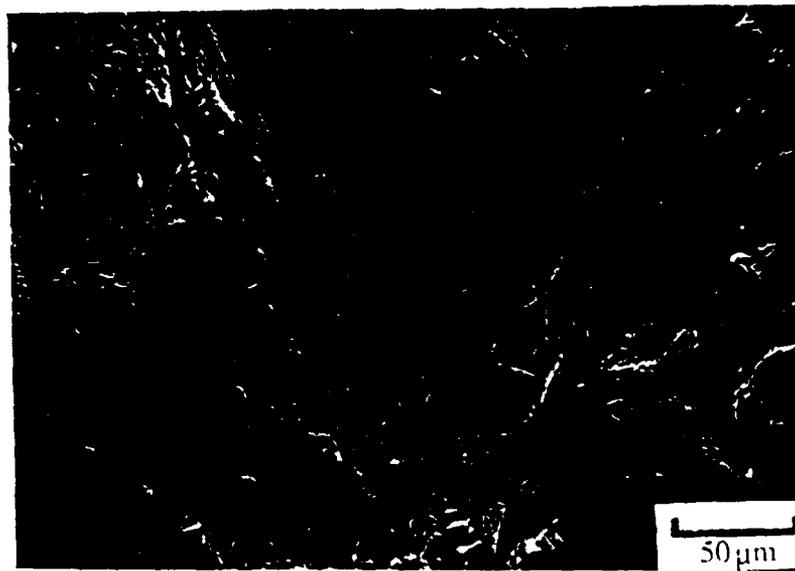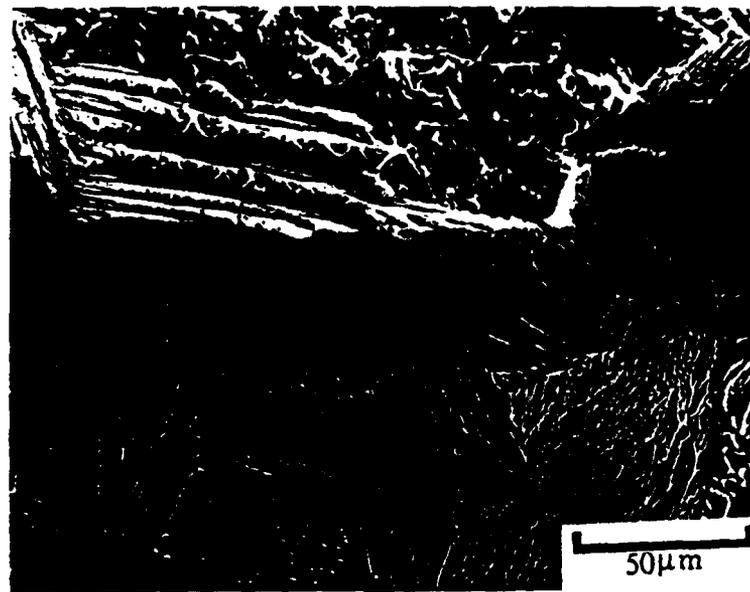
Fig. 4   Fractographs of the control-cool microstructure showing (a) the fracture surface and (b) a plateau etch.

425
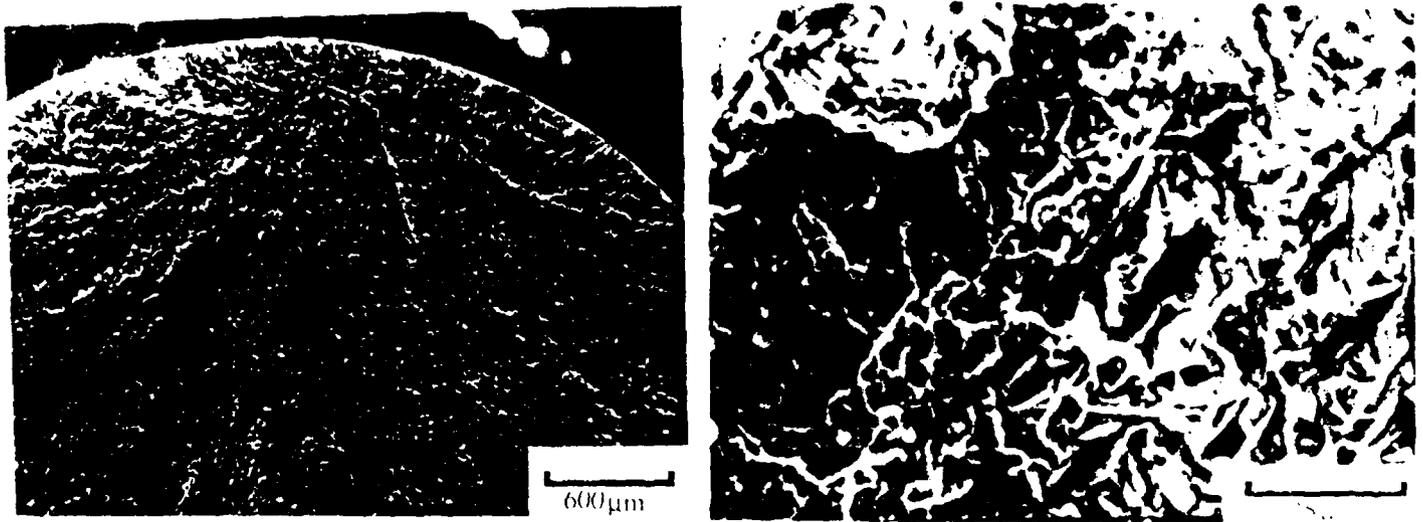
Fig. 5   Fractographs of the air-cooled material are shown in (a) and (b). A plateau
etch is shown in (c).
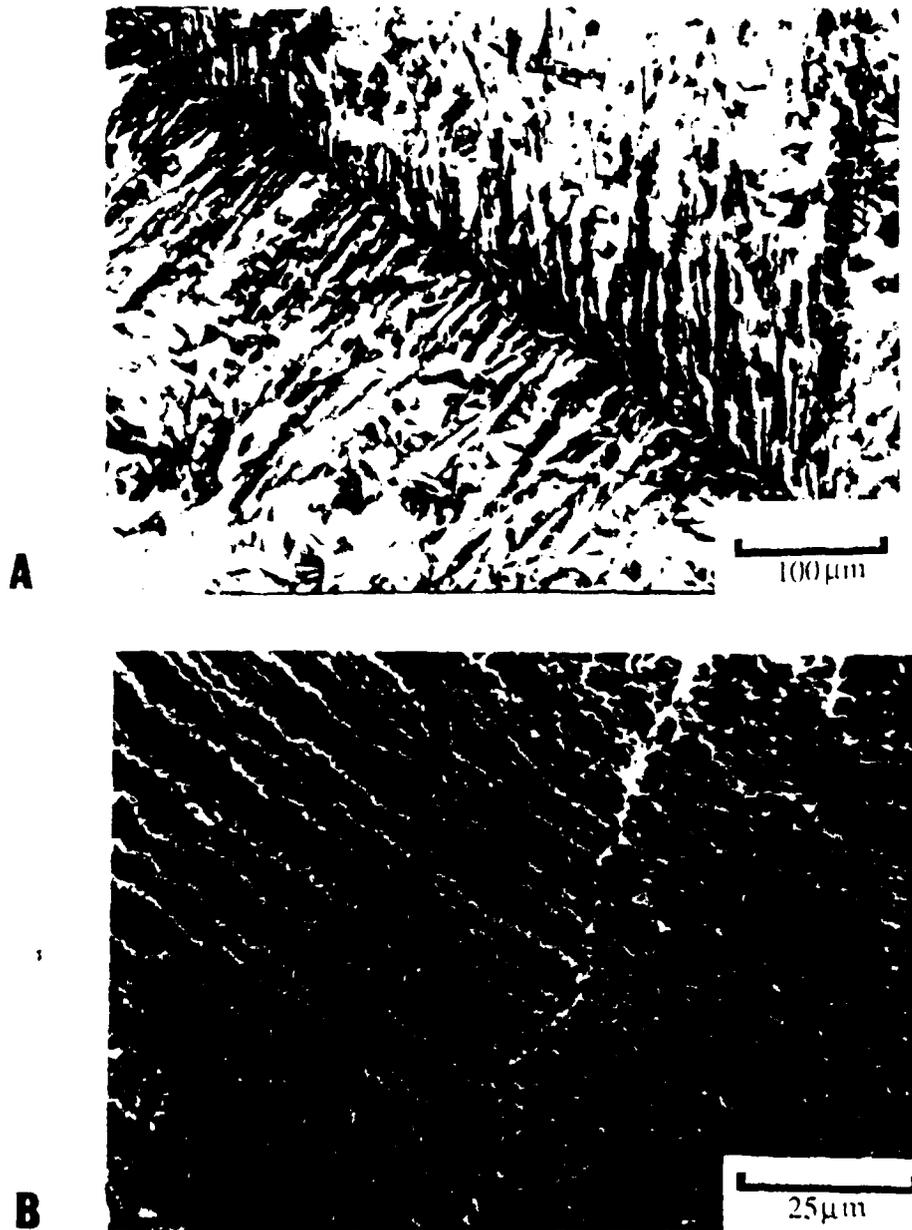
Fig. 6   Comparison of fracture surfaces of (a) the 700°C isothermal microstructure and of (b) the air cooled microstructure.

Fig. 7   Fractographs of the 400°C isothermal microstructure showing (a) a fracture
   surface and (b) a plateau etch.
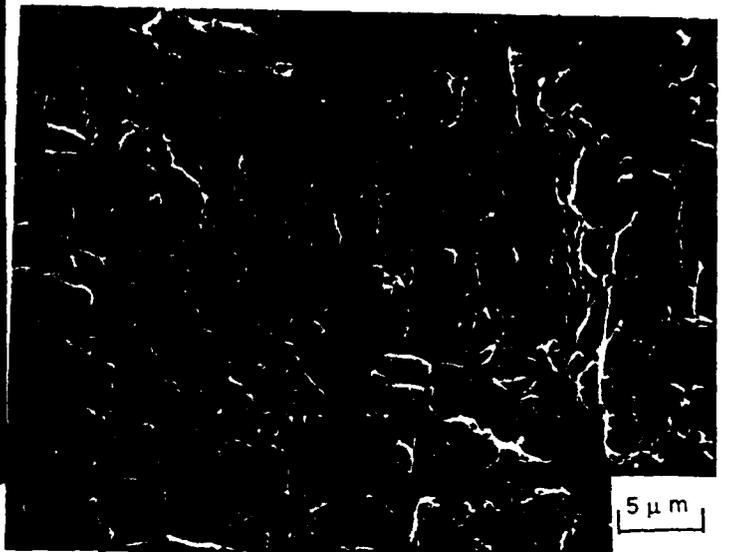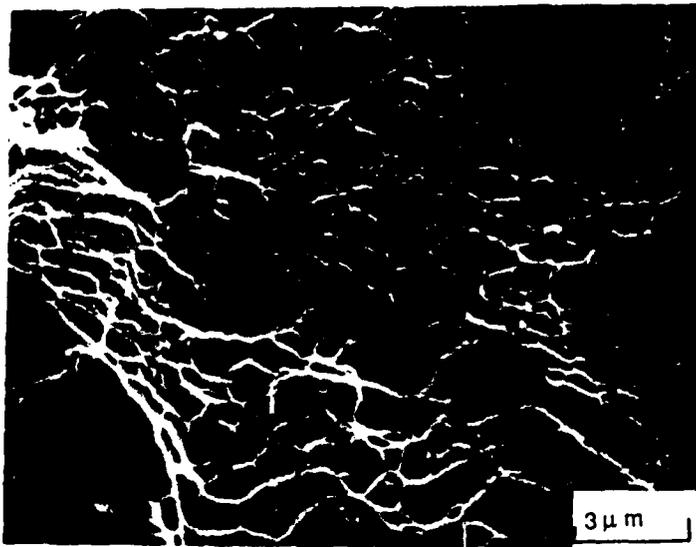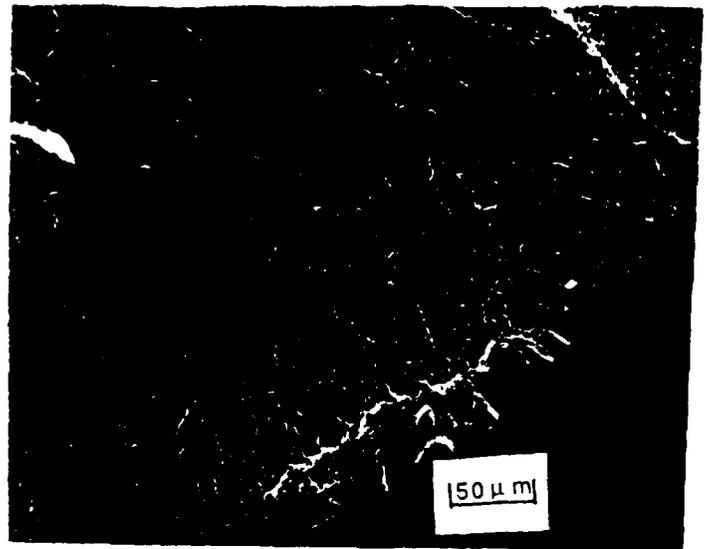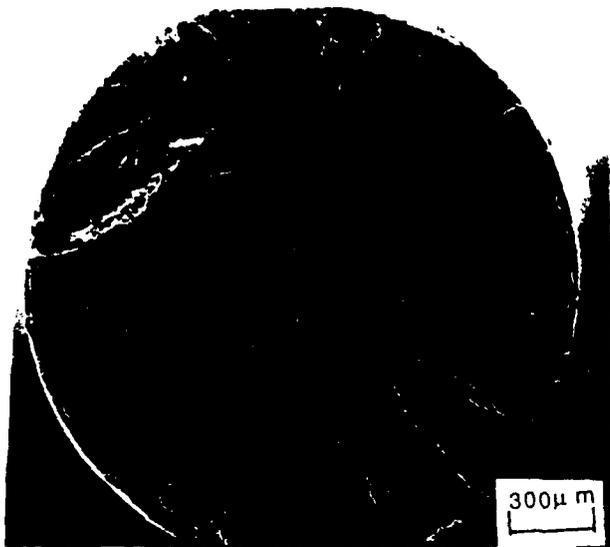
Fig. 8   Fractographs of the 700°C isothermally transformed material tested at room temperature.
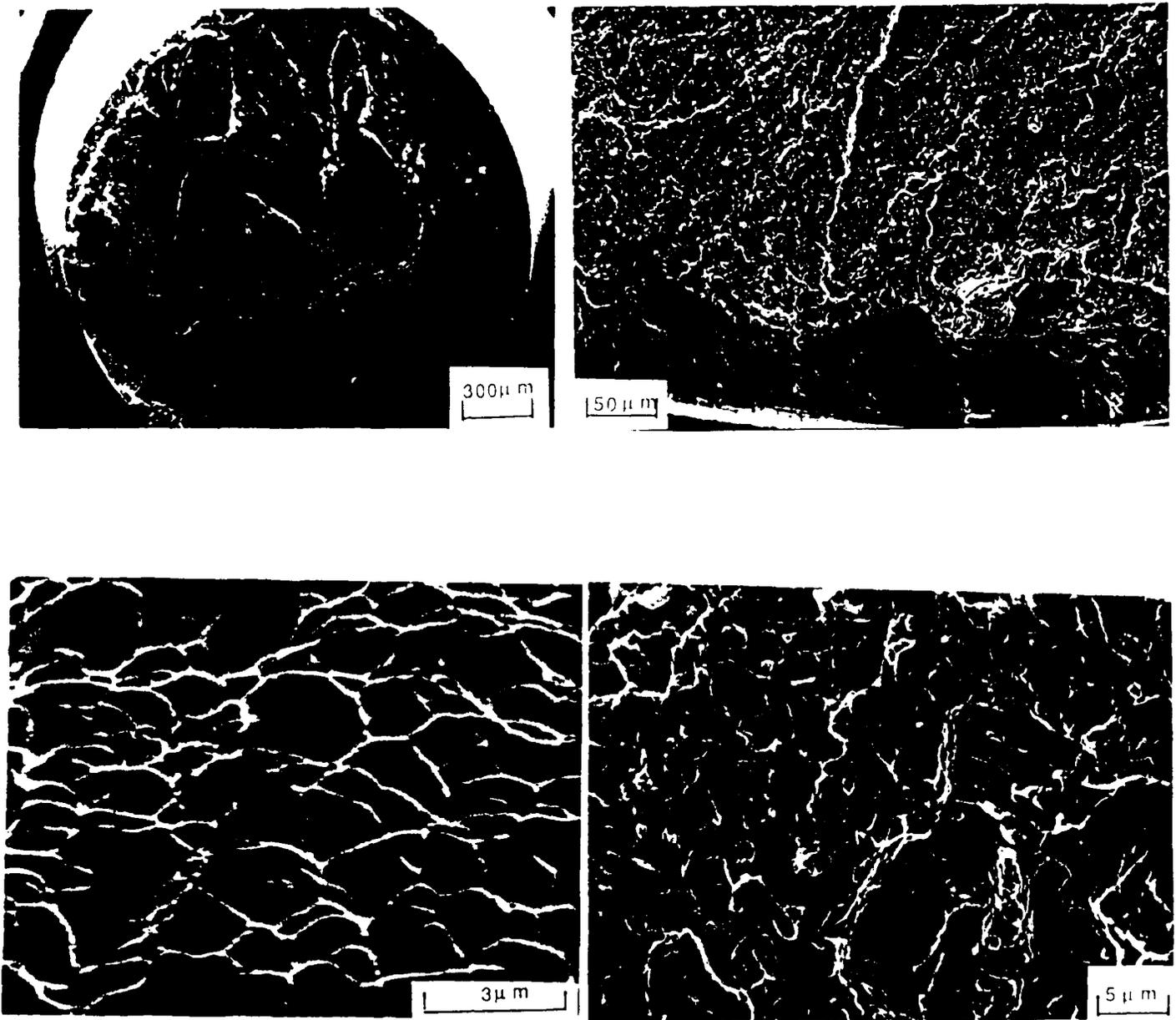
Fig. 9   Fractographs of the 700°C isothermally transformed material tested at 300°C.

Fig. 19   Fractographs of the 700°C isothermally transformed material tested at 500°C.